Dispersions of Graphene for use as Thermal and Functional Fluids

BENJAMIN PIRNIE DOBSON

Dispersions of Graphene for use as Thermal and Functional Fluids

Benjamin Pirnie Dobson

A thesis presented for the degree of
Doctor of Philosophy

Department of Chemistry
Durham University
United Kingdom

March 2018

Dispersions of Graphene for use as Thermal and Functional Fluids

Benjamin Pirnie Dobson

Submitted for the degree of Doctor of Philosophy

March 2018

Abstract:

Graphene's combination of properties makes it a material with great potential in a wide range of applications. High thermal conductivity and good tribological properties mean graphene has been proposed as an additive for both lubricants and thermal fluids; being used to form nanofluids with improved properties. However, the use of graphene in these applications requires the significant challenge of dispersing graphene in applied fluids to be overcome.

In this work graphene, and its functionalised derivatives were dispersed in both polar and non-polar fluids using a range of techniques, following which the properties of these fluids were analysed. Initially, the dispersibility of reduced graphene oxide (rGO) in water was investigated and a novel method of using N-methyl-2-pyrrolidone (NMP) to act as a dispersant for rGO in polar fluids was developed. Using this method dispersions of rGO in water were produced at over six times the concentration possible by standard dispersion.

Working in more applied fluids efforts were made to improve the dispersibility of graphene materials in applied polar fluids such as oils. Stable dispersions of graphene materials in commercial oils were produced through functionalisation of graphene, with a range of

reagents, to improve its compatibility with non-polar solvents. These functionalised graphenes were then dispersed in commercial lubricants to form stable dispersions and the tribological properties of these dispersions were tested showing that it was possible for functionalised graphenes to improve the performance of commercial lubricants.

To assess the impact of graphene on the thermal properties of applied fluids dispersions of graphene materials were prepared in a commercial coolant. The thermal properties of this nanofluid were then determined and it was shown that the addition of graphene materials can improve the thermal properties of applied fluids.

Declaration

The work in this thesis is based on research carried out in the Department of Chemistry, Durham University, United Kingdom. No part of this thesis has been submitted elsewhere for any other degree or qualification and it is all my own work unless referenced to the contrary in the text.

Acknowledgements

Firstly, I would like to express my thanks to my supervisor Professor Karl Coleman for his help, and advice on how to overcome the many challenges encountered throughout this project. Without the benefit of his experience and direction I have no doubt that I would not have reached many of the goals achieved in this project.

Alongside this I would also like to thank our partners on this work at Shell Global Solutions. Particular thanks go to Dr Andrew Greenall and Dr Jochen Lach, as well as other members of the motor sport team that I have worked with, for not only providing the funding for this work but also directing the project, providing samples of commercial fluids and performing tribological and viscosity testing which were essential for determining the success of the project.

The day to day experience of my PhD would not have been anywhere near as enjoyable without my colleagues in the Coleman group while I have been at Durham. In particular I would like to thank Dr David Johnson for being a great source of both good ideas and cynicism in equal measure, and Dr Rebecca Edwards for bringing me into the world of graphene research and passing on her wealth of knowledge.

I would also like to thank the many members of the chemistry department and wider university at Durham who have helped me to record and interpret the wide array of characterisation that is necessary when working with graphene. Douglas Carswell for performing the TGA and DSC analysis detailed in this work. Kelvin Appleby in the electronics workshop for his help in designing and producing the transient hot wire apparatus used for measuring thermal conductivity. Finally to Bhudika Mendis for training me to use the TEM, a technique which I have grown to love and has allowed me to enjoy spending many hours sitting in a dark basement looking at graphene sheets.

Thanks are also extended to the members of the National Engineering and Physical Sciences Research Council (EPSRC) XPS Users' Service at Newcastle University (NEXUS) as well

as the mass spectrometry and NMR services at Durham University.

Whilst all of these people have been essential in completing my PhD from a technical standpoint there are a number of other people I have to thank who have helped me immeasurably in other ways. Before all others, my Fiancée, Kerry, for her “Morrow” support, patience, and being the inspiration I need to keep going every day. My house-mates for the first 3 years of my PhD, Tom and Matty, for being an endless source of entertainment and distractions as well as for answering all of my irritating Python and LaTeX questions. Bob, for being a colleague, a friend, and someone who occasionally let me drag him through the Pennines on a bike. Finally, but by no means least, Arti for keeping me sane, active and getting me out of the house whilst writing my thesis (and for not beagling too many things in the process).

CONTENTS

List of Figures

List of Tables

ABBREVIATIONS

ζ	zeta
0D	zero dimensional
1D	one dimensional
2D	two dimensional
3D	three dimensional
AFM	atomic force microscopy
AISI	American iron and steel institute
ASAP-MS	atmospheric solids analysis probe-mass spectroscopy
ASTM	American Society for Testing and Materials
BSE	back scattered electron
bwGO	base washed graphene oxide
CCD	charge-coupled device
CNT	carbon nanotube
CTAB	cetyltrimethylammonium bromide
CVD	chemical vapour deposition
DAQ	data acquisition
DCC	N,N'-dicyclohexylcarbodiimide
DDA	dodecylamine
DLS	dynamic light scattering
DMF	dimethylformamide
DMFrGO	DMF pretreated rGO
DMSO	dimethyl sulfoxide
DNA	deoxyribonucleic acid
DOPA	di-*n*-octylphosphinic acid
DOPO	di-*n*-octylphosphine oxide
DPP	dendritic polyphenylenes
DSC	differential scanning calorimetry
ED	electron diffraction
EDC	1-ethyl-3-(3-dimethylaminopropyl)carbodiimide
EELS	electron energy loss spectroscopy
EFTEM	energy filtered transmission electron microscopy
EG	ethylene glycol
f-rGO	functionalised reduced graphene oxide
FDGO	freeze dried graphene oxide
FET	field effect transistor
FTIR	fourier transform infrared spectroscopy
FWHM	full width at half maximum
GIC	graphite intercalation compound

GO	graphene oxide
GTL	gas to liquid
HATU	1-[bis(di-methylamino)methylene]-1H-1,2,3-triazolo[4,5-b]pyridinium 3-oxid hexafluorophosphate
HDA	hexadecylamine
HDA-rGO	hexadecylamine functionalised rGO
HOPG	highly oriented pyrolytic graphite
HPLC	high performance liquid chromatography
HREM	high resolution transmission electron microscopy
IPA	isopropyl alcohol
IR	infra-red
ITO	indium tin oxide
MOPA	mono-*n*octylphosphinic acid
MS	mass spectroscopy
MTM	mini traction machine
MWNT	multi-wall carbon nanotube
NI	National Instruments
NMP	N-methyl-2-pyrrolidone
NMPrGO	NMP pretreated rGO
NMR	nuclear magnetic resonance spectroscopy
OA	octylamine
OD	oxidative debris
ODA	octadecylamine
ODA-GO	octadecylamine functionalised GO
ODA-rGO	octadecylamine functionalised rGO
ODOP	*n*-octyl-di-*n*-octylphosphinate
OL	oleylamine
OL-rGO	oleylamine functionalised rGO
OLED	organic light-emitting device
OPA	*n*-octylphosphinic acid
OPV	organic photovoltaeic
PAG	poly(alkylene glycol)
PAH	polyaromatic hydrocarbon
PAO	poly(alpha-olefin)
PMMA	poly(methyl methacrylate)
PP	poly(propylene)
PVA	poly(vinyl alcohol)
PVP	poly(vinylpyrrolidone)
rGO	reduced graphene oxide

SAED	select area electron diffraction
SDBS	sodium dodecyl benzene sulfonate
SDS	sodium dodecyl sulfate
SE	secondary electron
SEM	scanning electron microscopy
SiC	silicon carbide
SLS	static light scattering
SSNRM	solid state nuclear magnetic resonance spectroscopy
STEM	scanning transmission electron microscopy
SWNT	single-wall carbon nanotube
TEGO	thermally expanded graphene oxide
TEM	transmission electron microscopy
TGA	thermogravimetric analysis
THF	tetrahydrofuran
THW	transient hot wire
TMS	tetramethylsilane
TOP	trioctylphosphine
TOP-rGO	trioctylphosphine functionalised rGO
TOPO	trioctylphosphine oxide
TOPO-rGO	trioctylphosphine oxide functionalised rGO
TRIS	tris(hydroxymethyl) aminomethane
USV	ultra-shear viscometer
UV-Vis	ultraviolet-visible
XPS	x-ray photoelecton spectroscopy
XRD	x-ray diffraction

Chapter 1

Literature Review

Carbon is the 6th element of the periodic table and the 4th most abundant element in the solar system.[1] Carbon containing compounds have applications in almost all branches of chemistry, and its range of allotropes, different structural arrangements of pure carbon, have also attracted much attention. Some of these allotropes, such as diamond and graphite, form naturally have been known and used for millennia while other forms have only relatively recently been discovered with those that have attracted the most attention being carbon nanomaterials due to their remarkable range of potential properties.

Interest in the field began with the work of Kroto *et al.* in 1985 on buckminsterfullerene (C_{60})[2] which led to Kroto, Curl and Smalley being awarded the 1996 Nobel Prize in Chemistry. Following on closely were reports of both multi-wall carbon nanotubes (MWNTs)[3] and single-wall carbon nanotubes (SWNTs)[4] in 1991 and 1993 respectively which were shown to have exceptional mechanical strengths,[5,6] as well as good thermal[7,8] and electrical conductivities.[9] The newest chapter in the carbon nanomaterial story came in 2004 with the publication of the seminal paper by Novoselov *et al.* on the isolation of graphene and measurement of its electrical properties[10] which led to Geim and Novoselov being awarded the 2010 Nobel Prize in physics; the second Nobel Prize to be awarded for work on carbon nanomaterials.

Such has been the excitement surrounding this new form of carbon that academic and industrial research into graphene has grown at unprecedented levels, with over 12 000 publications reporting the use of graphene released in 2015. This unprecedented level of interest is a result of the remarkable combination of properties that graphene displays meaning it has huge potential to be a disruptive technology in a wide range of fields.[11]

1.1. Structure of Graphene

Ever since the structure for graphite was determined the existence of individualised sheets of graphite, graphene, has been suggested and studied by theorists.[12] Graphene is defined as a single, two dimensional (2D), sheet of sp^2 hybridised carbon atoms; which create a planar sheet of hexagonally positioned atoms with partially filled, delocalised, π orbitals above and below the sheets. Even though both theory and experiment appeared to show that graphene, and other 2D materials, could not be isolated due to their thermal instability[13,14] Novoselov *et al.* proved that this was not the case and that it is in fact possible to isolate individualised sheets of graphene.[10] It has been proposed that this apparent contradiction is due to the fact that single sheets of graphene do not form as perfect 2D crystals but actually contain microscopic roughness or corrugations which are essential to their stability.[14]

The structures of graphite, graphene and other carbon nanomaterials are all inexorably linked with graphene sheets being the building block for zero dimensional (0D) materials such as buckminsterfullerene, one dimensional (1D) materials such as carbon nanotubes (CNTs), and three dimensional (3D) materials like graphite (figure 1.1).[15]

In spite of its true definition as a single layer of carbon, graphene is often qualified with adjectives such as mono-layer, bi-layer or few-layer since, while only single and bi-layer graphene behave as zero-overlap semi metals,[10,15,16] materials with up to 10 layers continue to show graphene-like properties. When the number of graphene layers exceeds $\sim$10 layers then the properties of the material begin to tend towards those of graphite, showing semi-metallic behaviour, and so the name graphene should be avoided for materials over this thickness.[16]

The stacking behaviour of sheets within few-layer graphene is similar to that seen in graphite. Sheets in graphite have either Bernal (ABAB), or rhombohedral (ABCABC) stacking arrangements[17] with an inter-layer spacing of 3.35 Å,[17,18] whereas those in multi-layer

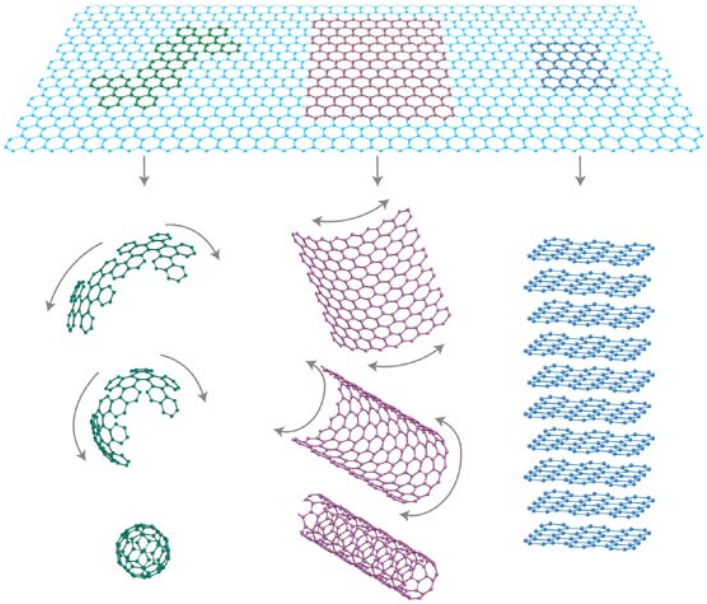

Figure 1.1: *2D graphene sheets as building blocks for 0D buckminsterfullerene, 1D CNTs and 3D graphite. Reprinted by permission from Macmillan Publishers Ltd: Nature Materials 2007,* ***6****, 183–191, copyright 2007.*

graphene have been observed to exhibit a range of stacking behaviours with the most common being: ABA (Bernal, figure 1.2 A)[19–22] stacking; however, ABC (rhombohedral, figure 1.2 B),,[19–22] AA (hexagonal),[23–25] and turbostratic (with no clear order)[26–28] stacking patterns have also been reported. Single-layer graphene can not be described using these stacking patterns and is commonly believed to consist of individualised sheets with microscopic roughness.[14,29,30] This wrinkling leads to the inter-layer spacings found in graphene to be larger than those found in graphite[26] meaning the inter-sheet forces are weaker in graphene than in graphite, facilitating rotation and exfoliation of the layers. The roughness of graphene sheets also inhibits their re-stacking meaning it is not possible to reform graphite from graphene.

In spite of its clear definition in terms of electrical properties graphene is a term that is used in the scientific literature to describe materials with a range of thicknesses and chemistries which can lead to confusion and ambiguity. In order to combat this several systems of nomenclature have been proposed for graphene and its related materials. However, these are not yet widely adopted and so researchers must often draw their own conclusions on the exact nature of materials claimed to be “graphene” by publications.[31,32]

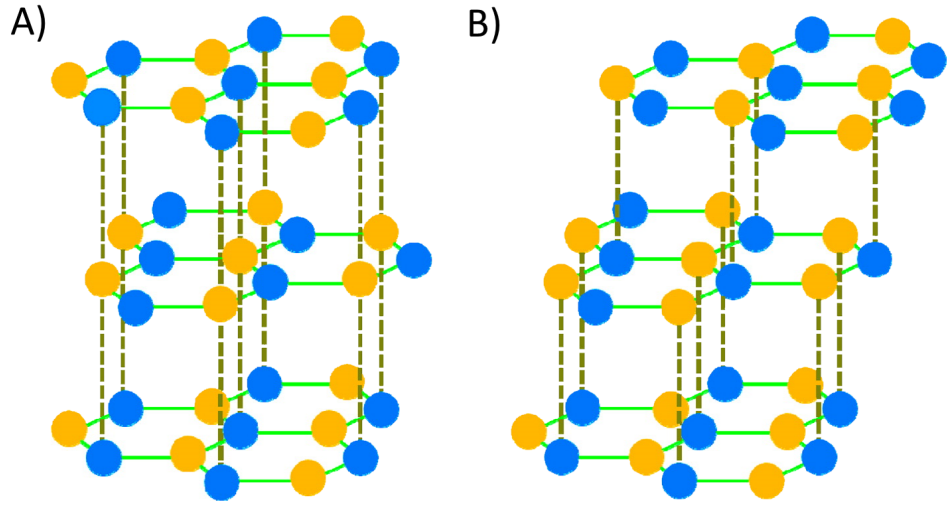

Figure 1.2: *Tri-layer graphene in A) ABA stacked configuration and B) ABC stacked configuration. Reprinted with permission from Nano Letters, 2011,* ***11****, 164–169. Copyright 2011 American Chemical Society.*

1.2. Properties of Graphene

The excitement surrounding the study of graphene has largely been due to its remarkable combination of properties. It has been vaunted as a "wonder material"[33–35] and has presented some of the most impressive physical properties ever measured which in turn has led to the use of graphene being suggested in a huge range of applications.

Graphene has been described as "the strongest material ever measured", with a Young's modulus of $\sim$1 TPa,[36] as well as being resilient to bending and folding without impacting on its other properties.[37–39] It is however, the electrical properties of graphene that have attracted the greatest excitement. Its electron mobilities have been measured at over 200 000 $cm^2\,V^{-1}\,s^{-1}$ with electron densities of $\sim 2 \times 10^{11}\,cm^{-2}$,[40] making graphene an excellent electrical conductor. This is due to the fact that electrons in graphene sheets are conducted *via* ballistic transport, where the electrons behave as massless fermions as described by the Dirac equation, rather than by the Schrödinger equation that normally applies.[41] This allows electrons to travel through the material at extremely high speeds over distances of the order of µm without being scattered.[10,42] Graphene has also been shown to exhibit some unexpected quantum mechanical properties such as the quantum Hall effect;[43,44] which, even more unusually, has been observed at room temperature.[45]

On top of these remarkable electrical properties, graphene's room temperature thermal conductivity has been measured to be in the region of 5×10^3 W m^{-1} K^{-1},[46] which is double that of diamond and over 10 times that of copper. Single-layer graphene has also been shown to absorb 2 % of the light passing through it;[47] a value that is remarkable for a material only one atom thick. Finally, graphene has demonstrated a complete impermeability to gas molecules, even at monolayer thickness.[48] A selection of the properties of graphene are presented in table 1.1.

Whilst each of these properties is impressive when taken in isolation it is the fact that they are all found within one material that makes graphene truly remarkable and has led to the unprecedented excitement that has surrounded its discovery.

Although the properties of graphene reported mean it shows great promise in many applications, care must be taken when examining the methods and materials used for testing as it is often the case that the most remarkable measurements are taken from pristine, isolated and very small sheets of graphene[10,45,46] and such impressive properties may not be achievable for other forms of graphene that can be synthesised using more scalable and practical routes.

1.3. Synthesis of Graphene

Graphene's properties, as described above, undoubtedly make it a great candidate for use in many applications. In spite of this, its uptake has so far been limited by a number of challenges. A major contributor to this has been the difficulty in making graphene in a scalable manner that also produces high quality material with good repeatability. Unlike other carbon nanomaterials, there are two approaches that can be taken when trying to synthesise graphene. These are commonly described as the "top down" and "bottom up" approaches and each has its own benefits and limitations.[35,49] The strengths and weakness of graphene synthesised by a range of methods are shown in figure 1.3. A wide range of

Table 1.1: *A selection of the properties of graphene that have been reported. Data taken from publications referenced in table.*

	Value for Graphene	Other Commonly Used Materials
Charge Carrier Mobility	200 000 $cm^2\ V^{-1}\ s^{-1}$ [40]	Semiconducting CNTs (100 000 $cm\ V^{-1}\ s^{-1}$), [53] Silicon (1400 $cm\ V^{-1}\ s^{-1}$) [54]
Thermal Conductivity	5×10^3 $W\ m^{-1}\ K^{-1}$ [46]	Diamond (2.1×10^3 $W\ m^{-1}\ K^{-1}$), [55] Silver (176 $W\ m^{-1}\ K^{-1}$), [56] Copper (157 $W\ m^{-1}\ K^{-1}$) [56]
Transparency	98 % at only one atom thick [47]	Diamond (>99 % at macroscopic thickness)
Surface Area	2630 $m^2\ g^{-1}$ [57]	Carbon Black (<900 $m^2\ g^{-1}$), [57] CNTs (100-1000 $m^2\ g^{-1}$) [57]
Young's Modulus	1 TPa [36]	MWNTs (250-970 GPa), [6] Steel (210 GPa) [58]

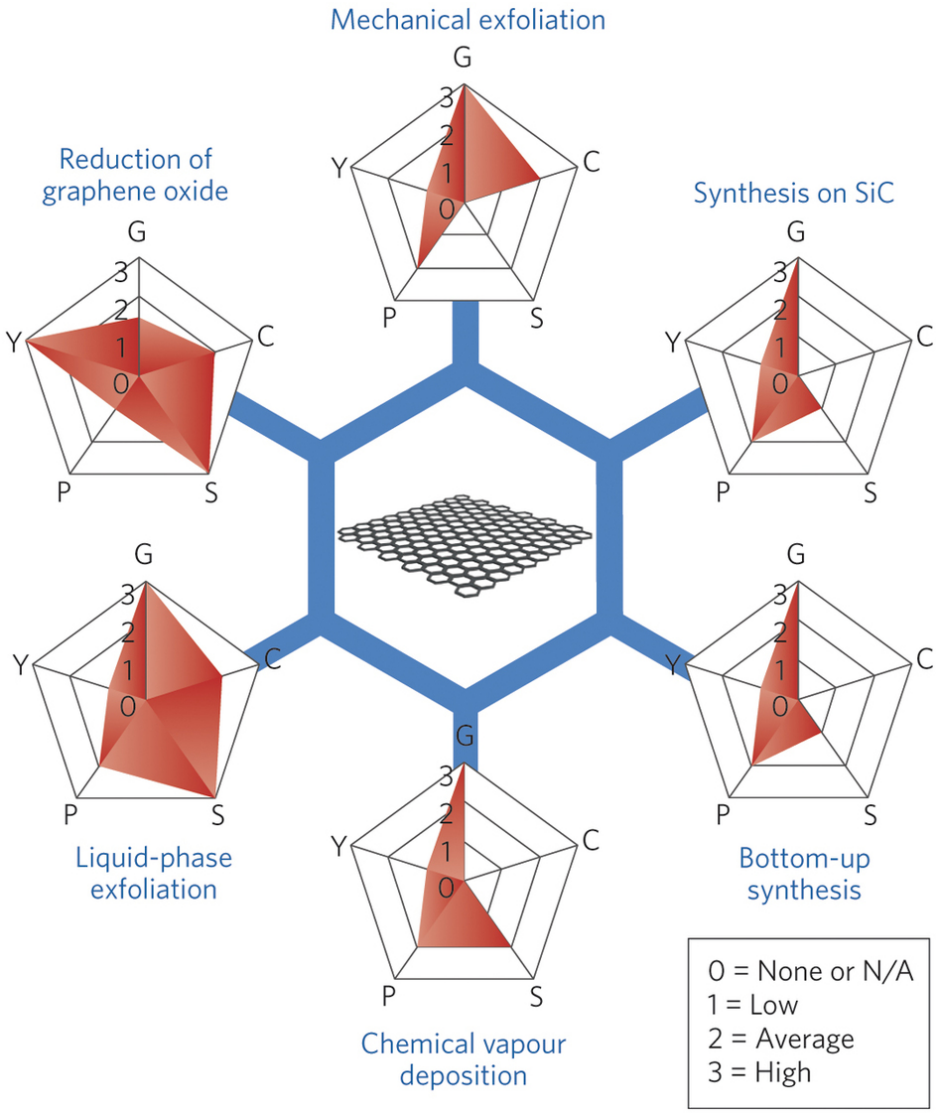

Figure 1.3: *A schematic of some of the most common graphene production methods evaluated in terms of graphene quality (G), cost (C; a low value corresponds to high cost of production), scalability (S), purity (P) and yield (Y) of the overall production process. Reprinted by permission from Macmillan Publishers Ltd: Nature Materials, 2015, **14**, 271–279, copyright 2015.*

methods utilising each of these approaches have been developed and the most widely used will be discussed further below. These and many other techniques for synthesising graphene have been widely reviewed elsewhere in the literature.[35,50–52]

1.3.1. "Bottom Up" Synthesis

"Bottom up" synthetic routes to graphene involve its production from carbon containing compounds that are smaller than the final product. These tend to be small carbon containing molecules, which are either directly used as a feedstock or are produced *in situ* by the

thermal decomposition of a precursor. "Bottom up" syntheses are usually performed under extreme conditions (high temperatures) and on small scales, but have the advantage of being able to produce extremely high quality, pristine, sheets of graphene. The most commonly used methods for the "bottom up" synthesis of graphene will be outlined below.

1.3.1.1. Chemical Vapour Deposition

Chemical vapour deposition (CVD) is generally considered the most popular "bottom up" route for synthesising graphene.[52] First reported as a method to synthesise few layer graphene in 2006,[59] CVD is a heterogeneous catalytic process in which carbon containing gasses are pyrolysed at extremely high temperatures in the presence of a solid catalyst, usually a transition metal, causing a graphene film to grow on the surface of the catalyst.[35] CVD can also be used as a method to synthesis CNTs,[60,61] and diamond[62] with the choice of catalyst, feedstock, and conditions being vital in controlling the morphology of the carbon material produced.

After synthesis by CVD, the graphene formed needs to be removed from the catalyst it was grown on. This is most commonly achieved through its transfer onto a support such as poly(methyl methacrylate) (PMMA) which is not a trivial process which and can be highly time consuming; often resulting in damage to the graphene.[63,64] This is one of the main factors limiting the scalability of CVD as a method of synthesising graphene.[65]

In spite of this, some of the best quality graphene produced has been made using CVD techniques.[51] This makes CVD graphene an ideal candidate for use in applications that require small quantities of films of highly electrically conducting graphene such as for use in device electrodes and as a replacement for indium tin oxide (ITO). The synthesis of graphene by CVD has been thoroughly reviewed elsewhere.[66]

1.3.1.2. Growth from Silicon Carbide

Another possible method for the synthesis of graphene is through its epitaxial growth on silicon carbide (SiC). It was first demonstrated in 1965 that it was possible to form graphitic carbon through the heating of SiC to >2000 °C.[67] The reaction proceeds through the preferential sublimation of silicon from the surface of the SiC to leave a film of carbon behind which is then graphitised by the high temperature (figure 1.4).[68] The first reports of this method to produce graphene were published in 2004,[69] the same year as Novoselov *et al.* reported the isolation of graphene through micromechanical cleavage, although it is possible that graphene was produced from SiC prior to this but not characterised as such.

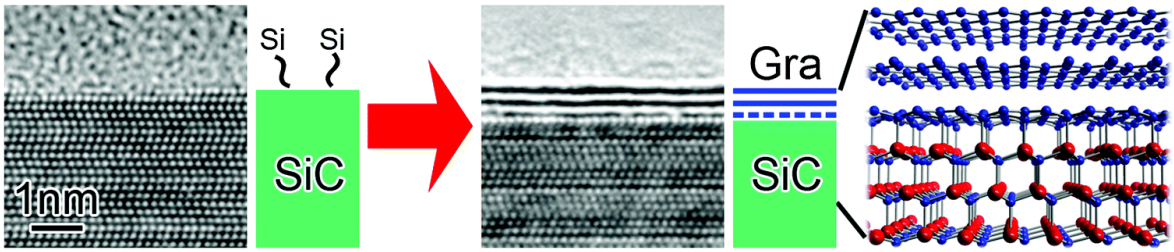

Figure 1.4: *A schematic showing the process by which graphene is produced from SiC, via the preferential sublimation of silicon. Reproduced from Physical Chemistry Chemical Physics, 2014, **16**, 3501–3511, with permission of the PCCP Owner Societies.*

Generally the synthesis of graphene from SiC requires very high temperatures (>1000 °C) at ultra-high vacuum pressures or in inert gasses.[68] This makes the production of graphene from SiC very expensive on a large scale meaning it is not a popular route of synthesising graphene industrially. The graphene produced, however, is of high quality and so has the potential to be used in electronic applications where small volumes of high quality materials are required. The synthesis of graphene from SiC has been recently reviewed in detail by Norimatsu and Kusunoki.[70]

1.3.1.3. Other "Bottom Up" Synthetic Routes

Alongside the methods discussed above a range of other methods for the production of graphene have been proposed in the literature. The majority of these remaining methods make use of building blocks containing polyaromatic hydrocarbons (PAHs), small aromatic

hydrocarbons containing at least two fused benzene rings, which can be chemically bound together to produce larger aromatic molecules. This process is then repeated to form graphene.

Graphenes produced using these methods generally fall into two categories: graphene molecules and graphene nanoribbons.[71] Graphene molecules is a name used to describe sheets of graphene with sizes of 1-3 nm. A wide range of graphene molecules can be produced and a selection of these are shown in figure 1.5. The most common route used to synthesise these molecules begins with dendritic polyphenyleness (DPPs) due to their plentiful and conveniently arranged benzene rings.[72] These DPPs can then be converted to graphene molecules by cyclodehydrogenation, usually using Lewis acids such as $FeCl_3$, and $AlCl_3$.[71,73] Careful control of the DPPs used allows the shape and size of the graphene molecules produced to be controlled as well as the exact shape and conformation of their edges.[71]

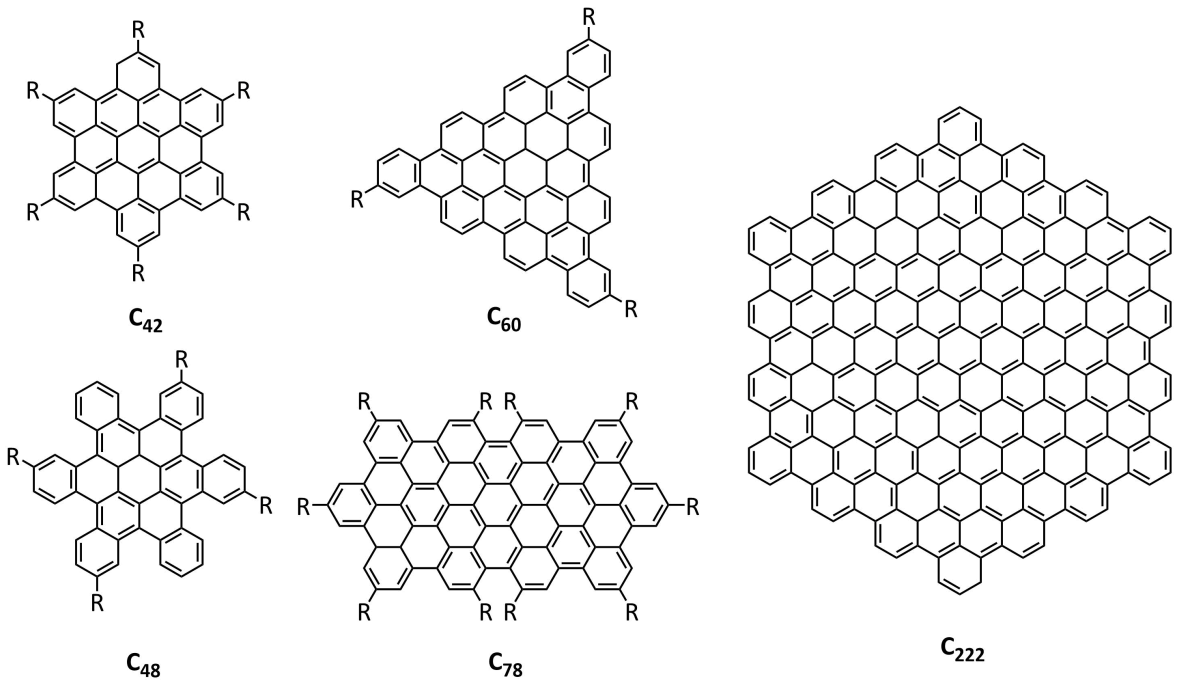

Figure 1.5: *The chemical structures of some commonly produced graphene molecules.*[71]

Graphene molecules have been shown to have similar properties to larger graphene sheets with poor solubility in most solvents meaning that functionalisation is often required in order to disperse them.[71,73] The logical next step from synthesising graphene molecules was to attempt to produce larger graphene nanoribbons with controlled edge chemistries

and sizes from 1D starting materials.[71] The challenge in producing these materials is the synthesis of appropriate precursor DPPs which must have the same shape as the desired graphene nanoribbons.[74] These DPPs can then be cyclodehydrogenated, as has been described above. However, it is also possible to produce graphene nanoribbons by other methods including Suzuki polymerisation, both conventionally[75] and using microwave assistance.[71]

One of the advantages of these chemical methods of graphene synthesis is that they produce graphene with well controlled sizes and structures as well as allowing for extremely small sheets to be produced which is not easily achievable using other synthetic methods. This also represents one of the greatest limitations of the molecular synthesis of graphene, in that it is only possible to produce small graphene sheets, which may not be suitable in all applications.

1.3.2. "Top Down" Synthesis

"Top Down" routes to synthesising graphene involve using a starting material which is larger than the final product - generally graphite. The layered structure of graphite allows it to be broken apart into individualised graphene sheets: a process known as exfoliation. However, the strong inter-layer forces present between adjacent sheets mean this is not trivial and requires a significant input of energy in order to separate sheets from the bulk graphite. As a result of this a number of techniques have been developed to either impart this energy or to reduce the energy required for exfoliation to occur. The "top down" synthesis of graphene is unusual when compared to the synthesis of other carbon nanomaterials, which is exclusively done by "bottom up" routes as both C_{60} and CNTs do not have a larger parent material that can be separated to produce them.

1.3.2.1. Mechanical Exfoliation of Graphite

Also known as micromechanical cleavage; mechanical exfoliation of graphite was the method originally used to isolate graphene in the seminal work by Novoselov *et al.*[10] Starting

from either natural flake graphite or highly oriented pyrolytic graphite (HOPG), mechanical stresses are used to overcome the forces holding the layers together, producing single sheets of graphene. Several approaches can be used to apply this mechanical force.

The simplest form of mechanical exfoliation involves the use of adhesive tape to repeatedly cleave HOPG forming thinner and thinner sheets, until ultimately single layer graphene can be produced. This gives this process its more common name of the "scotch tape" method. While Novoselov *et al.* [10] are widely credited with being the first to use this method, in 1999, Lu *et al.* also reported a similar method of cleavage of HOPG and although they did not successfully produce graphene they theorised that it should be possible to do so by more rigorous exfoliation.[76] This procedure produces extremely high quality graphene with very few defects but is highly labour intensive and generates very small quantities of graphene. Flakes can be produced with sizes of the order of millimeters,[33] limited by the size of the single crystalline grains in the starting graphite.[77]

An alternative approach that can be used to mechanically exfoliate graphite is the use of ball milling. Dry ball milling usually requires chemically inert salts to be added to the graphite to increase abrasion and allow exfoliation to occur.[78,79] However, in spite of ball milling's potential scalability, it is not without its drawbacks. The energies required are so high that sheets of graphene produced are small with large numbers of defects in the sp^2 lattice, which can impact on its properties,[80] and exfoliation to single layer graphene is not usually achieved.[78,79] The mechanical exfoliation of graphite has been reviewed elsewhere.[77,80]

1.3.2.2. Liquid Phase Exfoliation of Graphite

Mechanical exfoliation is not the only method for the production of graphene by delamination of graphite. It has also been shown it is possible to obtain graphene by exfoliation in the liquid phase.[81,82] This process was first reported in 2008 when Hernandez *et al.* showed that it was possible to obtain monolayer graphene *via* the bath sonication of graphite in NMP.[81] The following year it was reported that the exfoliation of graphite to form graphene

could also be performed using water as a solvent when combined with a carefully selected surfactant.[82] In this process the shear forces produced during sonication, combined with cavitation - the formation and collapse of microbubbles between graphene sheets, leads to exfoliation of the graphitic sheets.[83,84] A schematic of the process of liquid phase exfoliation is shown in figure 1.6

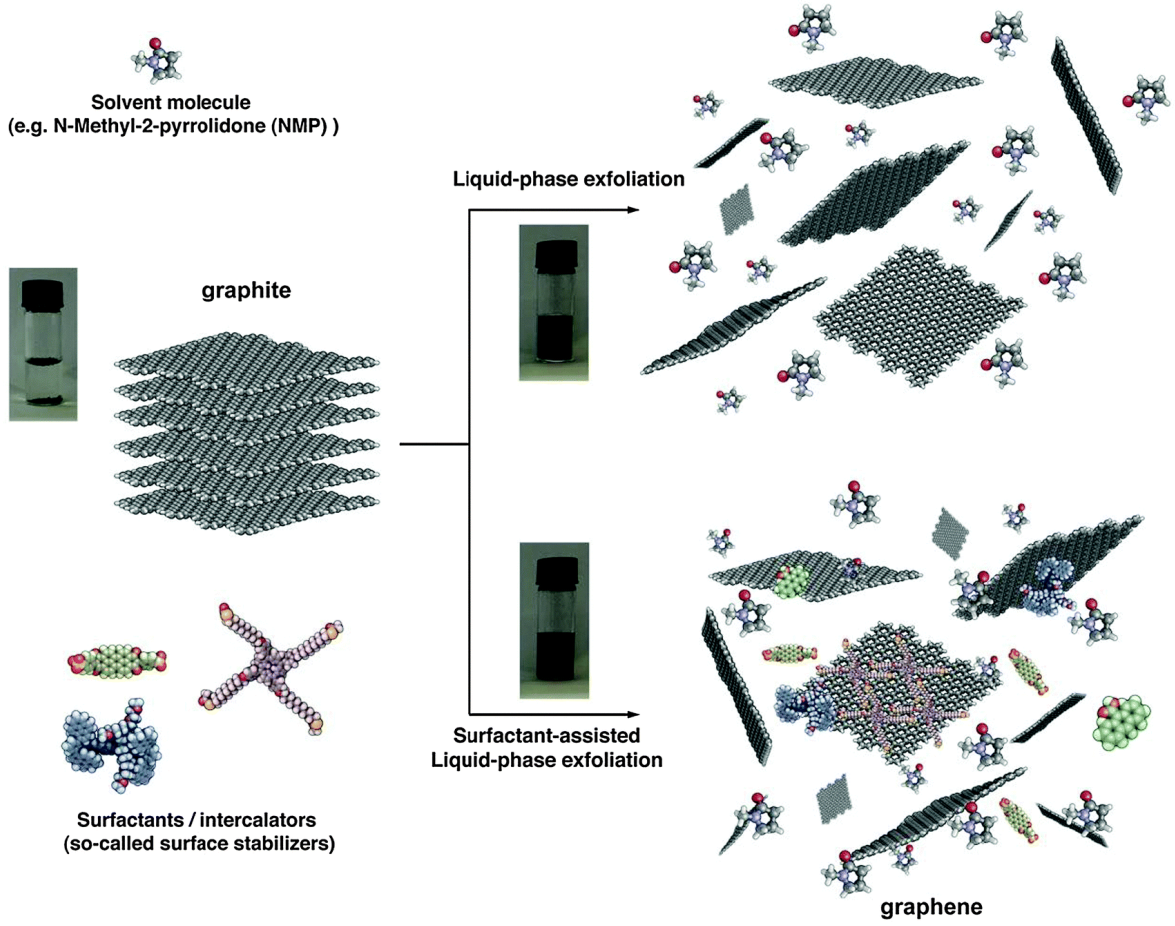

Figure 1.6: *A schematic representation of the liquid phase exfoliation of graphite; either through the use of solvents (top) or surfactants (bottom). Reproduced from Chemical Society Reviews, 2014,* ***43****, 381–398, with permission of The Royal Society of Chemistry*

The choice of solvent and surfactant are both extremely important when exfoliating graphite.[85] Key factors that influence their ability to exfoliate graphite to graphene include the surface tension of the solvent as well as its solubility parameters. The best solvents for the production of graphene are those which match the Hansen solubility parameters of graphene with NMP able to produce the highest proportion of single layer graphene at 29 % of all sheets produced while cyclopentanone gave the highest concentration of few layer

graphene sheets.[86] Surfactant based exfoliation of graphite is usually performed in water, using one of a range of surfactants including sodium dodecyl benzene sulfonate (SDBS),[82] sodium cholate,[87] and cetyltrimethylammonium bromide (CTAB).[88] It is believed that surfactants improve the compatibility between the water and graphite allowing sonication to act more effectively on the layers within the graphite sheets.[84] Certain surfactant molecules are also believed to be able to intercalate between the graphite layers, aiding exfoliation.[89]

Whilst sonication is the most common method, liquid phase exfoliation can also be performed using high shear mixing.[90] Several reviews on the liquid phase exfoliation of graphite can be found in the literature.[83–85,91] Even with the aid of carefully selected solvents and surfactants the exfoliation of graphite in the liquid phase is not trivial and requires significant amounts of energy from ultrasonication or high shear mixing which can result in damage to the graphene sheets produced, impacting on their properties[92] although it is claimed that liquid phase exfoliation is able to produce graphene that is relatively defect free in spite of the high energy processing used.[85]

1.3.2.3. Graphite Intercalation Compounds

It is possible to reduce the energy required to exfoliate graphite to graphene by increasing the spacing between adjacent sheets within the graphite. This can be achieved by introducing compounds into the space between the graphene sheets, pushing them further apart; a process known as intercalation. The compounds formed are commonly known as graphite intercalation compounds (GICs). There are a great number of reagents that can be used to intercalate graphite ($\gg$100); however, for the synthesis of graphene certain intercalants are favoured including: alkali metal ions such as Li^+ and K^+, bisulfates (HSO_4^-), and perchlorate (ClO_4^-).[17]

The precise nature of the GIC produced is dependent on both the intercalant chosen and the degree of intercalation obtained. The most important characteristic of a GIC is its stage index, *n*, where *n* denotes the number of graphite layers between the layers of inter-

calant (figure 1.7).[17,93] Certain intercalants are known to preferentially form different stages of GICs and this can affect the graphene that it is possible to produce using them as a starting material. GICs which have a low stage index and so have a greater proportion of intercalant will exfoliate more easily. However, there is a greater chance of damage to the graphene sheets during the exfoliation. As the stage index increases, the relative number of layers of intercalant decreases and so the likelihood of producing mono-layer graphene is reduced. However, the material produced is likely to have fewer defects. Therefore a balance must be achieved when producing graphene using GICs.

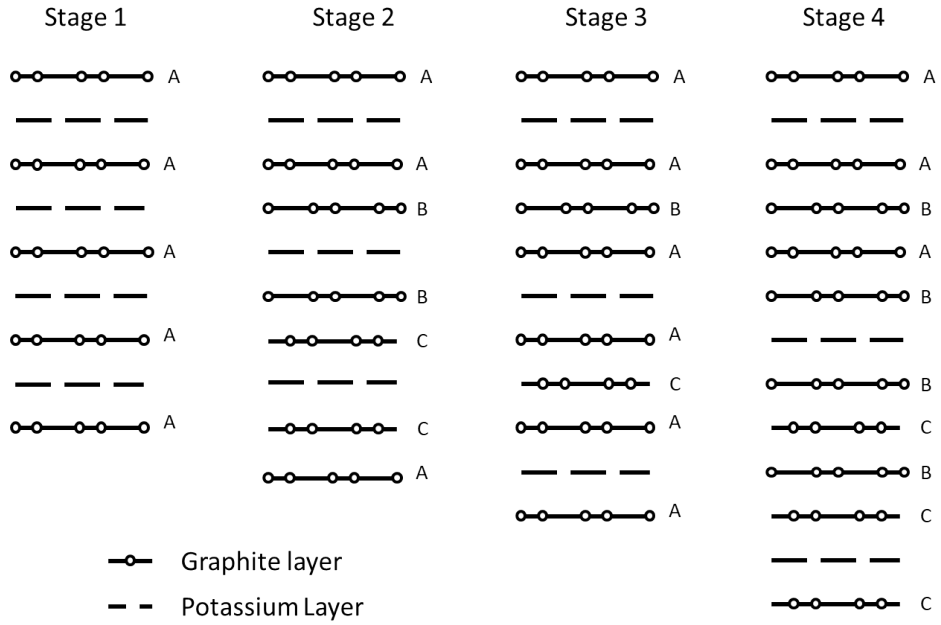

Figure 1.7: *An illustration of the structure of GICs with different possible stage indices for a potassium-graphite GIC for $1 \leq n \leq 4$.*

Once a GIC has been formed it can then be exfoliated *via* either solvent assisted sonication or thermal expansion. In either of these processes gasses are produced as a result of the intercalants between the layers which forces the adjacent sheets further apart, and leads to exfoliation. It has also been reported that certain solvents can cause specific GICs to spontaneously exfoliate to form graphene due to the production of gasses between the layers.[94]

Research on GICs began many years before their use as a precursor for graphene was known. Bisulfate GICs have been been used for many years in industry as a material known

as “expandable graphite”. When thermally or microwave expanded[95,96] this GIC expands to over 2 times its original volume forming “expanded graphite” which is widely used in application such as gaskets, seals, and thermal insulators, amongst others.[97] This expansion is not enough to completely exfoliate the sheets and they still remain inter-connected. It has since been shown that further processing of “expanded graphite”: either by grinding in oleum,[98] or sonication in NMP[99] can produce graphene sheets. Using HOPG as a starting material, instead of natural graphite, allowed graphene to be produced by simply grinding the “expanded graphite” in solvents.[100]

The main flaw in this approach is that, even after intercalation, exfoliation is often still not a trivial process meaning the material produced often has many layers or is very small, due to damage caused during exfoliation.[98,99,101,102] The reason for this is that the compounds used to intercalate the graphite not only affect its inter-layer distance, but also the binding energy of adjacent sheets. Charge transfer between sheets through intercalated molecules can actually lead to stronger inter-sheet interactions than are found in graphite in spite of the increased inter-layer spacing.[93] Yoon *et al.* found that commonly used intercalants such as lithium and potassium caused an increase in binding energy whereas intercalating neutral species, such as KCl or benzene decreased the interaction energy between sheets as well as increasing the inter-layer spacing meaning exfoliation should be easier (figure 1.8).[93]

1.3.2.4. The Graphene Oxide Route

One of the most widely used routes for the synthesis of graphene is *via* graphene oxide (GO). This method may even have led to the first synthesis of graphene in 1859 by Brodie although he did not have the tools to characterise what he had produced at the time.[103] The process begins with natural flake graphite which is oxidised: increasing the inter layer spacing and facilitating exfoliation. Individualised sheets can then have their oxygen functionality removed to form rGO, which has many of the same properties as pristine graphene even though its structure still contains some defects. GO is a complex and diverse material which is the main focus of this thesis and so merits detailed discussion. The synthesis,

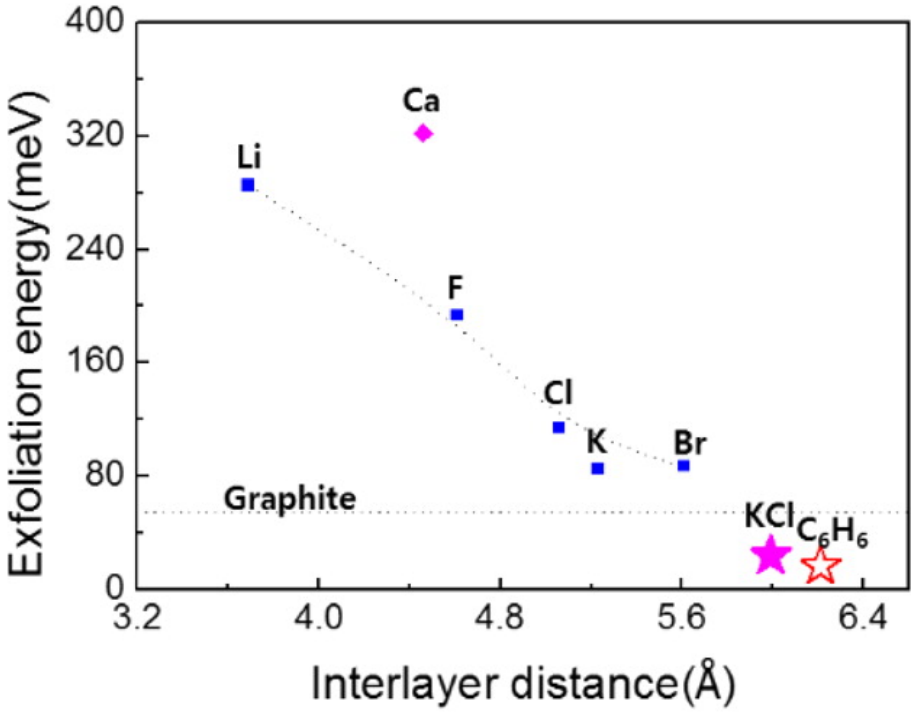

Figure 1.8: *A plot of exfoliation energy versus inter-layer distance for GICs intercalated with a range of intercalants. Reprinted with permission from Chemistry of Materials, 2015,* ***27****, 2067–2073. Copyright 2015 American Chemical Society.*

properties, and structures of GO and rGO are covered in depth in section 1.5.

1.3.2.5. Unzipping of Carbon Nanotubes

An alternative possible method for the "top down" synthesis of graphene is to use CNTs as a precursor material as opposed to graphite. These are cut lengthwise, using one of a range of processes, to give graphene sheets (figure 1.9). One of the main advantages of this method is that the dimensions of the graphene sheets produced are determined by the dimensions of the starting CNTs. This means that the products of unzipping CNTs have consistent dimensions and shapes and are generally referred to as graphene nanoribbons due to their shape. The methods used to produce graphene nanoribbons from CNTs include: the use of highly oxidising conditions,[104,105] plasma etching,[106–108] excimer laser irradiation,[109] sonication,[110] and cryo-milling;[111] nanoribbons can be produced using either SWNTs[104,107] or MWNTs[105,106,108–111] as a starting material. Depending on the choice of reagents used the nanoribbons produced can be either graphene like[110] or more similar to GO.[104,107]

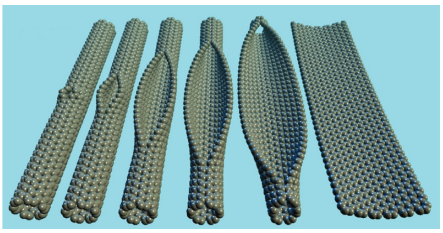

Figure 1.9: *A representation of the unzipping of a CNT to form a graphene nanoribbon. Reprinted by permission from Macmillan Publishers Ltd: Nature, 2009,* ***458****, 872–876, copyright 2009*

The restrictions on the size and aspect ratios of graphene produced *via* these methods could be seen as a limitation for the unzipping of CNTs. However, for some electronic applications graphene sheets with these aspect ratios can be highly desirable as their confined dimensions make them semiconducting; unlike graphene which is a semi-metal and CNTs whose electronic properties depend on their exact chirality.[106] This means unzipping of CNTs is a method that can be used to produce graphene with a band gap, without the need to induce one which can be challenging to achieve.

1.4. Applications

As a result of graphene's incredible range of properties, discussed in section 1.2, it is understandable that its use in a wide range of applications has been suggested. For each of these potential applications certain of graphene's properties will be key, whilst others will have less relevance. The fact that graphenes synthesised by different methods often have different properties means that end application must be taken into consideration when choosing the method used to produce the graphene.[35] The key properties for some of graphene's main applications are shown in table 1.2. This section will cover some of the more widely discussed applications in which attempts have been made to utilise graphene.

1.4.1. Electrical Applications

Much of the excitement surrounding the development of graphene is due to its potential in electronic applications. A main driving force in the field of electronics is to reduce

Table 1.2: *The important properties of graphene for a range of applications. A tick indicated that the property is important, a cross that is not essential, and a blank indicates the property may be important. Reproduced from Nanoscale, 2013, **5**, 38–51, with permission of The Royal Society of Chemistry.*

	Electrical Conductivity	Mechanical Strength	Elasticity	Surface Area	Thermal Conductivity	Chemical Inertness	Gas Impermeability
Transistors	✓	✗	✗	✗	✗	✓	✗
Energy Storage Devices	✓	✗	✗	✓	✗	✓	✗
Electrodes	✓				✗	✓	✗
Conductive Inks	✓	✗	✓	✗	✗	✓	✗
Polymer Composites	✓	✓	✓	✓	✓	✓	✓
Sensors	✓	✗		✗	✗	✓	
Functional Fluids	✓	✗	✗		✓	✓	✗

the size of devices as well as improving performance.[112] Graphene's structure and electrical conductivity make it an ideal candidate to replace conventional semiconductors, such as silicon, or metallic conductors which both perform poorly at extremely small sizes.[112] However, pristine graphene has the handicap that it is naturally a zero-band-gap material and so in order to utilise graphene as a semiconductor, chemical changes must be made in order to create the "on" and "off" states required.[113] This can be done either by using graphene of strictly confined dimensions, such as nanoribbons,[114,115] doping the graphene with heteroatoms such as nitrogen[116,117] or hydrogen,[113] or by straining the sheets.[118] It has also been observed that pristine bilayer graphene can exhibit a band gap which is believed to be due to small asymmetries being present between the two sheets.[119,120]

The semiconducting properties of these graphene materials mean that they have potential applications in transistors, principally in field effect transistors (FETs).[121] It is believed that current techniques used to produce FETs are reaching a size limit, and that in order to continue the drive for smaller transistors new approaches must be taken.[121] Graphene is believed to be a good candidate to replace the traditional silicon and metal oxides used in FETs with the first example of a graphene FET demonstrated in 2007;[122] with rapid progress being made in the field and gigahertz graphene FETs being reported in 2008.[123] Graphene transistors have been reviewed elsewhere.[121]

An alternative side of the electronic applications of graphene is its potential to be used in both organic photovoltaeic (OPV) and organic light-emitting device (OLED) applications, as a range of components within each of these devices. Both OPVs and OLEDs contain transparent electrodes, usually composed of ITO; however, this it is far from an ideal material in many applications as it is costly, brittle and of limited availability.[124] Graphene's transparency, flexibility and electrical conductivity make it an obvious replacement for ITO in transparent electrodes and graphene electrodes have been demonstrated in both OPVs[125–127] and OLEDs.[128,129] As well as acting as an electrode material graphene has also been shown to have potential as an electron acceptor,[130] or a hole transport layer[131] in OPVs.

One great advantage of graphene's use in photonic applications is that its flexibility brings us closer to fully flexible devices.[132] The use of graphene in OPV[124,133] and OLED[133] applications has been recently reviewed in detail elsewhere.

1.4.2. Energy Storage Applications

Graphene has been proposed as a material for use in a range of energy storage applications, both as an active material or as an inactive component.[49] Super-capacitors are energy storage devices that exhibit extremely fast charge and discharge rates over large numbers of cycles, whilst still maintaining high energy densities[134–136] and graphene has been shown to have good potential as an electrode material in electrochemical capacitors due to its electrical conductivity, high surface area, flexibility and the the range of chemistries that it can undergo.[136]

These same properties have also aided graphene in its use as both an anode[137] and cathode[138] material in conventional lithium ion batteries, an electrode material[139,140] and a sulfur immobiliser[141] in lithium-sulfur batteries, and as an electrode material[142,143] and a catalyst[144] in lithium-air batteries. Some of the potential applications for graphene in energy storage applications are shown in figure 1.10.[145]

Finally, it has been shown that, when correctly processed, graphene can act as a catalyst for the oxygen reduction reaction that occurs within fuel cells,[146] as a support for more traditional catalyst materials,[147,148] as well as having potential as a membrane material.[149] This topic has been reviewed in greater detail elsewhere in the literature.[49,150,151]

1.4.3. Mechanical Applications

The mechanical properties of graphene, mentioned in section 1.2, have led to suggestions for its use in many applications in order to enhance mechanical strength. Due to the nature of graphene, and the difficulty of producing it, it is not suitable to use pure graphene

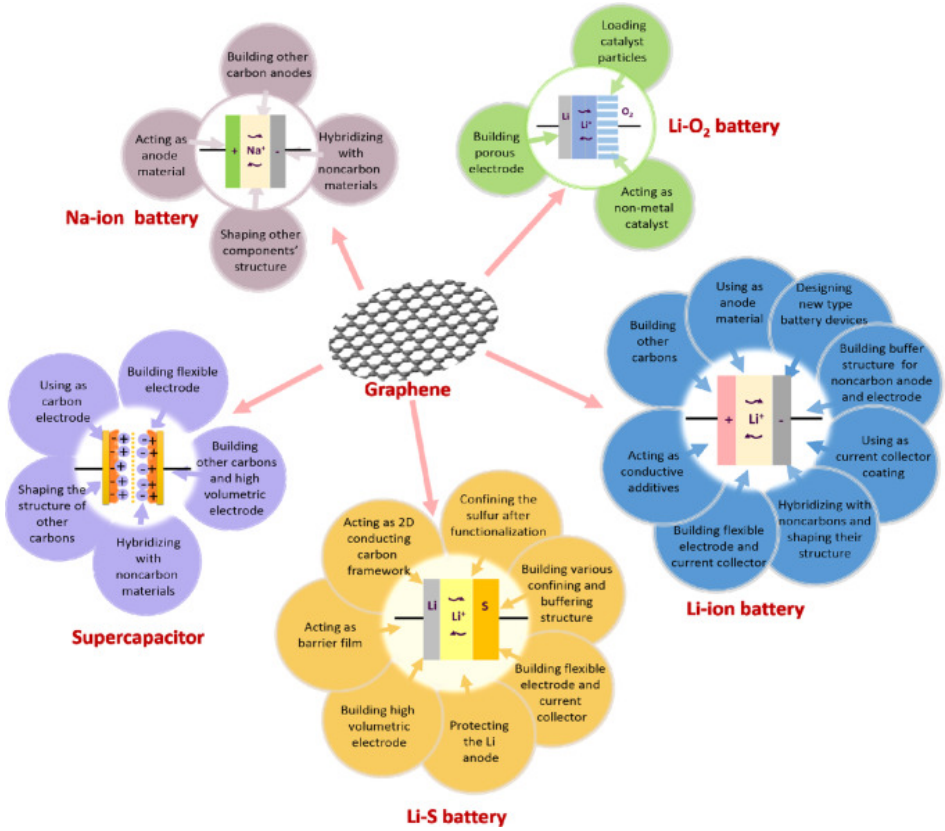

Figure 1.10: *A range of the potential applications for graphene materials in energy storage devices. Reprinted from Energy Storage Materials, **2**, W. Lv et al., Graphene based materials for electrochemical energy storage devices: Opportunities and challenges, 107–138, Copyright 2016, with permission from Elsevier*

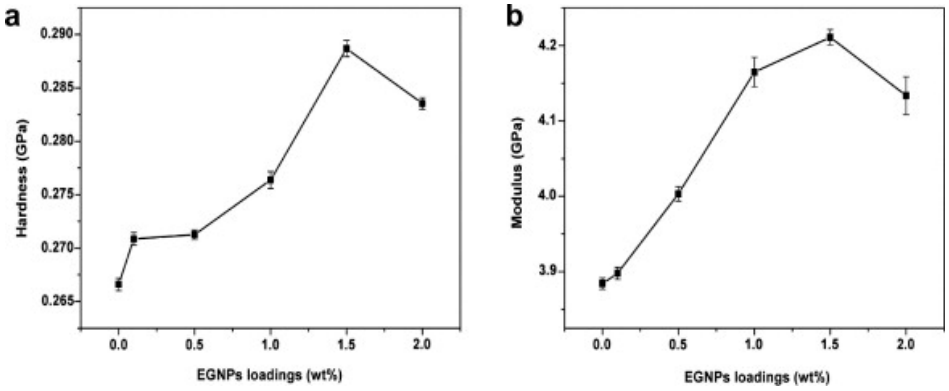

Figure 1.11: *The A) hardness and B) modulus of graphene nano-platelet (EGNP), epoxy composites at a range of loadings of EGNPs, showing mechanical enhancement. Reprinted from Chemical Physics Letters, **531**, S. Chatterjee et al., Mechanical reinforcement and thermal conductivity in expanded graphene nanoplatelets reinforced epoxy composites, 6–10, Copyright 2012, with permission from Elsevier.*

in mechanical applications. Graphene can, however, be used to create composite materials with mechanical properties that are greatly improved over those of the bulk material.[11,152]

The most commonly used graphene composites are polymer composites. In these a

graphene filler material is added into a bulk polymer matrix. In order for graphene's properties to have a significant impact, it must be used at a concentration where an interconnected network of sheets can form within the matrix; a process known as percolation. In theory, for graphene, this should occur at $\sim$0.1 vol. %[153] however, in practice percolation thresholds have been detected for polymer-graphene composites at between 0.1-0.3 vol. %.[153–156]

The main challenge in obtaining mechanical enhancement in graphene composites is ensuring the compatibility of the graphene with the surrounding matrix to get both good dispersion and improved mechanical properties.[157,158] Obtaining sufficient compatibility often requires modification of the graphene's surface since graphene does not inherently interact well with polymers.[157,159]

Nanocomposites are generally produced by either *in situ* polymerisation, melt processing or solvent processing. Solvent processing involves producing a good dispersion of graphene and polymer in a solvent, from which the composite can then be isolated.[153,160,161] In *in situ* polymerisation the graphene is dispersed in a monomer which can then be polymerised. This fixes the graphene into the polymer matrix.[162,163] Melt processing involves blending the graphene with molten polymer to form the composite.[164] However, melt processed composites generally do not have as good properties as those prepared *via* solvent processing.[165] Composites have also been produced through covalent bonding of polymer chains onto graphene sheets before blending, thereby compatibilising the graphene with the matrix.[166] Graphene polymer composites have been reviewed in detail elsewhere.[158,167,168]

1.4.4. Thermal Applications

Graphene has been shown to have a thermal conductivity higher than any other material,[46] giving it potential in a range of thermal applications. Principle among these is as an additive in thermal fluids. The use of high thermal conductivity additives to increase the overall thermal conductivity of fluids was developed by Maxwell in 1873 and is well known.[169] Therefore it was a logical progression to attempt to utilise graphene, with its high thermal

conductivity, in thermal fluids. Wei *et al.* were the first to report the thermal conductivity of GO dispersed in ethylene glycol (EG) and observed increases in thermal conductivity of up to 60 % due to the additives.[170]

Other studies have shown similar results, with the greatest improvements in thermal conductivity being observed in fluids with low initial thermal conductivity.[171] In order to improve thermal fluids further, endeavours have been made to replace the GO in these dispersions with less defective graphenes which have higher thermal conductivities.[172,173] Various groups have reported the use of rGO as an additive in thermal fluids.[174–176] This work has however been hindered by the fact that rGO is inherently less soluble in most common solvents than GO and so frequently the use of surfactants or covalent modification is required in order to produce stable dispersions for thermal fluids.

An alternative strategy that has been proposed is the *in situ* reduction of a GO dispersion in EG using NaOH to produce a stable dispersion of rGO with thermal conductivity increases of 6.5 % at 25 °C increasing to 36 % at 50 °C (with a maximum thermal conductivity of 0.34 W m^{-1} K^{-1}), in spite of low concentrations of rGO (0.14 vol. %) being used.[177]

1.4.5. Other Applications

Alongside acting as a thermal additive for functional fluids, as described above, graphene can also be used to modify their tribological properties. The first reports of this came in 2006 when Huang *et al.* reported the coefficient of friction for a dispersion of ball-milled graphite nano-sheets in paraffin oil and showed that the presence of graphite nano-sheets caused a significant fall in the coefficient of friction (figure 1.12).[178] A natural continuation of this work was to switch graphite nanosheets for graphene. Lin *et al.* showed that graphene, dispersed by stearic and oleic acids, could improve both the wear and friction behaviours of liquid paraffin.[179] Other groups have since shown that the addition of graphene to lubricants can reduce wear and friction respectively by: 14 % and 17 %,[180] 9 % and 26 %,[181] and 33 % and 80 %[182] in base fluids ranging from water[183] to organic solvents[181] and oils.[180,182]

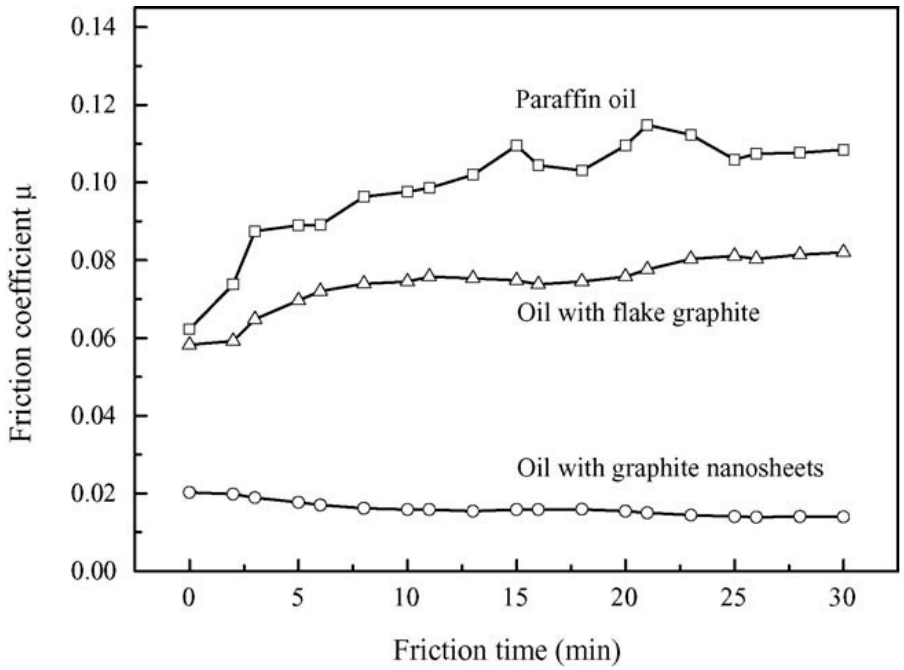

Figure 1.12: *Values of coefficient of friction against time for a 0.01 wt. % solution of graphite additives in oil and pure oil against time. Reprinted from Wear,* ***261****, H. D. Huang et al., An investigation on tribological properties of graphite nanosheets as oil additive, 140–144, Copyright 2006, with permission from Elsevier.*

One of the key advantages of using nanoscale additives to modify the tribological properties of fluids is that additive particles with smaller dimensions generally have a smaller impact on the viscosity of the fluids. This is important as viscosity has the potential to impact on both the thermal and tribological properties of the fluid produced.[184] Whilst nanoscale additives are believed to have a smaller impact on the viscosity of dispersions, this has not always been the case for dispersions of graphene with some groups reporting increases,[185] and decreases[186,187] in viscosity as well as nano-additives causing no change in viscosity.[188]

Another potential use of graphene in polymer composites is to improve the gas barrier properties of commodity polymers, principally for use in food packaging. The addition of graphene to poly(propylene) (PP) to form graphene - PP nanocomposites has been shown to decrease the oxygen permeability of PP by over 10 %[189] and poly(vinyl alcohol) (PVA) - GO nanocomposites were shown by Kim *et al.* to reduce oxygen solubility and permeation to 20 % of that of a pure PVA film.[190] The use of graphene as a gas barrier within composites has been recently reviewed in detail.[191] Graphene has also been shown to have good promise for environmental remediation applications.[192,193]

Finally, graphene's unique properties allow it to be used as an electrochemical sensor for substances including: hydrogen peroxide,[194,195] glucose,[196] and nucleic acids,[197] amongst other biomolecules,[198] as well as a range of gasses,[199,200] heavy metal ions,[201–203] explosives,[204] and pharmaceutical compounds.[205–207] These applications have been reviewed in detail.[198–200]

1.5. Graphene Oxide

One of the methods that has emerged as the most popular when synthesising graphene materials is the oxidation of graphite to graphite oxide, which can then be exfoliated to GO. As well as being an important precursor in the production of graphene, GO is also an interesting material in its own right. Many of its properties are the same as the beneficial ones of graphene, mentioned in section 1.2, but a few of its properties differ significantly, making it an interesting candidate in several applications where graphene has limitations.

1.5.1. Structure

As has been previously mentioned GO is a modified form of graphene in which the sheets are decorated by oxygen containing functional groups. However, while the oxygen content of GO is known to give a material with a carbon to oxygen ratio of $\sim$ 2.1-2.9:1,[208] the exact identity and location of the functional groups present on the sheets is still a subject of much debate. Various different models for the structure of GO and graphite oxide have been proposed, based on experimental data. A selection of the most popular models for GO is shown in figure 1.13.[209]

The earliest models generally assumed GO to be a crystalline material made up of repeated subunits, containing carbon and oxygen functionalities, in a discrete stoichiometric ratio. The Hofmann model is based on a repeating series of aromatic rings and ether groups,[210] while the Ruess model is similar but also incorporating hydroxyl groups.[211] The

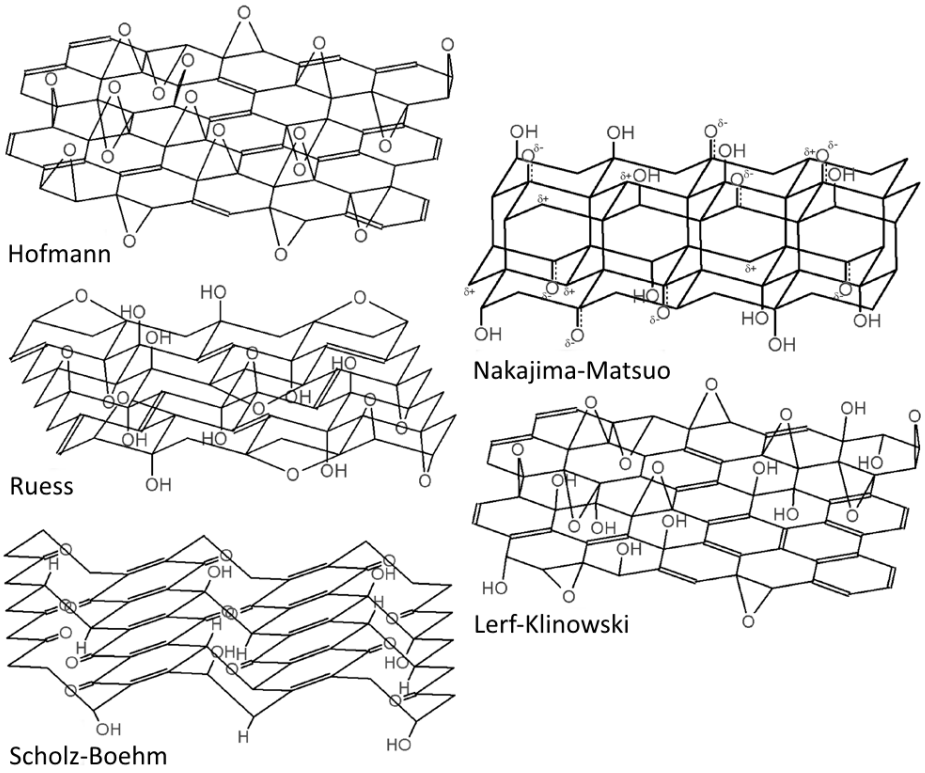

Figure 1.13: *Schematic representations of some of the proposed structures for GO. Reprinted (adapted) with permission from Chemistry of Materials, 2006,* ***18****, 2740–2749. Copyright 2006 American Chemical Society.*

Ruess model also incorporates a disruption to the sp^2 hybridised system of the graphene sheets to account for some of the properties of GO.[211] However, it has since been shown that GO is neither crystalline nor stoichiometric; indicating that the usefulness of these models are limited.

More recent models have taken this into account. The most commonly accepted model for the structure of GO is known as the Lerf-Klinowski model which was derived based on solid state nuclear magnetic resonance spectroscopy (SSNRM) studies of GO. Further studies involved exposing GO to a range of compounds and observing changes in the SSNRM spectra resulting from this. This model proposes that GO contains a mix of tertiary alcohols and 1,2-ethers as oxygen functionalities.[212–214] This differs from previous models that proposed 1,3-ethers[210] but Lerf *et al.* believed 1,2-ethers would be more likely to form under the conditions used to synthesise GO.[214] The model was later revised from its initial version to include the presence of terminal COOH groups at the edge of sheets, corresponding with results from other spectroscopic techniques such as fourier transform infrared spectro-

scopy (FTIR). Based on the reactivity of GO observed during these studies it was concluded that epoxy and alcohol groups must be very close to each other on the sheets, and that C=C environments are likely to exist as conjugated aromatic areas rather than isolated double bonds.[214] This concept of GO consisting of oxidised regions and other, more pristine graphitic regions was a novel one and is one that has since been confirmed by experimental techniques such as scanning transmission electron microscopy (STEM). It was also noted the strength of interaction between GO and the surrounding water molecules was extremely high, which is an important factor to consider when working with and processing GO.[212,213]

Many subsequent models have been suggested, closely based on the Lerf-Klinowski structure but making small adjustments in the relative abundance of functional groups to account for experimental data. In reality, while discussing and attempting to model the structure of GO and graphite oxide is undoubtedly an interesting topic, it should be noted that the exact structure of these materials depends on a large number of factors. These variables include the synthetic method, starting graphite, and degree of oxidation achieved meaning that the terms graphite oxide and GO actually describe a family of materials with a variety of structures and functional groups. The exact composition and structure of GO still remains a subject of debate. The structural models available for GO have been reviewed in greater detail elsewhere.[215,216]

1.5.1.1. Base Washing

An alternative structural model for GO was proposed in 2011 when Rourke *et al.* investigated the behaviour of GO when treated by base:[217] a procedure that has elsewhere been reported to reduce GO to rGO.[218,219] Basing their work on the oxidation of both carbon fibre[220] and CNTs[221–224] they suggested that GO is actually comprised of two components: mildly oxidised graphene sheets that they term base washed graphene oxide (bwGO), decorated with smaller, highly functionalised material that they call oxidative debris (OD) (figure 1.14).[217] Dilute NaOH can be used to remove this OD, which is also removed by harsher reductions,[225] to leave bwGO which has properties between those of GO and rGO.[217,225,226]

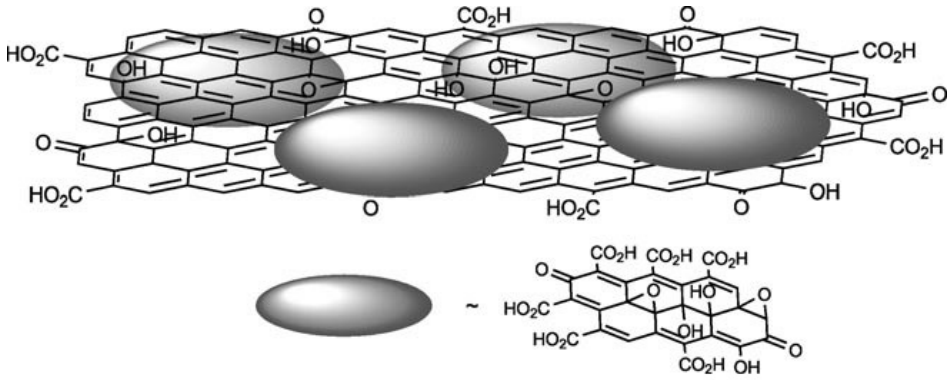

Figure 1.14: *A schematic representation of the structural model for GO proposed by Rourke et al. consisting of large, mildly oxidised graphene-like sheets and surface bound, highly oxidised debris (OD). Figure reproduced from Angewandte Chemie International Edition, 2011,* ***50****, 3173–3177. Copyright 2011 WILEY-VCH Verlag GmbH & Co. KGaA, Weinheim.*

However, whilst this model does fit with the characterisation data for GO is has not been widely accepted and it still not certain if base washing does remove OD or in fact is just a mild reduction technique. Aside from this, arguably if we define GO by its properties, as is frequently the case for carbon nanomaterials, then OD is an integral part of GO and so for many applications that require the properties of GO then bwGO would not be an appropriate choice of material.

1.5.2. Properties

One of the key impacts of the change in structure between graphite and graphite oxide is a marked difference in properties between these two materials. Natural flake graphite is a lustrous, grey powder, which is extremely hard to wet while graphite oxide is a much duller, brown material that that tends to dry to form a continuous film rather than a powder. This difference in properties is due to the changes in structure that occur during synthesis of GO: both due to disruption of the extended sp^2 network and the chemistry of the oxygen functionalities.

Possibly the most obvious change in properties between graphite oxide and graphite is their relative hydrophobicity. While graphite is well known to be hydrophobic, the introduction of oxygen functionalities on the sheets of graphite oxide completely changes this. Graphite oxide is very easy to disperse in water, and indeed has even been shown to be

hygroscopic.[103] Away from aqueous systems, oxidation also has the effect of making GO appreciably soluble in a range of solvents including: propan-2-ol, EG, tetrahydrofuran (THF), dimethylformamide (DMF), and NMP.[227] From an industrial perspective this makes graphite oxide and GO attractive materials as they are easier to process than many other forms of graphene.

Unfortunately, improved processability is not the only change in properties that occurs upon oxidation of graphite as many of graphene's properties come from its extended sp^2 network (as described in section 1.2). Oxidation to GO disrupts this network and so negatively impacts on both the electrical and mechanical properties of the material with the properties of GO being inferior to those of pristine graphene.[172,173,228]

In spite of this, due to its relative ease of synthesis and processing, GO is still considered to be a useful material with strong potential in many applications where it would not be practical to utilise pristine graphene. A final advantage of the use of GO is that a wide range of methods have been reported which can be used to convert GO to rGO, which has more graphene like properties, meaning it is possible to take advantage of both the good dispersibility of GO and the graphene-like properties of rGO reduction is able to be performed after the solution properties of GO have been used to produce a stable dispersion.

1.5.3. Synthesis

1.5.3.1. Oxidation

The first step in the production of graphene *via* GO is to oxidise natural flake graphite; forming graphite oxide. In order for this to be achieved, an extremely high oxidation potential is required. The first method proposed for this oxidation, by Brodie in 1859, involved the use of nitric acid and chlorate of potash ($KClO_3$) which, although effective, came with a high risk of producing explosive by-products.[103] Staudenmaier provided a more practical version of Brodie's method, by using sulfuric acid to increase the acidity and using multiple

additions of chlorate allowed a single reaction vessel to be used.[229] However, this method did not help with the inherent risks of working with chlorates

In 1958 Hummers and Offeman proposed an improved version of these methods avoiding the use of chlorates. The Hummers method, as it has become commonly known, involves the oxidation of graphite using a mixture of sulfuric acid (H_2SO_4), potassium permanganate ($KMnO_4$), and sodium nitrate ($NaNO_3$) - which generates nitric acid *in situ*.[208] This method is now the most widely used procedure for the oxidation of graphite.[35] Others groups have attempted to improve on the Hummers method and so a number of so called "modified" hummers methods have been reported in the literature.[230–234] These generally involve either changing the ratio of reagents,[231] the time over which oxidation occurs or the temperature used. Some however, also utilise alternative reagents to replace $NaNO_3$ such as $K_2S_2O_8$ and P_2O_5.[230] None of these have been universally accepted and produce similar material to that produced by the Hummers method.[35,215] It has been noted that care must be taken when performing the Hummers method as residual acetone can produce acetone peroxide dimers and trimers which are explosive.[232]

One challenge that must be overcome when working with graphite oxide is the fact that its synthesis results in the production of a slurry of graphite oxide in water. Whilst it is often possible to utilise graphite oxide without the need to isolate it from this water, this is not always the case and the additional water contained in this slurry can cause problems.

Drying of the as-produced graphite oxide slurry is possible, either through conventional evaporative drying or through freeze drying. Whilst drying graphite oxide by heating is the simplest approach, it is not without its drawbacks. Firstly, as discussed in section 1.6.1.3, holding graphite oxide at elevated temperatures can result in changes in chemical composition and even reduction of the oxygen functionalities on the material. For this reason temperatures <80 °C should be used which can lead to long times needed to achieve dryness. In addition to this, conventional drying of graphite oxide and GO can lead to sheets becoming turbostratically stacked which can inhibit the materials ability to redisperse.[11]

The alternative to this is to utilise freeze drying to remove water from graphite oxide and GO. Freeze drying is achieved by freezing the slurry of graphite oxide and water and maintaining its pressure below the triple point of water as the temperature increases, allowing the water to sublime away. As the graphite oxide is frozen when drying this means the conformation of the graphene sheets is fixed during dying, preventing the sheets from restacking. In addition to this, the low temperatures used in freeze drying avoids the problems with reduction associated with conventional evaporative drying at elevated temperature. For this reason it is preferred to either use wet GO in applications or to dry it through freeze drying.

When utilising either of these techniques it should be noted that due to the extremely hygroscopic nature of graphite oxide and the fact that water molecules become trapped between the graphene sheets, interacting through hydrogen bonding with the oxygen functionalities found on the sheets, drying graphite oxide may take a long time, and it may not be possible to achieve complete dryness with some intercalated water molecules impossible to remove.

1.5.3.2. Exfoliation

Whilst the synthesis of graphite oxide has been known for many years interest in it has peaked recently due to its potential as a precursor for graphene. The key to the conversion of graphite oxide to graphene is its exfoliation to GO. As described in section 1.3.2.1 exfoliation is the process by which adjacent graphene layers in a graphitic structure are split apart to form a isolated graphene sheets. In GO this process is aided by the increase the inter-layer spacing that occurs as a result of oxidation.[83] As the layers in graphite oxide are held together by van der Waals forces, which scale with a factor of r^{-6},[93] the oxidation of graphite greatly weakens the forces holding the sheets together.[83]

There are two mechanisms by which this change in inter-layer spacing occurs: firstly the presence of the oxygen functionalities acts as a physical barrier to aggregation, holding the sheets apart, and secondly the polar nature of these groups allows water molecules to

become intercalated between sheets. Using x-ray diffraction (XRD) the inter-layer spacing for GO has been shown to be between 6.5 Å and 7.5 Å,[18,235] depending on the level of hydration of the material,[236,237] compared to 3.35 Å for graphite.[17,18]

While the exfoliation of graphite to form graphene typically involves a mix of high energy techniques, specific solvents, or surfactants (as described in sections 1.3.2.1 and 1.3.2.2) exfoliation of graphite oxide to form GO can be performed under much milder conditions. GO's inherent hydrophilicity and the fact that it is hygroscopic[103] means that water is the most commonly used solvent for its exfoliation.[11] Aqueous dispersions of GO can be exfoliated by several methods ranging from gentle shaking[238,239] or stirring[240] to freeze-thaw[241] or sonication,[101,242,243] with the energy of the technique used able to give some control over the size of the sheets of GO produced.[243] For applications in which the use of water is not desirable, Paredes *et al.* showed that polar aprotic solvents such as DMF, THF, and NMP as well as ethylene glycol are able to exfoliate GO completely.[244] In addition; NMP and DMF have also been shown to be able to cause spontaneous exfoliation of GO without the need for mechanical agitation.[245] Finally, it is possible to cause exfoliation of GO in a range of other solvents with the use of intense sonication.[227] However, this is likely to induce defects and reduce the size of the sheets of GO due to the energy required.[241,243]

1.6. Reduced Graphene Oxide

The final step in the production of a graphene like material using the GO route is to remove the oxygen containing functional groups present on the sheets in a reduction reaction, thus restoring the graphene like properties of the material.[246]

1.6.1. Synthesis

The reduction of GO is a subject that has been widely studied and a vast range of methods have been proposed.[215,246,247] An overview of the most commonly used routes will be

given below.

1.6.1.1. Chemical Reduction

While the oxidation of graphite is a process that requires extremely high oxidation potentials, harsh conditions and carefully selected reagents, the same is not true for its reduction. A large number of reagents can be used for the chemical reduction of GO including both conventionally used reducing agents and some much milder reagents. Hydrazine was one of the first reducing agents used, and was known to reduce graphite oxide even before the discovery of graphene.[248] When it was realised that GO could be used as a precursor for graphene Stankovich *et al.* showed that hydrazine could also be used as a reducing agent for GO.[101,249] The mechanism for this reaction is still not well known, although several possible routes have been proposed (figure 1.15).[101,250,251] There are however, severe hazards associated with the use of hydrazine since it is both toxic and can potentially form explosive compounds.[252] Other strong reducing agents such as $NaBH_4$ and $LiAlH_4$ have also been shown to be able to reduce GO[246,253] but hydrazine has the advantage of not reacting with water,[215] making it ideal for the reduction of the most common state of GO, aqueous. In practice, the water sensitivity of most metal hydride reducing agents and the intercalated water in GO means that many can not be used to synthesise rGO.[246] However, it has been shown that $NaBH_4$ can be used to reduce GO under the correct conditions.[253,254]

A large number of other reagents have also been proposed as reducing agents for GO with the aim being to find milder, greener compounds which are safer to work with on large scales.[247] Zhang *et al.* were some of the first to propose a "green" alternative to hydrazine; showing that L-ascorbic acid could be used to produce rGO from GO.[255] Since then it has been shown that reduction can also be performed by: green tea,[256–258] reducing sugars (glucose, fructose, and sucrose),[259] L-arginine,[260] NaOH or KOH,[218,219] hydroiodic acid,[261,262] hydroquinone,[263] and hydroxylamine[264] amongst many other compounds.[246,247] Although with the more basic of these reagents there is some ambiguity as to whether the process occurring is truly reduction or if it is base washing as described in section 1.5.1.1.

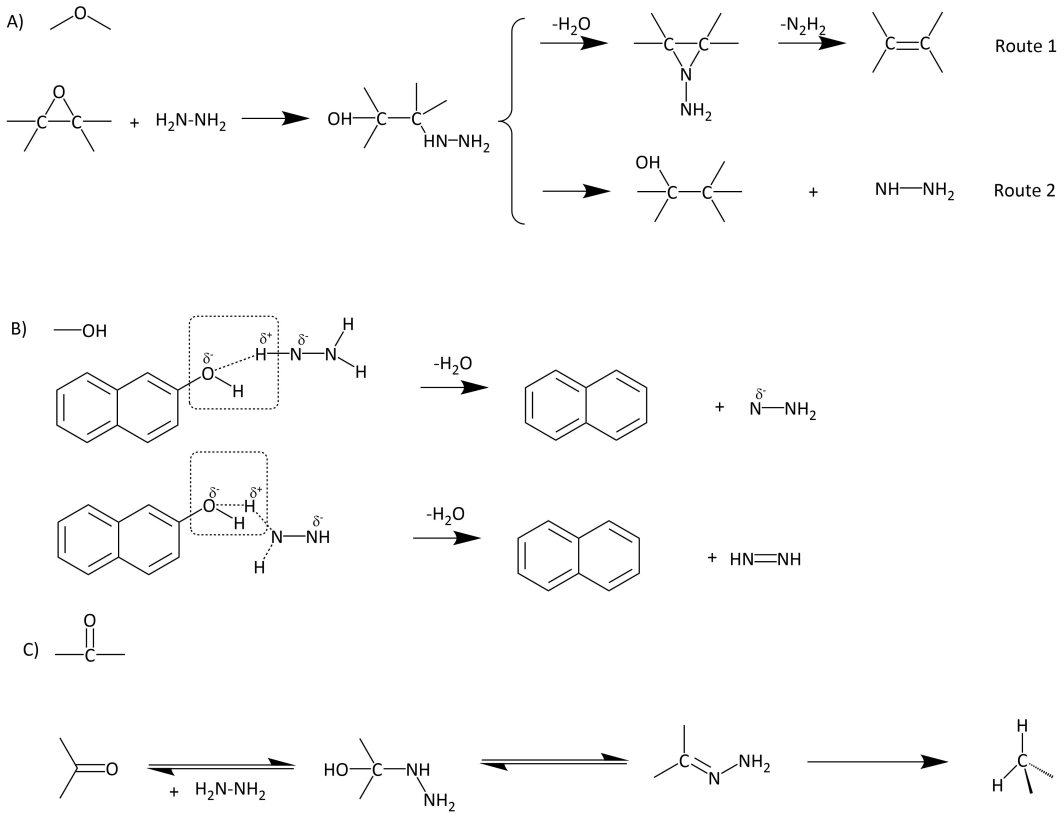

Figure 1.15: *The mechanism for the reduction of A) epoxide, B) hydroxyl, and C) carbonyl functionalities on GO by hydrazine proposed by Wang et al.. Reproduced from RSC Advances, 2013,* ***3****, 1194–1200, with permission of The Royal Society of Chemistry.*

In spite of its downsides and the range of other chemical reducing agents available for GO, hydrazine is still the most consistently used reagent in the literature for the chemical reduction of GO to rGO.[101,215,246,249,265–270]

1.6.1.2. Thermal Reduction

rGO can also be produced using a purely thermal reduction method. This was first reported by Brodie who showed that heating of graphite oxide causes thermal decomposition; although he did not explicitly show that reduction was occurring.[103] Heating of GO to high temperatures (>500 °C) causes changes in the carbon to oxygen ratio to occur as the oxygen functionalities on the sheets begin to decompose.[18] Heating to higher temperatures (>700 °C) causes further removal of oxygen, changing the carbon to oxygen ratio significantly.[18] The force generated by the intercalated gasses escaping, combined with the high temperatures burning off regions of defective carbon mean that the sheets produced

in thermal exfoliation of GO are generally small and wrinkled with many defects.[18,271]

Often thermal reduction is performed on graphite oxide without a prior exfoliation step due to the fact that exfoliation can occur spontaneously during the thermal reduction procedure. Sudden heating of graphite oxide leads to rapid production of gas, which forms between the layers of the material. This is produced from two sources: firstly the vaporisation of intercalated water molecules, and secondly the thermal decomposition of oxygen containing functionalities on the graphitic sheets which form CO_2 and CO.[18,271] This production of gas causes pressures of up to 40 MPa at 200 °C and up to 130 MPa at 1000 °C to build up between the graphitic sheets which forces them apart and causes exfoliation since it is predicted that only 2.5 MPa would be enough to fully exfoliate graphite oxide.[235] The material produced is often referred to as thermally expanded graphene oxide (TEGO).[168]

A range of conditions can be changed in order to affect the properties of the TEGO produced with both the atmosphere used and the temperature being significant. Temperatures of >750 °C can produce graphene with carbon to oxygen ratios of over 13, compared to less than 7 at <500 °C.[18] Parallel results have also been observed for the electrical conductivity of the TEGO produced, with the best conductivities only being observed in material that was produced at temperatures >1000 °C (figure 1.16).[272,273] Thermal reduction of GO can not be done in air as the presence of oxygen gas will lead to increased combustion of the GO at elevated temperatures and so either vacuums[274] or inert atmospheres[272] are used. However, it has been theorised that the oxygen atoms released from GO during thermal reduction are enough to cause some combustion and reduce the quality of the TEGO produced.[274] Therefore, some groups have begun to use reducing atmospheres for the thermal reduction of graphite oxide.[273]

Whilst thermal reduction is a promising method for the synthesis of rGO there are several issues that must be considered. Principle among these is the high temperatures required for effective reduction, meaning the process is high energy.[246] A final concern that must also be taken into consideration is that the thermal reduction, particularly of dry GO powders such

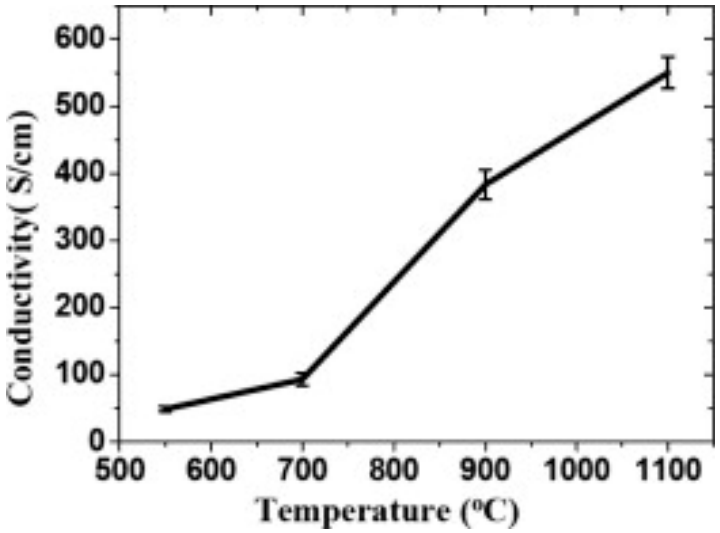

Figure 1.16: *The average conductivity of graphene films following reduction at different temperatures showing increased electrical conductivity following reduction at higher temperature. Reprinted with permission from Nano Letters, 2008,* ***8****, 313–327. Copyright 2008 American Chemical Society.*

as freeze dried graphene oxide (FDGO), has the potential to become an explosive, thermal runaway reaction.[275]

1.6.1.3. Hydrothermal Reduction

Following on from the thermal reduction of GO in gasses it is logical that rGO can also be produced by hydrothermal methods. GO is sealed into a container with a solvent and heated to high temperatures resulting in high pressures due to the sealed system. This method of reduction has been demonstrated to be effective in a range of solvents including water[276] and DMF.[277]

Finally, although not strictly a hydrothermal reaction it has been shown that rGO can also be produced by simply heating GO solvents including: water,[242] propylene carbonate,[278] NMP,[279,280] and a range of alcohols[281] to close to their boiling points at ambient pressure.

A major advantage of hydrothermal methods of reduction is that the product can be a stable dispersion of rGO sheets in a solvent; something that can be challenging to produce by other methods and that is desirable in many applications.

1.6.1.4. Other Reduction Techniques

Whilst the above list of reduction techniques covers many of those presented in the literature there are many that do not fit into the categories used above. It is also possible to reduce GO through the use of irradiation by microwaves[282,283] and by photo-illumination by visible light[182,284,285] or infra-red (IR) radiation,[286] including through the use of a LightScribe DVD burner,[287,288] although in these instances there is still debate as whether the mechanism of reduction is due to the heating effects of this radiation and simple thermal reduction as described in section 1.6.1.2 or is caused specifically as an effect of the incident radiation. Finally, it has been reported that GO can be reduced by soaking in flammable solvents followed by ignition which again, may be due to thermal effects.[289] More detailed reviews covering the reduction of GO can be found in the literature.[215,246,247]

1.6.2. Structure and Properties

As was discussed in section 1.5.1 the structure of GO differs significantly from that of pristine graphene leading to its distinct properties. When synthesising rGO the goal is almost always to produce a material with graphene like properties and as the structure and properties of graphene are intrinsically linked, then it should be evident that rGO must have a structure closer to that of graphene than of GO. Unfortunately the impact of creating oxygen functionalities during the oxidation of graphite is that the sp^2 network of the graphitic sheets is disrupted which makes it inevitable that the properties of rGO are not identical to those of pristine graphene.

The majority of reduction techniques used to produce rGO are only able to remove the oxygen functionalities and do not act to restore the sp^2 matrix. This means that rGO has a large number of defect sites still present within each rGO sheet where oxygen functionalities used to be present.[246] In spite of this rGO has been shown to be a material with some impressive properties including high thermal conductivity and mechanical strength[246] meaning it

can still be a promising candidate in many applications that require these properties. However, for applications that require graphene with good electrical properties an alternative route to synthesise this material is advisable.

The exact properties of the rGO produced depends on two factors. Firstly, the chemistry of the GO used to produce it, and secondly the method of reduction used to synthesise it. Harsher reduction methods produce materials with more graphene-like properties whereas those that are produced using milder reactions tend to be slightly more GO-like. For instance, the electrical conductivity of TEGO is higher than that of rGO produced using hydrazine. However, rGO produced using hydrazine is easier to disperse in solvents than TEGO. One key change in properties that occurs as a result of the reduction of GO to rGO is the change in colour from brown to black as a result of the restoration of electron conjugation which is often used as an indicator of the progress of the reduction reaction.

As a result of the differences in properties between GO and rGO it is often the case that properties can be used to monitor the reduction of GO. Electrical conductivity, for example, shows a marked increase in rGO compared to GO and can therefore be used as an indirect measure of the degree of reduction of a material. The two materials also have significantly different dispersibilities in many solvents, including water, and so a simple test of dispersibility can be a good indicator of the degree of reduction.

1.7. Modification of Graphene

Whilst graphene has many interesting properties it is frequently necessary to perform some form of modification in order to unlock its full potential in applications. This generally takes the form of the addition of functional groups to the surface of the graphene sheets, changing their chemistry and is generally done to improve the compatibility of the graphene with a solvent or a matrix. Modification of graphene can take one of two forms: covalent modification where the modifier is chemically bound to the surface, and non-covalent

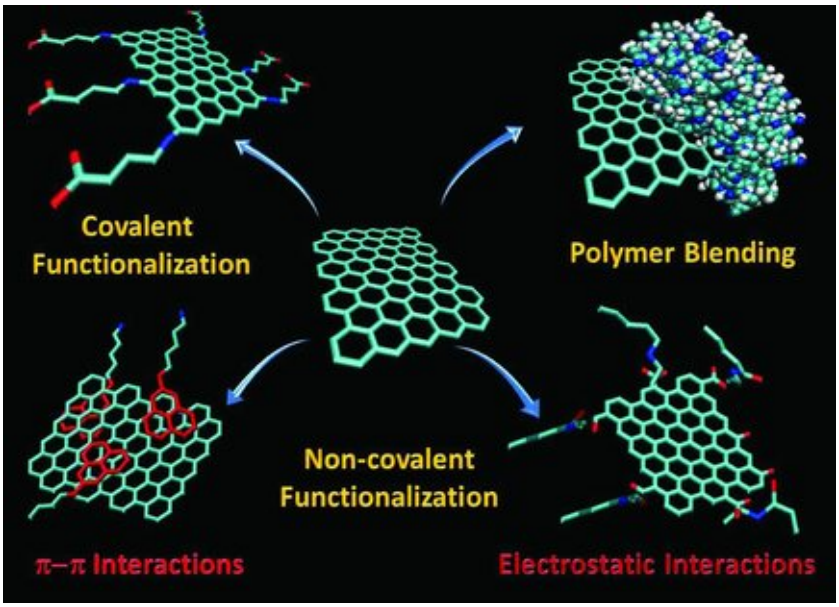

Figure 1.17: *A schematic showing the potential routes of functionalisation of for graphene. Figure reproduced from Advanced Materials, 2011, **23**, 5302–5310. Copyright 2011 WILEY-VCH Verlag GmbH & Co. KGaA, Weinheim*

modification where the modifier and the graphene interact in a non bonding manner.

The most commonly used form of functionalised graphene is GO, which has been discussed above. However, while GO has many useful properties, they are not suitable for every application. For this reason a wide range of alternative methods of functionalising graphene have been developed which can give graphene an extremely varied selection of properties.

One of the most common reasons for functionalising graphene is to alter its solution properties. As has been previously mentioned, graphene and related materials can be extremely challenging to disperse in many fluids and so altering its surface chemistry can greatly improve its solubility and dispersibility.[11] Alongside altering the dispersibility of graphene in solvents modification can also affect the interaction of graphene materials with polymers, where good compatibility between fillers and the bulk is required for improved mechanical properties. It is also possible that modification can affect other properties of the graphene such as electrical conductivity and mechanical strength.[11] It is also possible to use modification to alter electronic properties[290,291] and optical properties of graphene materials.[292] The functionalisation of graphene has been reviewed in detail elsewhere[11,292–295]

but the most relevant and popular techniques will be discussed below.

1.7.1. Covalent Modification

The covalent modification of graphene is a process in which other molecules or moieties are added to the normally pristine sp^2 carbon network of a graphene sheet. It is possible to bind a huge range of different groups to the surface of graphene. [292,296]

In spite of the theoretically inert nature of pristine graphene a wide variety of different chemistries can be used for its covalent functionalisation. An even greater range of possible syntheses can be performed if GO is used as the starting material as the oxygen moieties act as reactive sites for functionalisation. In fact, the production of GO itself can be viewed as covalent modification since the chemical structure of graphene is altered by the addition of covalently bonded adatoms; although GO is generally considered a separate material. [31]

1.7.1.1. Covalent Modification of Graphene

In order for pristine graphene to undergo covalent functionalisation a number of C=C bonds within the sp^2 matrix must be broken. This is usually achieved through the use of free radicals or dienophiles. [292] A range of dienophiles will react with the sp^2 matrix of graphene through a 1,3 dipolar cycloaddition including the azomethine ylide, [297,298] azides, [299,300] nitrenes, [301] and arynes [302] allowing for a wide range of chemical functionality to be added onto the surface of the graphene sheets. [292]

An alternative route to covalent functionalisation of graphene is the use of free radicals. This proceeds through the attack of a radical on the sp^2 matrix of graphene, allowing a new covalent bond to form. The most commonly used radicals are generated by diazonium salts which have been used to produce graphene functionalised with nitrophenol [303,304] and hydroxylated aryl moeities [305] while radicals generated by benzoyl peroxide are able to produce graphene sheets decorated with phenyl groups. [306]

Whilst a brief summary of the possible products from radical and dienophile functionalisation of graphene is presented above, this is by no means exhaustive and a huge number of possible alternative functionalised graphenes can be found in the literature.

1.7.1.2. Covalent Modification of GO and Related Materials

While modification is frequently performed on pristine graphene, it is often easier to perform functionalisation on GO as the oxygen functionalities already present on the sheets gives an active site for chemistry to occur at. As has been discussed in section 1.5.1 GO contains a range of functional groups that can be leveraged in order to facilitate functionalisation. As discussed above, when working with GO the end goal is often to produce rGO and the same is true when functionalising GO. The reduction of functionalised GO is possible, using the usual methods of synthesising rGO. However, it should be noted that the presence of additional functional groups on the surface may decrease the degree of reduction that can be achieved and it is possible that the conditions used for reduction may even lead to the removal of the newly attached functional groups so extra care must be taken when trying to reduce functionalised GO.[279]

An alternative route to synthesise functionalised rGO is to perform the modification after reduction as some oxygen functionalities and defect site remain which can be used as active sites for modification. However, the greatly reduced number of active sites reduces the ease with which functionalisation can be performed.[215]

A large number of GO functionalisation reactions rely on the formation of amide or ester bonds between reagents and groups present on the surface of GO sheets. In order for these reactions to proceed the carboxylic acid groups must first be activated in order to increase their reactivity[215] which can be achieved through the use of a range of reagents including 1-ethyl-3-(3-dimethylaminopropyl)carbodiimide (EDC),[307–309] N,N'-dicyclohexylcarbodiimide (DCC),[310,311] thionyl chloride ($SOCl_2$)[312–315] or 1-[bis(di-methylamino)methylene]-1H-1,2,3-triazolo[4,5-b]pyridinium 3-oxid hexafluorophosphate (HATU).[316,317] This process allows GO

to react with molecules containing amines to form amide bonds[307,308] as well as hydroxyls to form esters.[310,311] Functionalised GO can then be reduced to form functionalised rGO which is chemically similar to functionalised graphene. In general, rGO is functionalised in order to improve its dispersibility in solvents and so the moieties chosen to functionalise the sheets should have similar chemistries to the solvent the material is to be dispersed in.[11]

As an alternative to functionalisation at the carboxylic acid groups of GO it is also possible to make use of other functional groups found in GO, principally epoxides, which can undergo ring opening reactions using a number of methods such as: potassium thioacetate or other sulfur nucleophiles[318] or the conversion of epoxy groups to hydroxyl groups using tris(hydroxymethyl) aminomethane (TRIS),[319] which produces new active sites to be functionalised. It has also been shown that malononitrile can add to epoxide groups leaving reactive nitrile groups for further functionalisation.[320]

The functionalisation of rGO often follows similar routes to those used to functionalise pristine graphene, discussed in section 1.7.1.1. In spite of the presence of residual oxygen functionality that could be used for GO-like modification reactions this option is not frequently used.[11]

1.7.2. Non-Covalent Modification

The non-covalent modification of graphene is an alternative to covalent functionalisation that generally involves the use of surfactant-like molecules. These interact with the surface of the graphene through non-bonding interactions such as van der Waals forces and π-π stacking and modify the properties of graphene.[292] Non-covalent modification has the advantage of being a non-permanent form of functionalisation allowing for their potential removal. Another advantage of this form of modification is that the sp^2 hybridised network of the graphene sheets is not disrupted by other atoms being bound to it meaning that, in theory, the properties of the graphene are better maintained.[292,321,322] Non-covalent modification is generally used to modify the dispersion properties of graphene and lends itself well

to modification of pristine graphenes due to their reduced chemical reactivities.

Graphene materials can interact non-covalently with modifiers through a range of interactions, depending on the chemistry of the modifier. Any functionaliser that contains an aromatic structure will be able to undergo π-π stacking with the extended sp^2 network of graphene. Molecules that have been shown to undergo π-π stacking with graphene include PAHs,[323–327] peptides,[328,329] deoxyribonucleic acid (DNA),[330] and conducting polymers.[331,332]

Cations will also interact with the extended π network of graphene through cation-π interactions.[333] Metal cations have been shown to improve the dispersibility of rGO in water, dimethyl sulfoxide (DMSO), and DMF.[334] However, more commonly it is organic cations that are used to modify graphene; principally imidazolium ions.[335,336] Functionalisers can also interact with graphene through a range of other ion-π interactions. However, this is beyond the scope of this discussion and covered elsewhere.[292]

A final, popular class of molecules that can be used to non-covalently modify graphene are surfactants. A wide range of commercially available surfactants have been shown to improve the dispersibility of graphene in solvents, principally water. Sodium dodecyl sulfate (SDS) is one of the most widely used commercial surfactants and in spite of its lack of aromatic character has been shown to improve the dispersibility of rGO in water at [SDS] >40 μM with dispersions stable for over a year.[337,338] Other surfactants that have shown promise for graphene dispersions include SDBS, sodium cholate and sodium deoxycholate with those that are able to undergo π-π stacking having the best ability to interact with graphene.[339] Polymeric surfactants such as Pluronic (PEO-b-PPO-b-PEO)[339] and poly(vinylpyrrolidone) (PVP)[340,341] are also able to improve the dispersibility of graphene in a range of solvents including: NMP, DMSO, DMF, isopropyl alcohol (IPA), ethanol, methanol, and water.[342]

Whilst non-covalent modifiers of graphene are not chemically bonded to the graphene sheets they interact with this still does not make their removal a trivial process.[11] Whilst in some cases it is possible to partially remove non-covalent functionalisers by washing with a

suitable solvent it is often necessary to heat the graphene to >500 °C to burn off the modifiers.[82] This approach may not be suitable in applications that can not tolerate high temperatures, such as those involving papers or polymers meaning it may only be possible to partially remove the functionalising molecules from the surface of graphene sheets.[246]

It is often the case that the molecules used to non-covalently modify graphene will interact through several of these methods of interaction as they have been deliberately chosen to have chemistries that are highly compatible with graphene. This can make it challenging to conclusively determine the mechanism by which functionalisation has occurred, since characterising graphene materials fully can be challenging. As the majority of reagents used to functionalise graphene inherently have favourable interactions with graphene it is likely that many functionalisations that are described as covalent are not exclusively so and involve a mix of both covalent and non-covalent interactions. For this reason it is prudent to exercise care when claiming exactly what interactions are occurring during functionalisation.

1.8. Dispersions of Graphene

As the problem of scalable synthesis of graphene is beginning to be addressed focus must turn to addressing the poor dispersibility of graphene in common solvents which remains a significant limiter for the uptake of graphene in industry.[343] Graphene's natural properties and surface chemistry means that in general it interacts poorly with both polar and non-polar solvents which makes solution processing of graphene difficult although some solvents including: NMP, DMSO, and DMF have shown promise for dispersing (and exfoliating) graphene.[86]

The dispersion of graphene in solvents requires an input of energy in order to break up aggregated graphene sheets and facilitate dispersion. This is usually provided through ultrasonication which can cause cavitation and high shear stress in the solvent aiding the dispersion of graphene.[344] It is believed that once a dispersion has been achieved layers of

solvent molecules confined near the surface of the sheets prevent reaggregation and help stabilise the dispersion.[345] The downside of dispersing graphene through sonication is that the high energy input used can be detrimental to the structure of the graphene with both reductions in sheet size and damage to the sp^2 network being observed.[92,160,346] In spite of this sonication is now an extremely common method for producing graphene dispersions but it is tricky to expand to a large scale. More recently an alternative to sonication has been proposed with several groups reporting the use of high shear mixers to create graphene dispersions.[52,90] This provides a potentially scalable method of creating graphene dispersions.

The original work on assessing the compatibility of graphene and solvents was based on Hansen solubility parameters.[347] Hernandez *et al.* determined the Hansen solubility parameters of graphene and then tested the dispersibility of graphene in solvents, showing that the best solvents for graphene are those with the closest solvent parameters to graphene.[86] The Hansen parameters and dispersibility of rGO have also been studied and been shown to be close to those of pristine graphene.[227]

Hansen solubility parameters are free energy parameters, originally developed to quantify the interactions occurring between molecules of polymer and solvents in solution, allowing the ideal solvents for different polymers to be determined.[347] Since their conception Hansen parameters have been applied to a wide range of materials away from the polymers they were originally designed to study, and have been used to good effect in the study of graphene and related materials.[86,227]

The Hansen parameters of a material consist of 3 numeric quantities, based on the properties of a material, and those materials with similar Hansen parameters will interact well with one and other. The three parameters the Hansen solubility parameter is made up from are:

δ_D – The dispersion cohesion parameter, arising from the energy of dispersive interactions between molecules

δ_P – The polarity cohesion parameter, arising from the energy generated by dipolar intermolecular forces

δ_H – The hydrogen bonding cohesion parameter, arising from the energy produced by hydrogen bonding

These three parameters can be treated as coordinates in a three dimensional Hansen space, with the proximity of molecules in this space determining the likelihood that they will be able to dissolve each other. The basis of the Hansen parameter theory is that like will dissolve like, and so materials that have closely matched Hansen parameters will have similar chemistry and most likely mix well, dissolving one and other. Therefore, when determining solvents for graphene it is key to find solvents which which have similar Hansen parameters to graphene. Hernandez *et al.* and Konios *et al.* have reported the Hansen parameters of both graphene and rGO respectively and these values are shown in table 1.3.[86,227]

Table 1.3: *Three part Hansen solubility parameters of graphene and rGO as reported by Hernandez et al. and Konios et al..*[86,227]

	$\langle\delta_D\rangle$ / MPa$^{\frac{1}{2}}$	$\langle\delta_P\rangle$ / MPa$^{\frac{1}{2}}$	$\langle\delta_H\rangle$ / MPa$^{\frac{1}{2}}$
graphene	18.0	9.3	7.7
rGO	17.9	7.9	10.1

It is unfortunate that that the number of solvents with Hansen parameters that coincide with those of graphene is few. Solvents that were already known to disperse other carbon nanomaterials, such as CNTs, well were shown by Hernandez *et al.* to have Hansen parameters close to those of graphene with NMP being the most effective closely followed by DMF. Other, less commonly used, solvents that can be used to disperse graphene materials include cyclopentanone, cyclohexanone, N-formyl piperidine and vinyl pyrrolidone and these solvents have similar Hansen parameters to graphene materials.[86] However, all of these solvents suffer from the same problems already discussed, meaning that they either have high boiling points, or inherent hazards which limits their usability (particularly on a large scale).

Recent work has suggested that simple solvent compatibility may not be the only reason for the improved interactions of graphene in certain, amide based, solvents under sonica-

tion. Yau *et al.* [348] suggested that the sonication itself may be degrading the solvents which then react with the surface of the graphene, chemically modifying it and altering its solution properties. [348] However, this idea is still a new concept and is not yet widely accepted.

1.9. Conclusion

Ever since its discovery graphene has attracted great interest from the scientific community due to its incredible combination of properties and the wide range of applications that is has potential for. In spite of this there remain challenges that must be overcome for graphene materials to realise this potential. Large scale synthesis of high quality graphene is a problem that is beginning to be overcome through progress in CVD, the liquid phase exfoliation of graphite, and developments in the production of GO although progress is still needed in order for commodity graphene to become an economically available material. The second challenge that must still be met is the need for processable graphene; its inherent poor dispersibility in solvents is a challenge that is still being overcome.

Chapter 2

Project Aims

As highlighted in chapter 1, graphene has a remarkable collection of properties that can all be exploited from a single material. For this reason it has attracted a great deal of interest and its use in a wide range of applications has been proposed and in spite of the remaining challenges in producing and dispersing graphene commercial products containing graphene are beginning to make it to market. One application of graphene that has not yet been commercially exploited is the use of graphene materials as additives for functional fluids, specifically those used by the automotive industry as lubricants and coolants. Graphene's remarkable thermal and tribological properties make it an ideal candidate for use in this application.

Recent concerns about climate change and the impact of fossil fuel emissions has led to a significant shift in priorities for many companies in the automotive industry, with a far greater drive towards increased fuel economy, smaller engines and reduced emissions. When attempting to produce smaller, more efficient engines, one of the greatest limiters is dealing with the build-up of heat that naturally occurs during combustion. Lubricants and thermal fluids both play a key role in the dissipation of this heat and so improving the thermal properties of these fluids can play a key part of improving the efficiency of engines and reducing emissions. In addition to this, the performance of lubricants directly impacts the efficiency of power units as a lubricant with improved tribological properties will cause reduced energy loss through friction in the system.

More efficient engines can be utilised in one of two ways: either the same volume of fuel can be used to produce an increased engine output power, which can be useful in applications such as high performance engines or motor sports, or the same power output can be obtained from a smaller amount of fuel which will reduce fuel consumption and emissions

while maintaining engine performance. In addition to this, more efficient thermal fluids will mean that lower total volumes of coolant will be required by the system, reducing the weight of the power unit and again improving the efficiency of the system.

In this project we aim to produce thermal fluids and lubricants with improved thermal and tribological properties through the addition of graphene materials to commercial lubricants and coolants. In order to be commercially relevant the dispersions produced must be stable and contain a sufficient concentration of graphene materials to impact on their properties. The thermal and tribological properties of these dispersions will then be tested in order to assess the potential of these dispersions.

Achieving these aims will require a number of challenges to be overcome. Principle among these is the difficulty, noted in section 1.8, of dispersing graphene in almost all solvents due to its unusual surface chemistry. It is essential that any dispersions produced have excellent stability over long time periods if these nanofluids are to be relevant in a commercial setting where they may need to be stored for an extended period of time before being used. For this reason a major focus of this body of work will be on the compatibilisation of graphene materials with relevant solvents, including its modification by a range of methods in order to produce stable dispersions of graphene materials.

Due to the differences in the properties of fluids used for each of these applications, different approaches will need to be taken for the dispersion of graphene in polar coolants compared to non-polar lubricants. For this reason the work on each of these groups of fluids will be undertaken using different approaches in order to achieve optimal results.

As a result of this, the choice of graphene starting material is important for this project, and must meet certain criteria. Firstly, it must be readily available in sufficient quantities to produce dispersions on the scale required for testing in applied systems and secondly it must be possible to modify the solution properties of the material in order to achieve the best possible dispersions in a wide range of fluids. For this reason graphene materials produced *via* the GO route will be utilised. The synthesis of GO and its related modified

graphenes is simple compared to many other forms of graphene and can be scaled to produce the volumes of material required. In addition to this the oxygen functionalities present on GO provide a perfect platform for functionalisation, which can significantly impact on the solution properties of the material, enabling stable dispersions to be produced in the range of solvents required.

Once stable dispersions of graphene in thermal fluids and lubricants have been achieved their relevant properties can then be assessed in order to determine the impact of the graphene additives on these fluids. In lubricants the key properties of interest will be their tribological properties, including coefficient of friction under a range of conditions, rates of wear and viscosity whilst in thermal fluids the key properties of interest will be thermal properties such as thermal conductivity and specific heat capacity. Measurement of all of these qualities will require specialist equipment, with tribological properties being measured in collaboration with Shell Global Solutions and thermal properties being measured in house with the measurement of thermal conductivity requiring the construction of a bespoke instrument.

Through the methods described above stable dispersions of graphene materials will be produced in functional fluids and their impact on properties relevant to their application in automotive applications will be analysed to assess the potential of this “wonder material” to improve the efficiency of internal combustion engines and reduce their fuel consumption and emissions.

Chapter 3

Characterisation of Graphene and Related Materials

Graphene, and its related materials, present some challenges when it comes to their characterisation. To this day there is no single technique that can give a full picture of the chemical and physical structure of graphene; this is especially the case in more complex systems such as GO or functionalised graphene where it is extremely difficult to determine the location of, and identity of functional groups. Because of the nature of graphene and graphitic materials it is necessary to combine data from a wide range of characterisation techniques in order to build up a full picture of the material. Some of the key techniques used to characterise graphene materials are detailed in this chapter. More information on these techniques, and the wide range of other methods used to characterise graphene can be found in the scientific literature.

3.1. Transmission Electron Microscopy

Transmission electron microscopy (TEM) is one of a range of electron microscopy techniques that can be used for the characterisation of graphene and similar materials. As is described by its name, this technique relies on the detection of electrons that have been transmitted through the material being studied. By necessity this means the substance to be studied must be very thin, $<$10 nm in order to allow a sufficient number of electrons to pass through it making carbon nanomaterials ideal candidates for TEM.

The material to be examined is placed in the path of a high energy electron beam. As the electrons are transmitted through the sample their energy changes, and some electrons are

scattered. The transmitted electrons are detected by a charge-coupled device (CCD), and give information on the sample being analysed. A range of beam voltages can be used, with higher voltages meaning greater numbers of electrons striking the detector and so giving better contrast. The downside of this is that higher voltages can cause beam damage to the sample with voltages as low as 100 keV having been shown to cause damage to carbon materials.[349]

3.1.1. Imaging

The most common use for TEM is for imaging of samples at very high magnifications with resolutions well below the diffraction limit that restricts optical microscopy. This makes it an extremely useful technique for carbon nanomaterials which exist on scales which can be tricky to image using other methods.

Bright field TEM images, such as that shown in figure 3.1 A, can be used to see the overall shape, and dimensions of a sheet as well as giving an idea of quality and the degree of folding or crumpling. Taking statistically significant numbers of images of sheets can allow for analysis of sheet sizes to be performed. The thickness of sheets can also be qualitatively determined through the comparison of contrasts between different sheets as thicker sheets will permit fewer electrons to pass through, giving a darker appearance in the micrograph.[350]

In order to gain more information from TEM then high resolution transmission electron microscopy (HREM) can also be performed. This, as is expected from the name, utilises the full resolution capabilities of the technique to see detailed structural information about the material being imaged. An example of a HREM image is shown in figure 3.1 B.[350] In other carbon nanomaterials, such as CNTs, it is possible to see individual tube walls and end caps. In graphene and related materials HREM can be used to visualise the number of layers in a graphene flake due to the fact that the edges of graphene sheets tend to fold back over themselves at their fringes, presenting the layers parallel to the beam as shown in figure 3.1 D.[350] These show as parallel fringes in the micrograph recorded and using a histogram of

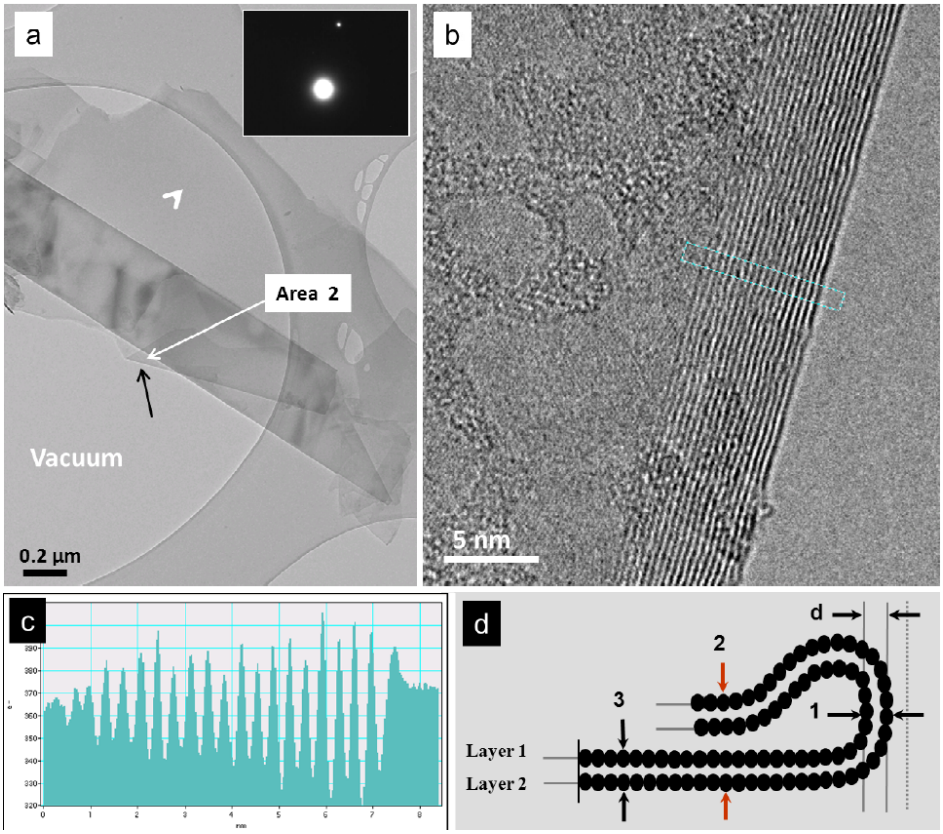

Figure 3.1: *A) TEM image of a single graphene sheet, B) High resolution image of the folded edge of the sheet imaged in panel A, C) the intensity profile of the folded edge of the sheet imaged in panel B showing the number of layers present in the sheet to be 17-18, and D) a schematic of the folded edge of the sheet showing how the sheet becomes parallel to the beam of the electrons allowing the number of layers of a flake to be counted. S. Rubino et al., A Simple Transmission Electron Microscopy Method for Fast Thickness Characterization of Suspended Graphene and Graphite Flakes, Microscopy and Microanalysis,* ***22****, 250–256, reproduced with permission.*

brightness across the edge of the sheet (figure 3.1 C) allows for the number of graphene layers within a sheet to be counted.[350]

3.1.2. Electron Diffraction

Another use of TEM on graphene materials is electron diffraction (ED). As electrons pass through the material they are scattered elastically by crystalline latices within the sample. The diffracted electrons interfere constructively and destructively to produce maxima and minima which form a diffraction pattern that gives information on the crystalline structure of the material. The information afforded by this technique is comparable to that derived from XRD, which is a similar diffraction based method. In order to obtain information on

specific areas of the sample apertures within the microscope can be used to isolate certain regions of the sample; this process is known as select area electron diffraction (SAED).

As graphite and graphene have distinct crystallographic structures, they also have subtly different electron diffraction patterns. The key difference is the absence of the $(0\,0\,2)$ peak which arises from the interlayer spacing present in graphite, but absent in graphene materials. Aside from this the diffraction patterns for graphite and graphene materials are similar, as the structures of layers within graphite and graphene are the same. The most commonly observed peaks in ED of graphene, as for XRD, are the $(1\,0\,0)$ and $(1\,1\,0)$ peaks.

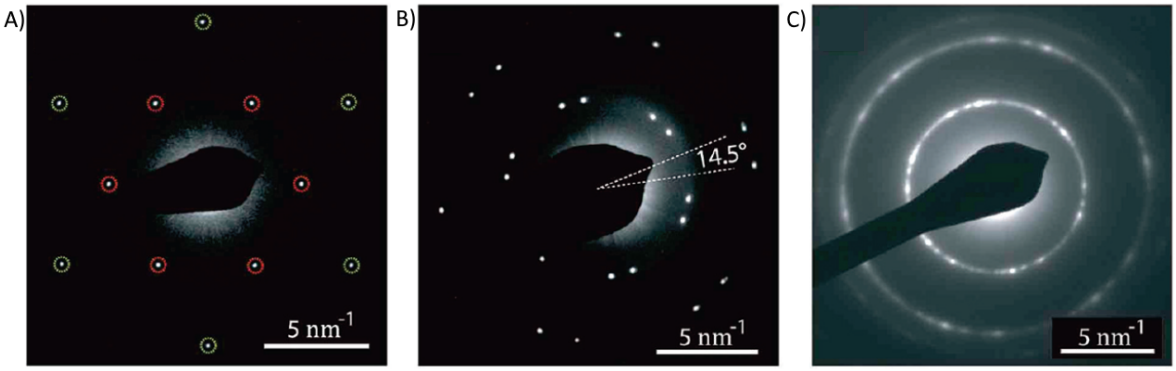

Figure 3.2: *SAED pattern for A) a single graphene oxide sheet, highlighting the two different sets of diffraction spots, B) two overlapping graphene oxide sheets that are offset by 14.5°, and C) ED pattern from a film of graphite oxide about 15-20 layers thick which illustrates rings of spots. Reprinted with permission from ACS Nano, 2009, **3**, 2547–2556. Copyright 2009 American Chemical Society.*

The diffraction pattern of a single sheet of pristine graphene consists of spots with 6-fold rotational symmetry, appearing in a hexagonal pattern (figure 3.2 A). However, what is frequently observed is either multiple sets of rotated spots (figure 3.2 B) or even rings composed of overlapping spots (figure 3.2 C) in diffraction patterns for graphene; this is due to the presence of graphene sheets stacked on top of one and other, with their crystalline domains rotated at slightly different angles. This leads to diffraction patterns of these sheets being rotated with respect to the first sheet, leading to the rotated spots or rings observed. A final possible use of ED is to determine the number of layers present in a graphene material as it has been shown that the relative intensity of the diffraction spots can be used to determine layer number as well as to determine the stacking sequence in multi-layer graphene

materials.[351,352]

3.1.3. Other Advanced TEM Techniques

Alongside the techniques discussed above there are also a range of other methods that can be used within TEM to study graphene and other nanomaterials. These include energy filtered transmission electron microscopy (EFTEM), electron energy loss spectroscopy (EELS), thickness mapping and element mapping. The use of these techniques to study graphene has been discussed elsewhere in the literature.[353–355]

3.2. Scanning Electron Microscopy

Scanning electron microscopy (SEM) is an alternative microscopy technique to TEM that can be used for the characterisation of graphene and its related materials. In contrast to TEM, which relies on the transmission of electrons through the sample, in SEM imaging relies on the detection of either back scattered electron (BSE) or secondary electron (SE) from the sample occurring due to the electron beam of the microscope. Beam energies are typically far lower than those used for TEM; within the range of 0.5-40 keV.

Whilst the resolution of SEM does not allow internal structural detail to be extracted, as is possible in TEM, it is still a useful technique that allows for information on the structure of graphene. The main advantage of SEM is the large sample areas that can be imaged as well as greater depths of field than TEM making it possible to obtain structural information about 3D graphene structures such as foams (figure 3.3).[356]

3.3. Atomic Force Microscopy

Atomic force microscopy (AFM) is a further microscopy technique that can be utilised in the characterisation of graphene. A very fine probe is passed over the sample and its posi-

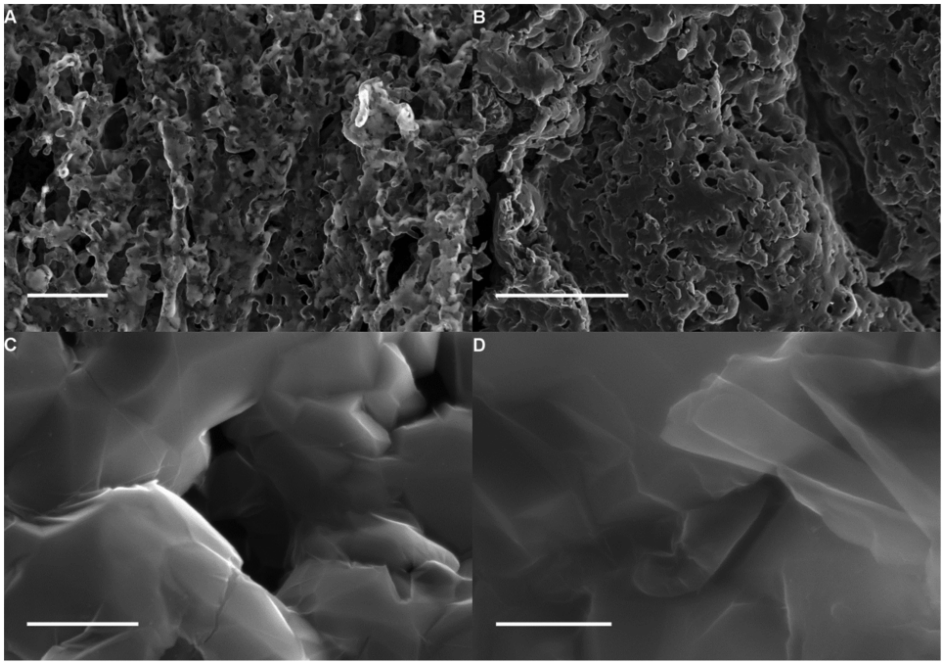

Figure 3.3: *SEM (SE) images of a graphene foam produced from a cobalt metal foam. Scale bars are 50 µm, 30 µm, 1 µm, and 500 nmrespectively and images are taken at 15 kV, 5 kV, 5 kV, and 15 kV respectively. Figure reproduced from Nanoscale 2016, **8**, 13303 - Published by The Royal Society of Chemistry.*

tion is measured extremely precisely. The structure of the sample being studied will affect the position of this probe and thus structural information on the sample can be determined.

AFM of graphene is principally used to derive information about the dimensions of sheets, both laterally and in terms of thickness with the resolution of the technique enabling single layers of graphene to be imaged under optimised conditions. The ability of AFM to image large numbers of sheets means it is often preferred to SEM and TEM when attempting to measure the size of a statistically relevant number of graphene sheets.Representative AFM images of a graphene sheet are shown in figure 3.4

Sample preparation for AFM is critical to obtain useful information as the graphene sheets must be deposited flat onto the substrate, sufficiently spaced to allow for measurement of individualised sheets, but not so sparsely dispersed that it becomes impossible to measure a statistical number of sheets. A variety of modes of operation of AFM are available such as contact, tapping and peak force. However their use is beyond the scope of this discussion and is widely covered in the literature.[357]

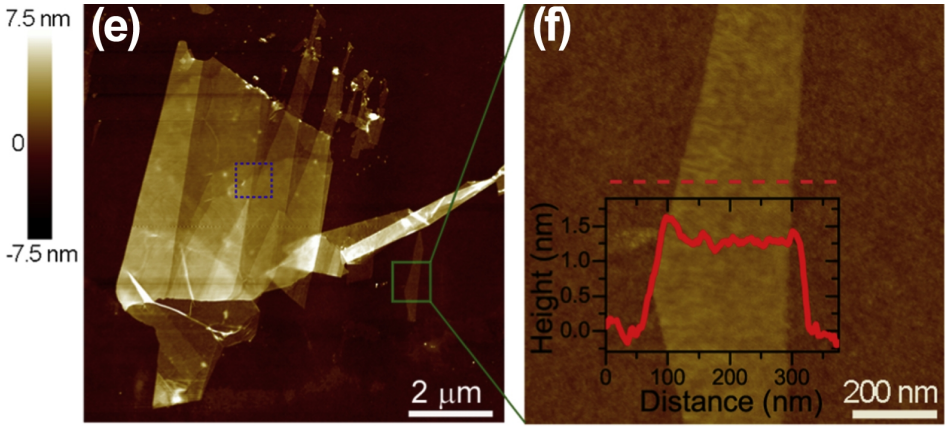

Figure 3.4: *AFM images of (e) the entire graphite flake and (f) higher magnification AFM image of the single layer area with (inset) cross section graph. Reproduced from Nanotechnology, 2016, **27**, 125704. Copyright IOP Publishing. Reproduced with permission. All rights reserved.*

3.4. UV-Vis Spectroscopy

One of the principle characterisation techniques for graphene dispersions is ultraviolet-visible (UV-Vis) spectroscopy. This technique is commonly used in many areas of chemistry, both for chemical identification from peak position and for determination of concentration through use of the Beer-Lambert law. UV-Vis spectroscopy of graphene dispersions can be used to derive the same information.

The UV-Vis spectrum of graphene contains only one characteristic peak at which is observed at $\lambda_{max} \sim$ 270-300 nm and is generated by the $\pi \rightarrow \pi^*$ C=C plasmon transition of the graphene.[358–360] GO has a similar UV-Vis spectrum to that of more pristine graphene. However the $\pi \rightarrow \pi^*$ plasmon peak is shifted by the presence of the oxygen functionalities to $\lambda_{max} \sim$ 230 nm.[361] In more oxidised materials the peak is more blue-shifted due to the lack of an extended conjugated network. Another feature is also exhibited with a shoulder at $\sim$ 300 nm attributed to the n $\rightarrow \pi^*$ transitions of C=O bonds.[244,358] Typical UV-Vis spectra for GO and rGO are shown in figure 3.5.

This change in the position of the $\pi \rightarrow \pi^*$, which occurs as a result of the restoration of conjugation during reduction, is a useful tool in the characterisation of graphene materials as peak position can be used to give an indication of the progress of reduction from GO to rGO.[120,259,358]

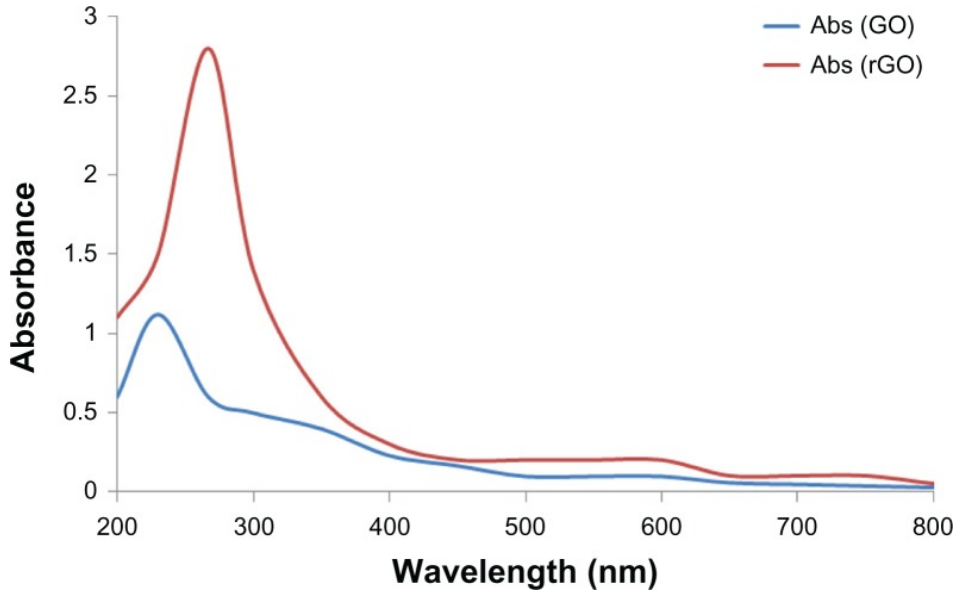

Figure 3.5: *UV-Vis spectra of GO and rGO showing the shift in position of the $\pi \rightarrow \pi^*$ peak as a result of the change in conjugation. Figure reproduced from Int. J. Nanomedicine, 2013,* ***8****, 1015–1027. Copyright 2013 Gurunathan et al. Publisher and licensee Dove Medical Press Ltd.*

Aside from the plasmon peaks mentioned above the UV-Vis spectra of graphene and its related materials are largely featureless. However, this allows useful information on the concentration of dispersions to be derived. As is the case for many compounds it is possible to use the Beer-Lambert law to calculate the concentration of a dispersion of graphene. The featureless region of the spectrum, above 500 nm, is ideal for measurement of concentration as there are no peaks to affect the absorbance.

$$A = \alpha c l \tag{3.1}$$

Making use of the Beer-Lambert law, equation 3.1, where A is the absorbance in the UV-Vis spectrum, α is the absorption coefficient, c is the concentration and l is the path length it is possible to determine the concentration of a dispersion from its UV-Vis spectrum. l is a constant and so is easily determined; however, α is not so easy to measure and an accurate value is needed for determination of concentration. In the literature a widely varied values for absorption coefficients of graphene exist. For example works by the group of J Coleman have reported values for α ranging between 1390-6600 ml mg^{-1} m^{-1} [81,82,362–364] and it is believed this variability is caused by changes in the material dispersed including: sheet

size, number of layers, and the functional groups contained in it.[365] Consequently, values of α are not necessarily transferable between different graphenes. In spite of this, the nature of the Beer-Lambert law means that even if accurate values of α are not available it is possible to compare the relative concentrations of dispersions of the same graphene material from their absorbance in a UV-Vis spectrum.

3.5. Raman Spectroscopy

A technique that can be used to give internal structural information on graphene and other carbon nanomaterials is Raman spectroscopy. A laser is used to illuminate the sample through a confocal microscope and photons striking the sample undergo inelastic scattering. These photons return through the confocal microscope and are detected using a CCD. Those photons that have been scattered by the sample have a different wavelength to those produced by the laser, and this wavelength is characteristic of the functionality that caused the scattering to occur. The result of this is that the presence of certain groups can be identified using Raman spectroscopy due to the peaks present in the spectra recorded.

For carbon nanomaterials, including graphene, there are several significant peaks in Raman spectroscopy. Principle among these is the band known as the *G* band, also seen in graphite, which occurs at 1582 cm^{-1} and is associated with the E_{2g} vibrational mode of the sp^2 graphene lattice, corresponding to in plane stretching of sp^2 carbon atoms. This vibrational mode is universally present in graphene materials making the *G* band highly characteristic of aromatic carbon molecules.[26,366,367] The *G* band is the only normal first order band in graphene materials as the remaining *G'* band and *D* band both result from second order processes involving 2 phonons in the case of the *G'* band and a defect and a phonon for the *D* band.[26] The *D* band occurs at $\sim$1355 cm^{-1} and is a second order resonance resulting from the breathing modes of the aromatic rings requiring both a phonon in the sp^2 network adjacent to a defect in the graphene sheet[366–368] and is activated by a double resonance.[369] Finally, the *G'* band, also referred to as the *2D* band, is an overtone of the *D* band generated

from phonons at the edge of sp^2 regions that also cause the *D* band.[370] However, while the *D* band is only visible in the spectra of materials with defects this is not the case for the *2D* band as this peak originates from a process involving two phonons with opposite wave vectors, thus satisfying momentum conservation.[369] The result of this is that the *2D* band is present even in samples with no defects and is observed at $\sim$2700 cm^{-1}.[369,370]

As the *D* band occurs as a result of defects in the sp^2 lattice of graphene it is only observed in materials which have disruptions in their structure, and its intensity can in fact be used as a measure of the degree of defectiveness of a material. While the intensity of the *G* band depends on the number of carbon atoms present,[366] that of the *D* band is related to the number of defects.[367] Therefore, by taking the ratio of the *D* and *G* peaks it is possible to get a quantitative measure of the defectiveness of a material. There is however, some debate as to whether it is more appropriate to utilise the peak area ratio ($A_D : A_G$) or intensity ratio ($I_D : I_G$) which give slightly different results due to the full width at half maximum (FWHM) of the *D* band and *G* band being determined by different factors.[371,372]

When characterising graphene the shape and size of the *2D* band has been shown to be significant in determining the number of layers present in a sample of pristine graphene. The shape of the *2D* band changes with the thickness of the sample, as is show in figure 3.6.[369,370] In graphite the *2D* peak is made up of two components: $2D_1$ and $2D_2$ which combine to form a peak with a height between half and quarter that of the *G* peak.[369] As the number of graphene layers increases to >5 the shape of the *2D* becomes indistinguishable from that of graphite. When the number of layers is <5 the shape of the *2D* peak begins to change, as does its intensity relative to that of the *G* peak. In mono-layer graphene the *2D* peak has transitioned into a single sharp peak with an intensity of around 4 times that of the *G* peak appearing at a smaller Raman shift than that of the graphite *2D* peak (figure 3.6 B).[370] In comparison the *2D* peak of bilayer graphene appears differently to that of both mono-layer graphene and graphite and is believed to be made up of as many as 4 component peaks.[370]

In non-pristine graphene materials, such as GO, functionalised graphene, and rGO Ra-

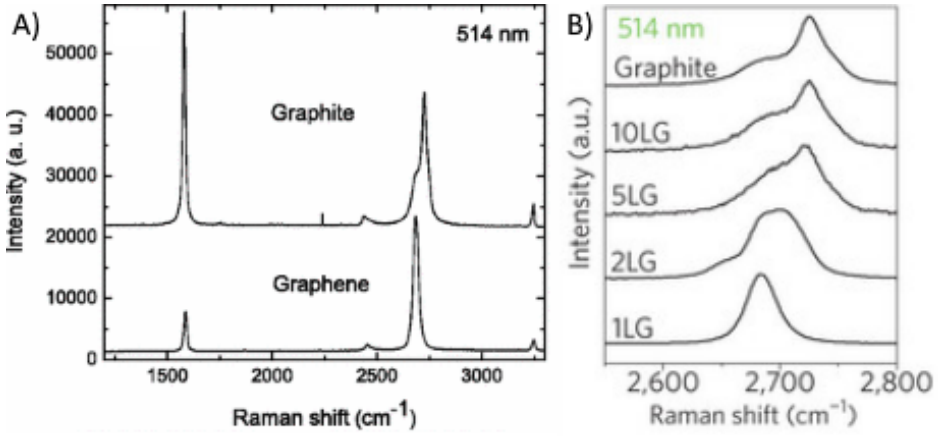

Figure 3.6: *A) A comparison of the Raman spectra of graphite (top) and pristine graphene (bottom) showing the G band at ∼1600 cm^{-1} and the 2D at ∼2700 cm^{-1}. In both cases spectra are normalised to the intensity of the 2D band. Reprinted figure with permission from A. C. Ferrari et al., Physical Review Letters,* ***97****, 187401, 2006. Copyright 2006 by the American Physical Society. B) The 2D peak as a function of layer number for single-layer graphene (1LG), bi-layer graphene (2LG), 5 layer graphene (5LG), 10 layer graphene (10LG) and graphite. Reprinted by permission from Macmillan Publishers Ltd: Nature Nanotechnology, 2013,* ***8****, 235–246, copyright 2013.*

man spectroscopy can also be used to give important information on their chemistry. As is evident from the origin of the *D* band, this peak will have a much higher intensity in materials where the sp^2 matrix is disrupted. In GO it is common for the $I_D : I_G$ ratio to be close to 1. Of particular note is the *D* peak of rGO; one would expect that, as rGO is graphene-like, the reduction of GO would cause a decrease in the intensity of the *D* peak as the oxygen functionalities are removed. In reality it is observed that the *D* peak actually increases in intensity as a result of the reduction reaction. It is believed that this is due to the structure of rGO which contains small sp^2 domains surrounded by more defective regions. These sp^2 regions have high large numbers of edge atoms adjacent to defects, required for the *D* peak to be observed and so causing an increase in its intensity upon reduction.[215] However, In these materials the *2D* band has a much lower intensity and a less well defined shape, if it is seen at all, meaning that its use is not a possible method to determine the number of layers in the sample and far less information can be derived from Raman spectroscopy of GO and rGO than is possible for pristine graphenes.[373]

3.6. Thermogravimetric Analysis

Thermogravimetric analysis (TGA) is a process involving the precise measurement of the mass of a sample as its temperature is changed under strictly controlled environmental conditions. In general this involves the heating of samples at a controlled heating rate, either in air or in an inert gas, which gives information on either the thermal decomposition or the ignition of the material being examined.[374] Examining the changes in mass that occur at specific temperatures allows information on the chemical structure of a material to be determined. TGA can also be used to give an indication of the levels of inorganic impurities, such as metals or inorganic salts, in a material as these materials will not burn off in air at high temperatures. Therefore, taking the residual mass of a sample after heating to high temperatures (>900 °C) allows a relative composition of these impurities to be determined.

The temperature at which carbon materials decompose has been shown to be related to the number of defects that are present in their structure with those with the higher proportion of defects decomposing at lower temperatures.[375] The decomposition temperatures of a range of carbon nanomaterials are well reported in the literature. Graphite, diamond, and CNTs are relatively defect free and so decompose at higher temperatures of ∼645 °C, ∼630 °C, and ∼695 °C in air respectively while C_{60} and amorphous carbon, being more defective, decompose at lower temperatures of ∼420 °C and ∼585 °C.[376,377]

Modified graphene materials exhibit a range of thermal behaviours dependant on the chemistry of the material in question; materials with the most intact sp^2 network such as CVD graphene decomposing at the highest temperatures. It would be expected that the thermal decomposition of graphene would occur at a similar temperature to that of graphite. In reality graphene's decomposition occurs at about 150 °C lower (∼500 °C).[95] This is not due to an increase in the number of defects in the structure, but is in fact as a result of the reduced intermolecular forces between sheets in graphene.[95] Thermal stability has been shown to be linked to layer number, with bi-layer graphene having significantly more thermal

stability than mono-layer graphene.[374]

Graphite oxide and GO are known to begin to decompose at much lower temperatures of 100-300 °C in both inert atmospheres and air due to the decomposition of the oxygen functionalities on the sheets.[235,378,379] However, the carbon network of the GO sheets also decomposes at lower temperatures than those of pristine graphene due to the increased sp^3 content.[379] These differences allow TGA to be used as a method to examine the degree of oxidation and reduction of graphene materials.[269,359]

One of the major uses of TGA when characterising modified graphene materials is in the characterisation of f-rGOs. In almost all functionalised graphenes the functional groups decorating the surface of the sheets will thermally decompose at a lower temperature than the sheets themselves. Therefore, by examining the TGA plots for these materials and comparing them to that for the unmodified material, it is possible to determine the mass loss that is caused by the thermal decomposition of the surface functionalities, enabling a wt. % and mol. % of functionalisation to be determined.[380]

3.7. X-Ray Diffraction

XRD is a technique principally developed in the early 20th century by Bragg and his father, W. H. Bragg, based on the early work on x-rays by M. von Laue.[381] For this work von Laue was awarded the Nobel prize for physics in 1914 with the Braggs receiving the same award the following year for their work. X-rays are known to be able to provide detailed information on the crystalline structure of materials.

X-rays incident on the sample are diffracted due to the crystalline nature of materials and these scattered rays are detected and recorded. The angles at which the x-rays scatter are the important information when determining crystal structure. Using Bragg's law it is possible to convert this diffraction angle into interlayer spacing with equation 3.2 where n is a positive integer representing the order of the difftaction peak, λ is the wavelength of

incident x-rays used, d is the inter-plane distance and θ is the angle at which the x-rays are diffracted.[382]

$$n\lambda = 2d\sin(\theta) \tag{3.2}$$

In the context of graphene materials the information most commonly elicited from XRD is the inter-layer spacing of the material. In graphite this is a well defined, consistent value, referred to as the $(0\,0\,2)$ spacing which has the value of 3.35 Å.[26] Mono-layer graphene does not show this spacing in its diffraction pattern as there is no consistent inter-layer spacing in the material. Graphene materials without consistent interlayer spacing tend to exhibit either a broad hump in their diffraction patterns or show present no peaks at all.[383]

XRD is an important technique when studying the exfoliation of graphite tp graphene, or from graphite oxide to GO as the broadening, or even disappearance, of the $(0\,0\,2)$ peak can be taken as an indication of exfoliation.[270] Graphite oxide has a different XRD pattern to that of graphite. While the $(0\,0\,2)$ peak is still the main one expressed, the inter-layer spacing increases significantly during oxidation, as discussed in section 1.5.3.2, due to the oxygen functionality and intercalated water molecules causing the $(0\,0\,2)$ peak to shift from its initial position of 3.35 Å to between 6 Å and 12 Å with the exact peak position being dependent on the level of hydration of the graphite oxide.[269,384,385] Representative X-ray diffraction patterns for GO, graphene and graphite are shown in figure 3.7.

Other diffraction peaks from within the sp^2 matrix of graphite and graphene sheets (such as the $(1\,0\,0)$ and the $(1\,1\,0)$) should theoretically be visible in XRD patterns of these materials. However this is frequently not the case with only the $(0\,0\,2)$ appearing. This is believed to be due to the planarity of the graphene or graphite sheets which all hold one orientation meaning the remaining peaks are not expressed. This is particularly the case for powder XRD but less so for capillary XRD.

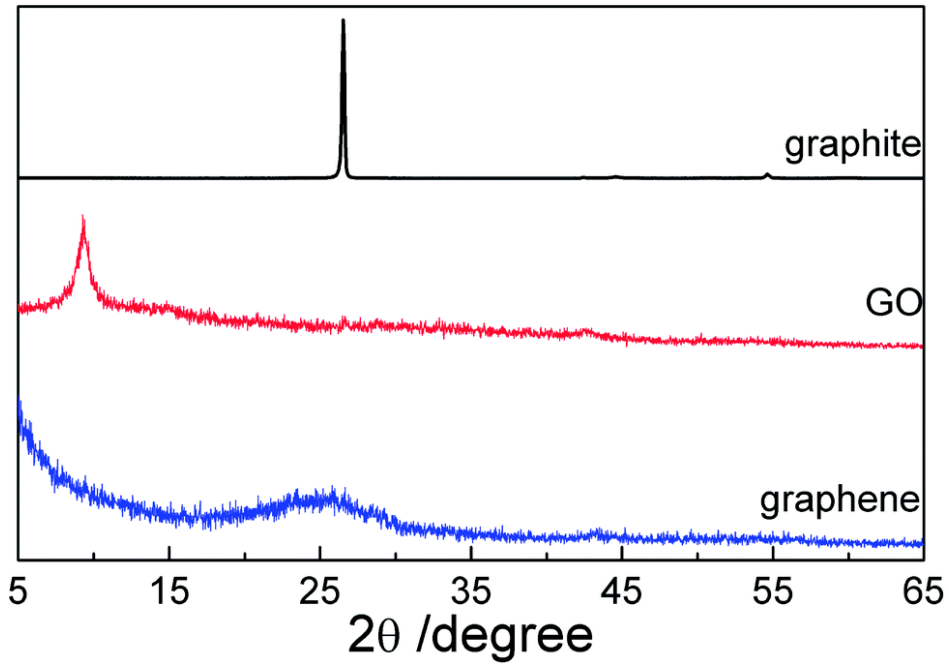

Figure 3.7: *XRD patterns of graphite, GO and graphene. Reproduced from Nanoscale, 2014,* ***6****, 2299–2306 with permission of The Royal Society of Chemistry.*

3.8. X-Ray Photoelectron Spectroscopy

X-ray photoelecton spectroscopy (XPS) is an x-ray based analytical technique which is commonly used for sample surface analysis. This makes it an interesting technique when studying graphene as, since graphene is only one atom thick, it can be used to elicit a great deal of information. XPS is performed by irradiating a sample, *in vacuo*, with soft x-ray radiation (commonly Al or Mg K_{α}). X-rays penetrate into the solid sample, where they interact with the core electrons contained in it, transferring their energy to these electrons and causing photoemission. The information derived from XPS is based on the measurement of the energy of these emitted electrons and gives information on the binding environments present within the sample. When an x-ray, of known energy, penetrates the sample and causes photoemission of an electron from a core orbital some of the energy of the x-ray is utilised to remove the electron from its binding environment, while the remainder is transferred to the electron as kinetic energy (figure 3.8). Therefore, by measuring the difference in kinetic energy between the ejected electrons and the incident x-rays a picture of the binding environments present within a material can be determined.

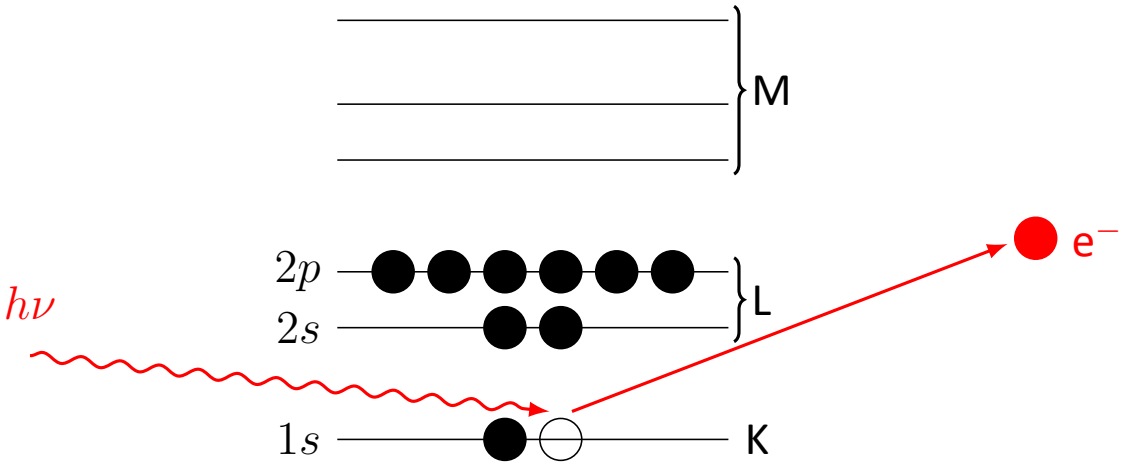

Figure 3.8: *A Jablonski diagram showing the x-ray stimulated photoemission process that occurs during XPS.*

When performing XPS a range of information can be obtained depending on the exact measurement parameters used. Generally the first scan performed is the survey scan. This is a plot of binding energy against electron intensity across a wide range of energies. As the peaks that occur at specific binding energies are characteristic of the orbitals present in certain elements in the sample, this scan can be used to determine the elemental composition of a material, and the intensities of the peaks can even be used to calculate a relative proportion of each of the elements present within the material being studied. This can be used to prove the presence of functionalisers on the surface of the graphene sheets, however proving the mechanism by which this functionalisation has occurred is not always possible. Using the survey scan it is also possible to detect the presence of many impurities, or contaminations in the sample that can not always be detected using other characterisation methods.

The depth of penetration of the soft x-rays used in XPS is of the order of microns. However, the emitted electrons from the material are only able to escape from the first few layers of molecules. Hence one of the limitations of XPS is that only the surface of a sample can be analysed. Whilst this is a limitation for some materials that have inhomogeneous compositions, such as those with a surface oxide layer, this is not such a concern for graphene materials, as the sheets are thin enough that x-rays will permeate throughout. However, this does lead to another challenge associated with XPS of graphene materials, as the thin

sheets lead to the substrate used to hold the sample producing signal in the XPS. Whilst silicon the most common choice of material to analyse samples on with XPS it does present some challenges. For the analysis of the C1s peak there is no issue, as the binding energies of silicon do not overlap with those of carbon. However, when studying materials that contain oxygen such as GO the layer of SiO_2 that is naturally present on silicon contributes to the peak in the O1s region of the spectrum making it impossible to determine the elemental composition of the sample precisely. This peak also overlaps with the peaks produced as a result of carbon-oxygen bonding environments and making it difficult to fit and interpret this region of the spectrum. Whilst other substrates are used for XPS many of them exhibit the same problem and create overlap in either the C1s or O1s regions of the spectrum that are generally of interest when analysing graphene. Generally, the C1s region is that of most interest and so silicon is generally used as an XPS substrate, at the cost of clear measurements in the O1s region.

Using the information derived from the survey scan, each of the peaks produced by the atoms contained in the sample can then be studied in greater detail. These core peaks will be rescanned using a much greater resolution of binding energy to provide a plot of binding energy against electron intensity over a narrow range of binding energies. The peak, or peaks, in the region studied are actually composed of overlapping bands resulting from electrons in specific chemical environments, with each environment creating a subtle shift in binding energy.

In order to gain further information about the chemical composition of the sample being studied it is possible to fit component peaks within the core peaks in order to produce a combination of peaks that have a sum that matches the lineshape of the core peak. In order to fit these component peaks it is important to understand the material being examined and know what binding environments are likely to be present within it. The positions of peaks for these binding environments can then be found in the literature. Fitting of the C1s peak is a commonly used method for characterising oxidised carbon materials such as GO and peaks commonly found in these materials are shown in table 3.1.[213,214,270,386,387] It is important to

remember, however, that these peak positions are not always the same and that the exact composition of the sample can cause small shifts in the positions of each peak.

Table 3.1: *The binding energies of C1s peaks for a range of C−C and C−O bonding environments.* [213,214,270,386,387]

Binding energy / eV	Assignment
285	Graphitic C=C (sp^2 carbon)
286	C≡N
287	C−O−C
288	C=O
289	O−C=O

Due to the potential subtle variations in peak positions and the range of widths possible for each peak it is possible that multiple combinations of peaks can create a fit envelope matching the spectrum recorded from the sample. Therefore care must be taken to ensure that the fit proposed makes chemical sense, and fits should endeavour to utilise the minimum number of peaks possible.

Different graphene materials will produce C1s spectra with significantly different lineshapes, depending on the composition of the material. Graphitic materials, such as graphene and rGO present similar lineshapes to that of graphite. The main component of this peak occurs at ∼285 eV and arises from sp^2 C=C binding environments within the graphene sheet (figure 3.9 B). [388] The asymmetry within this peak is expressed as a tail to higher binding energies and arises from inter-atomic Auger electron transfers that occur with valence electrons in nearby atoms as a result of the extended sp^2 network in in graphene sheets. [389] It is therefore common practice to derive the lineshape for the C=C peak from a previously acquired C1s spectrum of pure graphite, and then use this when fitting peaks produced by other graphene materials.

Materials containing oxygen functionalities exhibit significantly different XPS spectra than those without. Peaks for carbon-oxygen binding environments are expressed at higher binding energies than the C=C peak and increase the asymmetry of the overall lineshape. The degree to which these groups change the overall lineshape is dependent upon the degree of oxygenation of the sample. Samples that are highly oxidised exhibit 2 distinct peaks,

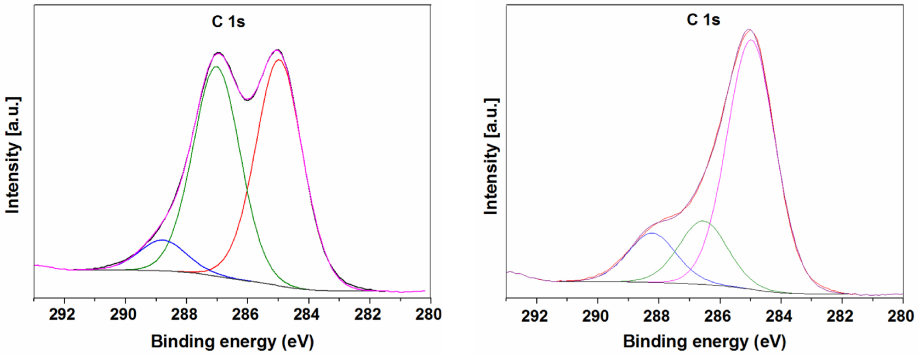

Figure 3.9: *C1s XPS Spectra of A) GO and B) rGO. Reproduced with permission from Optics Express, 2012,* ***20****, 19463–19473. Copyright 2012 The Optical Society.*

whilst those which only contain residual oxygen, such as rGO, merely have a single asymmetric peak.

A representative XPS spectrum for GO is shown in figure 3.9 A. This clearly shows the two main peaks, the peak at 285 eV arising from C=C and the peak at 287 eV arising from the primary carbon-oxygen functionality: C−O−C groups.[388] Other peaks also contribute to this overall spectrum, resulting in the overlap seen between the two peaks, caused by the range of other oxygen functionalities present in the sample.

rGO has a significantly different XPS spectrum from that of GO with a vast decrease in the height of the C−O−C peak and the C=C peak dominating the spectrum. This allows XPS to be used as a method of measuring the degree of reduction of rGO. One important consideration when using XPS to study rGO produced using hydrazine is that it is expected that a peak arising from C≡N bonding environments will be present as a result of the hydrazine reduction, alongside residual carbon-oxygen bonding environments and this must be taken into consideration when fitting the C1s peak for rGO

Whilst the peak in graphene materials that can be used to derive most information is the C1s peak, it is also sometimes possible to fit other peaks in the spectrum, most commonly the O1s peak. However, the proximity of the component peaks, and their similar lineshapes means it is challenging to get a definitive fit. Care must also be taken when examining the O1s peak as it may contain contributions from other sources, such as oxide layers on the

substrate used, as discussed above.

CHAPTER 4

NANOFLUID CHARACTERISATION

The aim of this project is to produce graphene containing nanofluids with properties that are improved over those of the base fluids. In order to assess the properties of the nanofluids produced it is necessary to use a range of characterisation techniques. The key properties of interest are the thermal and tribological properties; however, it is also important to examine the chemical properties of the dispersions such as concentration and stability.

4.1. Concentration and Stability of Dispersions

Concentration of dispersions is classically determined using UV-Vis spectroscopy, as has been discussed in section 3.4, although it is also possible to use much simpler, gravimetric methods to obtain similar data. Simply by heating the dispersion to temperatures that allow the solvent to be driven off and taking precise measurements of mass before and after, either by hand or through the use of TGA, it is possible to obtain the concentration of dispersions.[390] This relies on being able to remove the solvent at a temperature below the decomposition point of the dispersed material, which is not always possible for GO due to its propensity for reduction at elevated temperatures (section 1.6.1). It can also be a tedious and time consuming process and so UV-Vis is generally the preferred method.

In order to characterise the stability of dispersions it is possible to utilise a range of techniques. The simplest, and only definitive, method to establish long term stability is simply to allow the dispersion to stand for the time period of interest measuring the concentration, or another property such as viscosity or conductivity that can be used to detect changes in concentration, at set intervals. Taking this approach when the dispersions are required to be stable for periods of up to years is not practical and so techniques are available that can

artificially accelerate settling.[391] These processes include: centrifugation, agitation, mixing and heating. It is then possible to extrapolate a dispersion's long term stability. However, it should be noted that these methods can all, unless used carefully, cause additional destabilisation that would not occur under normal conditions.[391]

Whilst most information on dispersion stability is usually gained from UV-Vis spectroscopy or gravimetric analysis of samples, as described above, it is also possible to infer information on stability from other techniques. A key method used to obtain this information is zeta (ζ) potential.

A material dispersed in a solvent develops a charge at the interface. This can be modelled as an electric double layer which is made up of three components. The bulk solvent, a closely bound Stern layer and a diffuse layer between them (figure 4.1). Somewhere in this diffuse layer is a slip-plane below which all components move as a single particle. The potential of this plane is the ζ potential.

The magnitude of the ζ potential ($|\zeta|$) is well known to correspond to dispersion stability, with larger values of $|\zeta|$ corresponding to more stable dispersions. In general, the most stable dispersions will have $|\zeta|$ of >60 mV, those with good stability will have $|\zeta|$ of 30-60 mV, dispersions with $|\zeta|$ of 10-30 mV will have some moderate stability, and those with $|\zeta|$ of 0-10 mV being unstable.[392] In spite of this it should be noted that some dispersions with lower ζ potentials can be stabilised sterically and so exhibit greater stability than their ζ potential

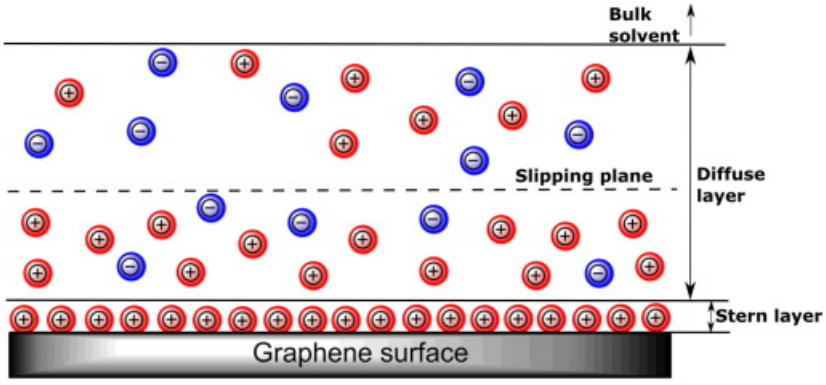

Figure 4.1: *A schematic of the ζ potential double layer model for a negatively charged graphene sheet. Reproduced from D. Johnson et al., A manufacturing perspective on graphene dispersions, Current Opinion in Colloid & Interface Science,* ***20****, 367–382, under a Creative Commons license .*

would indicate.[393]

Other techniques that can be used include dynamic light scattering (DLS) and static light scattering (SLS) which can both be used to determine particle size with SLS also being able to give information on shape. However, using these techniques with 2D materials do present some challenges as the models used are not optimised for particles with these aspect ratios.[11]

4.2. Thermal Properties

As the aim of this project is to produce improved lubricants and coolants for use in internal combustion engines, the thermal properties of these fluids is of great interest. The two key thermal properties are thermal conductivity (λ) and specific heat capacity (c_p) which are both measures of the thermal behaviour of a fluid. Another important, but less frequently mentioned, thermal property is the thermal diffusivity (κ) which links λ and c_p through equation 4.1 where ρ is the density of the material being measured.

$$\kappa = \frac{\lambda}{\rho c_p} \tag{4.1}$$

A range of techniques can be used to measure thermal properties of fluids and those most commonly used are discussed below.

4.2.1. Thermal Conductivity by the Transient Hot Wire Method

In the context of thermal fluids, the property that generally receives the greatest attention is thermal conductivity. This is a measure of the rate of transfer of thermal energy through a material at a specific temperature gradient with units of W m^{-1} K^{-1}. This makes it

a property of great interest when studying thermal fluids as changes in thermal conductivity can directly impact on the performance of these fluids in their applications.

Unlike solids, for which measurement of thermal conductivity is a comparatively easy task, in liquids it is possible for the transfer of heat to occur by either conduction or convection; this complicates the measurement of thermal conductivity in liquids as the effects of convection must be ruled out in order to obtain accurate results. Techniques for the measurement of thermal conductivity fall into two groups: transient and steady-state. Steady-state methods involve the use of long measurement times at constant temperatures and require simple apparatus but are not suitable for liquids since the effects of convection will impact on the values of thermal conductivity measured.

Transient methods, on the other hand, allow for thermal conductivity to be measured in isolation. They involve short measurement times and the temperature of the sample changes over the course of the measurement. The result of this is that the data recorded are more complex to process than for steady-state methods but this allows the effects of convection to cancelled out by careful experimental design. This makes transient methods ideal for analysis of the thermal conductivity of liquids.

The transient hot wire (THW) method is the most commonly used transient method of determining thermal conductivity. Early studies using a hot wire to measure thermal conductivity were reported as far back as the 1780s when scientists including Joseph Priestley and Count Rumford noted that the rate that a wire cooled from incandescence depended on the gas that surrounded it.[394] The full history of the THW method has been reviewed in detail by Assael *et al.*[394]

In principle the THW method is based on a platinum resistance thermometer, relying on the linear correlation of temperature and resistance in metals. In the THW method, this wire is used to heat the sample as well as recording changes in temperature. A thin platinum wire is immersed in the sample and a current is passed through this wire; the presence of the current causes the temperature of the wire to increase and hence its resistance also

increases. The magnitude of this temperature rise and the associated resistance rise in the wire can then be used to determine the thermal conductivity of the sample.

Even though reports of hot wire-like techniques can be found as far back as the 18th century it did not become a viable method of obtaining quantitative information on thermal conductivity until 1971 due to the technical complexities of controlling and recording data from an instrument.[395] However, since this time many developments have been made to the method and now an American Society for Testing and Materials (ASTM) standard test method is available.[396] In spite of this, there are few commercially available examples of instruments for measuring thermal conductivity and the majority of these are designed to test the thermal conductivity of soils, as opposed to liquids. This means that they only provide measurements with errors of $\pm 10\,\%$ making them unsuitable for detecting small changes in thermal conductivity occurring as a result of low concentrations of additives.[397]

4.2.2. Specific Heat Capacity by Differential Scanning Calorimetry

Whilst thermal conductivity represents the rate at which thermal energy can be transferred through a material, heat capacity corresponds to its ability to hold this thermal energy. Heat capacity is defined as the amount of energy required to cause a temperature rise of 1 degree in a material and as such as units of $J\,K^{-1}$. Specific heat capacity is the heat capacity per gram of a material, giving it units of $J\,K^{-1}\,g^{-1}$. This is an important property for thermal fluids, the higher the specific heat capacity, the lower the temperature rise that will occur in the thermal fluid when carrying away a given amount of thermal energy. Therefore, good thermal fluids will have high specific heat capacities alongside their high thermal conductivities.

Measurement of specific heat capacity of fluids is most commonly performed using differential scanning calorimetry (DSC). The standard procedure for this is laid out in ASTM

E1269-11.[398] The procedure for this test involves the heating of the material at a controlled rate and comparing the heat flow with that for a reference with a known specific heat capacity, generally synthetic sapphire.

Measurement of the specific heat capacity of a sample requires 4 consecutive runs to be performed. Firstly, 2 empty pans are heated at 20 °C minute^{-1} over the desired temperature range. The sapphire standard is then placed into one of these pans and the experiment repeated in order to obtain a reference specific heat capacity from the instrument. This process is then repeated for two empty pans, before the sample to be tested can be added to one of these pans, and the measurement repeated a final time. The heat capacity of the sapphire standard and the sample can then be isolated from the heat capacity of the pans by measuring the difference in heat flow between the measurements at a given temperature. Given that the heat capacity of the sapphire standard is well known it is then possible to convert the heat flow data for the sample to heat capacity, and then using the mass of the sample determine the specific heat capacity of the sample being tested.[398]

One challenge with this method is that the mass of the pans, and their contents, must remain constant throughout the measurement. Therefore, when testing liquids, which tend to be volatile and evaporate in the temperature ranges used, hermetically sealed pans are needed in order to avoid changes in mass of the sample, which will affect the final results.

4.2.3. Thermal Diffusivity by Laser Flash

Of the three thermal properties mentioned in this section, thermal diffusivity is possibly the most challenging to measure. Therefore it is common to use equation 4.1 to calculate this from specific heat capacity and thermal conductivity as opposed to measuring it directly. However, it is possible to determine thermal diffusivity by experimental methods with the most commonly used method being the flash method, detailed in ASTM E1461-13.[399]

Thermal diffusivity can be thought of as a measure of the rate of heat transfer through

a substance and has units of $m^2\ s^{-1}$. In materials with high thermal diffusivity, such as metals, temperature gradients will not persist for long periods across the substance as heat is transferred quickly, evening out gradients.

Measurement of thermal diffusivity of liquids once again employs transient methods of measurement. The flash method involves the rapid illumination of one side of a thin quantity of the sample with a high intensity energy pulse, most commonly a laser source. This causes a temperature rise in one side of the sample. Simultaneously the temperature of the far side of the sample is recorded and the thermal diffusivity can then be calculated from the thickness of the sample and $t_{1/2}$, the time taken for the far side of the sample to reach half of its maximum temperature.[399]

Measurement of thermal diffusivity requires specialist equipment in order to record the precise changes in temperature required and to isolate the sample from external influences on temperature. For this reason mathematical determination from specific heat capacity and thermal conductivity is often preferred.

4.3. Viscosity

In order to establish the potential of nanofluids in lubricant applications one characteristic that must be carefully monitored is viscosity. Commercial lubricants are formulated to have specific viscosities and use viscosity modifiers such as polymers in order to meet these criteria. However, the formation of nanofluids by the addition of graphene is likely to cause undesired changes in viscosity due to the presence of solid additives, in spite of their nanoscale dimensions. For this reason it is important to assess the viscosity of any nanofluids produced.

As a result of the varied conditions that lubricants are subjected to within an engine then the measurement of their viscosities must also take place under a range of conditions. For this reason, both the kinematic and high shear viscosities of the nanofluids produced will be

examined.

4.3.1. Kinematic Viscosity

The kinematic viscosity of a liquid can be thought of as its viscosity under low shear conditions, such as flow under gravity. This is the most commonly measured form of viscosity and is important for characteristics of a lubricant such as their ability to flow out of reservoirs and to coat components. Lubricants with too high a kinematic viscosity will not flow through the system they are supposed to be lubricating while those with a viscosity that is too low will simply flow off components and fall to the lowest point, which may not provide optimal lubrication.

Kinematic viscosity is highly dependant on temperature and for this reason it is measured at a range of temperatures, in order to understand the behaviour of the fluid under all conditions it may encounter during use.

Standard methods for measuring kinematic viscosity have been provided by ASTM: D445-06, and D446-07.[400,401] These standard documents describe the use of glass capillary kinematic viscometers to determine the kinematic viscosities of transparent and opaque liquids. In brief, a known volume of liquid is allowed to flow through a calibrated capillary tube under gravity and the time taken for this to occur is measured.[400] This time can then be converted to the kinematic viscosity through equation 4.2, where v is the kinematic viscosity in $mm^2\ s^{-1}$ or cSt, t is the time, in seconds, and C is the calibration constant of the viscometer, measured in $mm^2\ s^{-2}$.

$$v = Ct \tag{4.2}$$

With kinematic viscosity there is no general trend, such that higher or lower viscosity is preferable. However, each lubricant is specifically formulated to meet a certain kinematic viscosity range, which will perform best in the application it is designed for. For this reason,

when testing the kinematic viscosity of nanofluids with graphene based additives, the goal is that the additives make as little change in the kinematic viscosity of the lubricant as possible, in order to avoid the need to change the formulation to return the viscosity to the optimal range.

4.3.2. High Shear Viscosity

Alongside the measurement of kinematic viscosity, discussed above, it is also relevant to measure the viscosity of lubricants under more extreme conditions. In this case, those with a much higher shear rate, similar to those found within engine bearings. The testing of high shear viscosity was performed using an ultra-shear viscometer (USV); this instrument consists of a disc that rotates within the fluid being tested. The speed of this rotation is what induces the high shear on the sample whilst viscosity can be determined through careful measurement of the torque on the motor. Shear rates commonly measured using USV are in the range of 1×10^6-1×10^7 s^{-1}. As for the kinematic viscosity, the high shear viscosity is closely linked to temperature, and so this must be closely controlled alongside the recording of high shear viscosity over a range of temperatures to see its impact.

When studying the high shear viscosity of lubricants, their properties with changing shear rate depend on whether they are Newtonian or non-Newtonian. In general, the base fluids used for lubricants are Newtonian, meaning that their viscosity does not depend on the shear rate. For these fluids, testing of high shear viscosity is not very informative as viscosity and shear rate are proportional. However, when these base fluids are used to produce formulated oils they are mixed with a package of additives, one of which is usually a viscosity modifier. As a result of the presence of this modifier, formulated oils are non-Newtonian and exhibit shear-thinning. This means that measuring their viscosity under high shear is once again important as it is affected by shear rate.

As with kinematic viscosity, the high shear viscosities of lubricants are controlled carefully with their final applications in mind. Therefore, the aim when adding graphene based

modifiers to these lubricants is to avoid significant changes in their high shear viscosity. One other point of note is that it is possible that the presence of graphene based additives could result in the Newtonian properties of the fluid changing. Observing how the viscosity changes as a function of shear rate will give an indication of if the graphene based additives have caused any changes to the Newtonian properties of the fluid.

4.4. Friction and Wear

A final important set of characteristics for nanofluids when applied as functional fluids in automotive applications is their friction and wear properties. Functional fluids are frequently used as lubricants, coating moving parts and allowing them to slide past one and other, minimising the energy consumed by friction and preventing wear on the components. When examining the tribological properties of a lubricant the main property that is of concern is the coefficient of friction. This is commonly measured through the use of a mini traction machine (MTM). The behaviour of a lubricant is heavily dependant upon the conditions it is studied under, and for this reason coefficient of friction is often measured across a range of conditions in order to give a full picture of the behaviour of the lubricant.

A MTM consists of 2 components, which move relative to each other at a controlled force and speed. In general, the components are a steel ball and a steel disc which are independently driven against each other, in rotation, to produce a rolling-sliding contact.[402] The frictional force and applied load are recorded by the instrument and can be used to determine the coefficient of friction of the lubricant being studied over a range of speeds. The wear properties of lubricants can be studied simultaneously in MTM by examining the surfaces of the components before and after the test and looking for any scratches, pitting or obvious damage as a result of the forces applied. However, this is qualitative and relies on comparison of the results with those for other lubricants tested using similar measurement protocols.

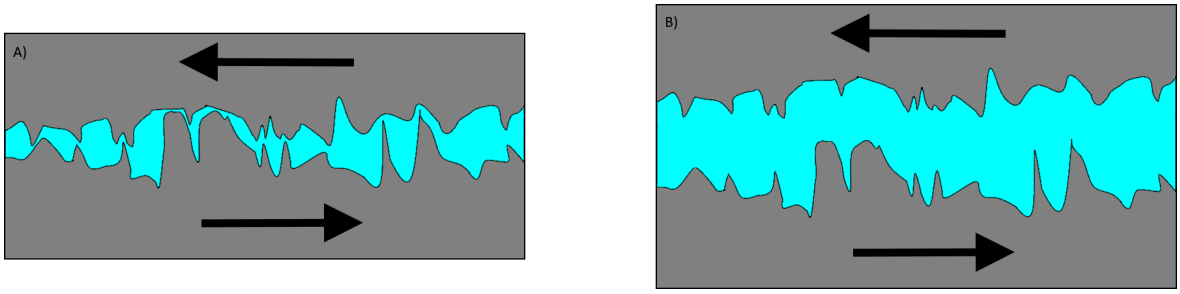

Figure 4.2: *A schematic to show the relative position of both the surfaces and the thickness of the lubricant layer in the A) boundary and B) hydrodynamic lubrication regimes.*

Measurement of coefficient of friction in MTM can follow different protocols depending upon the lubrication regime that is being studied. In this study two different methods were used to study the boundary regime, and the hydrodynamic regime. The differences between these lubrication regimes, and the measurement protocols used to study them are described below.

4.4.1. Boundary Regime

The boundary regime of lubrication is the behaviour that occurs when either the normal force, applied during the measurement, is high or the rotational speed is low. Under these conditions an extremely thin film of lubricant is all that can be held between the two surfaces being tested with some parts of the surface coming into contact as a result of microscopic surface roughness (figure 4.2 A). The result of this is that the coefficient of friction under this regime is largely determined by the properties of the surfaces as opposed to those of the liquid component of the lubricant. This is not to say, however, that lubricants can not have an impact on coefficient of friction under boundary conditions.

The principle method by which lubricants alter surface properties under boundary conditions is by the formation of tribofilms. These are films of material that coat the surfaces of the system, altering its tribological properties as the components slide over one and other. These tribofilms can form in several ways. In a simple lubricant system they can be composed of molecules of the lubricant base fluid, either trapped near to the surface by the pressure between the components, or self-assembling to form a film due to the chemistry

of the base fluid and the surface. However, in more complex lubricants, containing additives, these tribofilms are often formed through the deposition of these additives onto the surfaces of the components, forming a coating. Common additives used to form tribofilms include graphite,[403] MoS_2,[404] and C_{60}.[405]

As well as modifying the coefficient of friction in the boundary regime, tribofilms composed of additives may also improve the wear characteristics of a system by acting as a sacrificial layer between components which is worn away in preference to damaging their surfaces.

Measurement of the coefficient of friction in the dynamic regime in the MTM involves testing over a prolonged period of time (several hours) at low speeds (0.05 m s^{-1}). This prolonged duration allows the system to properly settle and for any tribofilms to form and their effects to become apparent in the value of coefficient of friction measured.

4.4.2. Hydrodynamic Regime

Increased measurement speeds from those which create boundary conditions cause a change in the lubrication regime of the system. Increasing speed leads to lubricant being drawn into the spaces between components from the surrounding reservoirs, pushing the surfaces of the components apart. The effect of this is that the properties of the surfaces no longer have an effect on the coefficient of friction between them, and this value is now determined solely by the properties of the fluid component of the lubricant. This change in behaviour is illustrated in figure 4.2 B.

As the surfaces within the test system no longer come into contact with one and other, their frictional properties no longer have an impact on the coefficient of friction of the system. This means that any tribofilms, formed from lubricants or additives will no longer be effective and the only way to alter the coefficient of friction of the system is to manipulate the properties of the fluid component of the lubricant. The key property that impacts on

the coefficient of friction in the hydrodynamic regime is the viscosity of the base fluid since fluids with higher viscosity have lower hydrodynamic coefficients of friction.[406]

Measurement of the coefficient of friction in the hydrodynamic regime is also performed in the MTM. However, unlike for testing in the boundary regime, which utilises a constant speed, an increasing speed is used, over a much shorter time. The speed is ramped from 0.01-4 m s^{-1} over a period of 5 minutes and the coefficient of friction is measured over this range of speeds.

4.4.3. Measurement of frictional and wear properties

The friction and wear characteristics of nanofluids were tested in conjunction with Shell Global Solutions at their laboratories in Hamburg. Analysis of the tribology of nanofluids was performed using MTM analysis.

Measurements of the coefficients of friction in both the boundary and hydrodynamic regimes were combined into one test protocol. This involved two test steps. The hydrodynamic step consisted of a speed ramp from 4-0.01 m s^{-1} over a period of 5 minutes and the boundary step consisted of measurement at a steady speed of 0.05 m s^{-1} for 60 minutes. The full test protocol consisted of testing in the hydrodynamic regime initially, followed by the boundary regime for 60 minutes. These steps were then repeated until a total of 180 minutes of testing under boundary conditions had been completed, whereupon a final step under the hydrodynamic regime was performed to complete the measurement. All testing was performed at 120 °C in order to mimic the operating conditions of an engine. Full experimental details can be found in section 8.1.11. The reason for the use of this integrated testing protocol, as opposed to testing the boundary and hydrodynamic regimes separately is that it more accurately mimics realistic conditions that the nanofluids would experience in an engine. The repeated test steps also mean that, in the event the nanofluid forms a tribofilm under one or other of the test regimes, the impact of this tribofilm under the other regime can then be assessed in the following step.

Making use of the suite of testing techniques describes above allows the tribological properties of nanofluids produced to be properly assessed and allows the impact of graphitic additives on these properties to be assessed.

Chapter 5

Surfactant-free Aqueous Dispersions of Reduced Graphene Oxide

5.1. Introduction

As has been discussed above, the production of stable dispersions of graphene is a significant challenge that must still be met. Within the context of this project, improving the dispersibility of graphene is of particular importance as in order for graphene materials to improve the thermal and tribological properties of lubricants and thermal fluids stable, high concentration dispersions will be required.

Whilst graphene's dispersibility is known to be good in solvents such as NMP and DMF these also have the drawback of being both high boiling and toxic,[407–409] making their use in large volume commercial situations less than ideal. Many applications for graphene require it to be in the form of a dispersion and so much research is focussing on finding methods of improving the dispersibility of graphene in safer, more practical, and more commonly used solvents.

Although a wide range of methods have been presented to improve graphene's dispersibility in a variety of solvents none of these are without drawbacks.[292] Most commonly these methods involve the modification of graphene (discussed in detail in section 1.7) which falls into the categories of covalent and non-covalent. Covalent methods of modification produce permanent functionalisation which can not easily be removed and can also disrupt the sp^2 network of the graphene sheets, with potential negative impact on many properties.[410] Non-covalent modifiers interact with the graphene sheets through non-bonding interactions

such as van der Waals forces or π-π stacking meaning the sp^2 network can remain intact. In spite of this, it has been shown that these modifiers can still impact on some properties such as electronic conductivity and their removal is not a trivial exercise, often requiring heating to high temperatures to burn off the modifier.[82]

As a result of this it is desirable to develop new methods of dispersing graphene in low boiling, commercially used solvents which are reversible, allowing the properties of the dispersed material to be restored. The work in this chapter describes a novel method for improving the dispersibility of graphene and its related materials in commonly used, low boiling solvents by making use of prior dispersion in good solvents for graphene.

5.2. High Concentration Dispersions of Reduced Graphene Oxide

In order to facilitate the large scale dispersion of graphene materials in commonly used solvents a novel method is presented to produce high concentrations, stable dispersions of graphene without the use of surfactants or covalent modification by making use of the favourable interaction and good dispersibility of graphene materials in solvents such as NMP and DMF. These small solvent molecules are used in a similar manner to surfactants to improve the dispersibility of rGO in more common, safer solvents such as water. Detailed procedure and analysis for this novel method is presented below.

High concentration, surfactant free, dispersions of rGO in common solvents were first achieved using a method involving pretreating rGO with NMP, followed by redispersion into other solvents such as water and ethanol to achieve high concentration, surfactant-free dispersions of rGO.

The rGO used to produced these dispersions was synthesised using a route, widely used in the literature. Briefly, graphite oxide was produced using the Hummers method (sec-

tion 8.3.1) and then exfoliated to produce GO as described in section 8.3.2 before being reduced using hydrazine monohydrate (section 8.3.4) to produce rGO. The rGO produced using this method was a black powder which exhibited poor dispersibility in water. This material was fully characterised and details of this are included in Appendix D.

5.2.1. Dispersion of Graphene using Predispersion

In order to improve the dispersibility of rGO it is necessary to modify its surface properties. This is achieved by pretreating the rGO by dispersing it in NMP using conditions that are known to produce good dispersions of rGO (ultrasonication was used to disperse rGO in NMP at concentrations of 1 mg ml^{-1}. Further details of this experimental procedure can be found in section 8.3.15). The result of this procedure was a stable, black dispersion of rGO in NMP.

In order to then disperse rGO in other, more practical, solvents it must be isolated from the NMP dispersion. This was achieved by pouring the dispersion into acetonitrile (MeCN), causing destabilisation, before the rGO was isolated from the solvent mixture using vacuum filtration. We refer to the isolated material as NMP pretreated rGO (NMPrGO). The MeCN acts to remove excess NMP from the NMPrGO.

NMPrGO displays different solubility behaviour to that exhibited by untreated rGO, with greatly improved stability in a range of non-polar solvents. Dispersions of NMPrGO in water and ethanol were produced, once again using ultrasonication to disperse the material, (as detailed in section 8.3.19) which were then centrifuged in order to remove any unstable particles of NMPrGO, forming stable, dark dispersions of rGO in solvents that are often considered to be poor solvents for rGO.

5.2.2. Concentration of Dispersions of NMPrGO

UV-Vis spectroscopy was used in order to establish the concentration of the dispersions of NMPrGO produced above. As has been discussed in section 3.4, UV-Vis spectroscopy of a solution allows its concentration to be established through use of the Beer Lambert law. For graphene and other carbon nanomaterials it is conventional to use the absorbance at $\sim$660 nm to determine the concentration of a dispersion. Whilst it would be ideal to measure the specific absorption coefficient, α, of NMPrGO this was unfortunately not possible as a result of the fact it was not possible to produce dispersions at precise, known concentrations in the range required. Determination of accurate and precise values of α, particularly for carbon nanomaterials, is known to be a notoriously difficult process.

As a result of this it was decided to make use of the values of α for graphene reported in the literature, with the most recently published result by Khan *et al.* believed to be the most accurate: α =3620 ml mg^{-1} m^{-1} at 660 nm.[364] Whilst this means that there may be some slight inaccuracies in the absolute concentrations of NMPrGO reported, the fact that absorbance is proportional to concentration means that relative values between comparable experiments , such as those performed in this study, are reliable. As a result of this efforts have been made to report concentrations as ratios, comparing the concentration of a control dispersion with that being studied, throughout this work.

Representative UV-Vis spectra of dispersions of NMPrGO, alongside control dispersions of rGO, in water are shown in figure 5.1. The production of dispersions has been repeated seven times to ensure reproducibility of the procedure used. Using the Beer-Lambert law, the concentration of these dispersions was determined and dispersions of NMPrGO were found to have concentrations of 19.9 $\pm$ 2.3 μg ml^{-1} which represents over a six-fold increase compared to the concentration of rGO in water (3.1 $\pm$ 0.3 μg ml^{-1}). The dispersions produced using this method were shown also shown to have excellent stability with concentrations showing no significant change in a period of over a year.

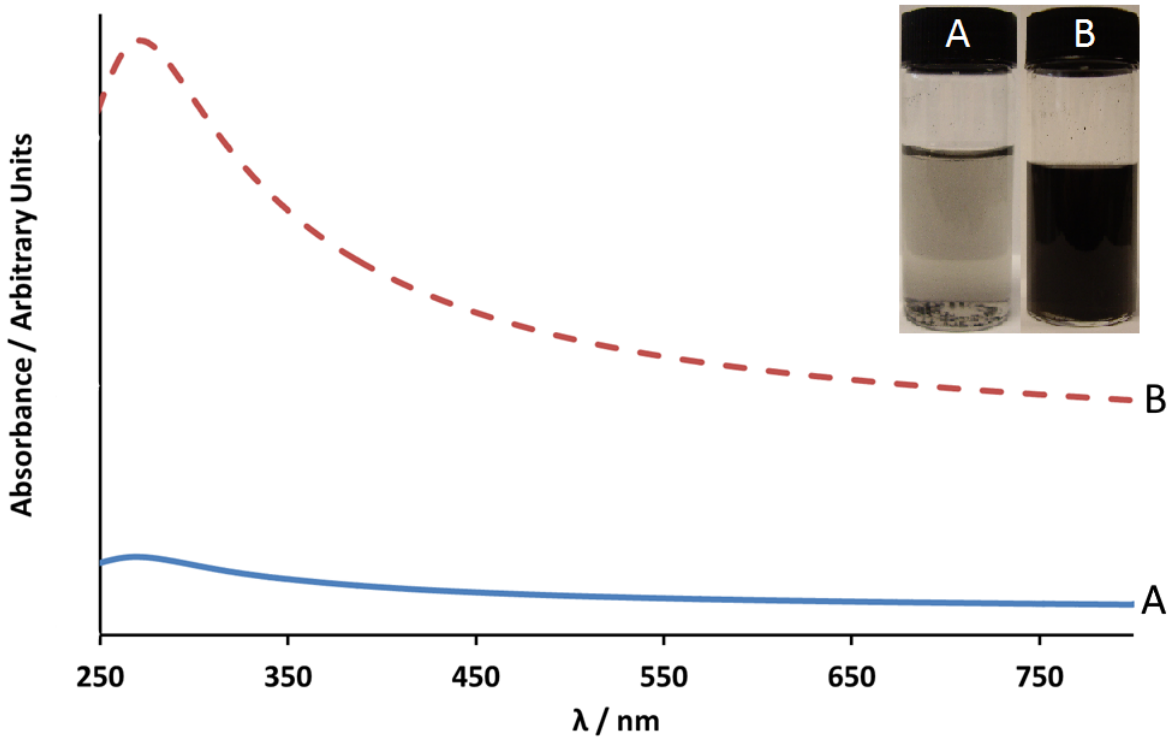

Figure 5.1: *UV-Vis spectra of dispersions of A) rGO in water, and B) NMPrGO in water. Inset: photographs of dispersions A, and B.*

Dispersions of rGO in water were produced to act as controls for these experiments using the method described in section 8.3.22.1 Analysis of these dispersions using UV-Vis spectroscopy, combined with the Beer-Lambert law, allowed their concentrations to be determined as described in section 3.4. Utilising the absorption coefficient determined by Khan *et al.* the concentration of these dispersions were found, as mentioned above, to be 3.1 ± 0.3 µg ml^{-1} (figure 5.1 A).

5.2.3. Mechanism of Improved Dispersibility

In order to better understand the processes occurring during the predispersion of rGO in NMP and the reasons for the improved dispersibility of graphene treated in this way it was necessary to perform further experiments. We postulated that the reason for the change in solution properties of NMPrGO could be due to the presence of small quantities of residual NMP remaining on the surfaces of the rGO sheets after the isolation of NMPrGO.

In order to test this hypothesis NMPrGO was produced in the manner described above,

but after its isolation was dried under vaccum ($<$ 10 mbar) at 60 °C overnight to induce evaporation of any residual NMP. Redispersion of this dried NMPrGO in water made it immediately apparent that the drying process had caused a change to the NMPrGO as its dispersibility in water had returned to a value close to that of untreated rGO. UV-Vis spectroscopy of the dispersions produced showed that the concentration of the dired NMPrGO was $\sim$6 µg ml^{-1}. This is over three times less than that of that of undried NMPrGO, and less than twice that of untreated rGO. The UV-Vis spectra of rGO, dried NMPrGO and NMPrGO in water are all shown in figure 5.2 along with photographs of the dispersions clearly showing the marked decrease in concentration that occurs as a result of drying NMPrGO. These data correlate well with our initial postulate that the presence of the NMP is the reason for the change in solution properties observed for NMPrGO.

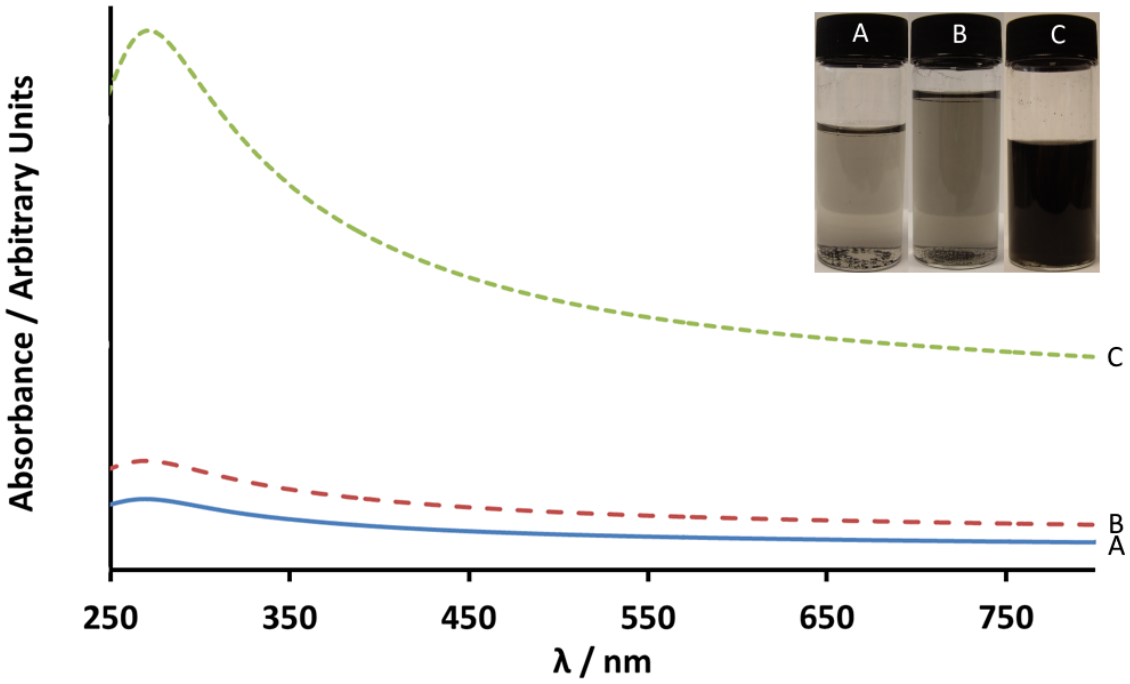

Figure 5.2: *UV-Vis spectra of dispersions of A) rGO in water, B) dried NMPrGO in water, and C) undried NMPrGO in water. Inset: photographs of dispersions A, B, and C.*

The reduction in dispersibility of NMPrGO after drying, described above, has a greater implication. This show that it is likely that the NMP used to predisperse rGO can be removed simply by heating under vacuum meaning that the process of predispersing rGO using NMP is reversible; this is not the case for either covalent functionalisation or the use of surfactants.

5.2.4. Detection and Impact of Residual NMP

In an attempt to detect the presence of this residual NMP, dispersions of NMPrGO in water were analysed by high performance liquid chromatography (HPLC). Known concentrations of NMP in water were prepared in the ranges of 0.05-0.5 vol. % and then analysed using HPLC in order to prepare a calibration curve for absorbance in the HPLC detector against concentration of NMP. These data are included in Appendix D. This calibration was then used to calculate the concentration of residual NMP that was present in dispersions of rGO and NMPrGO in water based on HPLC of the dispersions. These data are shown in table 5.1 and clearly demonstrate that residual NMP is present in dispersions of NMPrGO in water. Full details of this procedure are found in section 8.1.8.

Table 5.1: *The concentrations of residual NMP in dispersions of NMPrGO in water, as determined by HPLC.*

Description	Residual NMP Concentration / vol. %
rGO in water	0.00
NMPrGO in water	0.16 ± 0.05
Dried NMPrGO in water	0.00
NMPrGO prepared without MeCN	0.54 ± 0.04

HPLC also makes it apparent that the process of drying NMPrGO after its isolation leads to a significant reduction in the quantity of residual NMP; up to a point it is no longer detectable using HPLC. This correlates well with the change in solution properties of dried NMPrGO, observed above, and shows that the use of predispersion as a method of improving the dispersibility of rGO has advantages compared to conventional non-covalent methods of dispersing graphene, such as the use of surfactants, as it is possible to remove the residual dispersant through a trivial procedure, such as heating, whereas surfactants are notoriously difficult to remove.[410] These data also show that no NMP is present (as is expected) in the control dispersions of unmodified rGO in water.

As has been discussed in section 1.8 interactions between graphene and its solvents can be described by Hansen solubility parameters, with NMP having some of the most closely matched parameters to those of graphene, explaining graphene's relatively good dispersibil-

ity in this solvent.[86,227,347] Similarly, Hansen parameters also predict the poor dispersibility of graphene in solvents such as water as the values match poorly, with both of these facts being illustrated by the Hansen parameters shown in table 5.2.

Table 5.2: *Three part Hansen solubility parameters of graphene and rGO as reported by Hernandez et al. and Konios et al.[86,227] alongside those of known good solvents for graphene as reported by Hernandez et al. and Hansen.[86,347]*

	$\langle\delta_D\rangle$ / MPa$^{\frac{1}{2}}$	$\langle\delta_P\rangle$ / MPa$^{\frac{1}{2}}$	$\langle\delta_H\rangle$ / MPa$^{\frac{1}{2}}$
graphene	18.0	9.3	7.7
rGO	17.9	7.9	10.1
NMP	18.0	12.3	7.2
DMF	17.4	13.7	11.3
cyclopentanone	17.9	11.9	5.2
cyclohexanone	17.8	8.4	5.1
N-formyl piperidine	18.7	10.6	7.8
vinyl pyrrolidone	16.4	9.3	5.9
H_2O	15.5	16.0	42.3
Ethanol	15.8	8.8	19.4

Upon dispersion of rGO in NMP it has been shown, due to their well matched Hansen parameters that a layer of NMP will form close to the surface of the graphene.[345] During the isolation of NMPrGO we believe that this layer of NMP remains on the surface of the NMPrGO during its isolation and upon redispersion is the cause of the improved aqueous dispersibility described above, with the layer of residual NMP acting as a functional layer and mediating the interactions between rGO and water. This improves the concentration and stability of the dispersions that can be produced. A schematic representation of the final dispersion is shown in figure 5.3.

In order to attempt to prove this hypothesis, it would be necessary to detect the presence of this NMP on the surface of the NMPrGO sheets. However, achieving this is a challenge using the the techniques classically used to characterise graphene materials. One technique that could be potentially give valuable information on this subject is atmospheric solids analysis probe-mass spectroscopy (ASAP-MS). This is an advanced mass spectroscopy (MS) technique which can be used to detect volatile and semi-volatile solids and liquids at atmospheric pressure, developed in 2005 by McEwen *et al.* [411] In ASAP-MS, the sample to be analysed is introduced into the instrument on the exterior of a capillary tube, allowing both

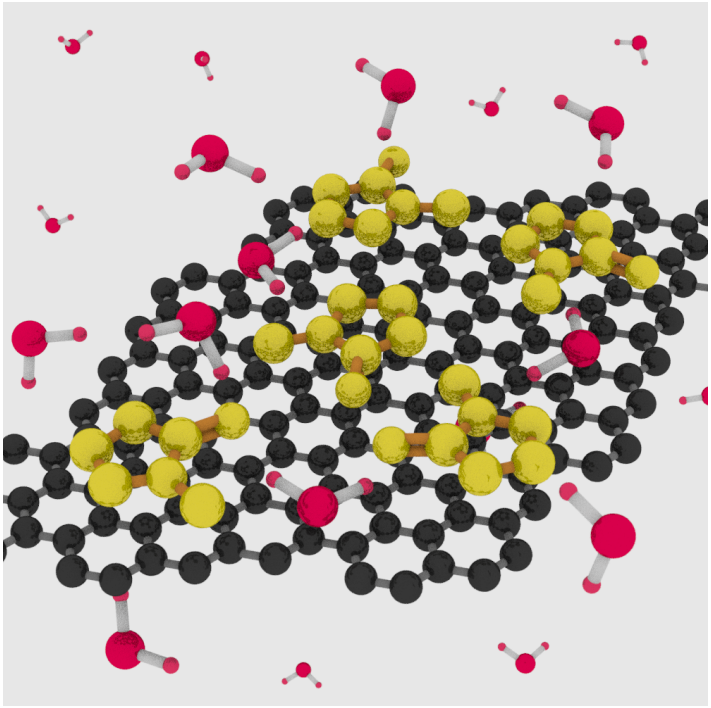

Figure 5.3: *A graphic representation showing the interaction of NMP molecules (yellow) rGO (grey). NMP reduces the amount of direct interaction occurring between rGO and water (red) resulting in the improved dispersibility of NMPrGO observed.*

solids and liquids to be analysed. The sample is vaporised using heated nitrogen before ionisation is achieved through corona discharge. This ionisation technique has the advantage of being extremely gentle and so little fragmentation is expected in this technique.

It is expected that, in ASAP-MS, graphene sheets will adhere to the surface of the capillary tube and any volatile substances on their surface will be vaporised and can be analysed in the spectrometer. This would allow the presence of NMP on the surface of NMPrGO to be detected.

As a proof of concept, the ability of ASAP-MS to detect NMP at the concentrations expected in dispersions of NMPrGO were tested. Aqueous solutions of NMP were prepared at concentrations of 0.1 vol. % and 0.3 vol. % and analysed by ASAP-MS. The spectra produced show that NMP was clearly observed in the spectra obtained (shown in Appendix D) with a clear peak at m/z=100.1 Da which corresponds to the expected peak for protonated NMP (M+H=100.1 Da).

Given the success of this trial it was then decided to examine aquoues dispersions of

NMPrGO using ASAP-MS to see if the presence of NMP could be detected. Aqueous dispersions of NMPrGO were prepared, as described in sections 8.3.15 and 8.3.19 and the ASAP-MS capillary tube was dipped into the dispersions before being placed in the spectrometer. Analysis of dispersions of NMPrGO by ASAP-MS showed the presence of a large peak at m/z=100.1 Da, which corresponds to M+H for NMP. The mass spectrum obtained from this dispersion is shown in figure 5.4.

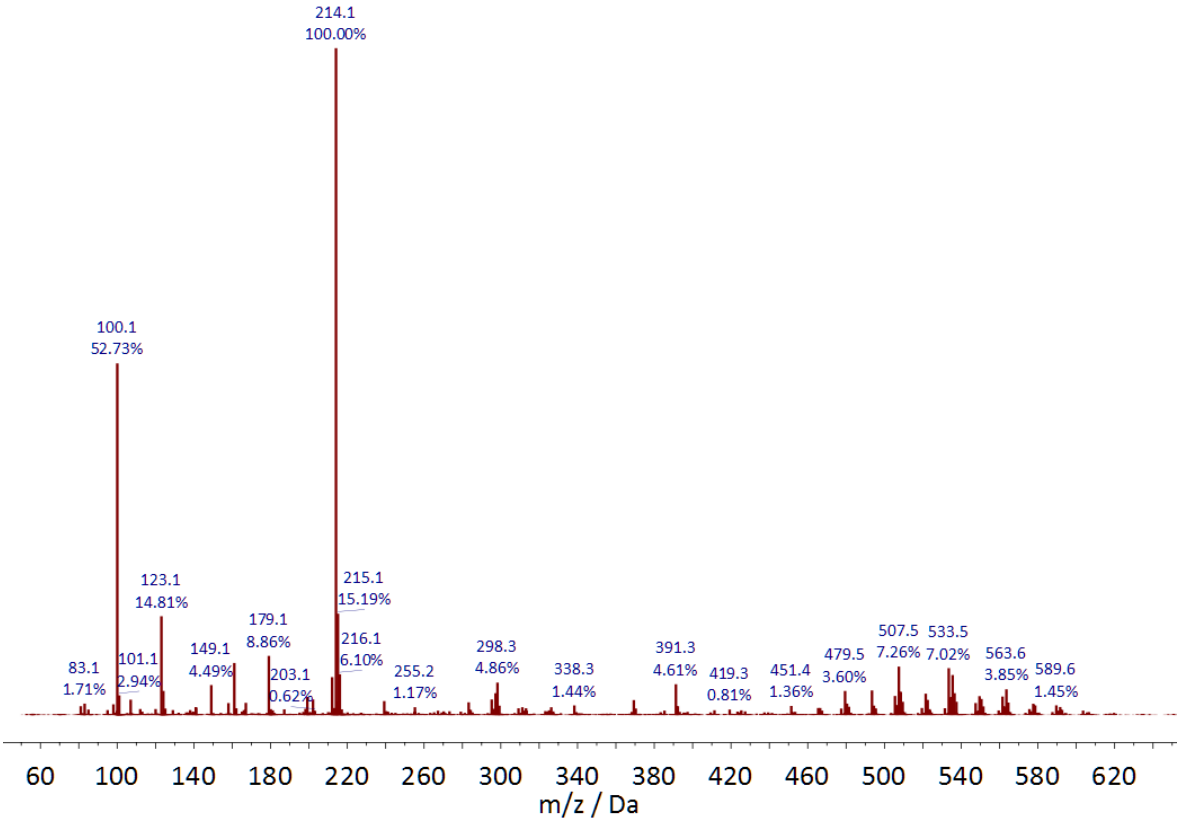

Figure 5.4: *ASAP-MS of a dispersion of NMPrGO in water, showing the presence of the expected M+H peak for NMP at m/z=100.1 Da. Peak at m/z=214 Da due to the presence of plasticiser.*

As a control, a dispersion of unmodified rGO in water was also analysed to show that there is no NMP present as well as that no fragments of rGO have masses that coincide with the peaks produced by NMP. The mass spectrum for this dispersion is shown in figure 5.5. Based on these data, it should be easy to detect the presence of residual NMP using ASAP-MS. It should be noted that the large peak present in figure 5.5 at m/z=214 Da arises from the presence of N-butyl benzenesulfonamide, a commonly used plasticiser, and is visible in all spectra obtained so should be ignored.

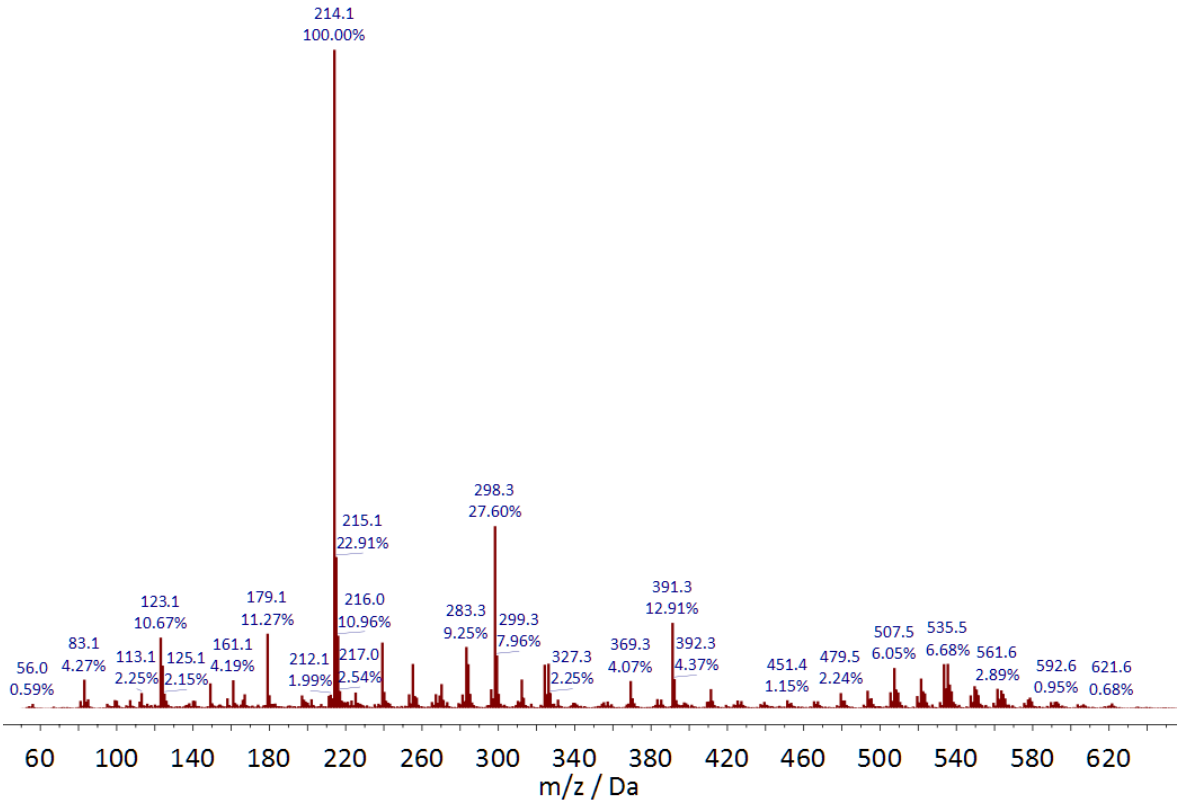

Figure 5.5: *ASAP-MS of a dispersion of unmodified rGO in water, showing the absence of significant peaks in the range where the molecular ion for NMP is expected (∼ m/z=100 Da). Peak at m/z=214 Da due to the presence of plasticiser.*

ASAP-MS was also used to study other dispersions of rGO and NMPrGO to establish the presence or absence of NMP. These spectra are included in Appendix D and are summarised in table 5.3. Alongside this result, it was also found that NMP could be detected in other dispersions including in 0.1 vol. % and 0.5 vol. % aqueous NMP and NMPrGO that was produced with the omission of the MeCN step. On the other hand, it was not possible to detect NMP using ASAP-MS in dispersions of NMPrGO that have been dried (by heating overnight under vacuum) before being redispersed in water. This shows that simply heating NMPrGO has the effect of removing a significant proportion of the residual NMP off the surface of the rGO sheets, supporting our hypothesis for the mechanism of improved dispersibility of NMPrGO and meaning that this method of dispersion of rGO is reversible.

Following on from this the isolated solid NMPrGO was also analysed by ASAP-MS to see if NMP could be detected directly on the surface of the rGO sheets. In order to perform ASAP-MS on the solid sample, the capillary tube was dipped into the isolated graphene material,

Table 5.3: *A table showing whether the peak for M+H of NMP is present or absent in a range of dispersions of NMPrGO and rGO.*

Dispersion	NMP peak (m/z=100.1 Da)
rGO in water	✗
NMPrGO in water	✓
rGO in 0.1 vol. % NMP	✓
rGO in 0.5 vol. % NMP	✓
Dried NMPrGO in water	✗
NMPrGO in water (prepared without MeCN)	✓

which adhered to the tube. When this is exposed to hot gasses in the mass spectrometer volatile compounds on the surface of the rGO sheets are vaporised and can be detected by the spectrometer.

Using this technique, rGO isolated from water was analysed as a control to prove, once again, that no NMP could be detected. Following on from this, ASAP-MS was performed on the same dispersions as above, namely rGO isolated from aqueous NMP, NMPrGO, dried NMPrGO and NMPrGO prepared without MeCN as well as NMPrGO that had been isolated after being redispersed in water. The mass spectra for these materials are included in Appendix D, and the data is summarised in table 5.4

Table 5.4: *A table showing whether the peak for M+H of NMP is present or absent in the mass spectra for a range of rGOs in the solid state that have been isolated from dispersions.*

Material	NMP peak (m/z=100.1 Da)
rGO isolated from water	✗
NMPrGO	✓
rGO isolated from 0.1 vol. % NMP	✓
Dried NMPrGO	✓
NMPrGO isolated from water	✓

These data clearly show the presence of residual NMP on the surface of the rGO sheets that had been exposed to NMP, supporting our hypothesis that its presence is the reason for the dispersibility of NMPrGO.

In order to rule out the possibility that sonication in NMP is damaging and fragmenting NMP, causing the changes in dispersibility observed, ^{1}H and ^{13}C nuclear magnetic resonance spectroscopy (NMR) was performed on NMP that had been sonicated using comparable conditions to those used to produce NMPrGO (section 8.3.21). Comparing the spectra recorded

for these samples with those for untreated NMP (Appendix D) shows that there is no significant difference between the spectra, with no additional peaks being observed due to the presence of fragments. This implies that the conditions used to prepare NMPrGO do not cause fragmentation of NMP so the changes in dispersibility reported are not as a result of the presence of fragments of NMP.

While the interactions between rGO and NMP are described well by Hansen solubility paramters the same can not be said for the interaction between water and NMP with the two sets of solubility parameters having significantly different values in spite of the miscibility of the two solvents. This is due to one of the limitations of Hansen parameters which do not take into account the ability of molecules to act as donors and acceptors in hydrogen bonding reactions, instead only having a single parameter for hydrogen bonding. In order to fully explain these interactions it is necessary to examine an alternative set of solubility parameters: the Kamlet-Taft parameters.[412,413] These are a set of two-part solubility parameters that can be used to describe the hydrogen bonding activity between two materials. They are composed of: α - the hydrogen bond donor acidity[412] and β - the hydrogen bond acceptor basicity.[413] Solvents with a high value of α will act as hydrogen bond donors to those with high values of β. Water and NMP have values for α of 1.17 and 0.00, and for β of 0.18 and 0.77 respectively.[414,415] This explains their good miscibility as water will act as a hydrogen bond donor to NMP. Whilst the Kamlet-Taft parameters take a different approach to determining molecular interactions than the Hansen parameters, it has been shown it is an equally valid system for the prediction of good solvents for graphene and so can still applied in this system.[270]

Given the low residual amounts of NMP found using HPLC in dispersions of NMPrGO it might be expected that merely the presence of this NMP would be enough to improve the dispersibility of rGO. In order to test this, aqueous solutions of NMP were prepared concentrations of 0.1-0.5 vol. % and then were used to disperse rGO *via* ultrasonication using the same procedure as was used for the dispersion of rGO in water described above (section 8.3.22.1). After centrifugation, it was immediately obvious that the concentration of

rGO was much lower than for dispersions of NMPrGO in water. UV-Vis spectroscopy allowed the concentration of rGO in these dispersions to be determined, *via* the Beer-Lambert law, and showed that rGO could only be dispersed at $6.0 \pm 0.4\,\mu g\,ml^{-1}$ in 0.5 vol. % NMP - over three times less than the concentration of NMPrGO in water. Representative UV-Vis spectra and photographs of the dispersions produced are displayed in figure 5.6.

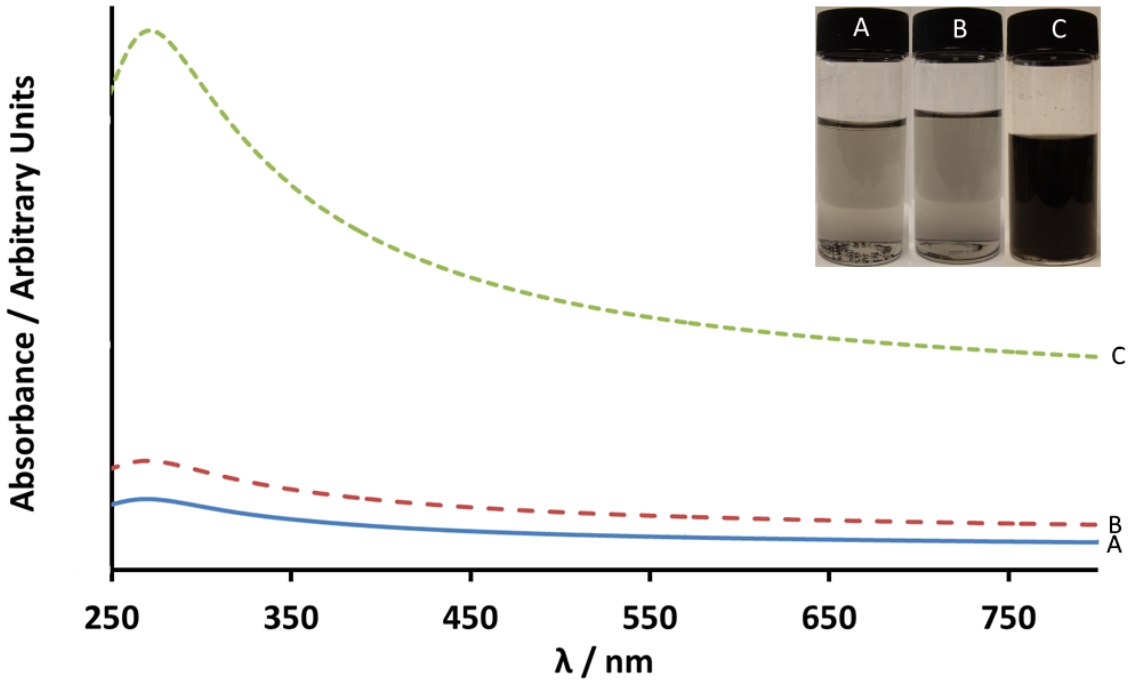

Figure 5.6: *UV-Vis spectra of dispersions of A) rGO in water, B) rGO in 0.5 vol. % NMP, and C) NMPrGO in water. Inset: photographs of dispersions A, B, and C.*

We believe that when rGO is dispersed in aqueous dispersions of NMP the majority of NMP molecules are already solvated by water meaning that when rGO is added and dispersed it is unable to interact with the NMP molecules, inhibiting the formation of the layer of NMP that is achieved by predispersion and is essential for improving the dispersibility of rGO.

Whilst, as we have demonstrated, the removal of NMP from NMPrGO can be achieved simply by heating it is still desirable to keep the concentration of NMP in the final dispersion as low as possible due its toxicity. This is the reason for the use of the MeCN when preparing NMPrGO. This step acts to remove as much NMP that is not interacting with the surface of rGO as possible; thus reducing the concentration of NMP when NMPrGO is dispersed

in water. HPLC was used to compare the concentration of NMP in aqueous dispersions of NMPrGO produced with and without MeCN (section 8.3.16) and it was found that the use of MeCN reduced the concentration of excess NMP from 0.49 $\pm$ 0.04 vol. % to 0.19 $\pm$ 0.05 vol. % (table 5.1).

UV-Vis spectroscopy of the dispersions of NMPrGO produced without MeCN revealed concentrations to be in the range 28.2 $\pm$ 1.1 µg ml^{-1} (compared to 19.9 $\pm$ 2.3 µg ml^{-1} for dispersions of NMPrGO produced using theMeCN), so whilst the MeCN does reduce the concentration of the final dispersion, it also has the effect of greatly reducing the concentration of free NMP. This allows the final dispersion to be tailored, depending on whether concentration of rGO or of residual NMP is most important. It should also be possible to tailor the concentration of the rGO dispersion by adjusting the amount of residual NMP.

In order to ensure that the presence of the MeCN itself was not causing an increase in the dispersibility of the NMPrGO, rGO was dispersed in water, added to MeCN, isolated through vacuum filtration and finally redispersed in water (full detail is given in section 8.3.22.2). Analysis of the dispersions produced by UV-Vis spectroscopy showed that this procedure created dispersions with concentrations of $\sim$6 µg ml^{-1}. Photos and UV-Vis spectra for these dispersions are shown in Appendix D. This represents an increase of less than 2 times compared to dispersions prepared by simply by sonication of rGO in water ($\sim$3 µg ml^{-1}). This demonstrates that the use of MeCN acts to remove excess NMP whilst not being the cause of the improved dispersibility observed after NMP predispersion.

A final factor to take into consideration is that the production of NMPrGO involves two sonication steps, with a total duration of 40 minutes whereas production of control dispersions of untreated rGO in water used only a duration of 20 minutes. To ensure this factor did not cause a significant increase in dispersibility rGO was dispersed in water, as described in section 8.3.22.1, but using a sonication time of 40 minutes. This produced pale grey dispersions which, when analysed by UV-Vis spectroscopy, were found to have concentrations of $\sim$6.0 µg ml^{-1}. Photos and UV-Vis spectra for these dispersions are shown in Appendix D.

Whilst this is an increase in concentration over that of dispersions produced using 20 minutes of sonication, the increase in concentration is less than two-fold. This indicates that the increase in sonication time is not the reason for the improved dispersibility of NMPrGO.

5.3. Characterisation of NMPrGO

In order to ensure that no chemical or physical changes were occurring in the preparation of NMPrGO from rGO that could be causing the changes in its dispersibility observed above, thorough characterisation of both rGO and NMPrGO has been carried out.

5.3.1. TEM

In order to ensure that the methods used to produce NMPrGO do not cause any damage to the structure of the graphene sheets or change their size TEM was used to examine sheets of NMPrGO and compare them to sheets of unmodified rGO. If the process used to produce NMPrGO caused changes in the size of sheets this would be another possible cause for the changes in dispersibility observed,

Micrographs of both rGO and NMPrGO are shown in figure 5.7. Similarities between the two materials can clearly be observed with both samples appearing to universally contain thin and flat sheets with lateral dimensions of the order of a couple of microns. In both micrographs it is clear that the rGO sheets contain many folds. The implication of these data is that the processing used to predisperse rGO in NMP does not have an impact on the structure of the rGO as there is no evident decrease in size or apparent damage to the structure of the sheets. This means that the reason for the increased dispersibility of NMPrGO is not likely to be due to the use of sonication in its production.

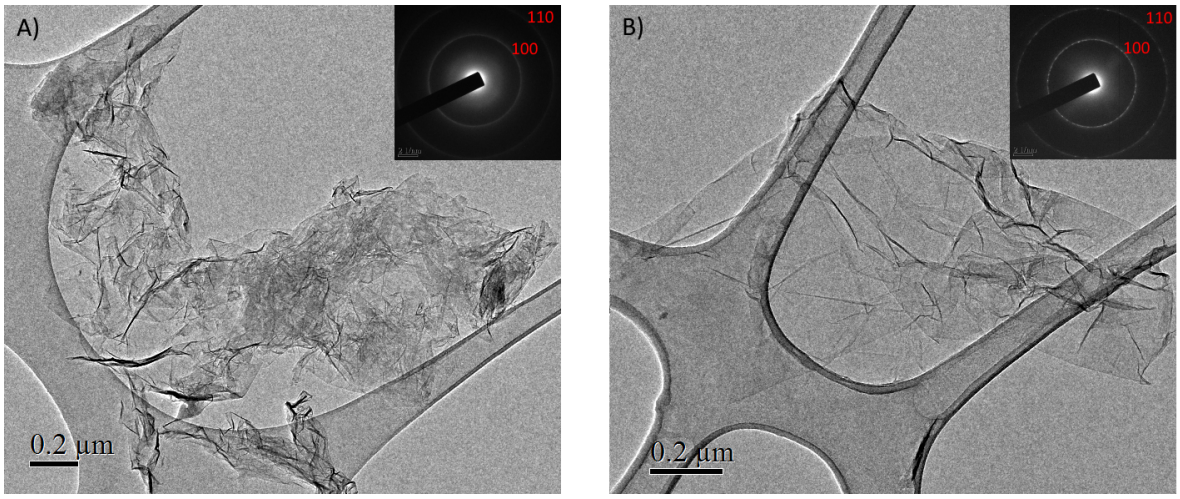

Figure 5.7: *Representative TEM micrographs of sheets of A) rGO and B) NMPrGO showing thin, flat sheets of material both before and after processing. No change in sheet dimensions is observed. Insets show the SAED patterns of both materials.*

5.3.2. Raman Spectroscopy

In order to characterise the effect that predispersion has on the sp^2 network present within the graphitic sheets both rGO and NMPrGO were characterised using Raman spectroscopy. As described in section 3.5 this technique can be used to give information on the quality of graphene materials. Raman spectra for undispersed rGO and NMPrGO are shown in figure 5.8. The key features of interest in the Raman spectra of rGO are the relative intensities of the *G* and *D* bands which allow the $I_D : I_G$ ratio to be calculated as 1.34 $\pm$ 0.03 for NMPrGO which is the same as is measured for rGO (1.34 $\pm$ 0.01). This ratio acts as in indicator of the proportions of sp^2 and defective carbon in the rGO sheets, therefore the fact that the $I_D : I_G$ ratios of NMPrGO and untreated rGO are within error implies that predispersion of rGO does not cause changes in the sp^2 network of the rGO sheets and therefore the changes in dispersibility observed are likely to be due to the presence of residual NMP rather than damage to the rGO sheets occurring during the predispersion process.

For completeness the Raman spectrum of rGO that had been dispersed in water, without the use of NMP was also recorded and is included in Appendix D. This also shows that there is no change in the $I_D : I_G$ ratio when compared to NMPrGO or rGO that has not been dispersed.

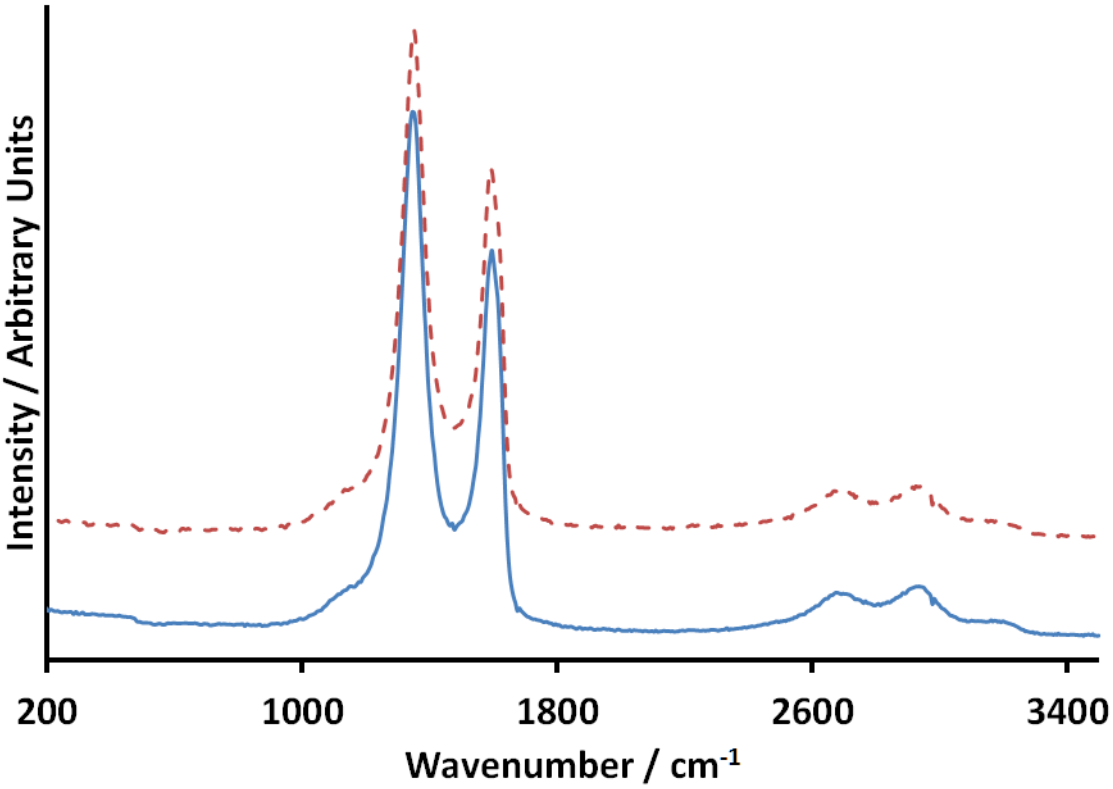

Figure 5.8: *Comparable Raman spectra of rGO (blue line), and NMPrGO (red dashed line) (intensities normalised to the height of the G band and offset by 0.2 for clarity). Spectra show strong D (1350 cm^{-1}) and G (1595 cm^{-1}) bands as well as overtone 2D (∼2800 cm^{-1}) bands. Spectra are normalised to the intensity of the G and vertically offset for clarity.*

5.3.3. XPS

In order to further confirm this, GO, untreated rGO and NMPrGO were all examined using XPS which provides in depth information on the elemental composition within a sample as well as the covalent bonding environments present (more detail on XPS is provided in section 3.8). Analysis of the C1s peak for rGO and NMPrGO allowed a comparison of the carbon covalent environments present in each material to be made. Representative spectra are shown in figure 5.9. The key feature of the C1s XPS spectrum of rGO is the large peak at 285 eV assigned to C=C bonding environments. Peaks from other environments present in rGO appear at higher energies than the C=C peak but in rGO have much lower intensities which leads to the overall C1s peak having an asymmetric shape. When comparing this to the shape of the spectrum for GO the chemical change between these two materials is apparent, with a large C−O−C peak present in the spectrum of GO, at 287 eV that is

no longer present after reduction.[213,214,270] Another change that can be seen as a result of hydrazine reduction is the emergence of a peak caused by CN environments which arise from the use of hydrazine.[386]

Peak fitting of the C1s peak, as detailed in section 8.1.4.2, allows the height and position of each of these peaks to be determined. Briefly, spectra were fitted using a Tougaard background. Then the C=C peak was then fitted to these background corrected spectra using the line shape of the C1s peak of pure graphite after which the remaining peaks were added based on the likely functionalities within the sample using GL(30) line shapes. Residual oxygen containing groups contribute to peaks at 288 eV and 289 eV, assigned to C=O and O−C=O groups respectively[213,214,270] while a final peak at 286 eV is known to arise due to carbon-nitrogen bonding environments present in rGO due to the reduction using hydrazine hydrate.[386] The presence of this peak in both the XPS spectrum of rGO and NMPrGO is unfortunate as it makes the detection of the residual NMP on NMPrGO impossible using this technique (although the high vacuum nature od XPS meant this was already unlikely). Whilst some slight variation is evident between the spectra shown in figure 5.9 A and figure 5.9 B this is smaller than the variation observed between readings taken at different locations within the same sample so these changes are not significant.

These data confirm what was suggested by Raman spectroscopy, that the procedure used to prepare NMPrGO causes no significant chemical change within rGO supporting our belief that the increased dispersibility is due to residual NMP and not some other chemical change.

5.3.4. UV-Vis Spectroscopy

As has been discussed in section 3.4 the position of peak arising due to the $\pi \rightarrow \pi^*$ transition in the UV-Vis spectrum of GO and rGO is indicative of their degree of reduction and conjugation. UV-Vis spectroscopy of of NMPrGO in water was performed and the position of the $\pi \rightarrow \pi^*$ peak was compared to that of rGO (figure 5.10) and the positions of λ_{max}

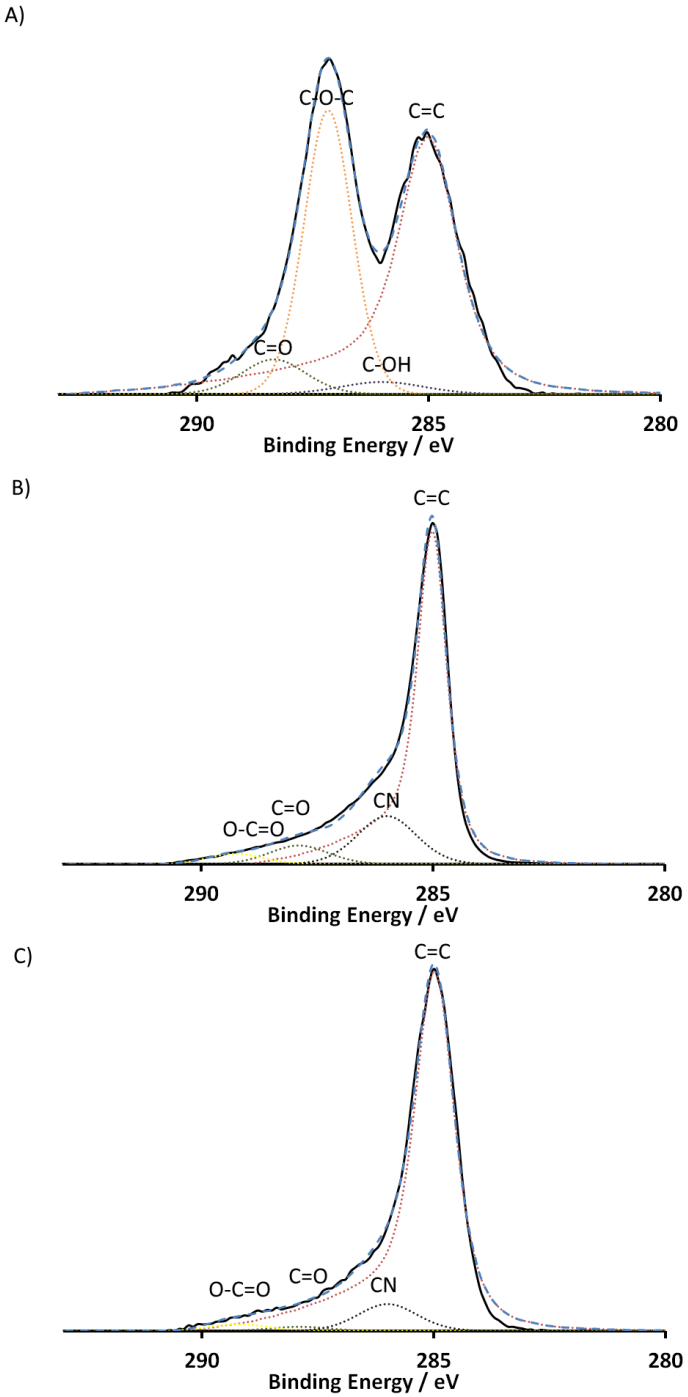

Figure 5.9: *Representative, background corrected XPS C1s peaks for A) GO, B) rGO, and C) NMPrGO showing the C1s spectrum (black line), the fit envelope (blue dashed line) and the fitted peaks (dotted lines). The spectrum for GO shows a large peak for the C=C environment alongside an equally significant peak for C—O—C and smaller peaks for other carbon-oxygen bonding environments. Both spectra for rGO and NMPrGO show the dominating C=C bonding environment with limited remaining oxygen functionalities and residual nitrogen environments from the reduction procedure.*

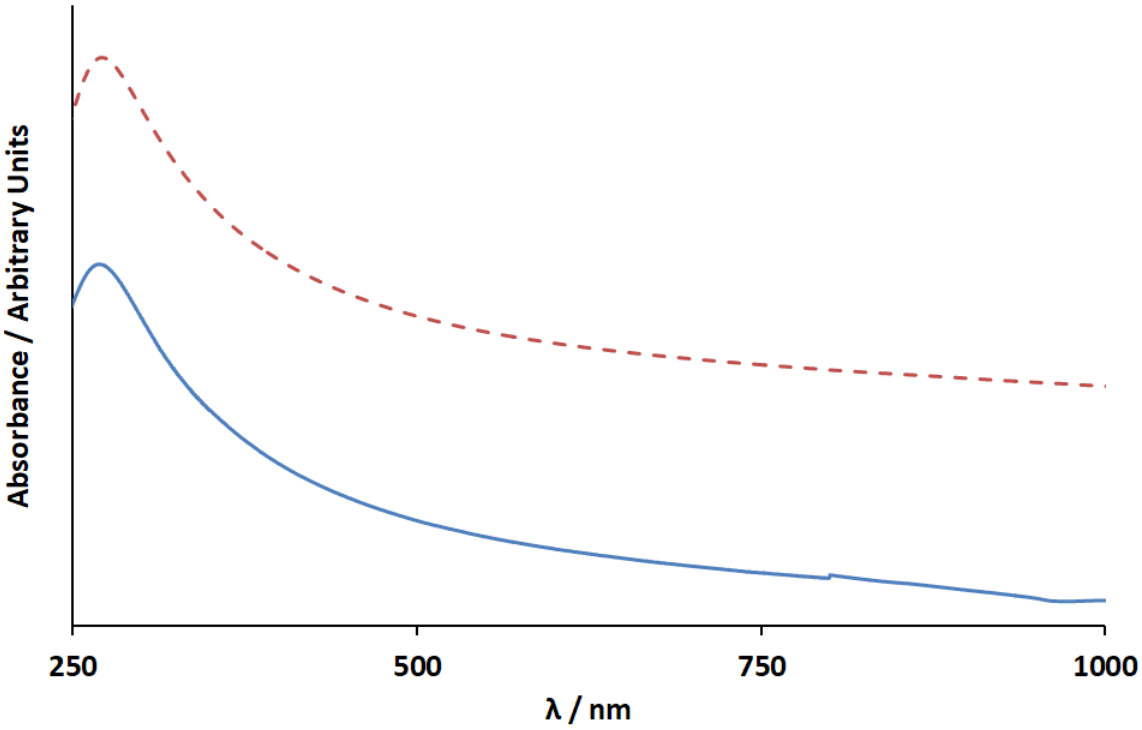

Figure 5.10: *UV-Vis spectra of rGO (blue line) and NMPrGO (red dashed line) in water, showing the position of the $\pi \rightarrow \pi^*$ is the same in both materials.*

was determined (table 5.5). In both materials there is no significant change in the position of the peak which indicates that the degree of reduction and conjugation is similar in both untreated rGO and NMPrGO. This, once again, provides evidence that the predispersion procedure does not cause damage or chemical changes to rGO in spite of the fact that its dispersibility is altered.

Table 5.5: *The position of the $\pi \rightarrow \pi^*$ plasmon peak in the UV-Vis spectra of dispersions of NMPrGO and unmodified rGO in water.*

	Position of $\pi \rightarrow \pi^*$ plasmon peak / nm
NMPrGO	270.1
rGO sonicated in water (control)	269.3

Through the use of these techniques we have showed that the process of preparing NMPrGO does not have any effect on the structure and chemistry of starting rGO and this in turn means that the improved dispersibility of NMPrGO, described above, is not due to any chemical change in the graphene sheets but is likely to be due instead to the residual NMP arising from the predispersion process. It also shows that, as the properties of graphene are intrinsically linked to its structure,[80,92] the properties of the dispersed rGO should be

the same as those of the unmodified rGO. As a result of the theoretical ease of removing the NMP from NMPrGO it should be easy to restore and make use of these properties in applications: a process that is not possible for covalently modified rGO or material dispersed by surfactants which are much harder to remove.

5.4. Predispersion of rGO using other solvents

Since the dispersibility of rGO is similar in both NMP and DMF and NMP and DMF have almost identical Hansen parameters (table 5.2)[86,270] it is logical assume that predispersion in DMF might have a similar effect on the dispersibility of rGO as predispersion in NMP. In order to test this, rGO was dispersed in DMF using a procedure analogous to that used to produce NMPrGO (section 8.3.17). This produced a material that will be referred to as DMF pretreated rGO (DMFrGO).

As was the case for NMPrGO, the dispersions produced were of a dark colour and appeared to have a high concentration of rGO and good stability. Therefore, it appears that DMFrGO also exhibits similar improved dispersibility in water to NMPrGO. Analysis of the dispersions of DMFrGO using UV-Vis spectroscopy indicated they had concentrations of $20.6 \pm 1.3\ \mu g\ ml^{-1}$. A six-fold increase over the concentrations achieved for untreated rGO in water produced using comparable methodology ($3.1 \pm 0.3\ \mu g\ ml^{-1}$). Representative UV-Vis spectra and photographs are shown in figure 5.11.

As with the dispersions of NMPrGO dispersions of DMFrGO were also subjected to analysis by HPLC, as described in section 8.1.8, in order to detect the presence of residual DMF. Calibration was achieved by performing HPLC on aqueous dispersions of DMF at known concentrations and these results were compared to the concentrations of DMF in dispersions of DMFrGO (calibration graphs can be found in Appendix D). It was found that the residual concentration of free DMF in in aqueous dispersions of DMFrGO was 0.26 ± 0.03 vol. %.

Control experiments, dispersing rGO in 0.3 vol. % aqueous DMF , produced dispersions

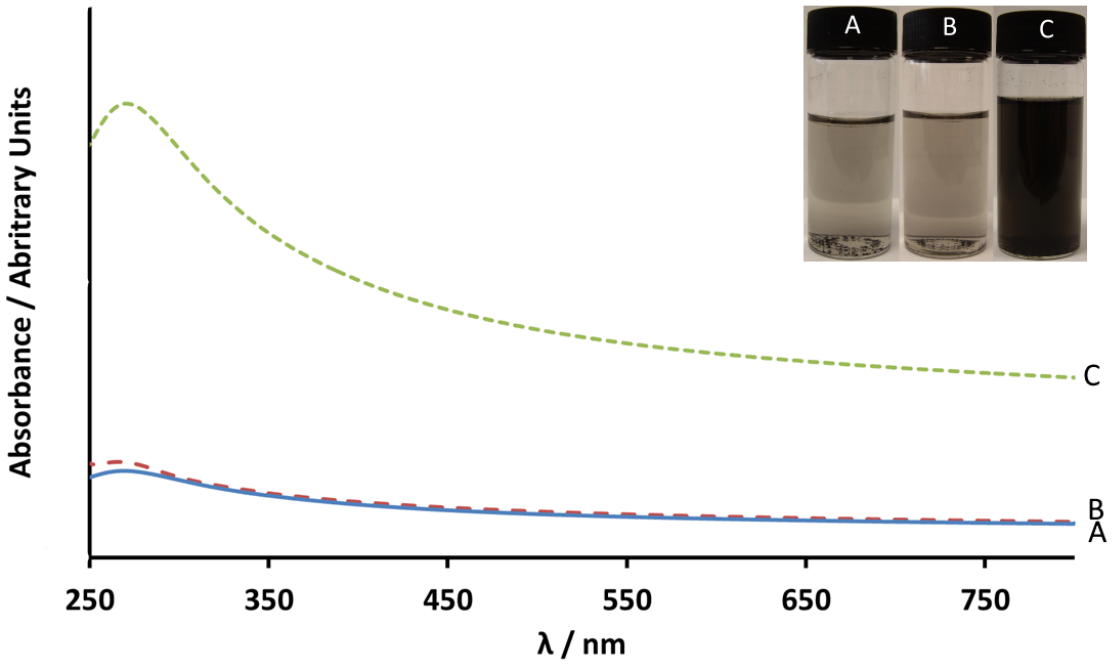

Figure 5.11: *UV-Vis spectra of dispersions of A) rGO in water, B) rGO in 0.3 vol. % DMF, and C) DMFrGO in water. Inset: photographs of dispersions A, B, and C.*

with concentrations, by UV-Vis, of 4.2 $\pm$ 0.1 µg ml^{-1} (figure 5.11) which is only a marginal improvement over the dispersibility of untreated rGO in water (3.1 $\pm$ 0.3 µg ml^{-1}). These results mean it is likely that the improved dispersibility of DMFrGO occurs due to the same mechanism as proposed for NMPrGO in section 5.2.3. DMFrGO was characterised in the same manner as described in section 5.3 and these data are presented in Appendix D. As was the case for NMPrGO these data showed there was no detectable chemical change that occurred during the production of DMFrGO and so changes in dispersibility are due to the presence of residual DMF.

As with NMPrGO, DMFrGO was also dried under vacuum before being dispersed in water. This had the effect of reversing the improved dispersibility of DMFrGO described above with concentrations of dried DMFrGO, detected by UV-Vis spectroscopy, found to be $\sim$5 µg ml^{-1} (figure 5.12). HPLC on the dispersion produced showed, as for NMPrGO that the concentration of free DMF was reduced dramatically, from 0.23 vol. % to 0.00 vol. % and we believe that this is the reason for the change in dispersibility.

Finally, dispersions of DMFrGO were also prepared without the use of MeCN (as de-

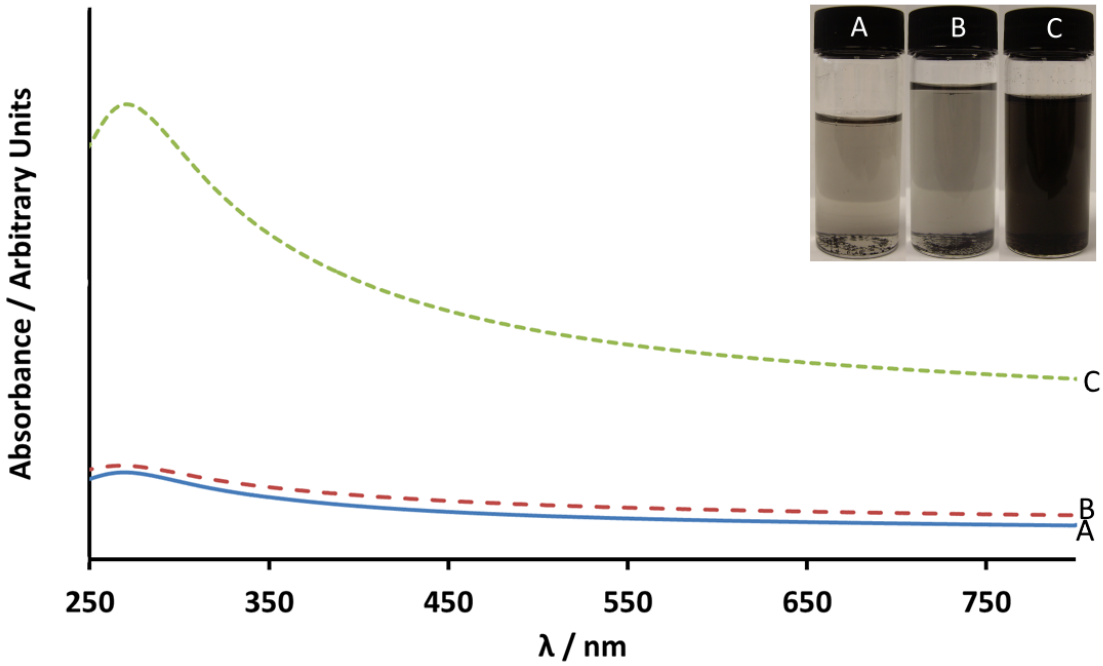

Figure 5.12: *UV-Vis spectra of dispersions of A) rGO in water, B) dried DMFrGO in water, and C) undried DMFrGO in water. Inset: photographs of dispersions A, B, and C.*

scribed in section 8.3.18) in order to confirm that the presence of MeCN, once again, have the effect of washing away excess DMF without impacting on dispersibility. The dispersions produced were analysed by UV-Vis spectroscopy and this showed that the concentration of DMFrGO was $\sim$ 15 µg ml^{-1} - similar to that of dispersions of DMFrGO prepared using MeCN. HPLC of the dispersions produced without the use of MeCN allowed for the concentration of residual DMF to be established and it was found that the use of MeCN reduced the concentration of free DMF in dispersion from 0.86 vol. % to 0.23 vol. % without impacting on dispersibility. This result matches closely with that observed for NMPrGO.

The results described above for the dispersion of DMFrGO in water are very similar to those presented for NMPrGO. For this reason we believe that the mechanism of dispersion is similar in both cases; a fact that should be expected given the similar Hansen parameters and dispersibility of rGO of DMF and NMP.

Given the success of predispersion in improving the dispersibility rGO in water the dispersibility of NMPrGO and DMFrGO were tested in a range of other polar protic solvents. Solvents were chosen based on their Kamlet-Taft parameters, as those with similar parame-

ters to water, likely to show similar behaviour due to their similar solution properties.

Of all solvents tested the one that showed the greatest improvements in dispersibility for NMPrGO vs rGO was ethanol. NMPrGO was produced using the method described in section 8.3.15 and then dispersed in ethanol using the procedure described in section 8.3.19. This produces stable dispersions of NMPrGO with dark colours similar to those of dispersions of NMPrGO in water. Using UV-Vis spectroscopy (figure 5.13), the concentrations of dispersions of NMPrGO in ethanol were measured and found to be in the range 17.3 ± 5.0 µg ml^{-1}. This represents an increase of over 2.5 times compared to the concentrations of untreated rGO in ethanol by comparable methods (which have concentrations of 7.1 ± 0.7 µg ml^{-1}).

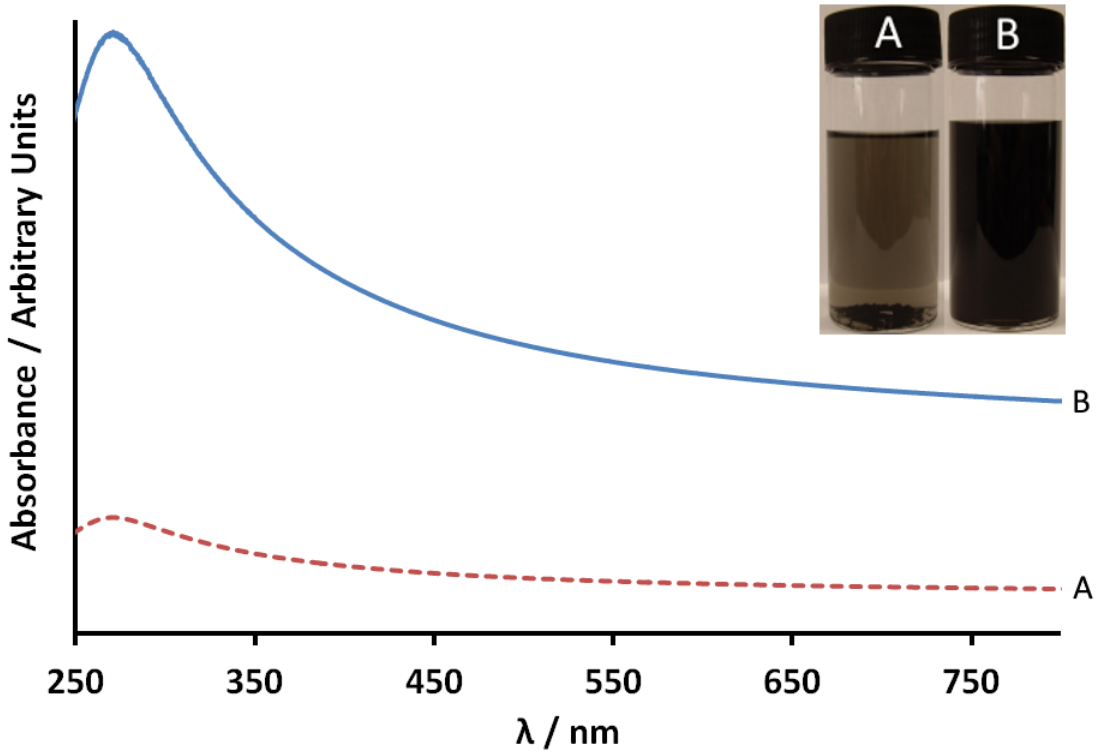

Figure 5.13: *UV-Vis spectra of dispersions of A) rGO in ethanol and B) NMPrGO in ethanol. Inset: photographs of dispersions A and B.*

5.5. Conclusion

Throughout this chapter a novel method of dispersing rGO in common, safe, solvents such as water and ethanol has been discussed. This method avoids the use of covalent

functionalisation, which can be costly and time consuming, and the use of surfactants which are difficult to remove. Making use of the good compatibility of graphene with solvents such as NMP and DMF it has been shown that predispersing rGO in these solvents can improve the aqueous dispersibility of the rGO reversibly, and without the use of surfactants.

In order to achieve this increase in dispersibility, rGO was first predispersed in NMP before being, isolated and then redispersed in water and it was found that this process increased the concentrations of dispersions of rGO in water by over 6 times, to give concentrations of $19.9 \pm 2.3\,\mu g\,ml^{-1}$, compared to the concentration of untreated rGO. It was also discovered that switching out the NMP for DMF in this process had a similar impact on the dispersibility of rGO also causing an increase in concentration of over 6 times, to $20.6 \pm 1.3\,\mu g\,ml^{-1}$, compared to unmodified rGO. Thorough characterisation of the rGO that had been predispersed in NMP showed that this process does not impact on the chemical or structural properties of the rGO and so the reason for the change in dispersibility observed is due to the predispersion procedure.

In order to establish the mechanism for this improved dispersibility a range of experiments were carried out and it was found, using both HPLC and ASAP-MS that residual NMP can be detected at low concentrations ($\sim$0.2 vol. %) in dispersions of NMPrGO. Drying of NMPrGO before redispersion in water had the effect of reducing both dispersibility and the concentration of residual NMP whilst removing the MeCN step had the impact of increasing both the concentration of rGO and residual NMP. Dispersing rGO in equivalent low concentrations of NMP showed little improved dispersibility proving that it is the predispersion process and not simply the presence of NMP that causes this change in dispersibility. The results were mirrored when NMP was replaced by the use of DMF. It was also shown that the residual NMP and DMF can be removed by simple heating under vacuum, providing one of the major advantages of this method: its reversibility.

A comparison of the concentrations of dispersions achievable using the methods described in this chapter is presented in figure 5.14 which clearly shows the increase in dis-

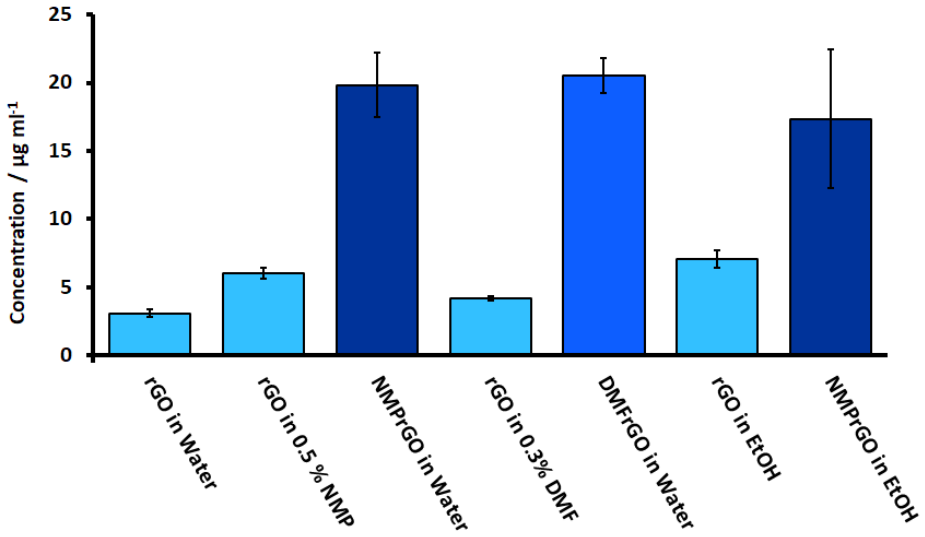

Figure 5.14: *Concentrations of dispersions of rGO (pale blue), DMFrGO (mid-blue) and NMPrGO (dark blue). Concentrations were determined from UV-vis absorbance at 660 nm using the Beer-Lambert law.*

persibility that can be achieved through the use of DMF or NMP as a dispersant without the need for covalent modification or the use of surfactants.

Through the data presented in this chapter we have shown the improved dispersibility of rGO in polar protic solvents through the use of predispersion in NMP or DMF and shown that the mechanism for this process involves the formation of an active layer of NMP or DMF that forms an interface between the rGO and the bulk solvent improving the dispersibility of rGO in the bulk solvent. This method allows the production of high concentration rGO dispersions in safe, cheap solvents avoiding the need to use large quantities of hazardous solvents or surfactants that can be hard to remove.

As a result of the fact that a large proportion of thermal fluids used in the automotive industry are water based, it is likely that this procedure could be used to create high concentration, stable dispersions of rGO in these fluids, enabling their thermal properties to be improved whilst avoiding the use of costly and time consuming covalent functionalisation or potentially undesirable surfactants that could impact on other properties of the thermal fluid.

5.6. Further Work

Whilst the use of NMP and DMF predispersion has been shown to successfully improve the dispersibility of rGO in polar protic solvents, there is still further work that could be done on this subject to better understand and optimise the process.

Given the success of the method in improving the dispersibility of rGO in pure solvents presented in this chapter, the next logical step would be to utilise this process to improve the dispersibility of graphene materials in thermal fluids, which are generally water based, and then to test the impact of this on their thermal properties.

Away from thermal fluids it may also be possible to utilise this methodology to improve the dispersibility of graphene materials in aqueous dispersions for other applications. One area of interests would be in the production of graphene-carbon fibre composites where water miscible phenoxy resins are used. If graphene could be dispersed in these resins, they could then be used to set the carbon fibre whilst also imparting the electronic and mechanical properties of graphene to the composite formed.

Whilst this process already shows promise for water based thermal fluids, applying it to lubricants, which are frequently utilise non-polar base fluids will be more of a challenge as NMP and DMF are unlikely to interact favourably with such non-polar fluids. It may however, be possible find an alternative solvent that could mediate the interactions between rGO and the lubricant base fluid. Unfortunately within the time frame for this project this was not a topic that could be studied in depth.

The characterisation of NMPrGO by XPS (section 5.3.3) was able to show that there was little change between the covalent bonding environments present in NMPrGO and rGO it was unfortunate that this technique could not detect the presence of residual NMP present on the surface of NMPrGO. In order to try to overcome this and use XPS to detect residual NMP it would be necessary to remove the nitrogen containing functionalities present on the

surface of rGO that occur as a result of the use of hydrazine in its synthesis. The easiest way to achieve this would be to use an alternative method of reduction to produce the rGO. A large number of alternative methods are detailed in section 1.6.1.

However, even in spite of making this change it still may not be possible to detect residual NMP using XPS due to the fact that XPS is an ultra-high vacuum technique. This means it is possible that residual NMP would evaporate from the sample inside the instrument before a spectrum could be recorded, making it impossible to detect the residual NMP.

As has been discussed in detail in section 5.2.4 it has become apparent from HPLC that the concentration of NMPrGO that can be dispersed in solvents is linked to the concentration of residual NMP in the water dispersion. It should therefore be possible to vary the concentration of rGO dispersed by varying the concentration of residual NMP.

Depending on the priorities in the final application it may either be more important to have a high concentration of rGO at a cost of higher concentration of NMP or to maintain a low concentration of NMP at the cost of a slightly lower concentration of rGO. With further work it should be possible to tailor the predispersion, MeCN and drying steps of the predispersion in order to achieve the desired concentrations of NMP and rGO in the final dispersions. It may also be possible to achieve even higher concentrations of rGO by optimising the sonication times and intensities, as these were not changed during the work performed in this chapter.

Finally, whilst thorough chemical characterisation of the NMPrGO and DMFrGO produced was performed, and used to show that the predispersion method proposed in this chapter had no discernible effect on the chemistry of the rGO dispersed, analysis of the physical properties of these materials were not carried out.

Further work on this topic could include the testing of the electronic, thermal and mechanical properties of NMPrGO and DMFrGO in order to establish if the predispersion process has any effect on these physical properties compared to those of unmodified rGO. As

the chemical properties and physical properties of graphene materials are widely regarded to be linked, it is likely that there will be little change in physical properties. However as these physical properties are those that are utilised in applications of graphene it would be important to understand the impact of predispersion on mechanical,thermal and electrical properties to establish which applications this technique would be useful for. When investigating the physical properties of NMPrGO, particularly electrical properties, it is worth remembering it has been shown above that NMP can be removed from the surface of NMPrGO through heating under vacuum, and that this process may be useful in achieving the optimal electrical properties for NMPrGO.

Chapter 6

Production of Graphene-Lubricant Nanofluids *via* Functionalisation of Graphene Oxide

6.1. Introduction

Lubricants play an essential role in automotive applications and are found in a wide range of components including, but not limited to, transmission systems, bearings and power units where they reduce the friction between moving parts and prevent wear. When utilised in internal combustion engines they also take on another key role, that of transferring heat away from its source and transferring it to cooling systems. This means that, for lubricants, two sets of properties are essential for good performance: thermal properties and tribological properties, and anything that can be done to improve one or both of these will lead to a more effective lubricant that can give improved engine performance.

As has been discussed previously in section 1.2 graphene's collection of remarkable properties mean that, when well dispersed in fluids, it can greatly affect the properties of base fluids and could be used to impact both the thermal and tribological properties of lubricants. However, due to graphene's solution properties dispersing it in lubricants is not a trivial process, and good dispersions are essential to the successful modification of the fluid's properties.

The work contained in this chapter will focus on the production of stable dispersions of graphene materials in commercial lubricants, working to adjust the solution properties of

the graphenes through the use of functionalisation in order to produce dispersions with the highest concentrations possible. These dispersions will then have their properties tested to see if the addition of graphene has had the desired impact on thermal and tribological properties. In addition the viscosity of the dispersions will be monitored as the use of solid additives can cause large increases in viscosity, which would have a negative impact on the performance of the lubricant. However, it is hoped that the nanoscale nature of graphene means it will be able to impact on the thermal and tribological properties of the lubricants without causing large viscosity changes.

The commercial oils tested were provided by Shell Global Solutions. They consist of lubricants with a range of different solvent chemistries and viscosities, in order to give the best possible chance of achieving stable dispersions of graphene materials. The lubricants consist of 5 base oils as well as 3 formulated oils.

The base oils provided for this study are pure lubricant fluids, with a range of different chemistries. Base oils are not used in isolation as commercial lubricants and require other components to be added in order to achieve all the properties desired. However, for simplicity and to isolate the impact of graphene on the properties tested in this investigation it is preferable to test the impact of graphene on base oils as opposed to fully formulated oils.

The base oils provided for this project have a range of different chemistries: 2 are composed of ester-based oils with differing viscosities, denoted E1 and E2. These are both made up of 2-ethylhexyl esters of carboxylic acids containing between 8 and 16 C atoms. The fact that these oils are comprised of esters, albeit long chain ones, means that they are somewhat polar with their oxygen functionalities able to interact with polar compounds, whilst their long chain hydrocarbon tails will enable interaction with more non-polar groups. A further 2 base oils are made up from synthetic, hydrogenated poly(alpha-olefin)s (PAOs) with differing viscosities. These are denoted as P1 and P2, with P1 having a molecular weight of 287 Da and P2 of 554 Da. In contrast with the ester based oils, P1 and P2 are both highly non-polar and so will interact well with other non-polar molecules but less well with those

with polar functionalities. The final base oil is composed of an oil-soluble poly(alkylene glycol) (PAG) and is denoted as OSP-18. PAGs are much less commonly used oil bases than PAOs or esters, but have shown a great deal of promise in recent years. Their chemistry differs significantly from that of PAOs or esters due to the presence of ether linkages in the repeat unit of the backbone, making PAGs significantly more polar than any of the other groups of base oils described above. It is hoped that the range of polarities of these base oils will increase the chance of successfully dispersing graphene, or graphene derivatives, in one of these oils to form a nanofluid.

In order to produce a lubricant with the required properties, the base oils described above must be transformed into formulated oils. This is achieved by mixing one, or more, base oils with a commercially available additive package purchased from a third party supplier. These packages of additives are complex, sometimes containing as many as 20 different ingredients which act as: viscosity modifiers, pour point depressants, dispersants, anti-foam agents, friction modifiers, anti-wear additives, detergents, corrosion inhibitors, and antioxidants amongst others. These packages are tailored by their producers to create an oil with extremely specific properties and companies rarely disclose the contents of these additive packages making dispersion in these fluids more complex.

In spite of this, 3 formulated oils were provided by Shell Global Solutions and used to produce nanofluids. These were comprised of: F1- a mix of E1, P2 and a gas to liquid (GTL) base oil including a molybdenum based friction modifier, F2 - a mix of E1 and GTL base oils, and F3 - also containing E1 and GTL base oils. All three of these oils also contain additive packages. The kinematic viscosities and compositions of all of the commercial oils is detailed in table 6.1.

Table 6.1: *Information on the properties and composition on the Shell Global Solutions lubricants, taken from product data sheets.*

Oil	Type	Description	V_k40 / cSt	V_k100 / cSt
E1	Base	Mainly 2-ethylhexyl esters of C8 and C10 acids	3.2	1.3
E2	Base	2-ethylhexyl cocoate	5.5	1.8
P1	Base	Synthetic mix of hydrogenated polyalphaolefins	5.4	1.7
P2	Base	Synthetic mix of hydrogenated polyalphaolefins	30.7	5.8
OSP-18	Base	Oil-soluble polyalkylene-glycol	18.0	4.0
F1	Formulated	A mix of E1, P2 and GTL base oils with a molybdenum friction modifier	146.1	32.6
F2	Formulated	A mix of E1 and GTL base oils	70.3	19.0
F3	Formulated	A mix of E1 and GTL base oils	28.4	9.0

6.2. Dispersion of Unmodified Graphene Materials in Oils

In order to assess the potential of the base oils to form nanofluids, the dispersibility of unmodified graphene like materials in each of the fluids was studied. As GO is generally the start point when producing modified graphenes, and has a simpler synthesis than rGO, the dispersibility of GO in oils was investigated initially.

6.2.1. Dispersion of as Produced Graphite Oxide in Oils

Graphite oxide was synthesised as described in section 8.3.1 and was then dispersed and exfoliated in oils *via* probe sonication using the procedure described in section 8.3.5. The dispersions produced were allowed to settle and then were photographed (figure 6.1) and analysed by UV-Vis spectroscopy (figure 6.2).

As discussed in section 4.1 it should be possible to use UV-Vis spectroscopy to determine the concentration of the oil dispersions. However, in practice it has been found that determining an absorption coefficient for GO is extremely difficult and the absorbance of GO dispersions with stable concentrations has even been observed to vary over time. There

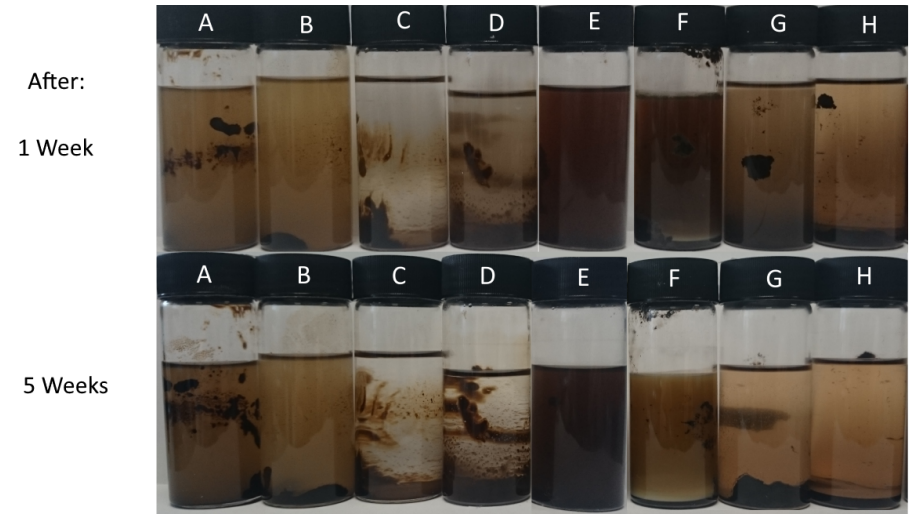

Figure 6.1: *Photographs of as produced graphene oxide in oils (top) 1 week and (bottom) 5 weeks after dispersion. (A) E1, (B) E2, (C) P1, (D) P2, (E) OSP-18, (F) F1, (G) F2, and (H) F3. Note that the colour of dispersion E is in part due to the colour of the oil.*

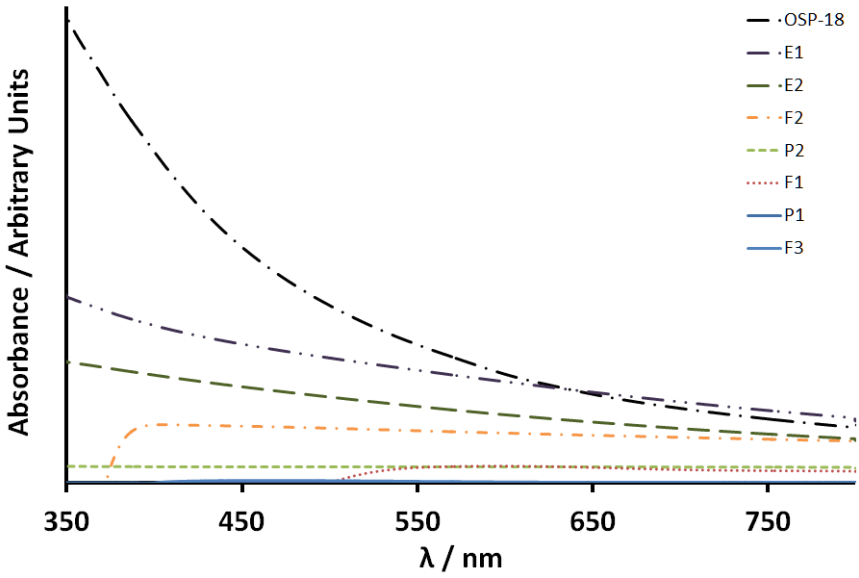

Figure 6.2: *UV-Vis spectra of as produced GO dispersed in oils by ultrasonication, used to calculate the concentration of the nanofluids produced.*

is no value for the extinction coefficient of GO that has been presented in the literature. For this reason, the only useful information that can be obtained from UV-Vis spectroscopy of GO is the relative absorbance between samples which can be used to give the relative concentration of the dispersions.

The absorbances of the dispersions of GO in oils produced are shown in table 6.2, along with their concentrations as a percentage of the most concentrated dispersion: E1. As can clearly be seen from the photographs in figure 6.1 the concentrations of the dispersions produced are not high with, in some cases, the GO appearing to prefer to stick to the glass vial than remain dispersed in the oil. As could be predicted from the fact that GO contains a significant proportion of polar functional groups, bound to non-polar sheets, those oils that can best disperse GO are those with a polar component: those that are ester based (E1, and E2) and OSP-18 which contains polar PAGs. Those base oils composed of non-polar PAOs (P1, and P2) were not able to disperse GO giving extremely low absorbances and clear dispersions. Of the formulated oils, GO was able to be dispersed in F2 at reasonable concentration. However, in F1 and F3 this was not the case in spite of them containing oils that could disperse GO reasonably well. This may be due to the presence of other components of the formulated oils impacting on their solution chemistry.

Table 6.2: *The absorbances at 660 nm of the UV-Vis spectra of the dispersions of as produced GO in oils as well as their relative concentrations as a percentage of the most concentrated dispersion (E1).*

Oil	Absorbance / Arbitrary Units	Relative Concentration of as produced GO / %
E1	1.36	100
E2	0.87	64
P1	0.00	0
P2	0.23	17
OSP-18	1.25	92
F1	0.22	16
F2	0.69	51
F3	0.01	1

Figure 6.1 shows that the long term stability of these dispersions was poor. Initially the dispersions were cloudy and turbid from which, over the period of a few hours, the GO generally began to settle out. After 5 weeks, the concentration of dispersed GO had fallen

significantly, leaving very little dispersed in the oil. These results indicated that the dispersion of GO in the oils would not be a successful route to nanofluids. This is likely to be due to an incompatibility between the surface chemistry of GO which is generally considered to be highly hydrophilic,[416] and the hydrophobic oil. Another issue encountered when preparing nanofluids using as produced graphite oxide is that this material contains a large proportion of water (95 % by TGA) which will be immiscible with the oils. This explains the turbidity of dispersions initially after sonication as emulsions of water and oil were formed which were then stabilised by the presence of GO which is known to be surface active and can be used to stabilise emulsions.[417] The addition of water to the oil dispersions is something that should be avoided as this has the potential to detrimentally impact on the thermal and tribological properties of the oils.

6.2.2. Dispersions of FDGO in oils

Using FDGO as an additive instead of wet graphite oxide avoids the addition of water to the base oils. FDGO was prepared as described in section 8.3.3 and then dispersed in base oils as described in section 8.3.5. The dispersions were allowed to stand before being photographed (figure 6.3) and analysed by UV-Vis spectroscopy (figure 6.4).

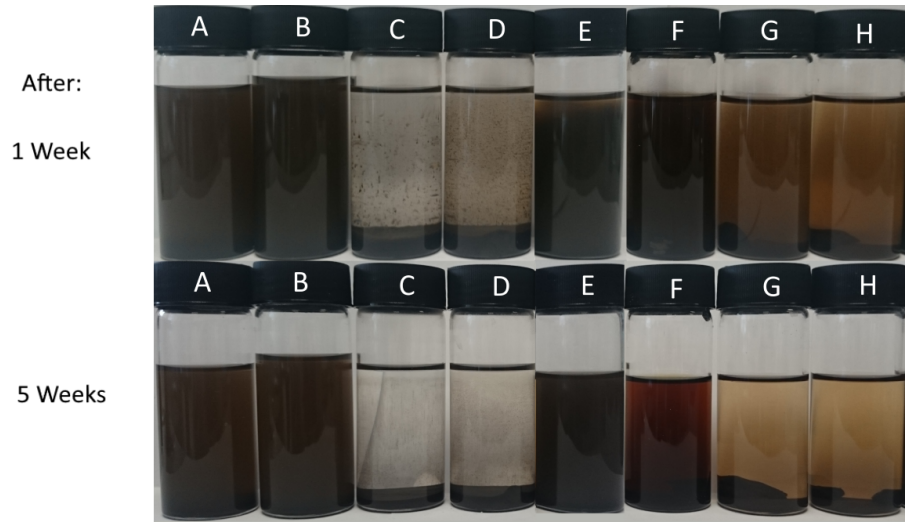

Figure 6.3: *Photographs of FDGO in oils (top) 1 week and (bottom) 5 weeks after dispersion. (A) E1, (B) E2, (C) P1, (D) P2, (E) OSP-18, (F) F1, (G) F2, and (H) F3. Note that the colour of dispersion E is in part due to the colour of the oil.*

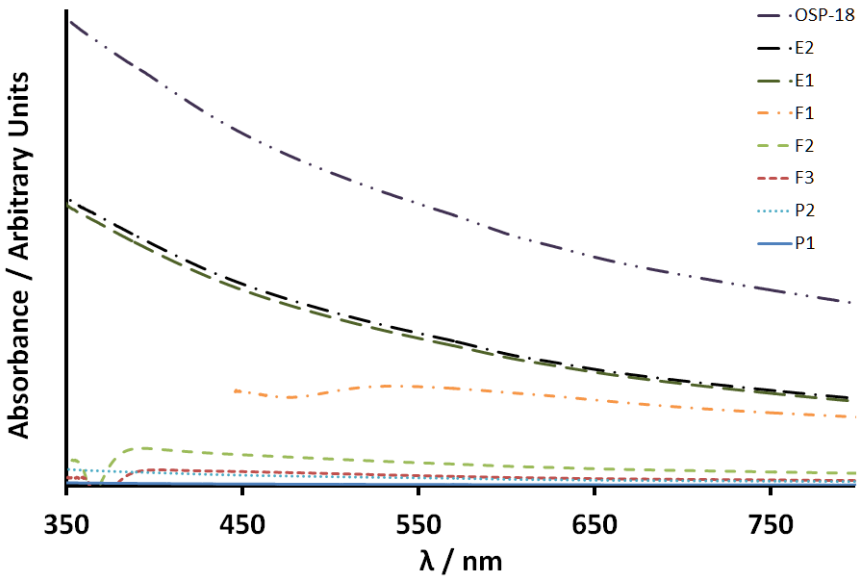

Figure 6.4: *UV-Vis spectra of FDGO dispersed in oils. Spectrum for F1 is truncated due to noisy data at <450 nm as a result of the characteristics of the oil.*

The relative absorbances of dispersions of FDGO are presented in table 6.3 and show that the oils that act best to disperse as produced GO are also those that work best to disperse FDGO, namely E1, E2 and OSP-18, with F1 also acting as a reasonable solvent for FDGO. This behaviour is what is expected when dispersing relatively polar GO as E1, E2 OSP-18, and F1 all contain a polar component. The remaining oils are only able to maintain minimal concentrations of GO in solution, which again is expected as a result of the polarities of the oils and GO.

Table 6.3: *The relative absorbances at 660 nm of the UV-Vis spectra of the dispersions of FDGO in oils as well as their relative concentrations as a percentage of the concentration of dispersions of E1.*

Oil	Absorbance / Arbitrary Units	Relative Concentration of FDGO / %
E1	1.16	100
E2	1.26	109
P1	0.25	22
P2	0.01	1
OSP-18	2.07	178
F1	0.06	5
F2	0.88	76
F3	0.17	15

As the conditions used for this experiment (volumes, mass of GO, sonication time and intensity) were the same as those used to prepare dispersions of as produced GO it is possible

to compare the absorbance, and therefore concentrations of the dispersions of as produced GO to those of FDGO in the oils (figure 6.5). It can be seen that the concentration of FDGO is either similar to that of as produced GO or greater than it across all the oils, with a significant increase in concentration being observed for FDGO in OSP-18. In addition to this impact on concentration the use of FDGO to form dispersions also removes the issue of addition of water to the final dispersions which will be advantageous in many applications. For both as produced GO and FDGO it is seen that the colour of the dispersions lightens over a period of 5 weeks (figures 6.1 and 6.3) indicating that the stability of the dispersions is still low and must be further improved.

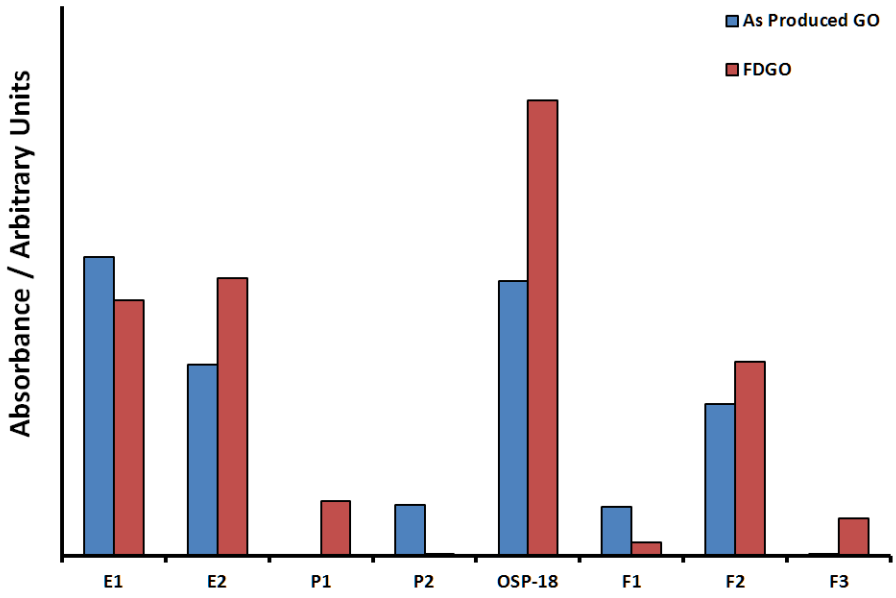

Figure 6.5: *A chart showing the UV-Vis absorbance at 660 nm for as produced GO (blue) and FDGO (red) in oils. This is proportional to the concentration of GO in these dispersions.*

Another important consideration when using GO as an additive in automotive applications is the impact of operating temperature as it has been reported that at temperatures of $>80\,^{\circ}C$ GO will begin to be reduced and form rGO in a range of solvents.[242,260,279–281] If this were to occur *in situ* in the oil and result in the additive crashing out of dispersion it could be detrimental to the properties of the fluid.

The combination of these factors led to the decision that GO is not an ideal additive for lubricant nanofluids in spite of some promising dispersions being produced and so efforts

moved onto the use of more hydrophobic graphene additives, with greater thermal stability.

6.2.3. Dispersions of rGO in oils

An obvious potential candidate for a material which might interact more favourably with hydrophobic oils than GO is rGO which, as explained in section 1.6, due to the removal of oxygen functionalities and restoration of sp^2 matrix is inherently less hydrophilic than GO. As an additive for thermal fluids rGO is also believed to have greater potential than GO due to its higher thermal conductivity resulting from the decreased number of defects in its structure.[172,173,262]

6.2.3.1. Dispersions of Hydrazine Reduced GO in oils

rGO was produced from GO using hydrazine reduction, *via* the procedure described in section 8.3.4, and dispersed in oils using ultrasonication, as described in section 8.3.5. After being allowed to settle for 24 h the dispersions were photographed (figure 6.6) and analysed by UV-Vis spectroscopy (figure 6.7) in order to establish the concentration of rGO in the oils.

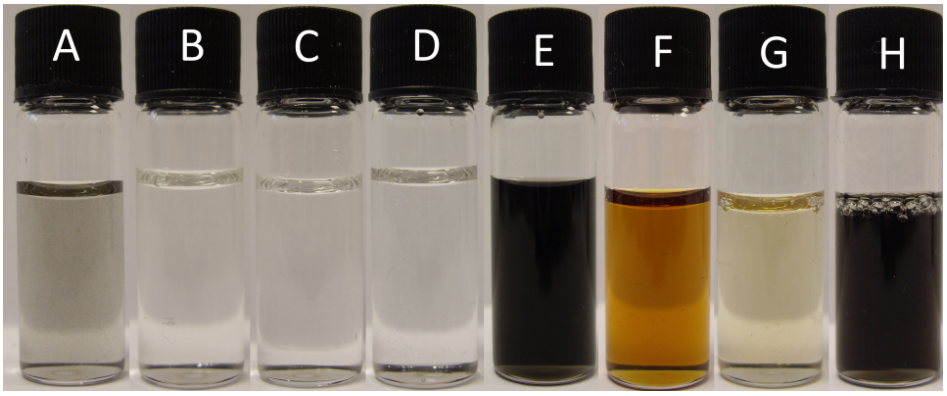

Figure 6.6: *Photographs of rGO synthesised using hydrazine in oils after dispersion and settling for 6 weeks. A) E1, B) E2, C) P1, D) P2, E) OSP-18, F) F1 (coloured orange due to the molybdenum friction additive present in the oil), G) F2, and H) F3.*

Unlike for GO the extinction coefficient for rGO is known and has been reported in the literature[364] and so concentrations of rGO dispersions can be calculated using the Beer-Lambert law. Table 6.4 shows the stable concentration of rGO in each of the oils. As can

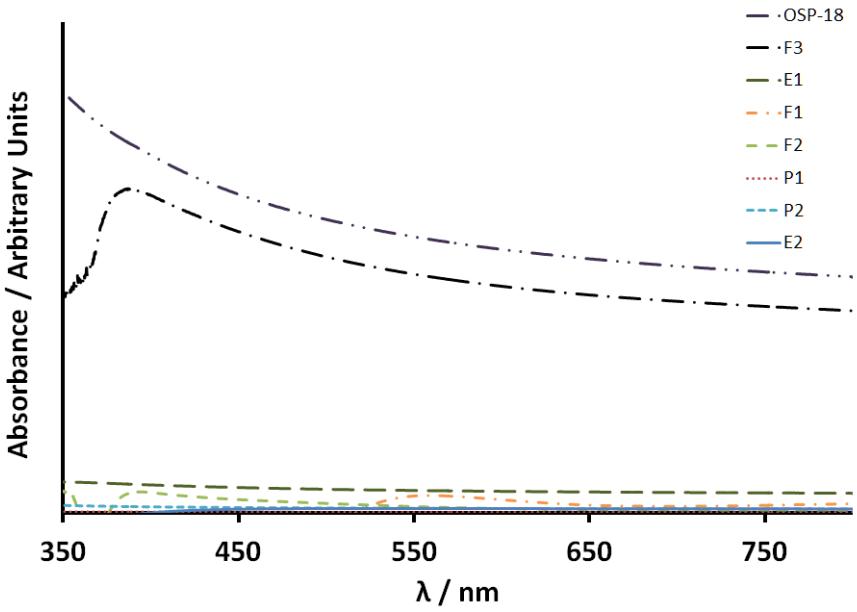

Figure 6.7: *UV-Vis spectra of hydrazine reduced GO dispersed in oils.*

be seen from these data, rGO did not form stable dispersions in most of the base oils; however, in OSP-18 and F3 concentrations of >60 µg ml^{-1} were observed, indicating that these oils have better compatibility with rGO than their other counterparts.

Table 6.4: *The concentrations of rGO produced using a hydrazine reduction method in oils; determined by the Beer-Lambert law taking the absorbance from UV-Vis spectroscopy at 660 nm.*

Oil	Concentration / µg ml^{-1}
E1	5.9
E2	1.2
P1	0.2
P2	1.2
OSP-18	68.5
F1	2.0
F2	0.9
F3	60.9

The dispersion behaviour of rGO in oils differs significantly from that exhibited by GO. The process of reducing GO has the effect of decreasing the polarity of the graphene sheets by removing the oxygen functionalities present and so it should be expected that rGO will disperse better in the less polar oils than GO will.

In reality however, the oils that best disperse rGO are those that still retain some polar component with the highest concentrations of over 60 µg ml^{-1} achieved in OSP-18 and F3. The least polar oils, P1 and P2 performed worst when dispersing rGO. This agrees with what

is well known about rGO, that residual oxygen functionalities on the sheets, not removed by reduction, mean it is more polar than pristine graphene[262] which will interact better with oils with some level of polarity than those that are entirely non-polar.

Dispersing rGO in oils has a key advantage over dispersing GO: that of improved thermal stability. This means that dispersions are much less likely to suffer changes to properties under real, elevated temperature, operating conditions.

One step in the method used to produce these dispersions that may be hindering the dispersibility of rGO in the oils is the drying step used in the isolation of rGO. This process has the potential to cause the agglomeration of rGO sheets, making them harder to disperse if it is not possible which do not break apart on redispersion, reducing their dispersibility.[418]

6.2.3.2. In situ Reduction of GO in Oils

As has been discussed above, one of the downsides of utilising GO as an additive in thermal applications is that it has the potential to spontaneously reduce in solvents at elevated temperatures, forming rGO. In order to turn this potential challenge into a useful property, attempts were made to synthesise rGO *in situ* by heating a dispersion of GO in oil. This *in situ* synthesis of rGO avoids the use of hydrazine, reduces the number of reaction steps needed and avoids the need to isolate the rGO before its dispersion in the oil, reduces the opportunity for the re-agglomeration of sheets to affect the concentration of the dispersion.

Dispersions of *in situ* rGO in oils were produced as described in section 8.3.6. Briefly, dispersions of FDGO were produced in oils at 1 mg ml^{-1} and then heated to 120 °C for 24 h before being allowed to cool and settle. The concentration and stability of rGO in these dispersions was then determined.

During heating it was observed that the characteristic brown colour of GO changed and darkened to black after between 5 h and 10 h, which is commonly used as an indication of its reduction to rGO. By the end of the 24 h reaction the colour of all the dispersions was

dark black, and rGO appeared to be well dispersed in all 8 oils (figure 6.8). The dispersions were then left to cool and stand for a period of weeks in order to establish their stability. After 4 weeks only 3 of the oils had retained the rGO in suspension at high concentration, E1, F1, and OSP-18, and were still dark and opaque whilst the remainder had only a very low concentration of rGO remaining in solution and so had returned to being transparent and clear or light grey.

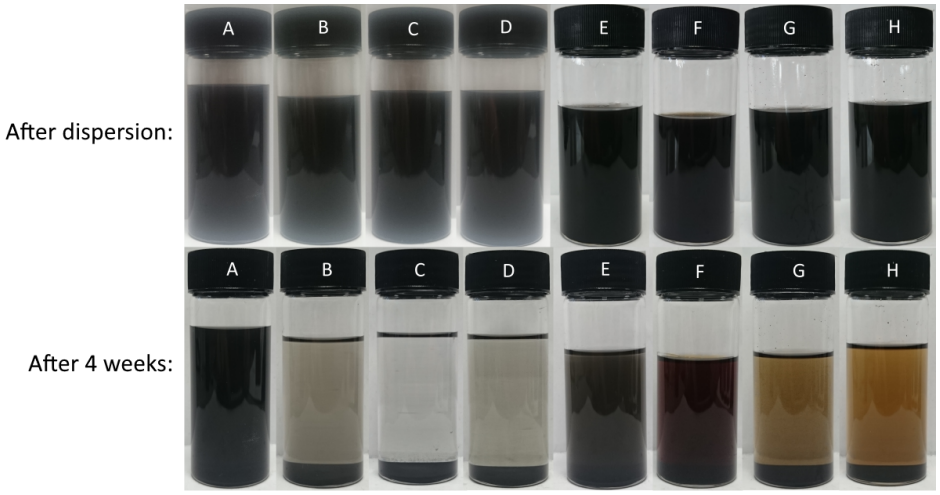

Figure 6.8: *Photographs of dispersions of in situ reduced GO in oils after (top) immediately and (bottom) 4 weeks after dispersion. (A) E1, (B) E2, (C) P1, (D) P2, (E) OSP-18, (F) F1, (G) F2, and (H) F3.*

Another observation from figure 6.8 is that the darkened colour of the dispersions in F2 and F3 is not due to dispersed rGO and so it is believed that the process of reducing GO has caused some chemical change in the oil. However, as the concentration of these dispersions is poor this detail was not investigated further.

The settled dispersions after 4 weeks were analysed by UV-Vis spectroscopy (figure 6.9) in order to establish the concentration of rGO remaining in each dispersion. The results are presented in table 6.5 and as expected from the photographs the data show the concentration of rGO is highest in E1 and OSP-18, with F1 also showing some stability. It should, however, be noted that part of the colour of the F1 dispersion shown in figure 6.8 is due to the colour of the oil itself and not due to dispersed graphene. Comparing this information with the known polarity of the oils, it is apparent that the rGO produced *in situ* has different solution behaviour than that produced using hydrazine (figure 6.10), with the highest con-

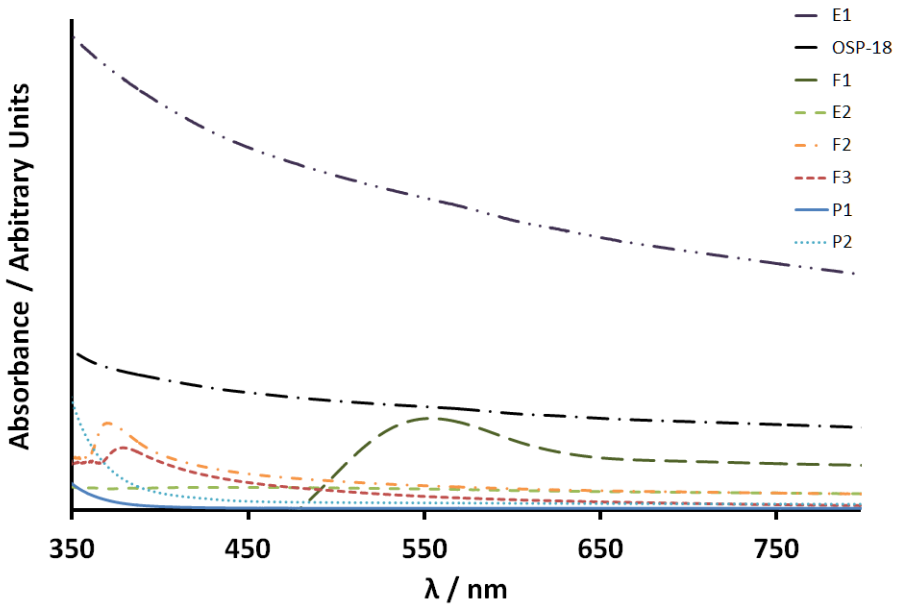

Figure 6.9: *UV-Vis spectra of dispersions of rGO produced through in situ reduction of GO in oils.*

centration dispersion of hydrazine rGO being in OSP-18, whilst the highest concentration of *in situ* rGO is found in E1 which is less polar than OSP-18. It is possible that this change is due to *in situ* rGO being less polar than rGO produced using hydrazine and the degree of reduction achieved using the *in situ* reduction method is greater than that possible using hydrazine. However, another factor that must be taken into consideration is that the avoidance of the drying step when producing *in situ* rGO also impacts on its dispersibility in the oils.

Table 6.5: *The concentrations of in situ rGO in oils 4 weeks after the production of dispersions; determined by the Beer-Lambert law taking the absorbance from UV-Vis spectroscopy at 660 nm. As a comparison, the concentrations of rGO produced using Hydrazine are also included in the table.*

Oil	*in situ* rGO Concentration / μg ml^{-1}	Hydrazine rGO Concentration / μg ml^{-1}
E1	60.6	5.9
E2	4.0	1.2
P1	0.3	0.2
P2	1.4	1.2
OSP-18	20.4	68.5
F1	11.4	2.0
F2	4.2	0.9
F3	1.7	60.9

In order to better determine if the degree of reduction, or the agglomeration of the

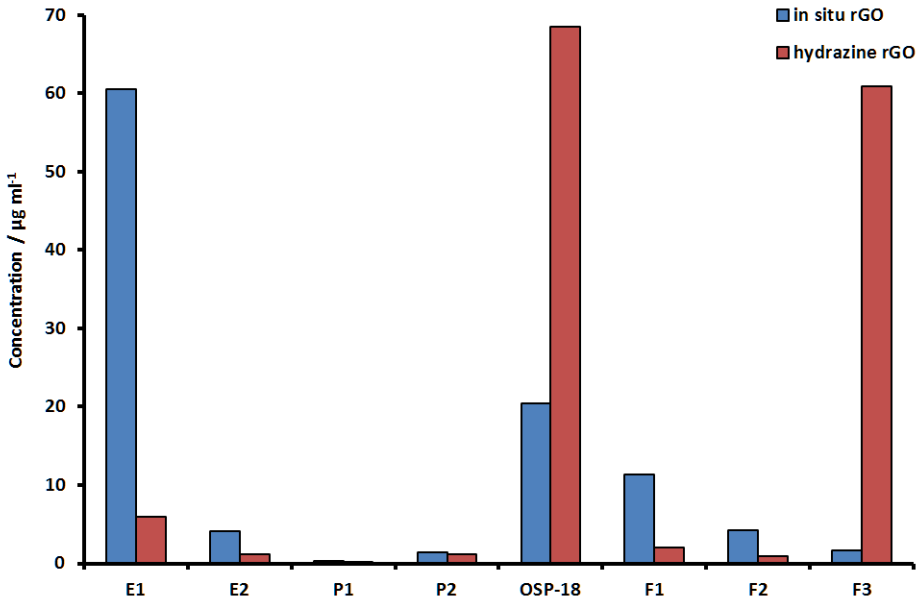

Figure 6.10: *Comparisons of the concentrations of dispersions in oils of rGOs produced using hydrazine (red) with that produced in situ (blue).*

material is the cause for this change in dispersibility, attempts were made to characterise the *in situ* rGO. Unfortunately this proved to be a challenge as it has not been possible to isolate rGO from the oils in order to fully characterise the products of the *in situ* reduction.

In spite of this challenge in isolating *in situ* rGO some characterisation techniques can give information on the chemistry of graphene materials in solution. As has been discussed in section 3.4, it is common for UV-Vis spectroscopy to be used as a means of characterising the degree of reduction for rGO. Unfortunately all of the oils tested do not transmit light at wavelengths of ≤ 350 nm making it impossible to asses the degree of reduction using the peak position in UV-Vis. Instead an alternative technique may be required to assess the degree of reduction. Unfortunately the difficulty of isolating the *in situ* rGO from the oils means that the usual techniques for assessing the reduction of GO are challenging. TGA is a common method of assessing the degree of reduction in graphene materials (section 3.6), however residual oils on the graphene sheets will cause significant changes in the burn profile making it difficult to draw reliable conclusions. XPS suffers from similar problems as the oils themselves contain significant carbon and oxygen atoms in similar bonding environment to rGO making it hard to isolate the portion of the spectra occurring as a result of rGO. For this reason, an alternative approach will need to be found to test the degree of reduction

of *in situ* rGO in oil dispersions. One proposed idea for overcoming this challenge would be the use of impedance spectroscopy to test for changes in conductivity of the oils. This topic will be discussed further in section 6.6.

In spite of the challenges of precisely determining the degree of reduction of *in situ* rGO, it has been clearly demonstrated that the solution properties of these materials have changed from those of the starting GO as a result of heating in the base oils. The reason for this change can only reasonably be attributed to a change in the chemistry of the starting GO and based on the known chemical behaviour of GO under heating, combined with the colour change observed from brown to black, it is highly likely that this change will be as a result of the reduction of GO to rGO.

6.3. Functionalisation of Graphene Oxide to Improve Dispersibility

Whist *in situ* rGO and hydrazine rGO both showed some promise as additives in oil based nanofluids higher concentration dispersions of graphene materials, at greater stabilities, in oils should provide more improved properties, and so are desirable. The ability of covalent functionalisation to modify the solution properties of graphene materials by changing their surface chemistry is well known (section 1.7) and so functionalisation of graphene was investigated as a method to increase the concentrations and stabilities of nanofluids.

A range of possibile routes for the functionalisation of GO and rGO were considered in order to improve the compatibility of graphene materials with the oils they were to be dispersed in. While the use of non-covalent modification provides an easier approach to improving dispersibility than covalent modification, the effects of any excess modifier on the properties of the oil would have to be carefully monitored to ensure any changes were as a result of the graphene additives.

Another aspect that must be considered is that the fully formulated oils contain carefully designed packages of additives which control properties such as viscosity and friction. The addition of graphene materials will already have an impact on these properties, but it was decided that it would be best to avoid the further potential complications that could be caused by free non-covalent modifiers in the system and so covalent modification will be used in this body of work.

6.3.1. Synthesis of ODArGO

As a start point for investigating the impact of covalent functionalisation on the dispersibility of graphene materials in oils it was decided to utilise a well established synthesis from the literature. Octadecylamine (ODA) was chosen as a an additive as it was believed that the long alkyl chain would give good interactions with the oils and the amine head group has the potential to react with oxygen containing functionalities on GO *via* a selection of chemistries such as an acid-base reaction with carboxylic acids or the formation of an amide bond. While $SOCl_2$ and EDC can both be used to functionalise GO with ODA a much simpler procedure was employed. This was adapted from the work of Jang *et al.* who functionalised GO with octylamine (OA), dodecylamine (DDA), and hexadecylamine (HDA).[380] This produced octadecylamine functionalised GO (ODA-GO), which was then be reduced using hydrazine to give octadecylamine functionalised rGO (ODA-rGO).

The procedure for this reaction is described in full in section 8.3.7. Briefly, a suspension of ODA in ethanol was added to a dispersion of GO in water and heated to 60 °C for 16 h. This formed a suspension of ODA-GO which was then reduced using hydrazine (hydrazine monohydrate, 1 µl per 3 mg of GO, 80 °C, 2 h, section 8.3.8) during this time the brown dispersion changed to form an insoluble black powder which was isolated *via* vacuum filtration over a nylon membrane and dried at 60 °C *in vacuo* for 24 h.

The dried ODA-rGO was a free flowing, dark grey powder; markedly different to rGO which normally has a much more granular texture. The colour of the ODA-rGO is also a

dark grey as opposed to the normal deep black of rGO. The material was characterised, as described below and then its dispersibility in a range of fluids was assessed.

As a control a batch of rGO was also produced using a comparable method. Briefly, GO was heated to 60 °C in water and ethanol for 16 h before undergoing reduction using hydrazine hydrate in comparable conditions to those described above. A full description of the procedure can be found in section 8.3.9. No noticeable change occurred to the GO after heating overnight in ethanol, and the material produced by the reduction reaction had the appearance of normal rGO and could not be distinguished by any characterisation method.

6.3.1.1. Characterisation of ODArGO

After ODA-rGO had been produced and isolated it was important to characterise it in order to assess both if the functionalisation reaction had been successful and if the conditions used in the reaction had caused any damage to the graphene sheets within the material. In order to obtain these data a range of functionalisation techniques were used and the results of these are detailed below.

6.3.1.1.1. TGA

A key factor to determine when dealing with the characterisation of functionalised graphenes is the ratio of functional groups to graphene sheets. The simplest way to determine this information is through the use of TGA, which is discussed in detail in section 3.6.

A TGA profile for conventionally produced ODA-rGO is shown in figure 6.11 A alongside that of the control batch of rGO produced as described in section 8.3.9 (figure 6.11 B). In both these TGA profiles there is some mass loss below 100 °C which is attributed to the evaporation of residual solvent. For this reason the profiles have been normalised to the mass at 100 °C such that any mass losses above this temperature can be compared.

A marked difference is observed between the burn profiles of ODA-rGO and rGO as the the temperature rises past 190 °C. While the burn profile of rGO shows a slow, consistent

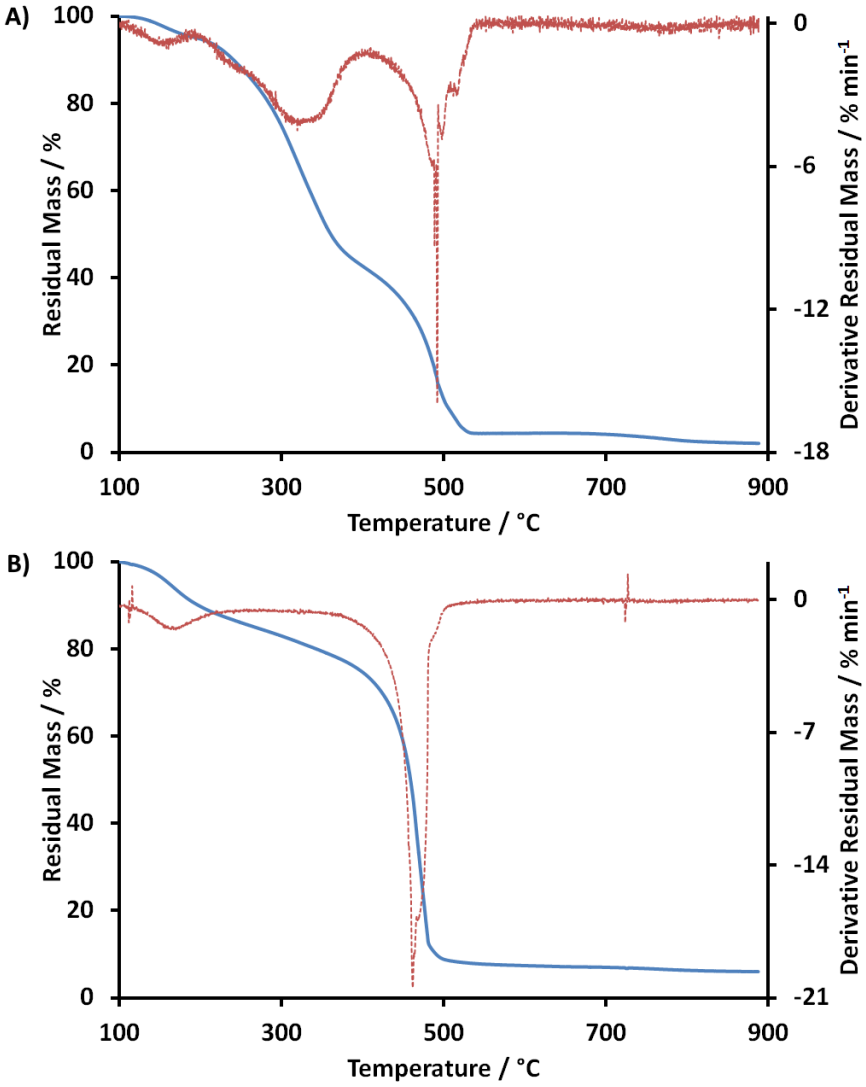

Figure 6.11: *TGA in air of A) ODArGO, and B) rGO showing the residual mass against temperature (blue) and their derivatives (red). These plots clearly show the extra loss in mass that occurs for ODArGO at 200-400 °C corresponding to the loss of ODA from the surface of the graphene sheets.*

decrease in mass, the profile for ODA-rGO undergoes a much greater mass loss in this temperature range. This difference between the two burn profiles is attributed to the thermal decomposition of ODA off the surface of the rGO sheets. The derivatives of the burn profiles clearly show this difference in thermal stability. Over this temperature range of 190-400 °C a mass loss of 52.6 % is observed for ODA-rGO, compared to only only 16.1 % for unmodified rGO, a change of 36.5 %. This additional mass loss occurs as a result of the functionalisation present on ODA-rGO and indicates that the degree of functionalisation of the ODA-rGO prepared is at least 36.5 % by mass, equating to a molar percentage of moles of ODA per mole of carbon of 2.55 mol. %. It is possible that the degree of functionalisation is higher than this

if some functional groups have sufficient thermal stability to remain present above 400 °C.

Once the temperature passes 400 °C the rate of mass loss in both materials is similar, as shown by the derivatives, indicating that the majority of functional groups in ODA-rGO have decomposed below this point and that above this temperature the change in mass is due to the thermal decomposition of the rGO sheets themselves.

This data is comparable with that measured by Jang *et al.* who determined that the hexadecylamine functionalised rGO (HDA-rGO) produced using a comparable method had a degree of functionalisation of 37 wt. % (2.92 mol. %) and that degree of functionalisation achieved, decreased with the length of the alkyl chain of the modifier.[380]

6.3.1.1.2. XPS

Of all the possible methods used to characterise f-rGOs, few of them are able to detect the elements present in the material, and show that the functionalising agent is explicitly present on the surface of the graphene sheets. XPS is used in order to give analysis of the elemental composition and bonding environments present in the material. The use of XPS in the analysis of graphene materials is described in detail in section 3.8. XPS samples of ODA-rGO were prepared and XPS spectra were recorded using the method described in section 8.1.4.1. The data obtained were analysed as described in section 8.1.4.2. Examination of the survey scan from these samples (Appendix D) show the presence of only carbon, oxygen, and nitrogen (silicon is also observed from the substrate and sodium from contamination). This gives two key pieces of data: firstly, that there are no unexpected elements present which would be an indication of contamination, and secondly, the presence of a N1s peak, the absence of which would clearly indicate a lack of the functionalising ODA in the sample.

Within the survey scan, the two peaks of most interest in the sample are the C1s peak and the N1s peak. The C1s peak of ODA-rGO is shown in figure 6.12 and the N1s peak is shown in Appendix D. Fitting of the C1s peak allows the carbon containing covalent binding

environments present within the material to be determined and so any chemical changes caused by functionalisation will become apparent. Whilst fitting the C1s peak can provide information on a material's chemistry the same is not usually possible for the N1s peak due to its poorer signal to noise ratio and less distinction between the binding energies of nitrogen bonding environments. Nevertheless, the presence or absence of this peak is still instructive in showing that it is possible that ODA is present on the surface of the rGO sheets.

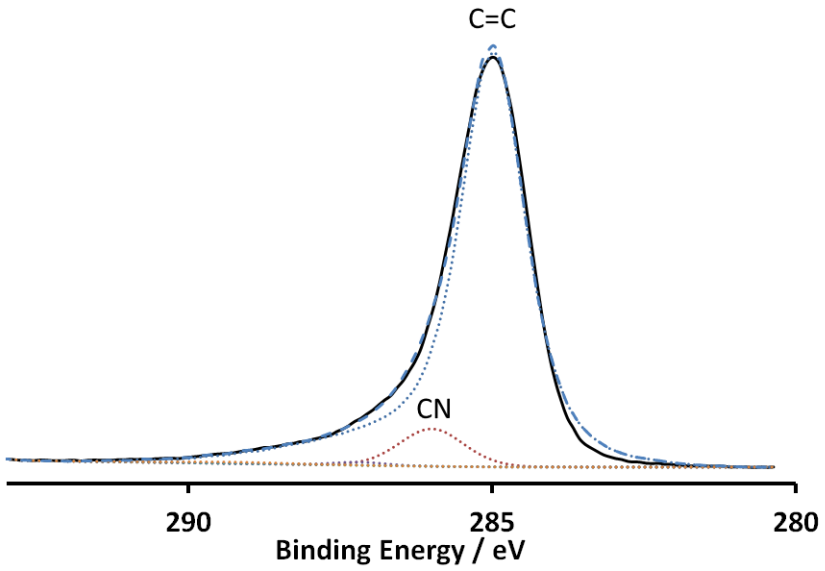

Figure 6.12: *A representative XPS C1s spectrum for ODArGO produced using the method proposed by Jang et al..*[380] *These data show the C1s spectrum (black line), the fit envelope (blue dashed line) and the fitted component peaks (dotted lines).*

It should be noted, however, that the N1s peak is observed in the XPS of both ODA-rGO and the control rGO (figure 5.9 B). This is believed to be due to the use of hydrazine, which contains nitrogen, as the reducing agent as it is believed that the reduction reaction can cause residual nitrogen containing groups on the rGO produced.[246] This is a limitation of XPS in this scenario and means that the presence of the N1s peak alone can not be used as proof of the presence of ODA. A comparison of these data with those recorded by Jang *et al.* show that C1s spectra of both materials have peaks for carbon-carbon bonding environments and carbon-nitrogen bonding environments. Slight differences between the levels of oxygen content based on the C1s peak are observed between the data presented here and by Jang *et al.*. However, this is mainly as a result of the fitting method chosen and our choice

to fit an asymmetric C=C peak with the overall lineshapes of both spectra being extremely similar.

6.3.1.1.3. UV-Vis Spectroscopy

As has been discussed in section 3.4, one of the common methods of studying the reduction of GO to rGO is to monitor the position of the $\pi \rightarrow \pi^*$ plasmon peak as it shifts from $\sim$230 nm in GO to $\sim$270 nm in rGO. In order to assess the degree of reduction of the ODA-rGO produced UV-Vis spectroscopy was performed (figure 6.13). This shows the position of the $\pi \rightarrow \pi^*$ plasmon peak to be 256 nm which indicates a that reduction has occurred during the procedure. However, this shift is not as great as for unmodified hydrazine rGO which has a peak at 270 nm, indicating that full restoration of conjugation has not occurred, possibly as a result of the presence of functionalising ODA groups. These data mirror those presented by Jang *et al.*.

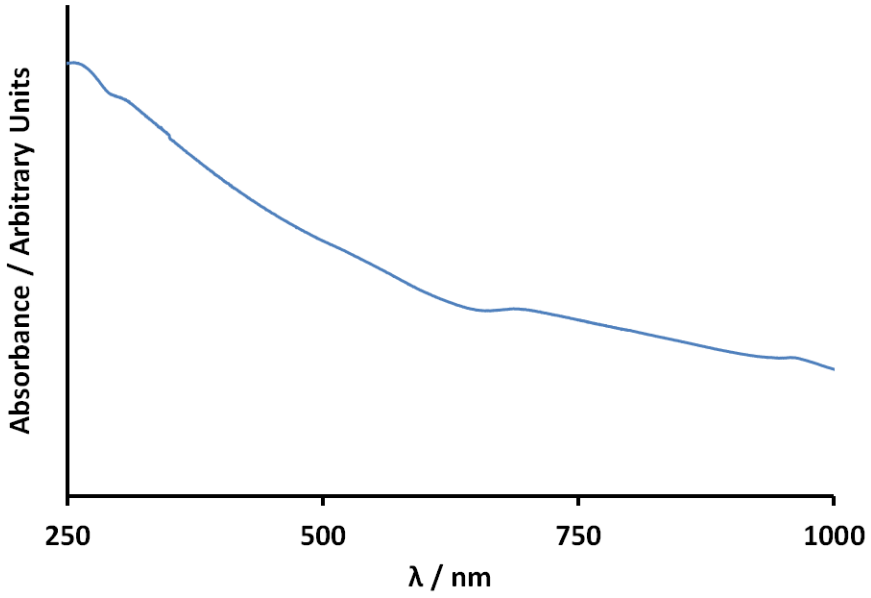

Figure 6.13: *UV-Vis spectroscopy of a dispersion of ODArGO produced the the method of Jang et al. showing the position of the $\pi \rightarrow \pi^*$ plasmon peak to be 256 nm.*[380]

6.3.1.1.4. Raman Spectroscopy

Raman spectroscopy of the ODA-rGO is presented in figure 6.14. The spectrum shows the presence of the D and G bands as would be expected in a defective graphene material

such as f-rGO as well as small second order bands. As described in section 3.5 the *D* band originates from the edges of sp^2 regions which may be caused by the presence of defects, whereas the *G* band arises from the sp^2 regions themselves. This means the *D* band has a greater intensity, relative to that of the *G* band in materials with a greater number of defects. The $I_D : I_G$ ratios of both materials were calculated from these spectra and found to be 0.96 $\pm$ 0.02 for ODA-rGO compared to 1.34 $\pm$ 0.01 for rGO.

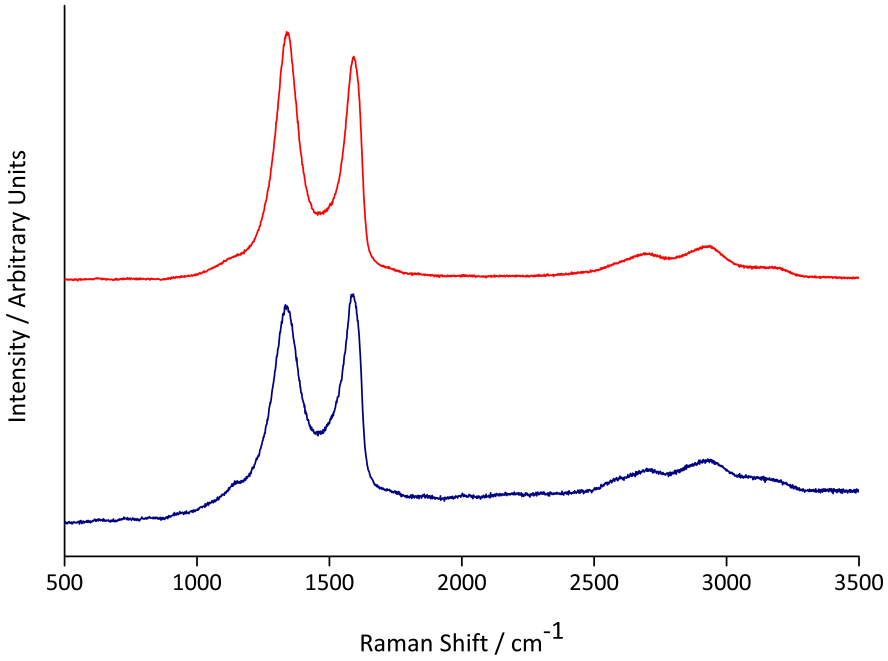

Figure 6.14: *A stack plot of Raman spectra for ODArGO produced by the method described by Jang et al. (blue) and for rGO produced by a comparable method (red) showing the presence of D (1350 cm^{-1}) and G (1595 cm^{-1}) bands in all materials as well as small 2D bands (∼2800 cm^{-1}). Intensities are normalised to the height of the G and spectra are vertically offset for clarity.*

This result can be explained by studying the Raman spectrum for GO which generally has an $I_D : I_G$ ratio of around 0.8. It is believed that when GO undergoes reduction to rGO small islands of sp^2 carbon form in the graphene sheets as oxygen functionalities are removed, leading to the change in $I_D : I_G$ ratio from ∼0.8 to ∼1.3 observed. In the case of ODA-rGO then, when reduction is performed ODA chains are present on the surface of the GO sheets, which will impact on the mechanism of the hydrazine reduction. As the $I_D : I_G$ ratio of ODA-rGO rises only to 0.96 $\pm$ 0.02 this indicates that the ODA-rGO does not have the same, large number of sp^2 domain edges found in unmodified rGO. Instead larger sp^2 domains appear to form possibly as a result of steric hindrance by the ODA chains.

6.3.1.1.5. TEM

TEM was used to assess the size of the ODA-rGO sheets produced by the above method, and to determine if the processing used was causing any damage to the sheets. It was also used to determine if sheets had been fully exfoliated during processing; meaning the material could truly be called functionalised graphene. Figures 6.15 A and 6.15 B show the sheets of ODA-rGO, showing that they are flat, thin sheets with only minor crumpling. SAED was used to show the graphitic character of the material. Diffraction patterns (figure 6.15 C) show spots for the diffraction of electrons through the material but the spots are extended with multiple spots being present at different angles, meaning that the pattern is produced from several stacked sheets that are not bound together.

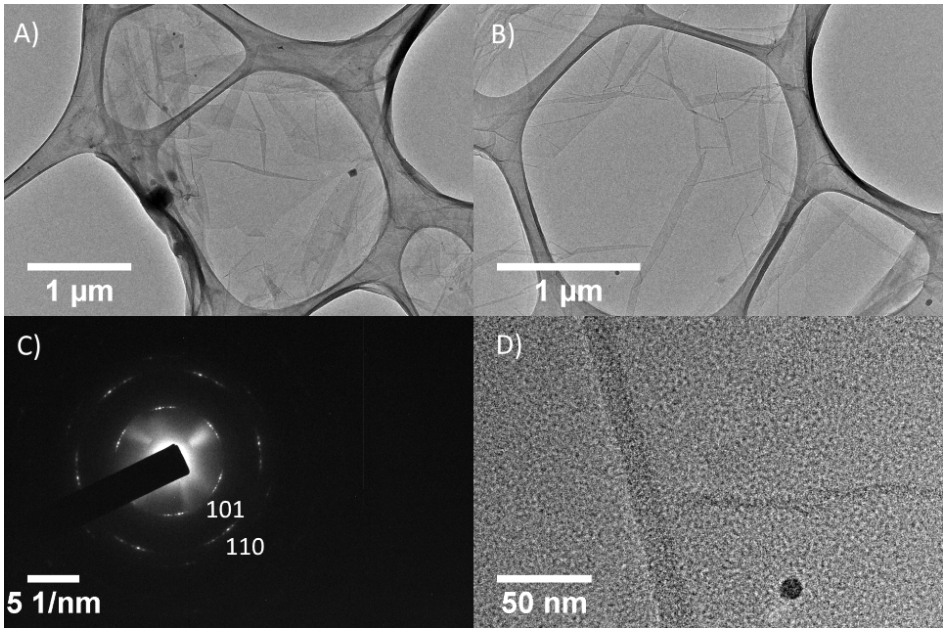

Figure 6.15: *Transmission electron micrographs of ODArGO produced by a synthesis proposed by Jang et al.. A) and B) representative micrographs of sheets of ODArGO showing that the sheets are thin, not crumpled and show little sign of damage by processing. C) SAED of an ODArGO sheet showing rings for the* $(1\,0\,1)$ *and* $(1\,1\,0)$ *spacings of graphene. D) HREM of a sheet of ODArGO showing the absence of any damage or holes.*

Whilst the characterisation methods described above do provide a great deal of information about changes in quality, size and structure of the graphitic sheets, and show that functionalisation has no detrimental effects on these properties, as well as allowing the detection of functionalising ODA they, unfortunately, do not allow the method of binding be-

Table 6.6: *The concentrations of ODArGO dispersions in oils; determined by the Beer-Lambert law taking the absorbance from UV-Vis spectroscopy at 660 nm. The concentrations of comparable dispersions of hydrazine rGO are also included as well as the percentage change in concentration.*

Oil	ODArGO Concentration / μg ml^{-1}	rGO Concentration / μg ml^{-1}	Ratio of concentrations (ODArGO:rGO)
E1	150.8	5.9	25.6
E2	119.2	1.2	99.3
P1	11.1	0.2	55.5
P2	104.1	1.2	86.8
OSP-18	152.5	68.5	2.2
F1	24.0	2.0	12.0
F2	20.3	0.9	22.6
F3	2.6	60.9	0.04

tween the ODA and the graphitic sheets to be established. However, for applications such as thermal fluids and lubricants the mechanism of functionalisation is not important so long as the stability and concentrations of the dispersions produced is improved by the technique.

6.3.1.2. Dispersibility of ODArGO

The definitive characterisation of functionalised graphene graphene materials is a challenging task and so one possible approach to assessing the success of functionalisation is to examine the impact that the functionalisation has on the material's dispersibility.

In order to establish the effectiveness of the functionalisation of rGO with ODA in the context of thermal fluids the dispersibility of the ODA-rGO in each of the oils was studied. In order to achieve this, 25 mg of dried ODA-rGO (produced as described in sections 8.3.7 and 8.3.8) was dispersed in each of the eight oils at a concentration of 1 mg ml^{-1} using probe sonication (full dispersion procedure described in section 8.3.5).

The dispersions of ODA-rGO were then left to stand for 24 h before being analysed by UV-Vis spectroscopy in order to establish the concentration of ODA-rGO that could be stably dispersed in each oil. The concentrations, determined using the Beer-Lambert law are shown in table 6.6 with the spectra they are calculated from being shown in figure 6.16.

As can be clearly seen from table 6.6 the functionalisation of rGO with ODA has had a

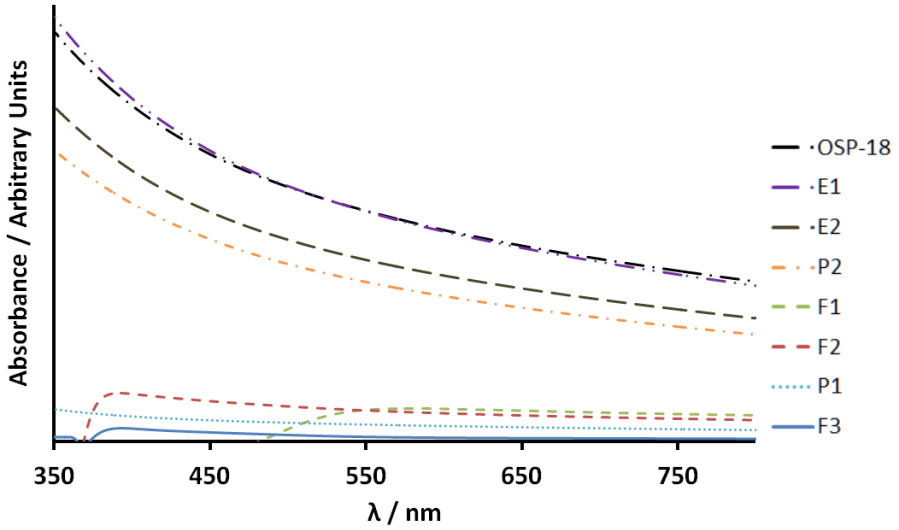

Figure 6.16: *UV-Vis spectra of ODArGO dispersed in Oils. It should be noted that in dispersions of F1, F2, and F3 a sharp fall in absorbance occurs above a certain wavelength threshold due to the characteristics of the oil.*

significant impact on its dispersibility in the oils with concentration increasing by nearly 100 times in some cases, compared to the concentration of rGO that can be dispersed. As the dispersion protocol is identical and no other changes have been made to the material it can be concluded that this improved dispersibility is due to the fact that the rGO has been functionalised with the ODA. This again agrees with the results of Jang *et al.* who also observed an increase in the dispersibility of f-rGOs in non-polar solvents at longer functionaliser chain lengths.

6.3.2. Improved, Solvent-Free in situ Functionalisation and Reduction of Graphene Oxide

Whilst the method used to modify GO with ODA (section 6.3.1) does have the potential to be successful this method contains many steps and is extremely time consuming. As a result of this it was decided to attempt to find an alternative method to improve the efficiency of this process. To achieve this, the functionalisation was combined with GO's ability to be reduced simply by heating to create a solvent free, *in situ* method for reduction and functionalisation without the need for a solvent.

The success of this method is depended upon the careful selection of the functionalising agent. Promising functionalisers will have two properties. Firstly, they will contain a reactive site that can either bind with, or non-covalently interact with oxygen functionalities present on GO and rGO. The functional group most commonly used to functionalise these materials is an amine, which can either react covalently with a range of oxygen functionalities to form an amide, or non covalently with similar sites on graphene through non-covalent interactions. Another group of reagents that were found to interact successfully were phosphines, which can interact with GO and rGO in a similar manner. The second concern when picking a functionaliser for this method of modifying graphene is its boiling point. In order to ensure full reduction of the GO occurs during heating as well as increasing the likelihood of a functionalisation reaction occurring the temperature of the reaction must be >100 °C. As this reaction is performed in the absence of solvent it is therefore essential that the boiling point of the functionaliser be sufficiently higher than this temperature that it will not evaporate in the course of the reaction.

Alongside this, in order for the functionalisation to have the desired effect of improving the dispersibility of graphene materials in oils it is important to consider how these functionalisers will interact with the oils themselves. The results shown previously in sections 6.2.1 to 6.2.3 indicate that both GO and rGO produce dispersions at higher concentrations in base oils that are more polar, such as E1 and OSP-18, and are more challenging to disperse in non-polar oils such as P1 and P2. For this reason the functionalisers chosen were picked in an attempt to add significant non-polar character to the graphene sheets.

Given the promising results, described above, for the dispersibility of ODA-rGO in oils the first functionaliser chosen was ODA. As well as being a promising reagent for this *in situ* method of functionalisation in its own right, with a long non-polar chain to interact with the oils, this has the advantage of allowing comparison of the material produced using the *in situ* method with that produced by a more conventional method of functionalisation, such as that discussed in section 6.3.1. In addition to ODA a selection of other modifiers were also chosen for their chemistries and high boiling points. These are shown in figure 6.17

and include trioctylphosphine (TOP), trioctylphosphine oxide (TOPO), and oleylamine (OL).

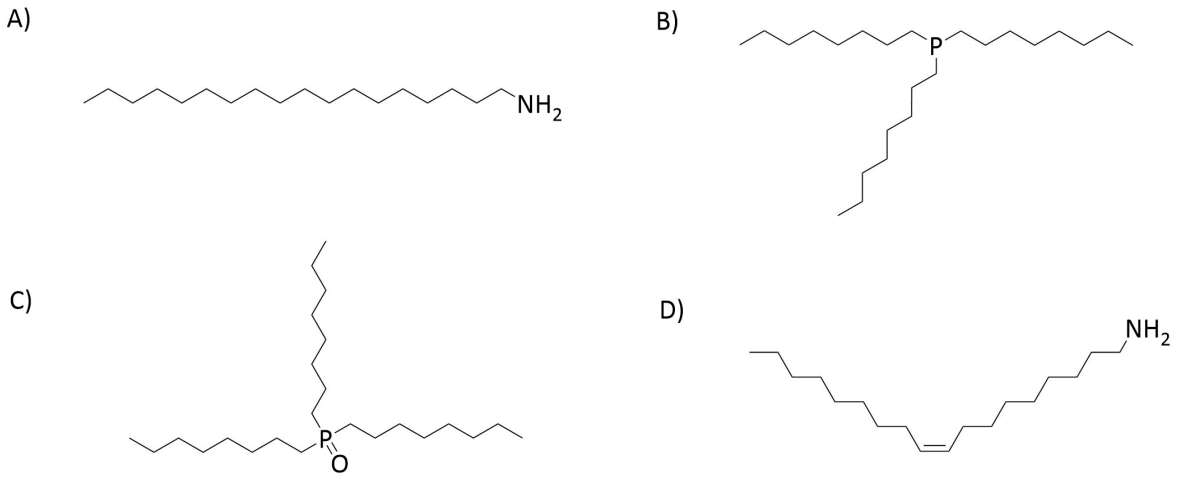

Figure 6.17: *The modifiers chosen to functionalise GO: A) octadecylamine, B) trioctylphosphine, C) trioctylphosphine oxide, D) oleylamine.*

OL ((Z)-Octadec-9-enylamine) is an unsaturated form of ODA which was chosen due to being chemically similar to ODA; giving it good potential to functionalise GO as well as having been shown to act as a reducing agent under certain conditions.[419] As with ODA it is hoped that the single, long alkyl chain present on OL will interact well with the non-polar, PAO, base oils and act to improve the dispersibility of the graphene materials in these oils. TOP and TOPO are both already known to act as high temperature solvents for carbon materials, most commonly in the synthesis of carbon dots,[420] which alongside their high boiling points led to their selection as potential functionalising agents. Both TOP and TOPO consist of three octyl chains bound to a phosphorous core with TOPO being an oxidised form of TOP with the oxygen bound to phosphorous. It is believed that the octyl chains will allow f-rGO to interact well with both the non-polar PAO oils as well as some of the more polar oils, while the fact that TOP can be oxidised to TOPO means it could potentially aid the reduction of GO to rGO by acting as a reducing agent at the same time as functionalising the GO.[421]

One step reduction and functionalisation was achieved by using the procedure described in section 8.3.10. Briefly, as produced graphite oxide was mixed with an excess of the chosen functionalising agent at room temperature. This mixture was then heated to 60 °C, allowing those functionalising agents that were solid at room temperature to melt before it

was then bath sonicated for 60 minutes at 60 °C in order to exfoliate the graphite oxide to GO. The reagents were then heated to 180 °C for 18 h during which time any residual water contained in the graphite oxide evaporated and the GO underwent a colour change from brown to black, indicative of reduction. The product of this reaction, f-rGO, was then isolated from excess residual functionaliser by washing *via* Soxhlet extraction for 72 h in toluene before being dried as a black powder. Alongside requiring fewer reaction steps than a traditional functionalisation followed by reduction approach to graphene modification our *in situ* reduction-functionalisation method also has the advantage that it avoids the use of harsh reducing agents such as hydrazine which are both potentially harmful as well as having negative environmental impacts.

6.3.2.1. Characterisation of In situ f-rGOs

f-rGOs produced using this *in situ* method of functionalisation were characterised in order to determine whether this method of modification had been successful using the techniques described below.

6.3.2.1.1. XPS

To determine the chemical binding environments present in the f-rGOs produced analysis by XPS was performed. Data from survey scans, including elemental composition, is shown in Appendix D. These spectra show the loading of phosphorous is 2 wt. % in both trioctylphosphine functionalised rGO (TOP-rGO) and trioctylphosphine oxide functionalised rGO (TOPO-rGO). The loading of nitrogen from each of these scans also correlates with the expected levels for each of the f-rGOs with both ODA-rGO and oleylamine functionalised rGO (OL-rGO) having 3 wt. % nitrogen. These scans also confirm the absence of any contaminating elements that can not be easily explained through the methods used to produce the samples (e.g. silicon from substrate, sodium from human sweat, and boron from borosilicate glassware or glass fibre Soxhlet thimbles).

As is common with other graphene materials the peak of greatest interest is the C1s

peak as this gives information on the carbon binding environments present in the material. Fitting the component peaks of the C1s peak gives information on the carbon containing chemical binding environments present in the materials. Fits of the C1s peaks for each of the f-rGOs are shown in figure 6.18. Spectra were fitted as described in section 8.1.4.2. Examining the component peaks of the C1s spectra shows some clear differences between the different f-rGOs produced using the *in situ* method. ODA-rGO and OL-rGO both contain very little residual carbon to oxygen bonding indicating that reduction of GO to rGO during the reaction is almost complete. Instead a significant peak corresponding to carbon-nitrogen bonding is observed indicating that the functionalisers, ODA and OL are present on the final f-rGO This is justified by the fact that these materials both contain a significant N1s peak in their XPS spectra (N1s spectra and survey scans shown in Appendix D). The C1s spectrum of TOPO-rGO contains more residual oxygen content indicating that the TOPO may inhibit the reduction of GO to rGO slightly. Finally the C1s spectrum of TOP-rGO shows significant differences to the other C1s spectra reported here with a significant peak corresponding to C−OH bonding of equal intensity to that for C=C bonding as well as peaks corresponding to other oxygen functionality. This shows that *in situ* reduction and functionalisation of GO in TOP is significantly less effective than in other functionalising reagents. It is possible that the reason for this is the lower polarity of TOP than ODA, OL, or TOPO prevents it from solubilising polar GO leading to aggregation of sheets which would inhibit reduction.

In the case of ODA-rGO and OL-rGO the presence or absence of the N1s peak at 400 eV can also be instructive as it should be possible to observe the nitrogen atoms within the ODA and OL functionalising chains. This is particularly the case in *in situ* f-rGOs as their synthesis does not involve the use of hydrazine, which is known to inherently cause a degree of nitrogen functionalisation on the sheets of rGO produced so any nitrogen detected must arise from the functionalisers present on the graphene sheets.[386] As would be expected based on this reasoning the N1s peak has been observed in the XPS of ODA-rGO and OL-rGO but is absent in those of TOP-rGO and TOPO-rGO. N1s spectra for f-rGOs are shown in Appendix D. However, the lower intensity and symmetric nature of this peak means attempting to derive

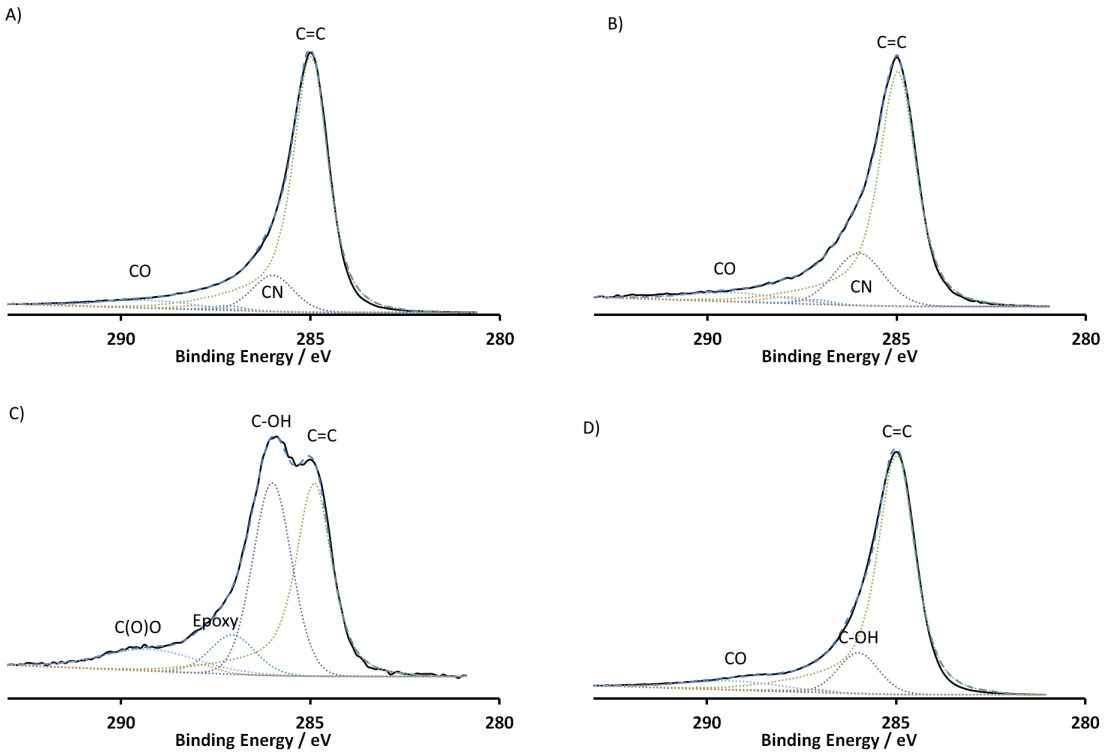

Figure 6.18: *A representative XPS C1s spectrum for A) ODArGO, B) OLrGO, C) TOPrGO, and D) TOPOrGO produced using the in situ method described here. These data show the C1s spectrum (black line), the fit envelope (blue dashed line) and the fitted component peaks (dotted lines).*

additional information through peak fitting is not possible.

Similarly, the presence of phosphorous in both TOP-rGO and TOPO-rGO means that the P2p peak should be detected in XPS at 133 eV for these materials. This peak is observed in the spectra for TOP-rGO and TOPO-rGO but is absent in the spectra for ODA-rGO and OL-rGO. P2p spectra for each of the f-rGOs can be found in Appendix D

These data correlate well with the expected chemical composition of all of the *in situ* f-rGOs and confirms that functionalisation has been successful.

6.3.2.1.2. UV-Vis Spectroscopy

In order to determine the degree of reduction achieved during the *in situ* reduction-functionalisation reactions the f-rGOs were dispersed into water before being analysed by UV-Vis spectroscopy (figure 6.19). From each spectrum produced the position of the $\pi \rightarrow \pi^*$ plasmon peak was analysed and are shown in table 6.7.

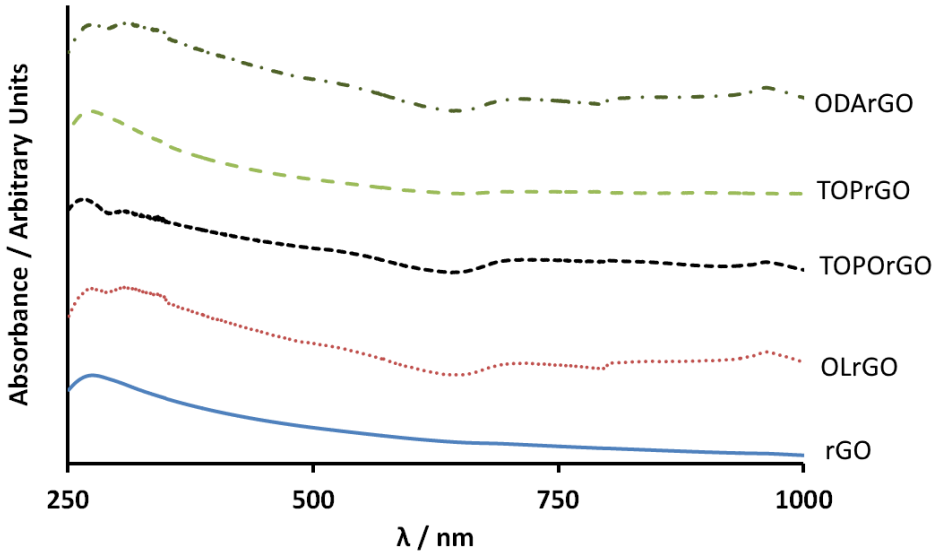

Figure 6.19: *UV-Vis spectroscopy of dispersions of in situ frGO functionalised by ODA, TOP, TOPO, and OL as well as unmodified rGO in water showing the position of the $\pi \rightarrow \pi^*$ plasmon peak.*

The f-rGOs produced using our *in situ* method all present peak positions of >265 nm indicting that the conjugated structure of the graphene sheets has been restored during the reaction. This is in contrast to the conventionally functionalised ODA-rGO produced by the

Table 6.7: *The position of the $\pi \rightarrow \pi^*$ plasmon peak in the UV-Vis spectra of dispersions of frGOs in water. Peak positions for GO and rGO are provided for comparison.*

	Position of $\pi \rightarrow \pi^*$ plasmon peak / nm
GO	230
rGO	270-300
ODArGO (conventional)	256
ODArGO (*in situ*)	266
OLrGO	276
TOPrGO	272
TOPOrGO	265

method of Jang *et al.* [380] which has a peak position of 256 nm (figure 6.13) indicating less restoration of the conjugated structure than was achieved using the *in situ* method.

The reason for this difference is believed to be a result of the order that reduction and functionalisation are performed in each method. The route of functionalisation used by Jang *et al.* to synthesise ODA-rGO involves the reduction of functionalised GO, and therefore it is believed that the presence of ODA chains on the surface of the graphene sheets will inhibit the ability of hydrazine to restore conjugation of GO and restore the sp^2 matrix within the graphene sheet. The *in situ* method proposed in this study involves a simultaneous reduction and functionalisation of GO and so reduction is not hindered by the presence of functional groups on the graphene sheets, allowing the conjugation to be restored more easily and with less hindrance.

6.3.2.1.3. TGA

Examination of the *in situ* f-rGOs by TGA allowed the thermal stability of the material produced to be determined, as well as giving an estimation of their degree of functionalisation. Thermal analysis profiles for *in situ* f-rGOs and rGO under a flow of nitrogen are shown in figure 6.20, along with their derivatives. Comparison of these data makes it clear that a significant mass loss occurs in all f-rGOs when heated above 200 °C which does not occur for unmodified rGO. This mass loss can be attributed to the removal of functional groups present on the surfaces of the rGO sheets and occurs in the temperature range of 200-600 °C. The mass loss in this region for each of the f-rGOs were calculated. Over this same region unmodified rGO displayed a mass loss of only 9.0 %, which allows a degree of

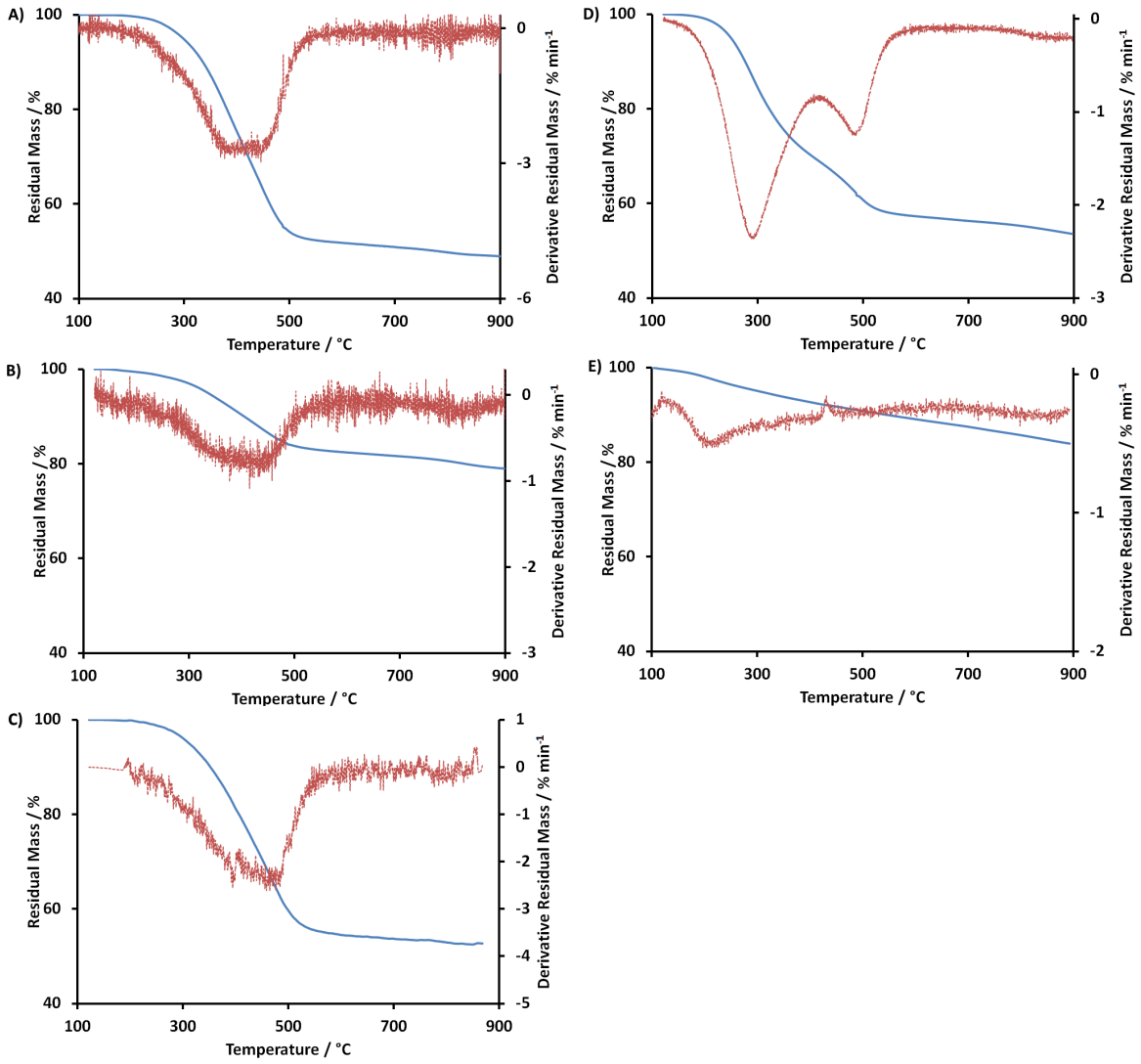

Figure 6.20: *TGA profiles for the heating of A) in situ ODArGO, B) in situ TOPrGO, and C) TOPOrGO, D) OLrGO, and E) rGO in helium between 100-900 °C showing the residual mass as a percentage of the mass at 120 °C (blue) and the derivative of this profile (red).*

functionalisation for f-rGOs to be approximated. These data are shown in table 6.8.

Table 6.8: *The degree of functionalisation, approximated by mass loss in TGA between 200-600 °C, for in situ f-rGOs functionalised using different reagents. *mass loss in TOPrGO may be partly due to the loss of residual oxygen content as well as functionalising TOP*

Functionaliser	Mass loss 200-600 °C / wt. %	% Functionalisation / wt. %	% Functionalisation / mol. %
unmodified rGO	9.0	-	-
ODA	47.9	38.9	2.84
TOP	17.0*	<8.0	<0.28
TOPO	41.8	32.8	1.52
OL	45.1	36.1	2.54

Comparing the degree of functionalisation of the ODA-rGO prepared using the *in situ*

method (38.9 wt. %) with that prepared by the method of Jang *et al.*,[380] described in section 6.3, of 36.5 wt. % shows that the *in situ* method of functionalising and reducing GO in one step can achieve similar, or even greater, degrees of functionalisation than methods conventionally used to functionalise GO whilst maintaining a simpler experimental protocol requiring fewer reaction steps and avoiding hazardous chemicals such as hydrazine.

Assessment of the degree of functionalisation of the remaining f-rGOs gave degrees of functionalisation of 32.8 wt. % and 36.1 wt. % for TOPO-rGO and OL-rGO respectively while TOP-rGO was calculated to have a degree of functionalisation of 8.0 wt. %. These data indicate that functionalisation of the graphene sheets has occurred with all functionalising agents, and under the conditions used the most effective functionalising agent is ODA, closely followed by OL both in terms of mass and molecular percent. By wt. % TOPO-rGO has a similar degree of functionalisation to other f-rGOs. However, the increased molecular mass of TOPO compared to ODA and OL means this represents a decrease in the degree of functionalisation of 46 % when using mol. %. The degree of functionalisation of TOP-rGO is the lowest of the f-rGOs produced at only 8 wt. % (which corresponds to only 0.28 mol. %). In addition the residual oxygen seen in the XPS C1s spectrum of TOP-rGO (figure 6.18) may also contribute significantly to this mass loss indicating the degree of functionalisation of this material is even lower than calculated. These results show that all methods of *in situ* functionalisation have an effect on graphene, although the effectiveness of the reaction is dependent upon the precise chemistry of the reagents used.

6.3.2.1.4. Solution State NMR

An interesting possibility, as a result of the presence of the phosphorous centre of TOP and TOPO, is to use ^{31}P NMR to characterise the by-products of the syntheses of TOP-rGO and TOPO-rGO. It is expected that, since the GO is reduced during the functionalisation reaction, changes in the oxidation state of TOP and TOPO will be observed. These changes are accompanied by large changes in chemical shift (figure 6.21) which can be easily observed and the transition from TOP to TOPO can be characterised by NMR. The use of phosphorous

NMR has an additional advantage in that phosphorous is a relatively uncommon element meaning that peaks from impurities or solvents are unlikely to be present in the spectra recorded making them easy to interpret. It should be noted that the exact chemical shifts of peaks in ^{31}P NMR are dependant upon hydrogen bonding and so many species will exhibit significantly different chemical shifts depending on solvents or other factors and so the position of peaks can not always be directly compared.[422]

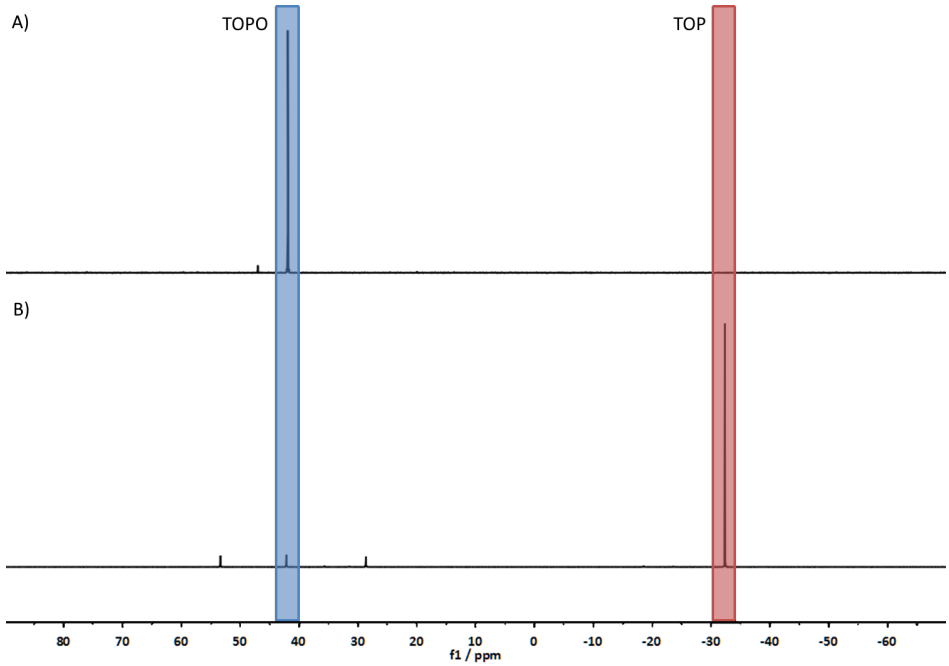

Figure 6.21: *Solution state ^{31}P NMR spectra for A) TOPO and B) TOP showing peaks corresponding to the P atoms in TOP at ∼−30 ppm, and TOPO at ∼40 ppm. Extra peaks present in spectrum B are as a result of impurities in the TOP received from Sigma Aldrich, in the form of partially oxidised trioctyl phosphines, including TOPO.*

Whilst it is also possible to use ^{1}H and ^{13}C NMR to study the f-rGOs produced the changes seen between the spectra of reagents and the by-products of the reactions are limited. This means that the use of NMR is limited when analysing GO functionalised by ODA or OL.

The first spectra recorded in this study were those for pure TOP and TOPO. These data are presented in figure 6.21 and show the significant chemical shift between the main peaks in the ^{31}P NMR spectra of TOP and TOPO with the peak for TOP occurring at −32 ppm, while the peak for TOPO is visible at 42 ppm. In both the spectra some low concentration impurities are present. These are accounted for by a range of oxidised octyl phosphine deriva-

tives. In TOPO (figure 6.21 A) the peak caused by impurities occurs at 47 ppm and is likely to be caused by the presence of *n*-octyl-di-*n*-octylphosphinate (ODOP) or di-*n*-octylphosphinic acid (DOPA) (figures 6.22 A and 6.22 B).[423] In the purchased TOP then 3 impurity peaks are observed which correspond to TOPO at 42 ppm, ODOP or DOPA at 53 ppm (figures 6.22 A and 6.22 B), and *n*-octylphosphinic acid (OPA), mono-*n*octylphosphinic acid (MOPA), or di-*n*-octylphosphine oxide (DOPO) at 28 ppm (figures 6.22 C to 6.22 E).[423]

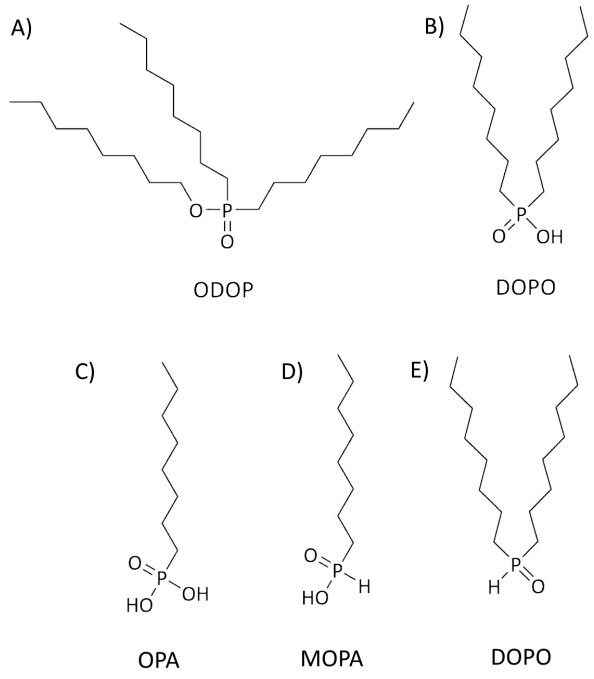

Figure 6.22: *Partially oxidised forms of TOP and TOPO.*

In order to isolate the by-products of the syntheses of TOP-rGO and TOPO-rGO the Soxhlet washings from these reactions (described in section 8.3.10) were evaporated to dryness, removing the toluene that had been used to wash the f-rGO. The residual material contained the by-products of the reaction and was a waxy white solid. This was then dissolved in d_8 toluene for analysis by NMR. Full details of this procedure are described in section 8.3.11.

To assess the impact of the GO present on the reaction described above, control experiments were also performed in which neat TOP and TOPO were heated under comparable conditions (section 8.3.12). The products of these control reactions where then prepared for analysis by NMR by dispersion in d_8 toluene by the method described above.

The ^{31}P NMR spectra from these samples are shown in figures 6.23 and 6.24. Examining the spectra for the by-products of the synthesis of TOP-rGO (figure 6.23 B) it is clear that a significant change has occurred during the reaction with the absence of a peak corresponding to TOP, at −32 ppm, after the reaction. There is however, a large peak present that corresponds to the P centre in TOPO, at 42 ppm, indicating, that as GO is reduced to rGO in the reaction TOP is simultaneously oxidised to TOPO. Also present in the spectrum of the products are peaks at 32 ppm and 54 ppm which correspond to other oxidation products of TOP, including those shown in figure 6.22 (ODOP and DOPA at 54 ppm with OPA, MOPA, and DOPO at 32 ppm). It is possible that some of these other oxidation products will functionalise the GO sheets during the reaction, however as these oxidation products will have similar solution chemistries to TOP and TOPO this should not impact on the behaviour of the f-rGO produced.

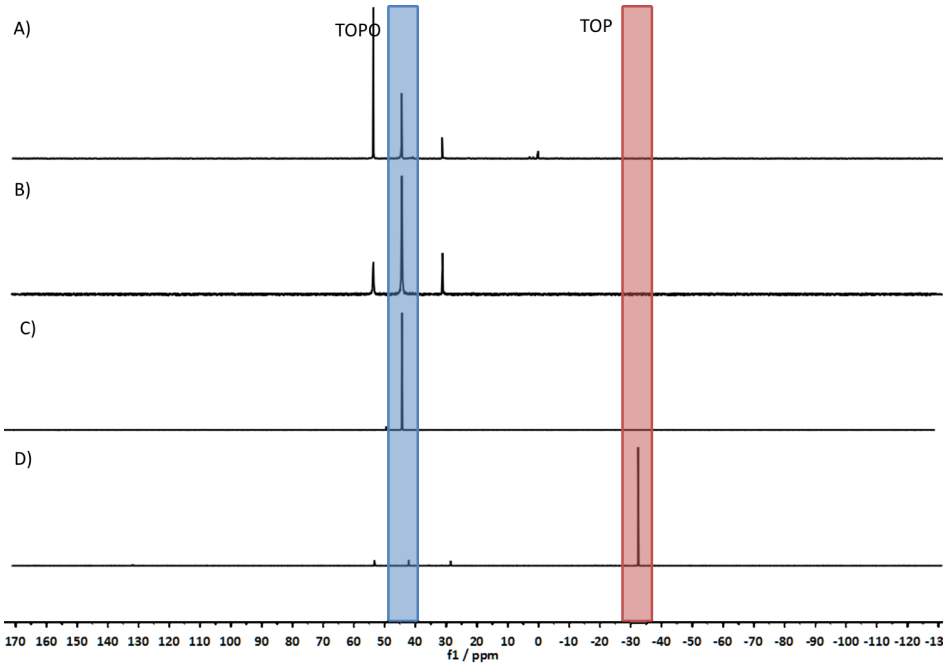

Figure 6.23: *Solution state NMR spectra of A) the products of the control reaction, heating TOP to 180 °C for 24 h, B)The by-products of the synthesis of TOPrGO, which involves heating TOP to 180 °C for 24 h, C) TOPO as received from Sigma Aldrich, and D) TOP as received from Sigma Aldrich. These spectra show that after heating, the peak from the spectrum of TOP (red region) has faded and been replaced by a peak in the same position as that in the spectrum of TOPO (blue region). 2 other peaks are also present which are believed to be alternative oxidation products of TOP (these peaks are also visible in A).*

Data from the control reaction, heating TOP in the absence of GO, is presented in fig-

ure 6.23 A and shows a similar absence of the TOP peak at −32 ppm with, instead a peak corresponding to TOPO present at 42 ppm. This shows that GO is not required for the oxidation of TOP to TOPO under the reaction conditions. This NMR spectrum also exhibits the same peaks for oxidised TOP (ODOP and DOPA at 53 ppm with OPA, MOPA, and DOPO at 28 ppm), meaning that the presence of GO is not essential for the synthesis of these by-products. However, it can be seen from figure 6.23 the presence of the GO does impact on the ratio of oxidation products observed.

A notable observation from these experiments is that before heating TOP is a colourless liquid, while TOPO is a white solid with a low melting point. However, after heating overnight both materials solidify, when cooled, as white solids. This correlates well with the NMR data described above showing that TOP is converted to TOPO in the course of the reaction.

Spectra produced from the by-products of synthesising TOPO-rGO are shown in figure 6.24 B. In this case there is little change between the reagents and products with the peak for TOPO, at 42 ppm present in the spectra for the starting material, the by-products of the functionalisation, and the control experiment: figures 6.24 A, 6.24 B and 6.24 D respectively. In all of these spectra the peak occurring at −32 ppm, corresponding to TOP is not observed. Peaks that arise from the by-products of the oxidation of TOP to TOPO are also not observed in any significant concentration after the heating of TOPO indicating that TOPO remains stable under the reaction conditions and does not form addition forms of oxidised TOP.

In this case, both the TOPO used as a reagent and the products of the reactions are white, waxy, low melting solids which correlates well with the lack of change recorded in the P NMR data.

^{1}H and ^{13}C NMR spectra were also recorded for all the materials tested above. However the presence of peaks for d_8-toluene and the similarity of the chemical environments of carbon and hydrogen in TOP and TOPO make these spectra much less informative than the ^{31}P spectra presented above. However, none of the spectra recorded contradict the conclu-

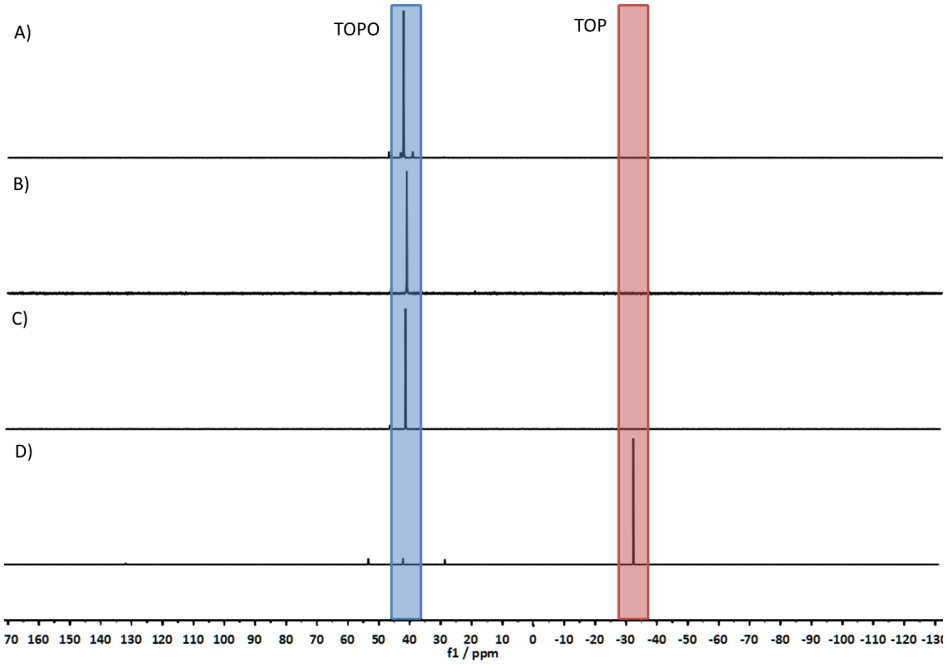

Figure 6.24: *Solution state NMR spectra of A) the products of the control reaction, heating TOPO to 180 °C for 24 h, B)The by-products of the synthesis of TOPOrGO, which involves heating TOP to 180 °C for 24 h, C) TOPO as received from Sigma Aldrich, and D) TOP as received from Sigma Aldrich. These spectra show little change occurs as a result of heating TOPO.*

sions drawn from the ^{31}P NMR data presented above. ^{1}H and ^{13}C NMR spectra are included in Appendix D.

6.3.2.1.5. TEM

In order to establish that neither the sonication nor the functionalisation procedure has an impact on the size, flatness and structure of the f-rGO sheets produced TEM was performed on the *in situ* produced f-rGOs. Representative micrographs for each of these materials are shown in figure 6.25. The material produced is observed to be composed of thin, flat sheets of around 1-3 µm across with a little crumpling or folding, especially around the edges. SAED was also performed on these materials and the patterns produced were indexed. All materials were observed to produce overlapping patterns of hexagonal spots, as is expected for graphitic materials. In some patterns these spots overlap, as a result of rotated, overlaying sheets, to form the rings seen in figures 6.25 A to 6.25 C. One thing to note from indexing these patterns is the absence of a $(0\,0\,2)$ peak arising from any of the f-rGOs. This implies that the materials are well exfoliated with no consistent interlayer spacing between sheets.

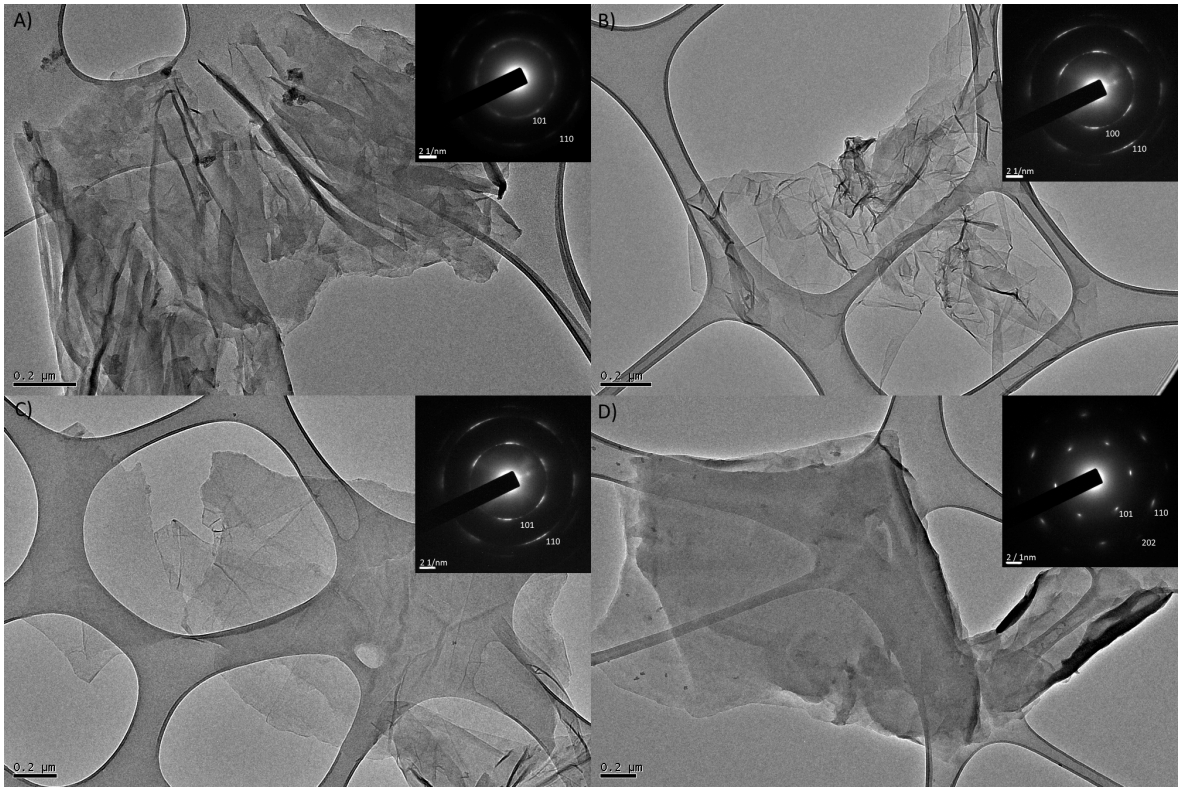

Figure 6.25: *TEM micrographs of representative sheets of A) in situ ODArGO, B) TOPrGO, C) TOPOrGO, D) OLrGO, with insets showing indexed SAED patterns from the same sheet. All samples show similar sheet sizes with no visible damage to sheets or agglomerated material.*

Comparing these micrographs with TEM of conventionally produced ODA-rGO, shown in figure 6.15, demonstrates that these materials appear to have a similar level of folding, thickness and sheet size.

6.3.2.1.6. Raman Spectroscopy

Raman spectroscopy was again utilised to investigate the sp^2 to sp^3 ratio of the f-rGOs produced. Examination of the *G* and *D* bands for each of the f-rGOs, and their relative intensities tells us about any changes in the number of defects in the materials relative to GO and rGO. Raman spectra of f-rGOs are shown in figure 6.26 along with $I_D : I_G$ ratios in table 6.9.

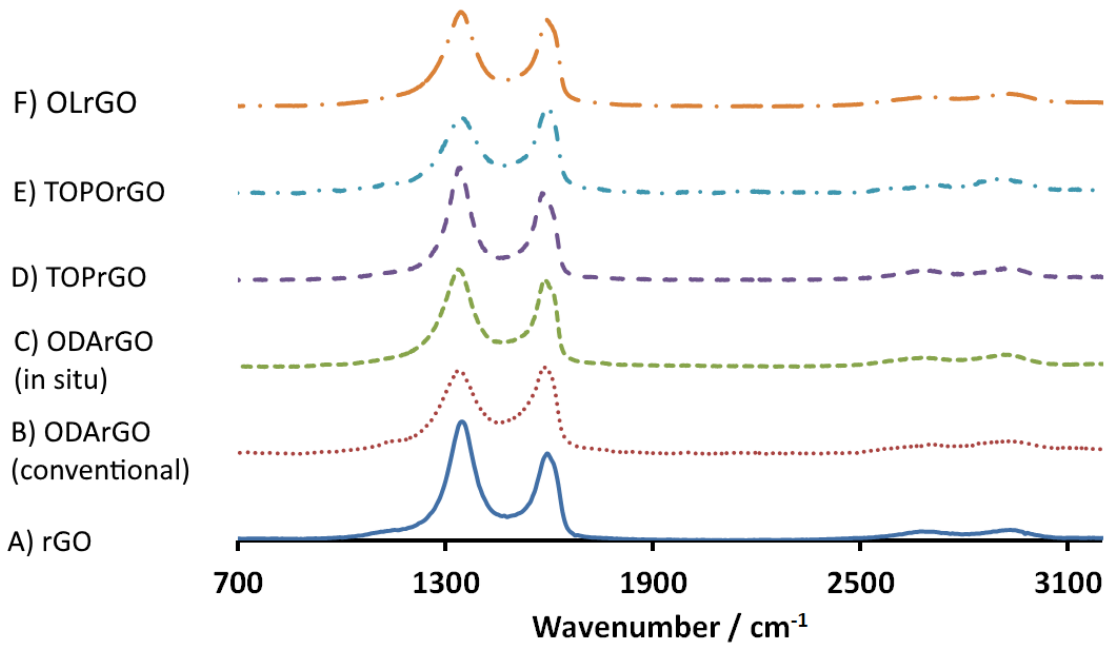

Figure 6.26: *Raman spectra of A) rGO and B-E) f-rGOs showing the presence of D (1350 cm^{-1}) and G (1595 cm^{-1}) bands in all materials as well as small 2D bands (∼2800 cm^{-1}). Intensities are normalised to the height of the G and spectra are vertically offset for clarity.*

Table 6.9: *The $I_D : I_G$ ratios derived from the Raman spectra of f-rGOs and rGO.*

Material	$I_D : I_G$ ratio
rGO	1.34 ± 0.01
ODArGO (Jang *et al.* 2014)	0.96 ± 0.02
ODArGO (*in situ*)	1.12 ± 0.01
TOPrGO	1.26 ± 0.02
TOPOrGO	0.87 ± 0.01
OLrGO	1.09 ± 0.00

Comparing these ratios to the degree of functionalisation of the f-rGOs derived from TGA (table 6.8) shows that TOP-rGO has both the lowest degree of functionalisation and the highest $I_D : I_G$ ratio of all the f-rGOs tested. C1s XPS for these materials also shows a difference between TOP-rGO and the other f-rGOs with TOP-rGO having a significantly higher content of C−OH bonds than any other f-rGO. This increase in the $I_D : I_G$, can be accounted for by residual oxygen content creating defects between a large number of small sp^2 domains. In other f-rGOs the sp^2 domains produced during reduction do not have as many edges (which are the origin of the *D* band) resulting in lower $I_D : I_G$ ratios.

6.3.2.2. Dispersion of in situ f-rGOs

As is the case with many graphene materials it is often instructive to examine changes in dispersibility as a method of assessing chemical changes. For this reason the dispersibility of the *in situ* f-rGOs, described above, was determined in each of the oils.

In order to create nanofluids, the f-rGOs were dispersed in the commercial oils provided by Shell Global Solutions. The procedure used is described in section 8.3.13 which created dispersions comparable to those of ODA-rGO produced above in section 6.3.1.2. Dispersions were allowed to settle overnight before being analysed in order to allow unstable particles of graphene materials to settle from the dispersion.

6.3.2.2.1. Dispersion of ODArGO

Dispersions of *in situ* ODA-rGO were analysed using UV-Vis spectroscopy in order to asses their concentration. Representative UV-Vis spectra for a dispersion in each oil is shown in figure 6.27 with the concentration of each dispersion shown in table 6.10 calculated using the Beer-Lambert law, taking the absorbance at 660 nm and α =3620 ml mg^{-1} m^{-1}.[364]

Comparing the concentrations of dispersions of *in situ* ODA-rGO with those of ODA-rGO produced using the method of Jang *et al.* [380] and with dispersions of rGO produced using hydrazine (figure 6.28) it is clear that these 3 materials all exhibit different solution chemistries.

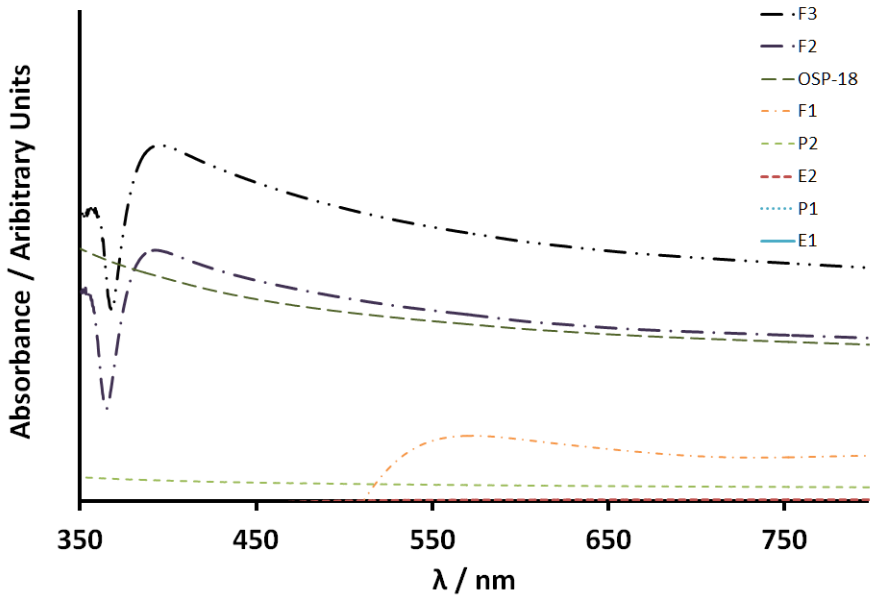

Figure 6.27: *UV-Vis spectroscopy of a dispersions of ODArGO in oils produced using our in situ, solvent-free reduction, functionalisation.*

Table 6.10: *The concentrations of in situ produced ODArGO dispersions in oils; determined by the Beer-Lambert law taking the absorbance from UV-Vis spectroscopy at 660 nm, α =3620 ml mg^{-1} m^{-1}.[364] The concentrations of comparable dispersions of hydrazine rGO are also included as well as the percentage change in concentration. The spectrum of F1 dropping below zero at approximately 500 nm is a result of the oil, F1, and is observed in the UV-Vis spectrum of the pure oil.*

Oil	ODArGO Concentration / µg ml^{-1}	rGO Concentration / µg ml^{-1}	Ratio of concentrations (ODArGO:rGO)
E1	0.0	5.9	0
E2	0.1	1.2	0.1
P1	0.0	0.2	0
P2	1.7	1.2	1.4
OSP-18	19.6	68.5	0.3
F1	5.9	2.0	3.0
F2	20.3	0.9	22.6
F3	29.3	60.9	0.5

As discussed in section 6.2.3 rGO exhibits the highest dispersibility in the most polar oils, OSP-18 and F3 with functionalisation of rGO with ODA using the method proposed by Jang *et al.* (section 6.3.1.2) causing the dispersibility to increase in almost all oils, due to the change of surface chemistry of the graphene sheets.

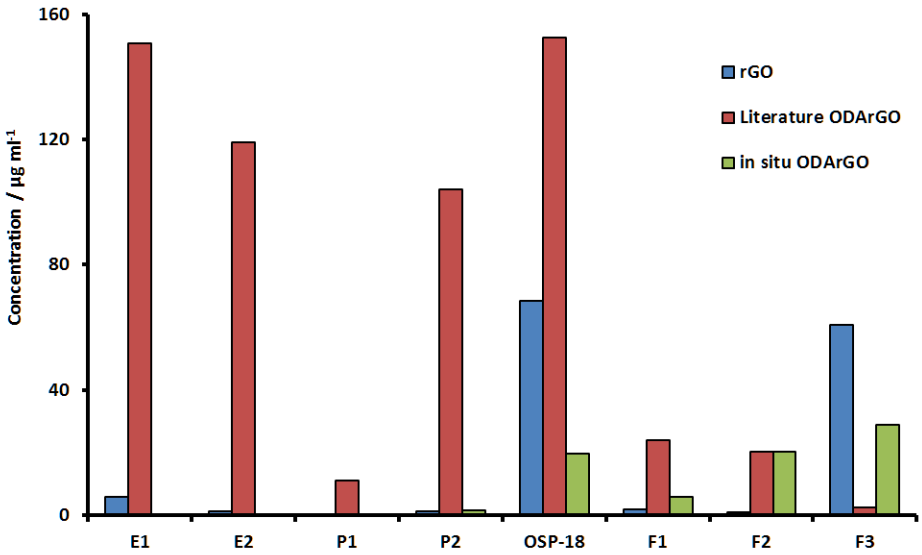

Figure 6.28: *A comparison of the concentrations of rGO produced using hydrazine (blue), ODArGO produced using the method of Jang et al.*[380] *(red), and in situ ODArGO (green) in oils, measured using UV-Vis spectroscopy and the Beer-Lambert law.*

Comparing these results with those recorded for *in situ* ODA-rGO shows again that the solution behaviour of this material differs from that of ODA-rGO prepared by the method of Jang *et al.*.[380] *In situ* ODA-rGO shows its highest dispersibility in OSP-18, F2, and F3, all of which have a significant polar component. It can therefore be surmised that, in spite of having a greater degree of reduction (by UV-Vis) and a greater degree of functionalisation (by TGA) that *in situ* ODA-rGO is more polar than ODA-rGO produced using the method of Jang *et al.*.[380]

In spite of the fact that the dispersions produced using *in situ* ODA-rGO had lower concentrations than those of conventionally produced ODA-rGO, significant differences in concentration can be seen between dispersions of *in situ* ODA-rGO and those of rGO. This shows, alongside the other characterisation techniques used, that *in situ* functionalisation and reduction has been successful and caused a change in the solution properties of ODA-rGO.

Therefore rGO functionalised using this *in situ* method of functionalisation, and the other functionalising agents described in section 6.3.2 was dispersed in the oils.

6.3.2.2.2. Dispersions of OLrGO in Oils

Dispersions of *in situ* OL-rGO in oils were produced as described in section 8.3.13 and analysed *via* UV-Vis spectroscopy. Spectra from dispersions in each of the oils are shown in figure 6.29 whilst concentrations of OL-rGO, determined using the Beer-Lambert law (taking the absorbance at 660 nm and α =3620 ml mg^{-1} m^{-1}),[364] are shown in table 6.11.

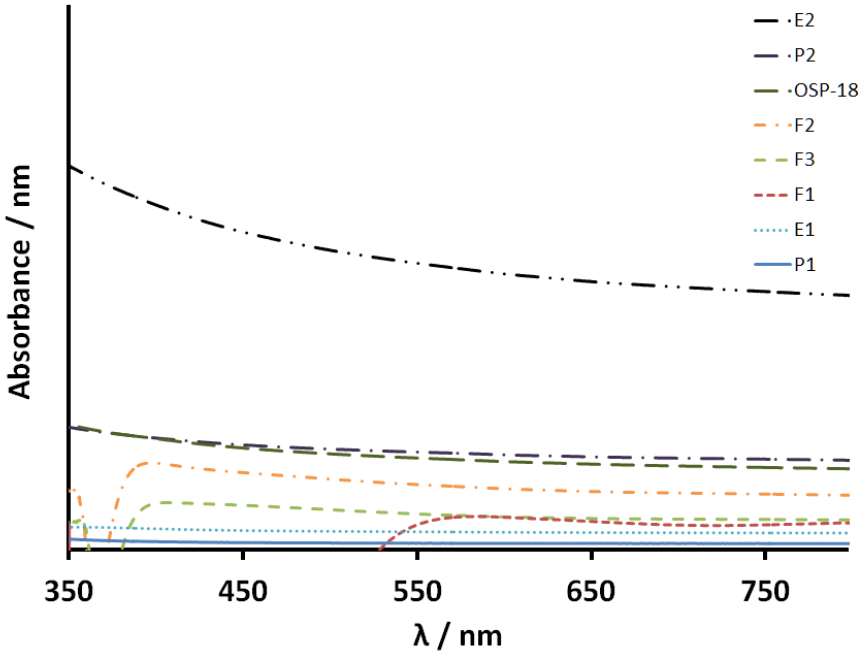

Figure 6.29: *UV-Vis spectroscopy of a dispersions of OLrGO in oils produced using our in situ, solvent-free reduction, functionalisation.*

These data show that functionalisation with OL once again changes the dispersion properties of the graphene sheets. Comparing the concentrations of dispersions of OL-rGO with those of unmodified rGO (figure 6.30) shows an increase in the concentration of the dispersions in a range of oils: in particular, E2, and P2 with some increase being seen in P1 and F2. These oils are some of the least polar of the selection of oils available and show that the functionalisation of of graphene sheets with OL has the effect of improving the compatibility of the sheets with non-polar solvents significantly. Similarly, the dispersibility of OL-rGO

Table 6.11: *The concentrations of in situ produced OLrGO dispersions in oils; determined by the Beer-Lambert law taking the absorbance from UV-Vis spectroscopy at 660 nm. The concentrations of comparable dispersions of hydrazine rGO are also included as well as the percentage change in concentration.*

Oil	OLrGO Concentration / μg ml^{-1}	rGO Concentration / μg ml^{-1}	Ratio of concentrations (OLrGO:rGO)
E1	2.2	5.9	0.4
E2	35.2	1.2	29.3
P1	0.8	0.2	4.0
P2	12.2	1.2	10.2
OSP-18	11.2	68.5	0.2
F1	3.6	2.0	1.8
F2	7.6	0.9	8.4
F3	4.1	60.9	0.1

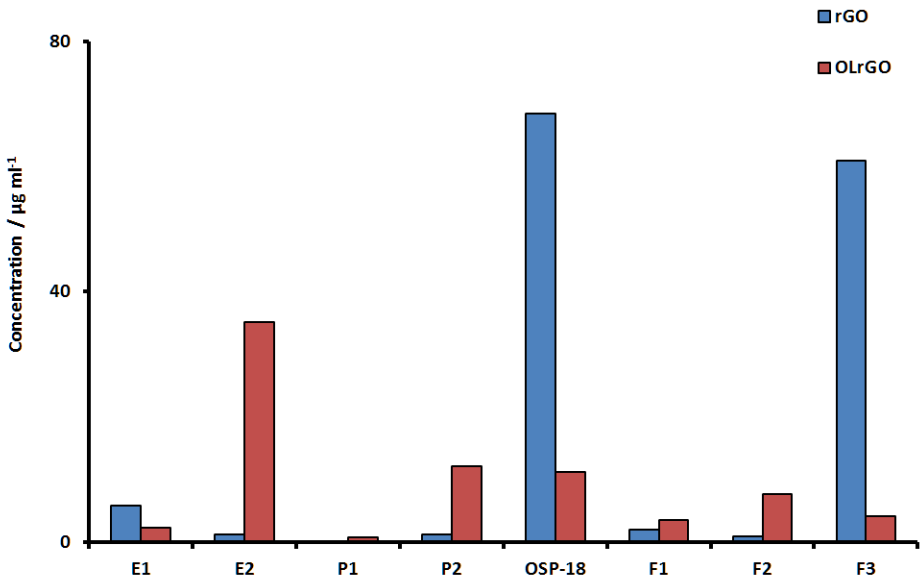

Figure 6.30: *A comparison of the concentrations of rGO produced using hydrazine (blue), and in situ OLrGO (red) in oils, measured using UV-Vis spectroscopy and the Beer-Lambert law.*

in the more polar oils such as OSP-18 and E1 shows a marked decrease when compared to that of unmodified rGO as a result of this functionalisation. It should be noted however, that high concentration dispersions were still not achieved in P1, which indicates that the chemistry of OL-rGO is still not a good match for that of this oil.

6.3.2.2.3. Dispersions of TOPrGO in Oils

As with OL-rGO and ODA-rGO, dispersions of TOP-rGO were analysed using UV-Vis spectroscopy with concentrations being determined by the Beer-Lambert law. Spectra from dispersions in each oil are shown in figure 6.31, with the concentrations derived from these spectra shown in table 6.12. The concentrations of the dispersions produced show that, as for the previously described reactions, the functionalisation of rGO with TOP causes marked changes in its dispersibility, with greatly improved concentrations being observed in dispersions using E1, E2, OSP-18, and F2 as solvents compared to dispersions of unmodified rGO.

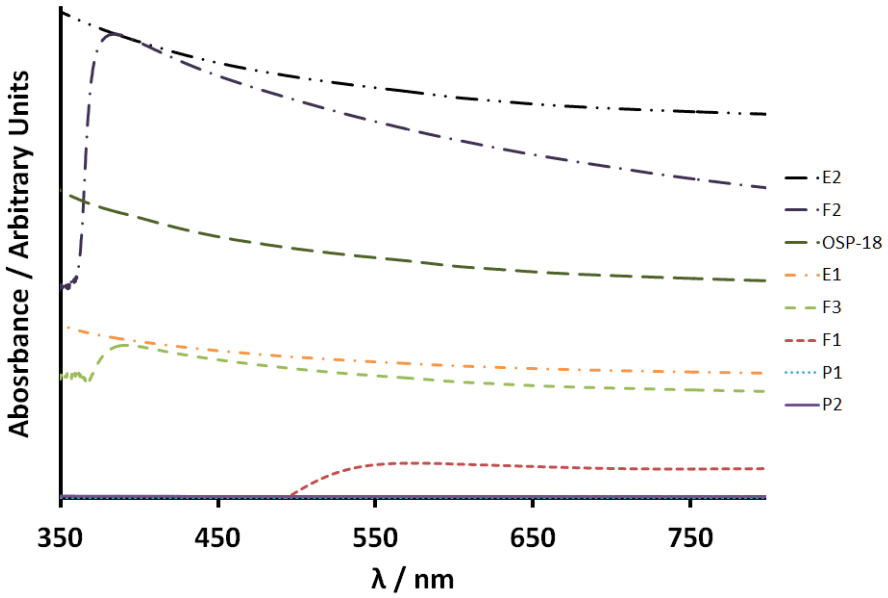

Figure 6.31: *UV-Vis spectroscopy of a dispersions of TOPrGO in oils produced using our in situ, solvent-free reduction, functionalisation.*

These changes in dispersibility indicate that the functionalisation of graphene sheets with TOP has the effect of improving their dispersibility in the more polar oils: those that are ester based and PAG based. This implies that the addition of the TOP functional groups to rGO has the effect of improving the compatibility of the graphene sheets with polar oils.

Table 6.12: *The concentrations of in situ produced TOPrGO dispersions in oils; determined by the Beer-Lambert law taking the absorbance from UV-Vis spectroscopy at 660 nm. The concentrations of comparable dispersions of hydrazine rGO are also included as well as the percentage change in concentration.*

Oil	TOPrGO Concentration / μg ml^{-1}	rGO Concentration / μg ml^{-1}	Ratio of concentrations (TOPrGO:rGO)
E1	52.3	5.9	8.9
E2	163.8	1.2	135.8
P1	0.0	0.2	0
P2	0.7	1.2	0.6
OSP-18	90.4	68.5	1.3
F1	12.7	2.0	6.4
F2	138.0	0.9	153.3
F3	45.3	60.9	0.7

This result correlates well with observations made from XPS (section 6.3.2.1.1) showing TOP-rGO to have a significantly higher content of residual oxygen functionality, due to incomplete reduction, than other f-rGOs which will increase the polarity of the graphene sheets and their compatibility with polar oils. The presence of TOP may hinder the interactions between these residual OH groups and the oil as TOP is expected to bind to the graphene sheets at its phosphorous centre leaving its non-polar octyl chains to interact with the oils. Another factor that must be taken into account is that the degree of functionalisation achieved for the synthesis of TOP-rGO, when measured by TGA (section 6.3.2.1.3) is only 8 % compared to >30 % for the other f-rGOs produced.

This would mean that the solvent oil molecules would have much greater access to the surface of TOP-rGO than in other f-rGOs allowing them to interact with residual, polar, oxygen functionalities present after the reduction of GO and thus increasing the compatibility of TOP-rGO in the polar oils as is observed.

6.3.2.2.4. Dispersions of TOPOrGO in Oils

Once again, the TOPO-rGO produced using the *in situ* reduction and functionalisation method was dispersed into the oils provided in order to establish the effect of this modification on the dispersion properties of the functionalised graphene.

The dispersions obtained were analysed using UV-Vis spectroscopy (figure 6.33) and then

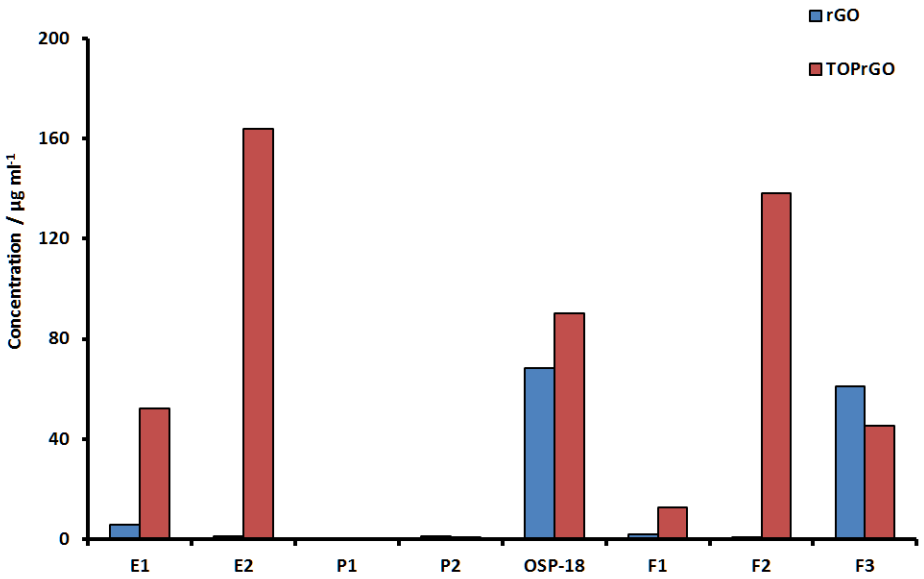

Figure 6.32: *A comparison of the concentrations of rGO produced using hydrazine (blue), and in situ TOPrGO (red) in oils, measured using UV-Vis spectroscopy and the Beer-Lambert law.*

their concentrations were determined using the Beer-Lambert law. These concentrations are shown in table 6.13 and show that functionalisation with TOPO has the effect of increasing the dispersibility, compared to that of unmodified rGO, of the functionalised graphene in ester based oils, E1 and E2. Little effect was seen on the dispersibility of this material in PAO based oils, P1 and P2, and a decrease in dispersibility was recorded in the PAG based oil, OSP-18. In the formulated oils, then an increase in concentration is recorded in the least polar oil mix, F1, with a decrease in concentration, relative to that of unmodified rGO, being observed in more the more polar mix F3.

Table 6.13: *The concentrations of in situ produced TOPOrGO dispersions in oils; determined by the Beer-Lambert law taking the absorbance from UV-Vis spectroscopy at 660 nm. The concentrations of comparable dispersions of hydrazine rGO are also included as well as the percentage change in concentration.*

Oil	TOPOrGO Concentration / µg ml^{-1}	rGO Concentration / µg ml^{-1}	Ratio of concentrations (TOPOrGO:rGO)
E1	30.7	5.9	5.2
E2	12.8	1.2	10.7
P1	0.32	0.2	1.6
P2	2.1	1.2	7.8
OSP-18	5.7	68.5	0.1
F1	11.4	2.0	5.7
F2	4.4	0.9	4.9
F3	3.1	60.9	0.1

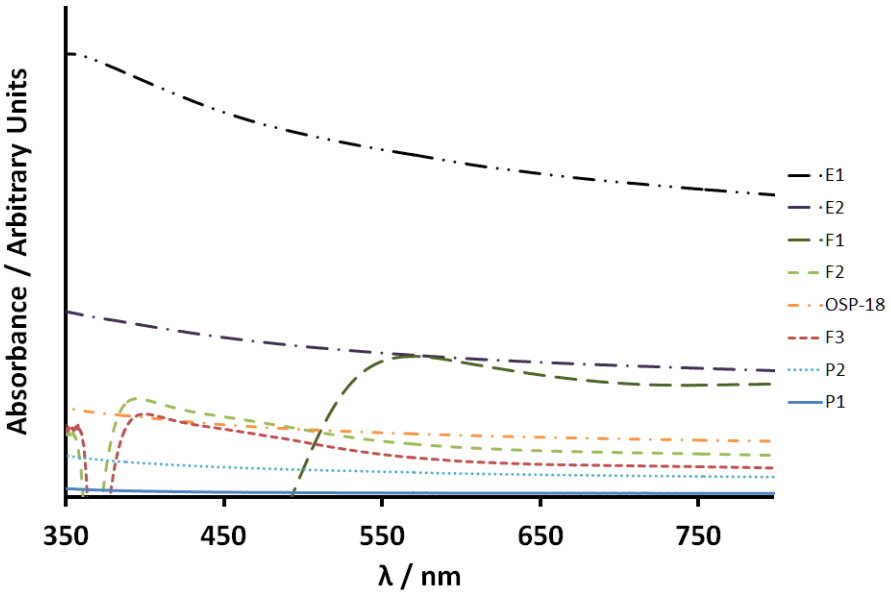

Figure 6.33: *UV-Vis spectroscopy of a dispersions of TOPOrGO in oils produced using our in situ, solvent-free reduction, functionalisation.*

These data indicate that TOPO-rGO has the best compatibility with oils with mid-polarity. This is likely to be due to the presence of the 3 octyl groups on each functionalising molecule of TOPO restricting the access of solvent oil molecules to the residual polar groups on the surface of the TOPO-rGO sheets occurring as a result of the reduction of GO,. However, the relative short length of these chains compared to the 18 carbon chains in ODA or OL means that the decrease in polarity of the f-rGO sheets is not as severe as is seen for ODA-rGO or OL-rGO. This gives the TOPO-rGO an intermediate polarity between that of unmodified rGO and that of ODA-rGO and OL-rGO. This explains the decreased dispersibility of this material in the most polar oil, OSP-18 although its dispersibility does increase in the relatively polar ester based oils E1 and E2. This change in surface chemistry is still not sufficient to cause TOPO-rGO to be easily dispersed in the least polar PAO oils, P1 and P2.

6.3.2.2.5. Comparison of Dispersion Concentrations

Whilst the concentration of dispersions of f-rGOs in oils has been discussed above in the context of the changing surface chemistry of f-rGO due to its modification, the goal of this work is to produce high concentration nanofluids for use as lubricants. To this end, the absolute concentrations of f-rGOs are compared in figure 6.35. The aim of producing

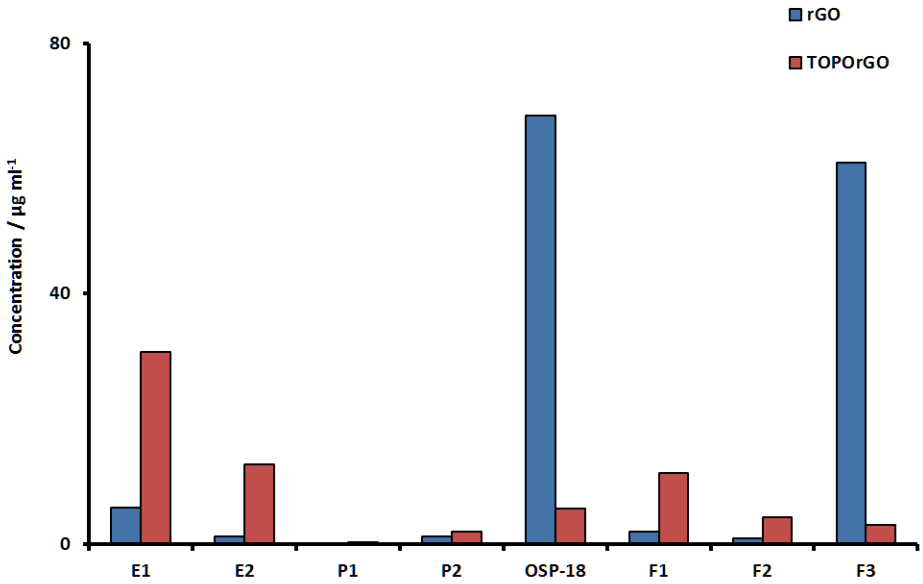

Figure 6.34: *A comparison of the concentrations of rGO produced using hydrazine (blue), and in situ TOPOrGO (red) in oils, measured using UV-Vis spectroscopy and the Beer-Lambert law.*

nanofluids is to improve the tribological properties of the lubricants through the addition of graphene based additives and it is believed that higher concentrations of additive will have greater effect on the tribological properties of the nanofluids. Therefore those combinations of f-rGO and oil that produce dispersions of the highest concentration will be most desirable.

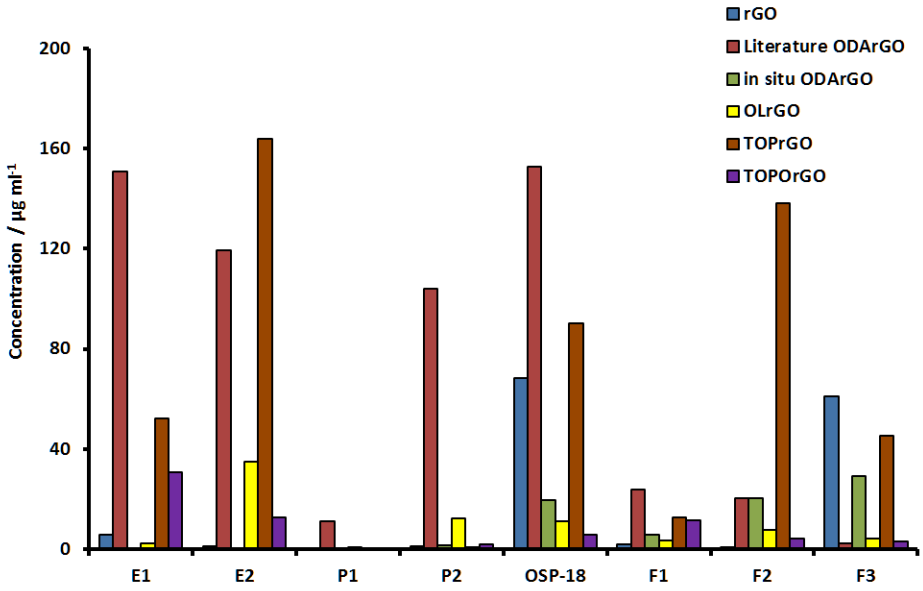

Figure 6.35: *Comparison of the concentrations of dispersions of f-rGOs in each of the oils.*

Due to the large number of combinations of oils and f-rGOs and the volume of each nanofluid required to properly analyse its properties, only those combinations that pro-

duced the highest concentration dispersions were selected to have their tribological properties tested.

Tribological testing required a larger volume of each nanofluid than was produced to test the concentration. However, due to the limited volume at which probe sonication is effective, scale-up was achieved by production of 25 ml batches of nanofluid, as described in section 8.3.5, which were then combined until 250 ml of nanofluid had been produced.

Those dispersions selected for tribological testing included: control dispersions of unmodified, hydrazine rGO in each of the oils, as well as those dispersions of f-rGO, both produced *in situ* and by the method of Jang *et al.*, which exhibited the highest concentrations and best stability as described in section 6.3.2.2. The combinations of f-rGO and oil that were scaled up for tribological testing are shown in table 6.14

Table 6.14: *The combinations of oils and f-rGO additives that were selected for further tribological testing based on the concentrations and stabilities of the dispersions produced.*

Oil	rGO	Conventional ODA-rGO	*in situ* ODA-rGO	OL-rGO	TOP-rGO	TOPO-rGO
E1	✓	✓	✗	✗	✓	✗
E2	✓	✓	✗	✓	✓	✓
P1	✓	✗	✗	✓	✗	✓
P2	✓	✗	✗	✗	✗	✗
OSP-18	✓	✓	✓	✓	✓	✓
F1	✓	✗	✗	✗	✗	✗
F2	✓	✗	✓	✓	✓	✗
F3	✓	✗	✓	✓	✓	✗

6.4. Properties of Nanofluids

Given the successful synthesis of graphene based nanofluids using both conventionally produced and *in situ* f-rGOs it is important to establish whether the presence of the graphene based additives has an effect on the properties of the nanofluids that are key to their desired application. In our case we are most interested in the use of nanofluids as functional lubricants in automotive engines and so the tribological properties of the lubricants are those that will be studied.

6.4.1. Tribological Properties

In order to assess the changes in the friction and wear properties of the nanofluids produced the coefficient of friction and viscosity of these fluids were measured and compared to those of the unmodified oils. Whilst viscosity does not directly impact on the performance of of the lubricant, it can cause changes in the coefficient of friction of the fluid. The coefficient of friction is the property that has the greatest impact on the performance of a lubricant as this determines the fraction of the energy that must be used to overcome internal friction. The lower the coefficient of friction of the lubricant, the less energy is required to overcome friction. As such decreasing the coefficient of friction of a lubricant is desirable.

The tribological properties of the nanofluids were measured in conjunction with Shell Global Solutions in Hamburg. The techniques used are described in detail in chapter 4.

6.4.1.1. Viscosity of Nanofluids

Initial testing of the properties of the nanofluids focussed on viscosity. Control of viscosity is an essential part of the formulation of lubricants as changes in viscosity can cause significant changes in the other tribological properties of the lubricant such as coefficient of friction. Ideally the use of a modifier should not change the viscosity of the oil whilst still decreasing its coefficient of friction in order to improve the performance of the lubricant.

It is also essential to examine changes in viscosity at different temperatures and shear rates as the addition of solid additives, even at the nanoscale, can cause properties such as shear thinning and shear thickening to change as well as the relationship between temperature and viscosity to be modified.

6.4.1.1.1. Kinematic Viscosity

The simplest measure of viscosity for nanofluids is the kinematic viscosity (V_K), discussed in detail in section 4.3.1. This was measured according to the ASTM standards: D445-06,

and D446-07.,[400,401] as described in section 8.1.9, at both 40 °C and 100 °C, which represent temperatures close to the lower and higher extremes of engine operating temperature. The kinematic viscosities of the pure oils were measured at 40 °C and 100 °C to give V_K 40 and V_K 100 respectively and these data are shown in table 6.15.

Table 6.15: *The viscosity of pure oils at 40 °C and 100 °C.*

Oil	Type	V_K 40 / cSt	V_K 100 / cSt
E1	Base	3.20	1.30
E2	Base	5.50	1.80
P1	Base	5.40	1.70
P2	Base	30.70	5.80
OSP-18	Base	19.30	4.00
F1	Formulated	156.30	35.50
F2	Formulated	70.34	19.00
F3	Formulated	28.35	9.05

The oils provided by Shell Global Solutions have a range of viscosities with F1 being the most viscous at 156.3 cSt at 40 °C and the least viscous being E1 at 100 °C with a kinematic viscosity of 1.3 cSt. Universally across all oils it is notable that the V_K 100 is significantly lower than the V_K 40. This is the expected behaviour for viscosity with temperature and this should be compared to the change in viscosity with temperature that occurs when graphene additives are combined with the oils to establish if the addition of graphene has any significant impact on this relationship.

In order to establish the effect of graphene on the viscosity of the base oils the dispersions of hydrazine rGO, produced as described in sections 8.3.5 and 8.3.9, were analysed and their V_K 40 and V_K 100 were determined. These values are presented in table 6.16 alongside the concentrations of each dispersion and the percentage change in viscosity compared to that of the neat oils.

The results presented here were somewhat unexpected and show markedly different behaviour between base oils and the fully formulated oils. Base oils show small changes in kinematic viscosity as a result of the addition of rGO (error on measurement is $\sim 1\,\%$) at either 40 °C or 100 °C. However, much larger changes are observed in the kinematic vis-

Table 6.16: *The viscosity of dispersions of hydrazine rGO at 40 °C and 100 °C, alongside their concentrations and the percentage change in viscosity compared to neat oils.*

Oil	rGO Concentration / μg mL^{-1}	V_K 40 / cSt	% Change	V_K 100 / cSt	% Change
E1	5.9	3.19	-0.3	1.27	-2.3
E2	1.2	5.27	-4.2	1.84	2.2
P1	0.2	5.21	-3.5	1.72	1.2
P2	1.2	30.75	0.2	5.82	0.3
OSP-18	68.5	19.53	1.2	4.20	5.1
F1	2.0	109.30	-30.1	25.37	-28.5
F2	0.9	49.32	-29.9	13.77	-27.5
F3	60.9	20.24	-28.6	6.54	-27.7

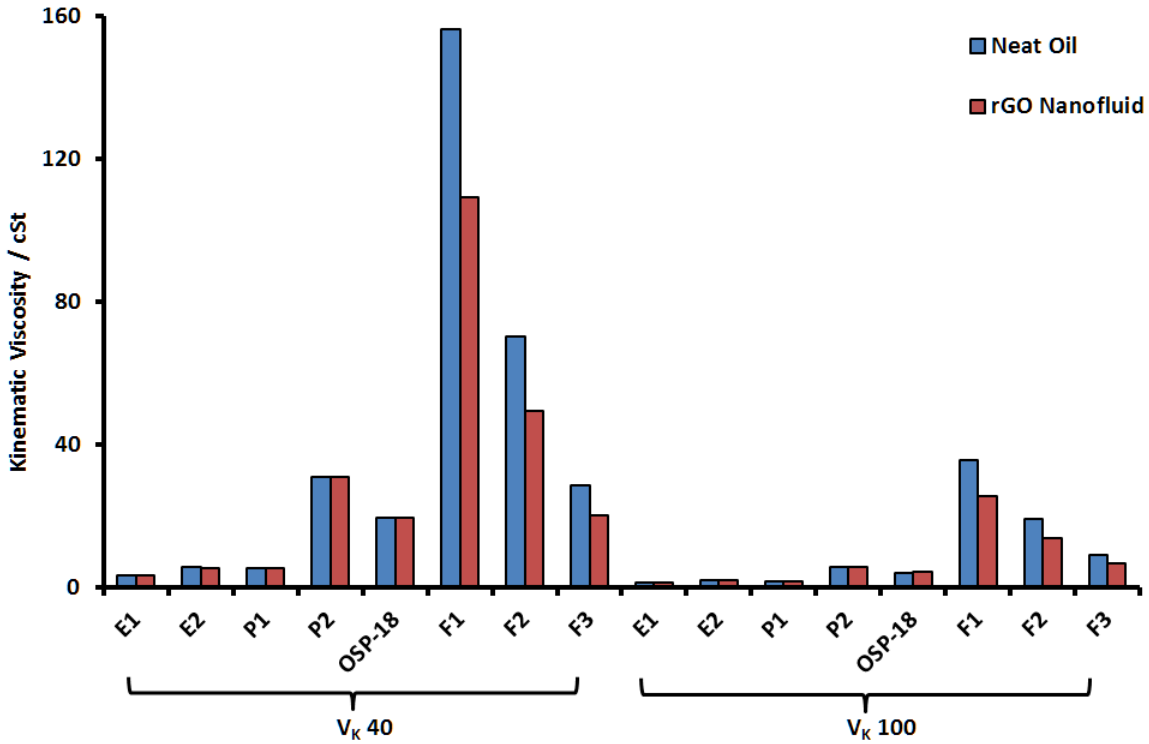

Figure 6.36: *The kinematic viscosities of neat oils (blue), compared with those of rGO oil nanofluids (red) at 40 °C and 100 °C.*

cosities of fully formulated oils as a result of the formation of rGO nanofluids with a $\sim$30 % decrease in V_K 40 and a $\sim$28 % decrease in V_K 100 observed.

There seems to be little correlation between viscosity and concentration of rGO. The implication of this is that any changes in viscosity observed are more likely to be due to the processing used to form the nanofluids than the presence of the rGO. We hypothesise that the this change in properties may be due to the high-energy ultrasonication used to produce nanofluids and that this process may be degrading some component of the oil, causing this change in viscosity observed.

In order to test this hypothesis the neat formulated oils were sonicated without the presence of graphene. 25 ml batches of neat oils were probe sonicated for 20 minutes, as described in section 8.3.14, and this process was repeated in order to produce the 250 ml of oil required for viscosity testing. The kinematic viscosities of these sonicated oils were measured at Shell Global Solutions at 40 °C and 100 °C and it can be assumed that any change in viscosities observed in these samples are due to the processing the samples have undergone as this has been the only change.

V_K 40 and V_K 100 for sonicated base oils are presented in table 6.17 and figure 6.37. This clearly shows that once again there is a marked difference between the viscosities of the sonicated and unsonicated oils, of around 20 % at 40 °C and 18 % at 100 °C.

Table 6.17: *The viscosity of sonicated, neat, formulated oils at 40 °C and 100 °C, alongside the percentage change in viscosity compared to unsonicated oils.*

Oil	V_K 40 / cSt	% Change	V_K 100 / cSt	% Change
F1	122.80	-21.4	28.20	-20.7
F2	56.98	-19.0	15.80	-16.8
F3	23.66	-16.5	7.60	-16.0

Across all three formulated oils at both 40 °C and 100 °C it can be seen from figure 6.37 that the viscosity of the unprocessed oil is the highest, followed by that of the pure oil that has been sonicated, and finally that of the rGO nanofluid being the lowest. It is clear from the change in viscosity observed between the untreated oils and those that have been son-

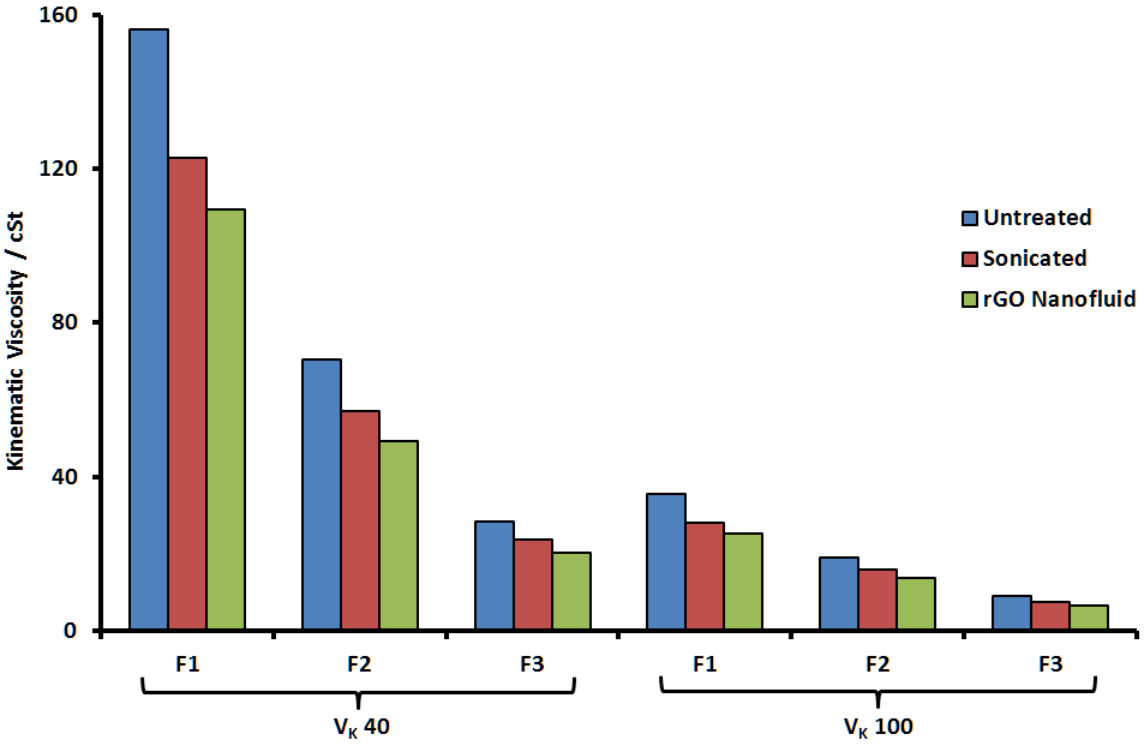

Figure 6.37: *The kinematic viscosities of formulated oils with no processing, that have been sonicated, and of rGO nanofluids at 40 °C and 100 °C.*

icated that the process of sonication is causing this change in viscosity, as this is the only change between the samples. It is our hypothesis that this is due to break-up of viscosity modifiers that are present in the fully formulated oils. These modifiers consist of short chain polymers and sonication has been shown to be able to cause decomposition of similar molecules.[424,425] This hypothesis is further confirmed by the fact that these drops in viscosity after sonication are not seen in dispersions in base oils, which do not contain these viscosity modifiers.

It is also noted from the data in figure 6.37 that, while a reduction in kinematic viscosity of the sonicated oils is observed, this decrease is not as large as the decrease observed for the rGO nanofluids. The reason for this has not been established, as the conditions used to generate both samples were the same, but it is possible that the rGO present in the nanofluid acts to increase the degree of decomposition of the viscosity modifier or that some of the viscosity modifier binds to the surface of the rGO sheets meaning it cannot impact on the viscosity of the oil.

Following on from the results described above for nanofluids containing rGO it was necessary to analyse the impact that the use of the f-rGOs, described in section 6.3.2, on the viscosity of the nanofluids produced using them. The combinations of oil and nanofluid selected, described in section 6.3.2.2.5, were analysed by Shell Global solutions in the manner described in section 8.1.9 in order to determine their V_K 40 and V_K 100. This gave us a dataset containing a large number of variables, with dispersions of different f-rGOs in different fluids all at different concentrations measured at both 40 °C and 100 °C. These data are presented in table 6.18.

Table 6.18: *The kinematic viscosities (V_K 40 and V_K 100) of nanofluids in a range of base oils containing different frGO additives along with the percentage difference between these viscosities and those of the pure fluids.*

Additive	Oil	f-rGO Concentration / µg ml^{-1}	V_K 40 / cSt	% Change	V_K 100 / cSt	% Change
Conventional ODArGO	E1	150.8	3.35	4.7	1.33	2.3
	E2	122.6	5.57	1.3	1.98	10.0
	OSP-18	157.1	20.58	6.6	4.49	12.1
In situ ODArGO	OSP-18	19.6	19.3	-0.1	4.17	4.3
	F2	20.3	51.19	-27.2	14.25	-25.0
	F3	29.3	20.28	-28.47	6.54	-27.73
OLrGO	E2	35.3	5.28	-4.0	1.85	2.8
	P1	0.8	5.21	-3.5	1.72	1.2
	OSP-18	11.2	19.29	-0.1	4.17	4.2
	F2	7.6	51.08	-27.4	14.23	-25.1
	F3	4.1	20.17	-28.9	6.51	-28.07
TOPrGO	E1	52.5	3.2	0.0	1.27	-2.3
	E2	159.1	5.32	-3.3	1.86	3.3
	OSP-18	96.3	19.44	0.7	4.21	5.2
	F2	138.0	51.04	-27.4	14.22	-25.2
	F3	49.2	19.38	-31.6	6.27	-30.7
TOPOrGO	E2	12.8	5.27	-4.2	1.84	2.2
	P1	0.3	5.20	-0.2	1.72	0.0
	OSP-18	5.7	19.3	-0.3	4.16	4.1

Given the discrepancy observed in the behaviours of the viscosities of the base oils compared to the fully formulated oils observed with rGO also appears to be present with the f-rGOs the data for the base oils was analysed separately from that for the fully formulated oils. Taking the data for the base oils first, the first factor considered was whether there is a link between the concentration of f-rGO in the dispersions and their change in viscosity. In

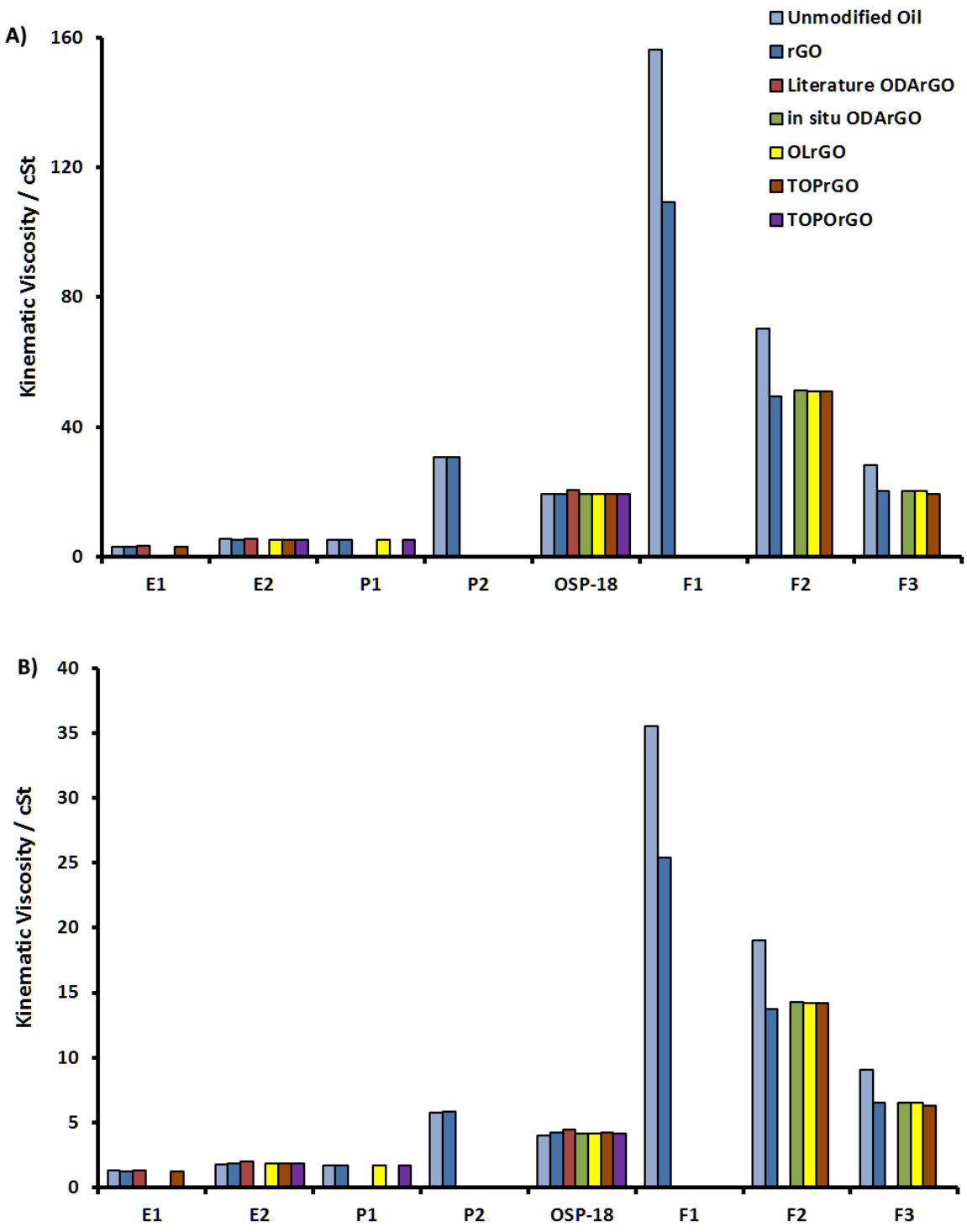

Figure 6.38: *The kinematic viscosities of unmodified oils and f-rGO oil nanofluids as A) 40 °C, and B) 100 °C.*

order to analyse this, the concentration of dispersions was plotted against the percentage change in viscosity when compared to the untreated, neat base oil. These data are presented in figure 6.39 for both V_K 40 and V_K 100 and from this chart it is clear that there is no correlation between the change in viscosity of a nanofluid and its concentration. In addition it is also notable that the magnitudes of the changes in viscosity observed for the base oil nanofluids are small. As above, this is a desirable result as for the most usable nanofluids, as they should have similar viscosities to the original solvent, but with modified tribological properties.

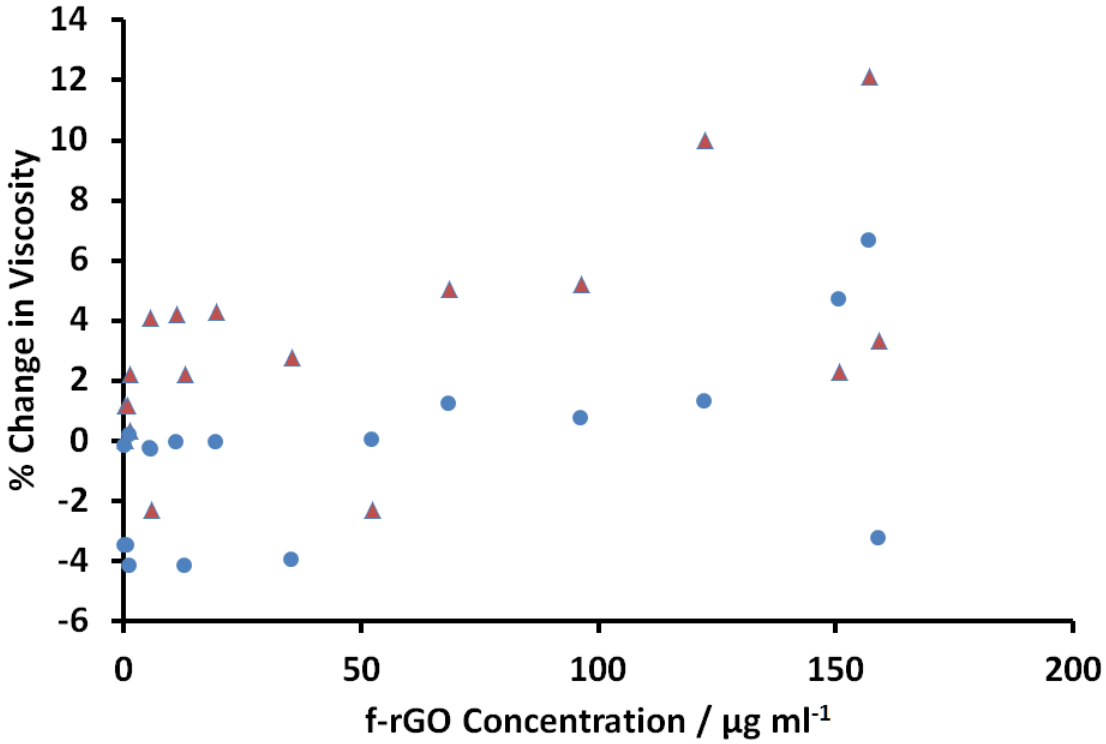

Figure 6.39: *A chart to show the lack of correlation between the concentration of f-rGO nanofluids and the percentage change in kinematic viscosity compared to that of the pure oil. The chart shows data for both V_K 40 (blue circles) and V_K 100 (red triangles).*

Again, mirroring the results observed for nanofluids containing rGO, those produced using f-rGOs in fully formulated oils had a much more pronounced change in viscosity than those utilising base oils. The kinematic viscosity data for these nanofluids is plotted in figure 6.40 against the concentration of f-rGO in the nanofluid and as was the case for all previous dispersions there appears to be no clear correlation between the concentration of nanofluids and their kinematic viscosity. The fact that nanofluids produced using f-rGOs and

formulated oils shows the same decrease in viscosity as mentioned above for other nanofluids produced using formulated nanofluids. This behaviour is what would be expected if the hypothesis regarding the decomposition of polymer viscosity modifiers present in the formulated oils due to sonication is correct.

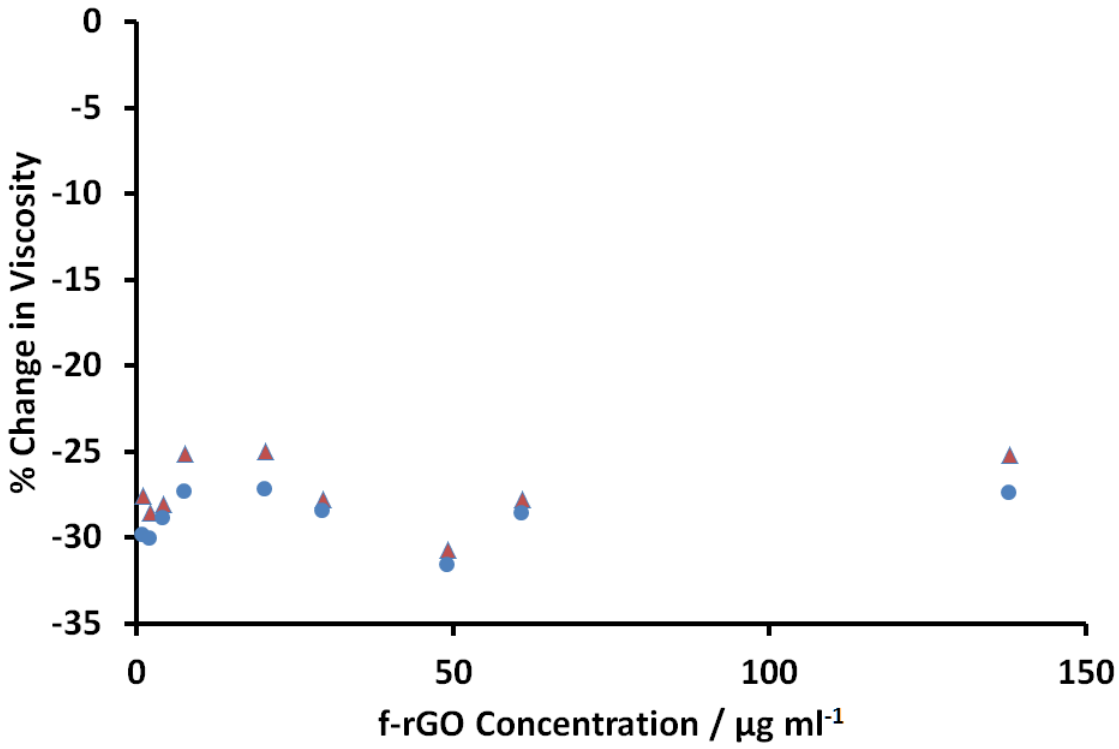

Figure 6.40: *A chart to show the lack of correlation between the concentration of f-rGO nanofluids in formulated oils and the percentage change in kinematic viscosity compared to that of the pure oil. The chart shows data for both V_K 40 (blue circles) and V_K 100 (red triangles).*

6.4.1.1.2. Dynamic Viscosity

In order to better understand the changes that the oils undergo during sonication and the preparation of nanofluids it was decided to analyse the high shear viscosities of the sonicated oils compared to the unmodified oils. In order to obtain these data the oils were analysed using a USV. This process is described in detail in section 4.3.2. The formulated oils are known to be non-Newtonian, exhibiting shear thinning as a result of the viscosity modifiers used and so it would be expected that this behaviour would be altered as a result of damage to these additives.

High-shear viscosity was recorded at shear rates of 1×10^6-1×10^7 s^{-1} at temperatures

of 100 °C, 120 °C and 150 °C and it was expected that degradation of the viscosity modifiers would alter the results compared to those of the unmodified oils.

As can be seen in figure 6.41 the process of sonicating the formulated oils has no significant effect on their dynamic viscosity in spite of the changes in kinematic viscosity observed. Small differences between the sonicated and unsonicated samples can be attributed to variation between repeat measurements and are not significant.

These results were somewhat unexpected as if the change in kinematic viscosity, described above, was due to a complete breakdown of the viscosity modifying additives then this would also be likely to cause a change in dynamic viscosity. It is believed that the reason for this disparity is that sonication of the formulated oils will cause the majority, but not all, of the viscosity modifier to break down. As the concentration of modifier required to effect a change on the kinematic viscosity is far lower than that to cause a change in the dynamic viscosity, this residual modifier will be sufficient to maintain the dynamic viscosity of the oils even though a significant change is observed in the kinematic viscosity of the same oils.

USV data were not recorded for the base oils as they do not contain viscosity modifiers meaning that they do not exhibit the same non-Newtonian behaviour as the formulated oils. As a result, viscosity does not vary with shear rate and, as has been noted above the kinematic viscosity of the base oils does not change as a result of sonication of the oils.

We have shown that the addition of rGO has little impact on the viscosity of the oils when nanofluids have been produced. This is extremely promising in the application of rGO as an additive for the modification of thermal and tribological properties of lubricants as if a significant change in viscosity had been observed this would have to have been accounted for through a change in the formulation of oils and the use of viscosity modifiers. The lack of change in viscosity means that this is not the case and rGO and f-rGO can simply be added to existing lubricant formulations without affecting the viscosity.

One caveat to this is that the processing used to form nanofluids can have a significant

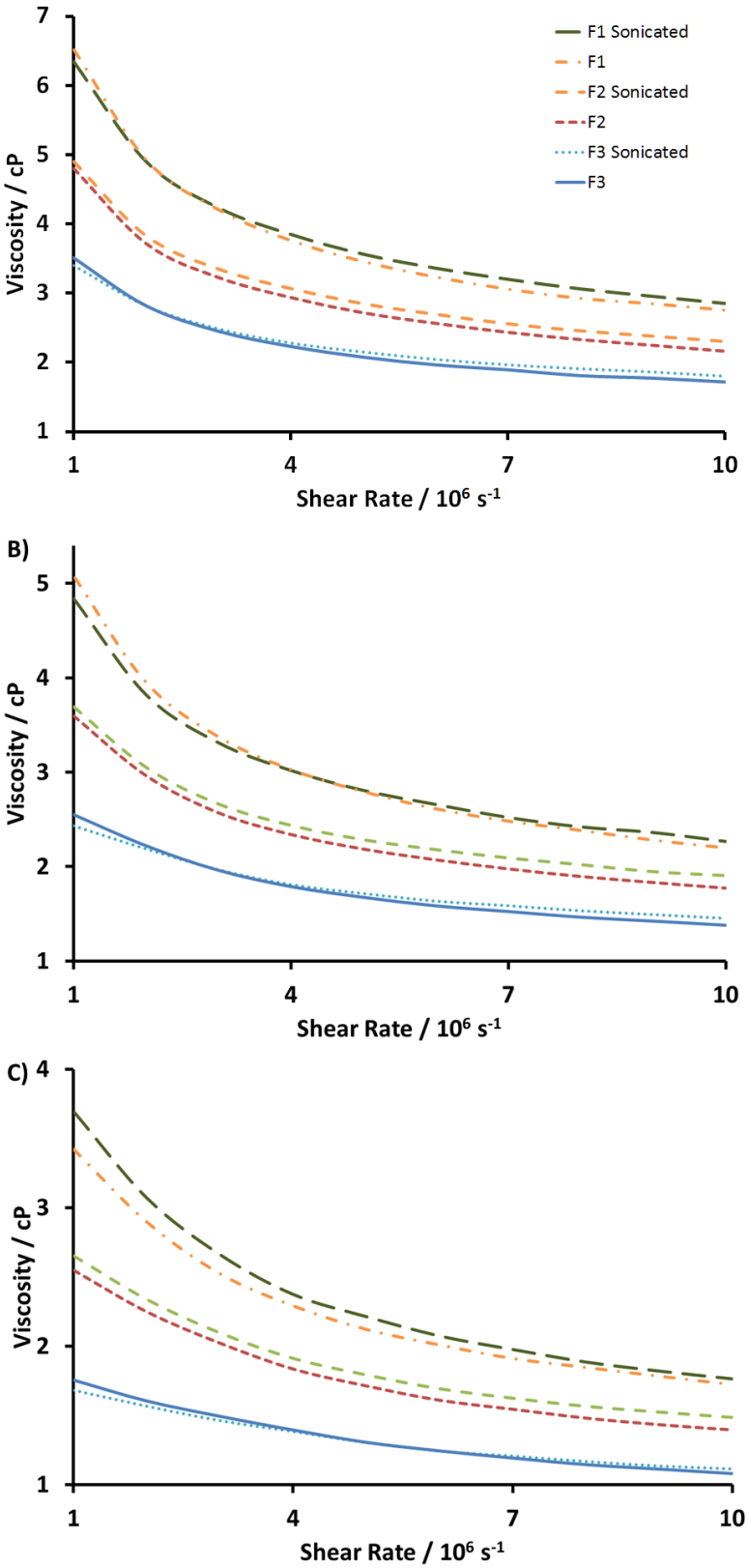

Figure 6.41: *The high shear viscosities of the formulated oils between $1 \times 10^6\ s^{-1}$ and $1 \times 10^7\ s^{-1}$ at A) 100 °C, B) 120 °C, and C) 150 °C showing data for both unmodified oils and for those that have been subjected to sonication.*

impact on the kinematic viscosity of the oils which we attribute to decomposition of viscosity modifying additives present in the formulations. The result of this is that care must be taken to form the nanofluid prior to the addition of additive package, which contains the viscosity modifier, to the base oil.

6.4.1.2. Friction & Wear Properties of Nanofluids

The promising lack of change in the viscosity of oils as a result of rGO and f-rGO additives, described above, means they have good potential for improving the wear of properties of nanofluids and means that any changes in wear properties observed are not a result of changes in viscosity. The dispersions produced were analysed using MTM in order to determine their coefficient of friction. The measurement of coefficients of friction was discussed in section 4.4 and the methods used are described in section 8.1.11. Briefly, the testing protocol involved placing the samples into the MTM and running the samples using American iron and steel institute (AISI) 52100 steel balls and discs with a 36 N load which exerts a contact pressure of $\sim$1 GPa. The test protocol is made up of 2 segments, to study both the boundary friction regime and the hydrodynamic friction regime for the nanofluids. These steps will be referred to as the boundary step and the hydrodynamic step, respectively.

The boundary step consists of measurement of friction at a constant speed of 0.05 m s^{-1} and load of 36 N for 60 minutes. The hydrodynamic step ramps the measurement speed up from 0.01-4 m s^{-1} over a period of 5 minutes at a constant force of 36 N. All measurements are taken at a constant temperature of 120 $^{\circ}$C, which mirrors that expected within an engine.

The measurement protocol begins with the hydrodynamic step, and then switches to running the boundary step for 60 minutes and then alternates between the two steps for a total of 180 minutes, ending with a final hydrodynamic step. The repeated testing protocol allows the surfaces to become fully coated with the lubricant and to allow any tribofilm to form on the surface which could impact on the tribological properties of the system.

6.4.1.2.1. Tribological Properties of Nanofluids Containing rGO and f-rGO

In line with the testing of viscosity performed on the nanofluids, the first dispersions to be tested for tribological properties were nanofluids containing hydrazine rGO as well as the f-rGOs described earlier in this chapter. The solvents used to test these additives were the base oils E1, E2, P1, P2, and OSP-18. The selection of combinations of base oils and additives was discussed in section 6.3.2.2.5 and the production of these dispersions in sections 6.3.1.2 and 6.3.2.2.

The combinations of additives and lubricants that were chosen for further testing were analysed using MTM in both the boundary and hydrodynamic lubrication regimes, in order to establish the effect of the additives on the tribological properties of the lubricants.

Data from the boundary regime section of the measurements are presented in table 6.19 and figure 6.42. In order to obtain the data presented in table 6.19 the percentage change in coefficient of friction between each nanofluid and the base fluid used to create it was calculated at each time point. An average of all of these percentage changes was then calculated to give an overall average percentage change in the coefficient of friction for each nanofluid.

When the effects of different rGO additives on given base oils are examined it quickly becomes apparent that different base fluids respond differently to the presence of graphene based additives. However, the nature of the additive and its concentration do not appear to impact on the change in coefficient of friction. This is shown most clearly in figure 6.42. In this figure, the solid blue line represents the coefficient of friction, in the boundary regime, of the neat oil while the other lines are for nanofluids containing different f-rGO additives. It is observed that for the most polar base oils, E1 and OSP-18, the presence of any of the graphene based additives causes an increase in coefficient of friction of 10-30 % for E1 and 30-60 % for OSP-18 (aside from some variation within the first 60 minutes of the measurement).

Table 6.19: *The mean coefficient of friction, and percentage change in coefficient of friction under boundary conditions compared to that of the unmodified base oil, for nanofluids utilising base oils as a solvent and f-rGOs as additives.*

Oil	Additive	Concentration / μg ml^{-1}	Mean Coefficient of Friction	% Change
E1	Oil	-	0.064	-
	rGO	5.9	0.074	16.2
	Conventional ODArGO	150.8	0.83	28.9
	TOPrGO	52.5	0.72	11.5
E2	Oil	-	0.066	-
	rGO	1.2	0.044	-33.6
	Conventional ODArGO	122.6	0.050	-23.9
	OLrGO	35.3	0.054	-17.0
	TOPrGO	12.8	0.040	-38.6
	TOPrGO	159.1	0.047	-28.8
P1	Oil	-	0.079	-
	rGO	0.2	0.080	0.3
	OLrGO	0.8	0.069	-12.0
	TOPOrGO	0.3	0.079	-0.1
P2	Oil	-	0.066	-
	rGO	1.2	0.068	5.0
OSP-18	Oil	-	0.067	-
	rGO	68.5	0.119	83.2
	Conventional ODArGO	157.1	0.099	52.0
	in situ ODArGO	19.6	0.088	34.4
	OLrGO	11.2	0.084	29.1
	TOPrGO	96.3	0.102	57.1
	TOPOrGO	5.7	0.098	51.1

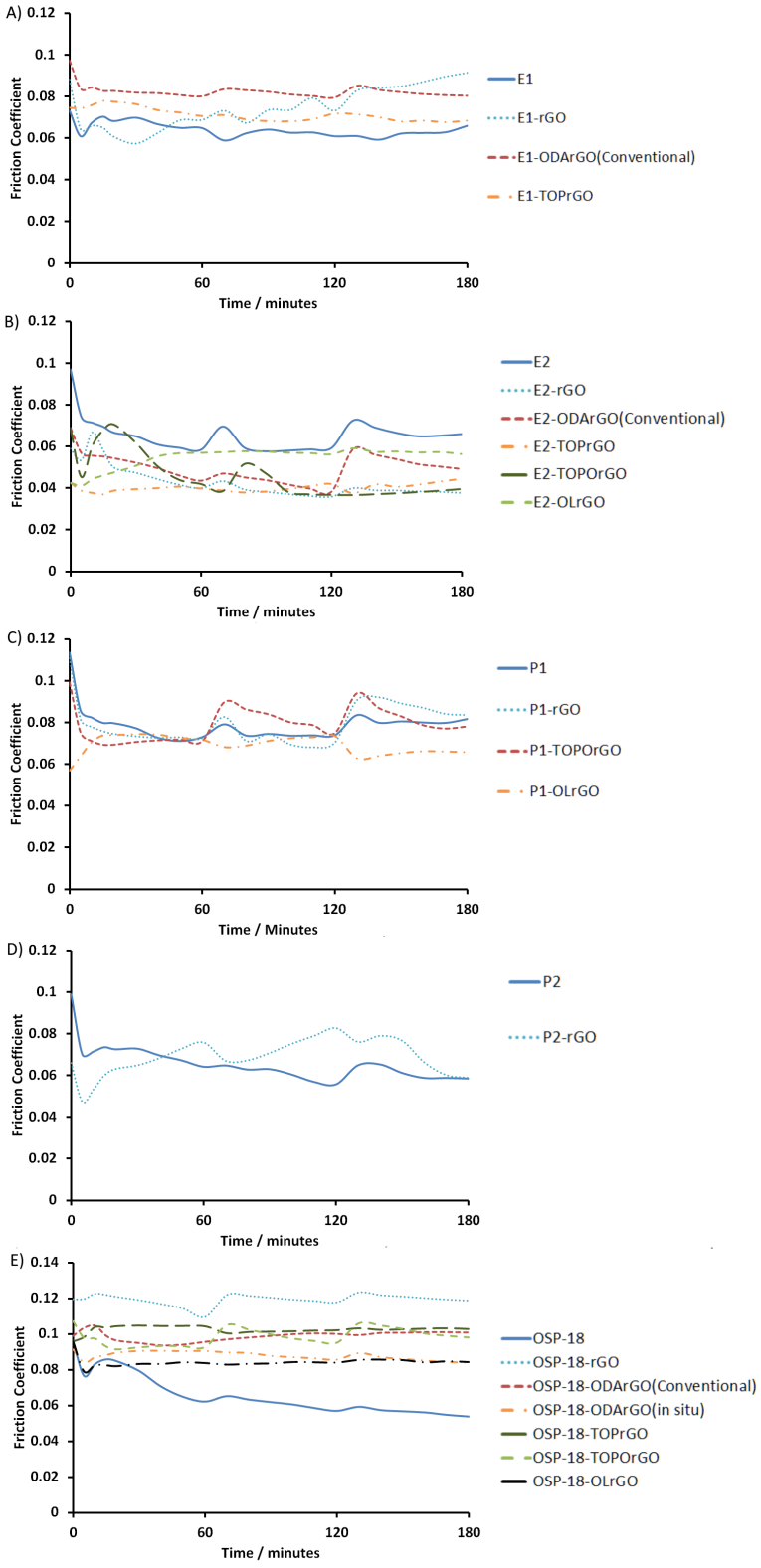

Figure 6.42: *The tribological behaviour of nanofluids containing f-rGOs as additives in A) E1, B) E2, C) P1, D) P2, and E) OSP-18 under the boundary testing regime with the behaviour of the untreated fluid (solid blue line) provided as a comparison.*

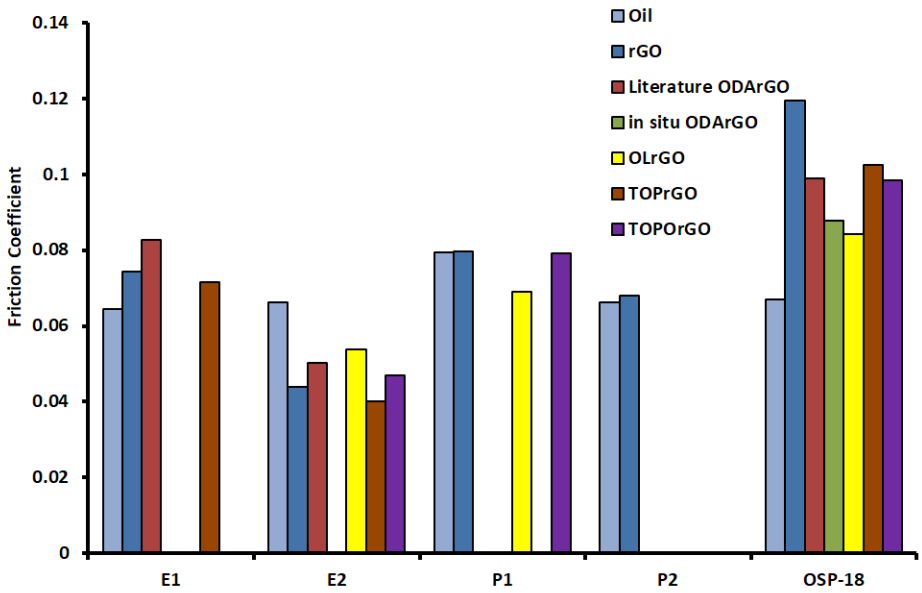

Figure 6.43: *The mean coefficient of friction, under boundary conditions, of unmodified oils and f-rGO oil nanofluids.*

In the least polar oils, P1 and P2, there is no consistent change in tribological properties of the nanofluids, with variation in the coefficient of friction over the measurement time being observed for all samples, at some times being higher than that of the pure oil and at other times being lower with little consistent pattern. However, taking the average of these changes in coefficient of friction over the measurement time shows that the average change in coefficient of friction is close to zero (table 6.19).

Finally, E2 shows markedly different behaviour to the other base oils with a universal decrease in the coefficient of friction, relative to that of the untreated oil, being observed for all samples containing graphene based additives with decreases of 20-40 % being observed. This indicates that E2 has the greatest potential as a base fluid for lubricants containing graphene based additives. E2 has a polarity that is between the least polar oils, P1 and P2, and the most polar oils, E1 and OSP-18. It is likely that the reason for this is that the surface energy of f-rGOs is closest to that of E2 meaning they form a more stable dispersion, with improved tribological properties.

Whilst, in general, the choice of f-rGO does not seem to determine the change in coefficient of friction there is one exception to this. In all combinations tested nanofluids produced using OL-rGO as an additive have some of the lowest coefficients of friction under

boundary conditions. This is most notable in P1, where nanofluids using rGO and TOP-rGO as additives exhibit the same coefficient of friction as the unmodified oil, whilst those using OL-rGO as an additive showed a 12 % decrease in coefficient of friction. This can be explained by the fact that P1 is non-polar and so its chemistry matches well with the long alkyl chain present on the surface of OL-rGO. Similar behaviour is also exhibited however for nanofluids using OL-rGO in E2 and OSP-18, which are significantly more polar. In both these oils OL-rGO nanofluids have relatively low coefficients of friction but are not the best performing nanofluids.

Once again, as for viscosity there appears to be little to no correlation between the concentration of the nanofluids and the impact of the additive on the coefficient of friction under boundary conditions. The reasons for this behaviour are as yet unclear as it was expected that both concentration and the compatibility of the additive with the base fluid would be the factors to have the greatest impact on coefficient of frication. It appears however, that the choice of base fluid is what has the greatest impact on the properties of a nanofluid, most likely due to the interaction between the f-rGO additive and the base oil.

Overall, the majority of nanofluid produced using graphene additives exhibited higher coefficients of friction than those of the unmodified oils. However, certain combinations were an exception to this and OL-rGO in P1 and all f-rGOs in E2 had improved coefficients of friction relative to those of the unmodified oils. Therefore, further investigations on graphene based nanofluids should focus on oils with mid polarities such as E2, or combinations which have well matched surface chemistries such as OL-rGO in P1.

Alongside the measurement of the coefficient of friction in the boundary regime, discussed above, the procedure also allows for analysis of the coefficient of friction at higher speed: the hydrodynamic regime. Whilst the data for the boundary regime is being recorded the measurement protocol switches every 60 minutes to record data in the hydrodynamic regime. These data are presented in figure 6.44.

For the most part, the data recorded in the hydrodynamic regime mirrors the patterns

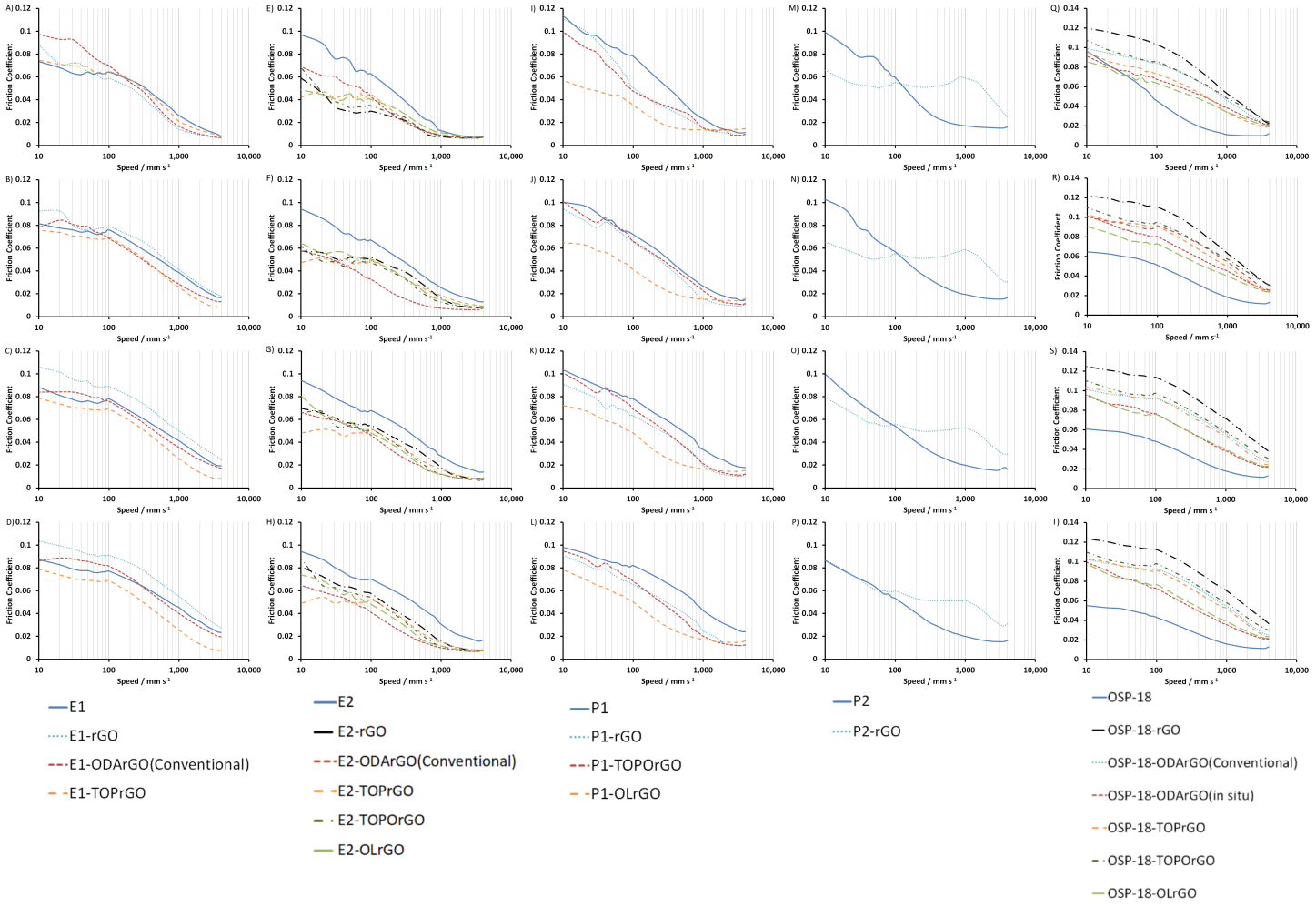

Figure 6.44: *The coefficient of friction of nanofluids containing rGO and f-rGOs utilising formulated oils as solvents along with the data for the pure formulated oils for A-D) E1, E-H) E2,I-L) P1, M-P) P2, and Q-T) OSP-18 under the hydrodynamic condition section of the testing regime after A,E,I,M,Q) 0 minutes, B,F,J,N,R) 60 minutes, C,G,K,O,S) 120 minutes, and D,H,L,P,T) 180 minutes of testing in the boundary regime.*

seen from the data recorded under boundary conditions with nanofluids using E1, and P2 giving little change in the coefficient of friction and dispersions using OSP-18 increasing in coefficient of friction as a result of the additives. Dispersions using E2, as above, behave differently then the other base oils and show a decrease in coefficient of friction across all measurement speeds, caused by the use of the additive but independent of its chemistry (figures 6.44 E to 6.44 H). The main difference between the data recorded in the boundary conditions and that in hydrodynamic conditions is in the behaviour of the nanofluids using P1 as a solvent (figures 6.44 I to 6.44 L). In these fluids there appears to be more difference in coefficient of friction as a result of the different additives, with OL-rGO showing the greatest decrease in coefficient of friction with all other additives showing slight decreases. This change is not mirrored in the boundary regime where a slight decrease in coefficient of friction is observed for OL-rGO and no change is observed for the remaining additives. This implies that the addition of f-rGOs to P1 to form nanofluids improves the tribological properties of the fluid, but does not have such a great effect on the surfaces within the test system leading to the decrease in coefficient of friction in the hydrodynamic regime observed here. This implies that the additives in these dispersions are particularly stable, and remain held in the fluid under test conditions rather than becoming deposited on the surfaces within the apparatus and affecting friction performance under boundary conditions.

As was the case in boundary conditions dispersions using OL-rGO as an additive showed favourable results, with this additive frequently showing the greatest decrease in coefficient of friction for any nanofluid, notably in E2 and P1, but also in OSP-18, where all f-rGOs caused an increase in coefficient of friction, nanofluids containing OL-rGO showed the smallest increases at all measurement speeds. Alongside this, nanofluids using TOP-rGO also performed well in E1 showing the lowest coefficient of friction after 180 minutes of any E1 nanofluid.

Whilst the majority of combinations of graphene additive and base fluid did not cause a decrease in the coefficient of friction, either in the hydrodynamic or the boundary regime, certain combinations of fluids did show improved tribological properties. Those nanofluids

that utilise E2 as a base fluid universally showed improvement in both the boundary and hydrodynamic testing regimes, indicating that both the properties of the fluid, and its interaction with the surfaces of the MTM were improved. Alongside this, a combination of P2 and OL-rGO showed improved properties in the hydrodynamic regime with only slight improvements in the boundary regime, indicating that the lubricity of the fluid has increased, whilst not impacting significantly on the properties of the surfaces of the MTM.

Alongside the coefficient of friction of the fluids produced, the wear caused on the moving components during testing is also significant. This is difficult to assess in a quantitative manner using the test methods employed, however it was noted by the operator performing the MTM testing that no noticeable wear was observed on the components of the MTM implying that the graphene based additives do not act as an abrasive and cause significant extra wear, which would be an extremely negative quality.

6.4.1.2.2. Tribological Properties of nanofluids containing in situ rGO

A final group of samples that was analysed were the nanofluids produced by *in situ* reduction of GO in base oils. Once again, only those combinations that produced high concentration dispersions were sent forward for tribological testing, those using E1 and OSP-18 as base fluids. These dispersions were produced as described in section 6.2.3.2 with GO being dispersed in oils *via* sonication before the mixture was heated to 120 °C for 24 h in order to reduce the GO to rGO.

As for previous nanofluids, the tribological properties of the *in situ* rGO nanofluids were determined by MTM as described in section 8.1.11 and the coefficients of friction under both boundary and hydrodynamic regimes were recorded.

The coefficients of friction against time in the boundary regime for the dispersions of *in situ* rGO in E1 and OSP-18 as well as the untreated base oils, for comparison, are shown in figure 6.45. These results show that the presence of the rGO additive has a clear impact on the coefficient of friction under boundary conditions in both E1 and OSP-18, causing an

increase in both cases. However, also in both cases the value of the coefficient of friction is not constant over time.

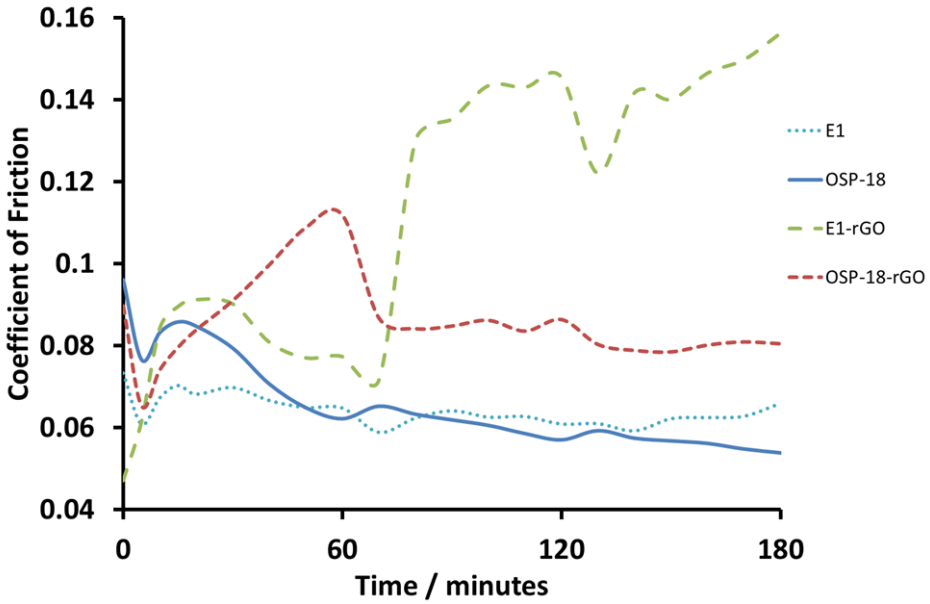

Figure 6.45: *The coefficient of friction of dispersions of rGO produced by in situ heating of GO in base oils E1 and OSP-18 compared to the coefficient of friction for the pure, untreated base oils under the boundary conditions of the testing regime.*

In the boundary testing regime in the MTM the rotation speed is low (compared to the hydrodynamic region) and as a result the main component to friction between components results from the surfaces of these components as opposed to the lubricant layer between them. It therefore follows that the reason for the change in coefficient of friction observed is due to the presence of a rGO layer forming on the surface of components and increasing boundary friction between them, implying that the dispersions of rGO do not remain stable under the test conditions.

Figure 6.45 shows that for the dispersion of *in situ* rGO in E1 the coefficient of friction is only marginally higher than that for untreated E1. However, after 60 minutes a marked increase in coefficient of friction is observed. It is hypothesised that the reason for this change is due to the destabilisation of the dispersion at the 60 minute mark, when testing in the hydrodynamic region occurs, causing the rGO to deposit on the surfaces of the components, having a significant impact on the boundary friction.

Conversely for the dispersion of *in situ* rGO in OSP-18 an increase in the coefficient of friction under boundary conditions is observed immediately, indicating that the rGO is having an immediate impact on the surfaces within the MTM, possibly due to the formation of a tribofilm. However, in this case the increase in coefficient of friction stops after the hydrodynamic testing at $\sim$60 minutes and this value begins to fall and stabilises. However, the final value is still significantly above that for untreated OSP-18. This behaviour could be explained by the slow formation of a layer of rGO over the surface of the components during the first 60 minutes, causing a rise in the coefficient of friction. This film is then disrupted by testing under hydrodynamic conditions causing the coefficient of friction to fall and stabilise as the system reaches equilibrium.

Overall, these data show that, in spite of being a method to from stable nanofluids, the synthesis of *in situ* rGO in oils acts to increase the coefficient for friction of the oil under boundary conditions, which is not desirable for most lubricant applications.

The tribological behaviour of the dispersions of *in situ* rGO under hydrodynamic conditions were also examined. The testing protocol used was as described in section 8.1.11.1 and this protocol was run at set intervals of 60 minutes during the testing of the boundary regime, giving data at 0 minutes, 60 minutes, 120 minutes and 180 minutes. These data are shown in figure 6.46. In the hydrodynamic regime the speeds are higher than in the boundary regime and the lubricant is pulled into the gap between the surfaces meaning that the greatest contribution to the coefficient of friction is due to the lubricant itself as opposed to the surfaces of the components

Figures 6.46 A to 6.46 D show the coefficients of friction against speed for nanofluids using E1 as a base fluid, while figures 6.46 E to 6.46 H contains data for nanofluids using OSP-18.

It is clear from these data is that the hydrodynamic friction behaviour of the unmodified lubricants does not change significantly with time, aside from the data taken at 0 minutes in OSP-18 (figure 6.46 E) where some time is required for the instrument and lubricant to

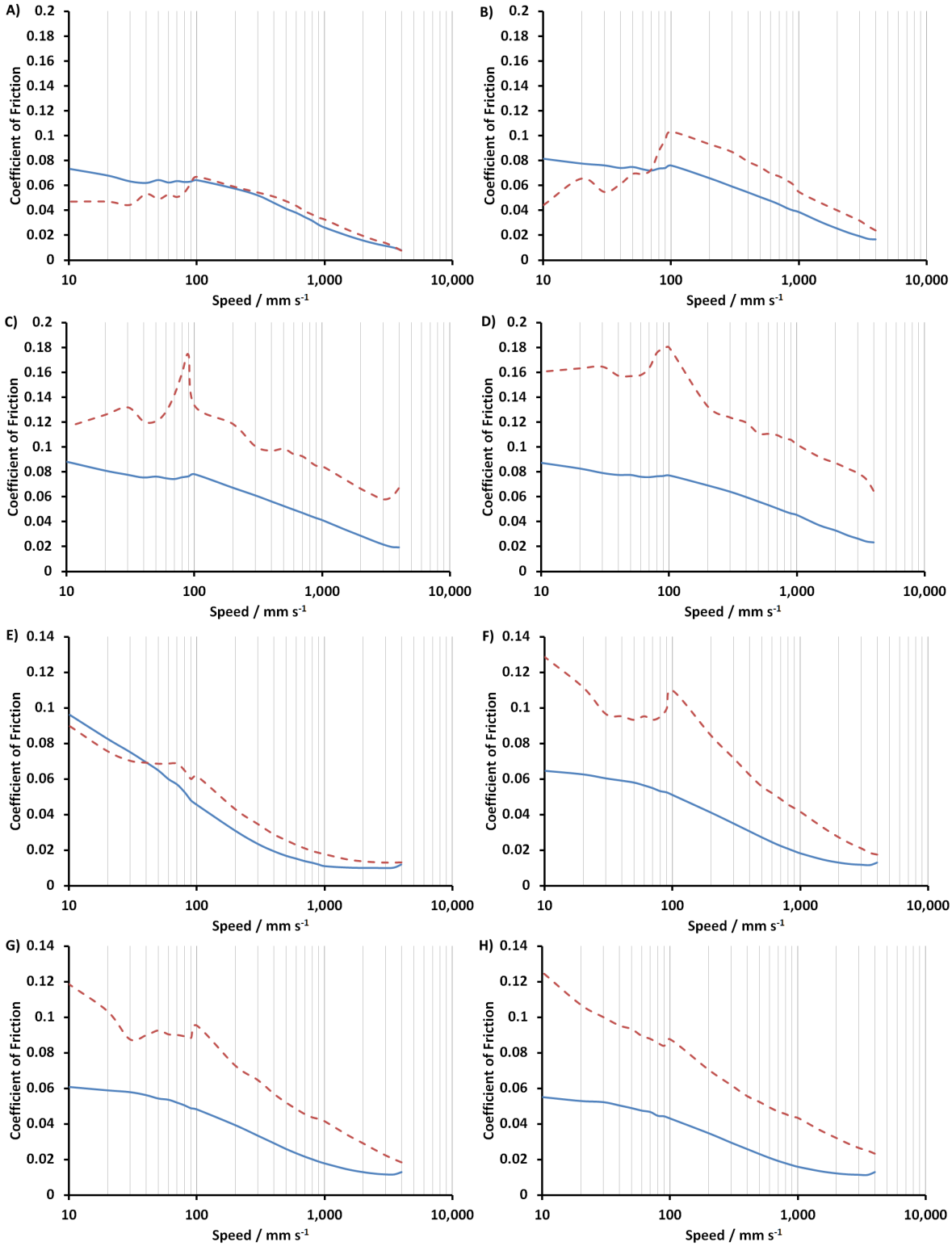

Figure 6.46: *Tribological behaviour in the hydrodynamic regime of both nanofluids containing in situ rGO (red dashed line) and unmodified base fluids (solid blue line) for nanofluids utilising E1 as a base fluid after A) 0 minutes, B) 60 minutes, C) 120 minutes, and D) 180 minutes of testing in the boundary regime and for those utilising OSP-18 as a base fluid after E) 0 minutes, F) 60 minutes, G) 120 minutes, and H) 180 minutes of testing in the boundary regime.*

bed in before consistent tribological behaviour is achieved. However, the data taken at 60 minutes, 120 minutes and 180 minutes shows consistent trends. Readings taken from nanofluids containing *in situ* rGO do not display this consistency with the tribological behaviour in the hydrodynamic regime changing at different recording points for both E1 and OSP-18 based nanofluids. Measurements taken at 0 minutes for both E1 and OSP-18 (figures 6.46 A and 6.46 E) the coefficient of friction for the nanofluid does not differ from that of the untreated base fluid significantly over the range of speeds tested. However, this is not the case for measurements taken after 60 minutes, 120 minutes and 180 minutes of testing under the boundary regime as can be seen in figures 6.46 B to 6.46 D and 6.46 F to 6.46 H.

For samples using E1 as a base fluid the coefficient of friction of the nanofluid rises relative to that of the untreated base fluid and continues to do so with time spent in under the boundary testing conditions (figures 6.46 A to 6.46 D). This implies that the conditions within the MTM are causing a degradation of the dispersion over time, reducing its tribological performance. This correlates with our hypothesis based on the data collected under the boundary regime: that the rGO in dispersion is destabilised during the measurement, and as it no longer forms a good dispersion both deposits on the surfaces whilst also impacting on the hydrodynamic properties of the lubricant.

Samples that use OSP-18 as a base fluid display subtly different behaviour as the elapsed time under the boundary testing regime increases (figures 6.46 E to 6.46 H). For these nanofluids the coefficient of friction under the hydrodynamic regime increases sharply during the first 60 minutes under boundary conditions and then remains relatively constant for the remainder of the measurement period. Again this correlates with our hypothesis of what is occurring in these nanofluids based on the data recorded under boundary conditions with the dispersion rapidly destabilising during the first 60 minutes before reaching a steady state with inferior tribological properties to those of the untreated base fluid.

Overall, the testing of the hydrodynamic coefficient of friction of these *in situ* nanofluids mirrored the changes observed in the boundary coefficients of friction, with both nanofluids

in E1 and OSP-18 exhibiting increases in coefficient of friction, which is not desirable in the applications these lubricants are used in.

It was noted by the operator performing the tests that no additional wear was observed on the components when testing the nanofluids meaning that the *in situ* rGO additives were not acting as an abrasive.

6.4.1.2.3. Tribological Properties of Nanofluids using Formulated Oils

Following on from the analysis of nanofluids produced using base oils, described above, the properties of nanofluids produced using formulated oils were also assessed under the same conditions.

Dispersions of hydrazine reduced GO as well as f-rGOs in fully formulated oils were analysed under boundary conditions and it was noted that in these oils, the addition of the f-rGO additives had a much greater effect on the tribological properties of these oils.

The coefficients of friction of these nanofluids during the boundary step of the measurement protocol are shown in figure 6.47, along with the average percentage change in coefficient of friction over the measurement period in table 6.20.

Table 6.20: *A table showing the percentage change in kinematic viscosity versus the percentage change in coefficient of friction under boundary conditions for nanofluids containing f-rGO dispersed in formulated oils compared to the unmodified formulated oils.*

Oil	Additive	% change V_K 40	% change V_K 100	% Change in Coefficient of Friction
F1	rGO	-30.1	-28.5	87.6
F2	rGO	-29.9	-27.5	58.0
	in situ ODArGO	-27.2	-25.0	43.7
	TOPrGO	-27.4	-25.2	39.4
F3	rGO	-28.6	-27.7	42.3
	in situ ODArGO	-28.5	-27.7	50.2
	TOPrGO	-31.6	-30.7	51.8
	OLrGO	-28.9	-28.1	52.2

These data clearly shows that there has been a significant change in coefficient of friction due to the addition of rGO based additives with the average increase in coefficient of friction

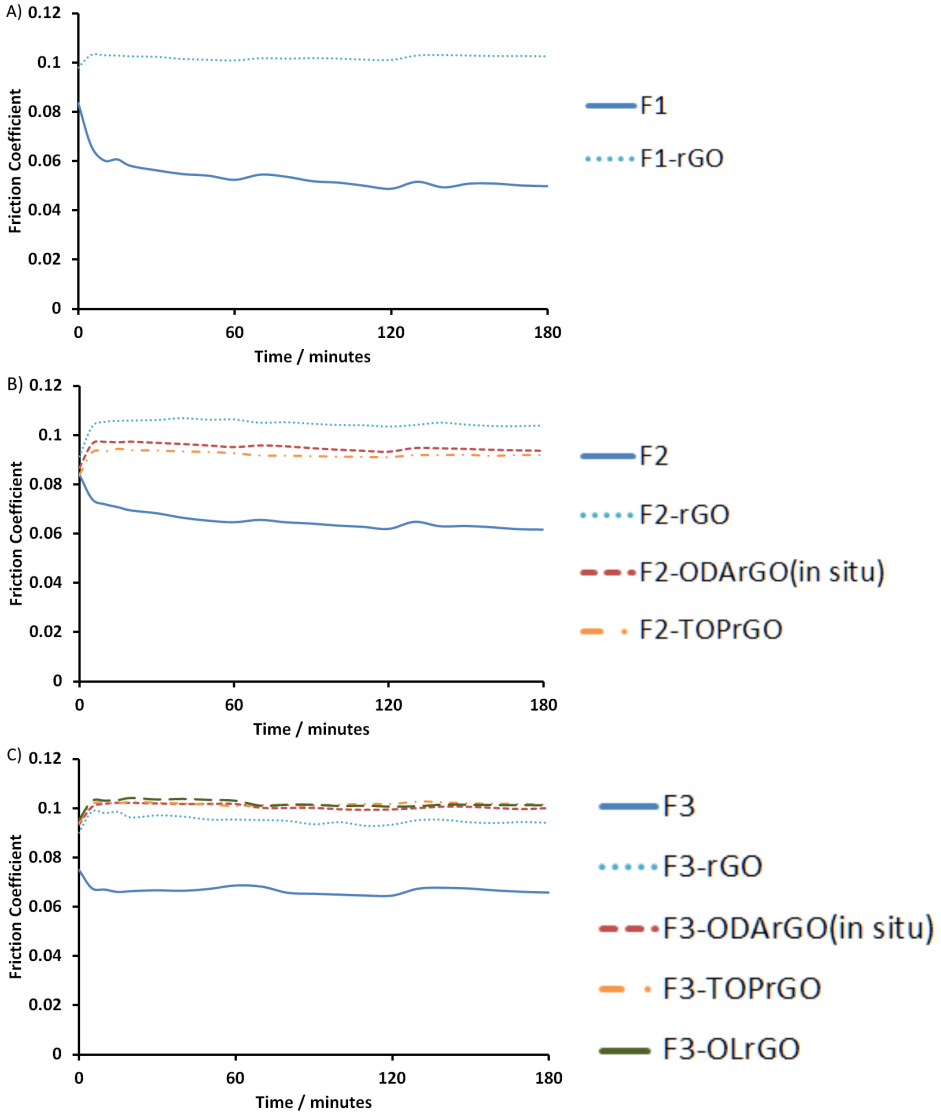

Figure 6.47: *The coefficient of friction of nanofluids containing rGO and f-rGOs utilising formulated oils as solvents along with the data for the pure formulated oils for A) F1, B) F2, and C) F3 under the boundary condition section of the testing regime.*

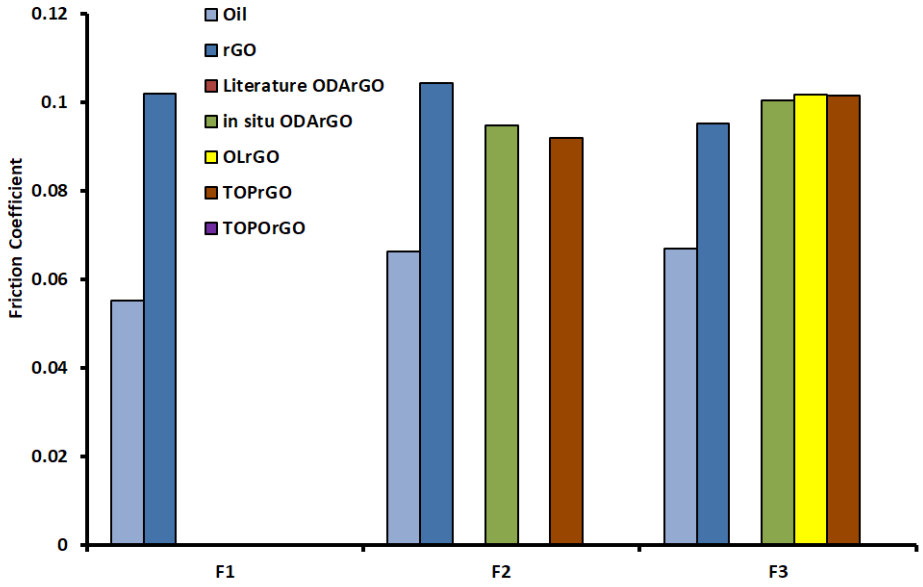

Figure 6.48: *The coefficient of friction of nanofluids containing rGO and f-rGOs utilising formulated oils as solvents along with the data for the pure formulated oils.*

being >39 % for all combinations when compared to the pure oils. Whilst the presence of the additive may play a part in this change; we believe that the processing used to form the nanofluids may be the factor causing the majority of this change. We have already noted that the formation of these nanofluids has a the effect of causing a significant change in kinematic viscosity due to the decomposition of polymer viscosity modifiers in the formulated oils (section 6.4.1.1) and have shown that this is due to the sonication used in the preparation of nanofluids rather than the presence of the f-rGO additives.

Relating the viscosities, and coefficients of friction for the neat, unmodified, formulated oils it can be seen that oils with lower kinematic viscosities have higher coefficients of friction under boundary conditions (table 6.21). This an expected behaviour for these oils. The impact of this, however, is that the changes in viscosity that are observed as a result of the sonication used to form nanofluids (described in section 6.4.1.1.1) are also likely to be the cause of the changes in coefficient of friction described above: not the presence of the f-rGO additives.

These same nanofluids were also analysed to determine the impact of graphene based additives under hydrodynamic conditions, where the characteristics of the lubricant fluid have the greatest effect on the coefficient of friction.

Table 6.21: *The mean coefficients of friction, under boundary conditions, and kinematic viscosities for the unmodified, formulated oils.*

Oil	V_K 40 / cSt	V_K 100 / cSt	Friction Coefficient
F1	156.30	35.50	0.052
F2	70.34	19.00	0.064
F3	28.35	9.05	0.066

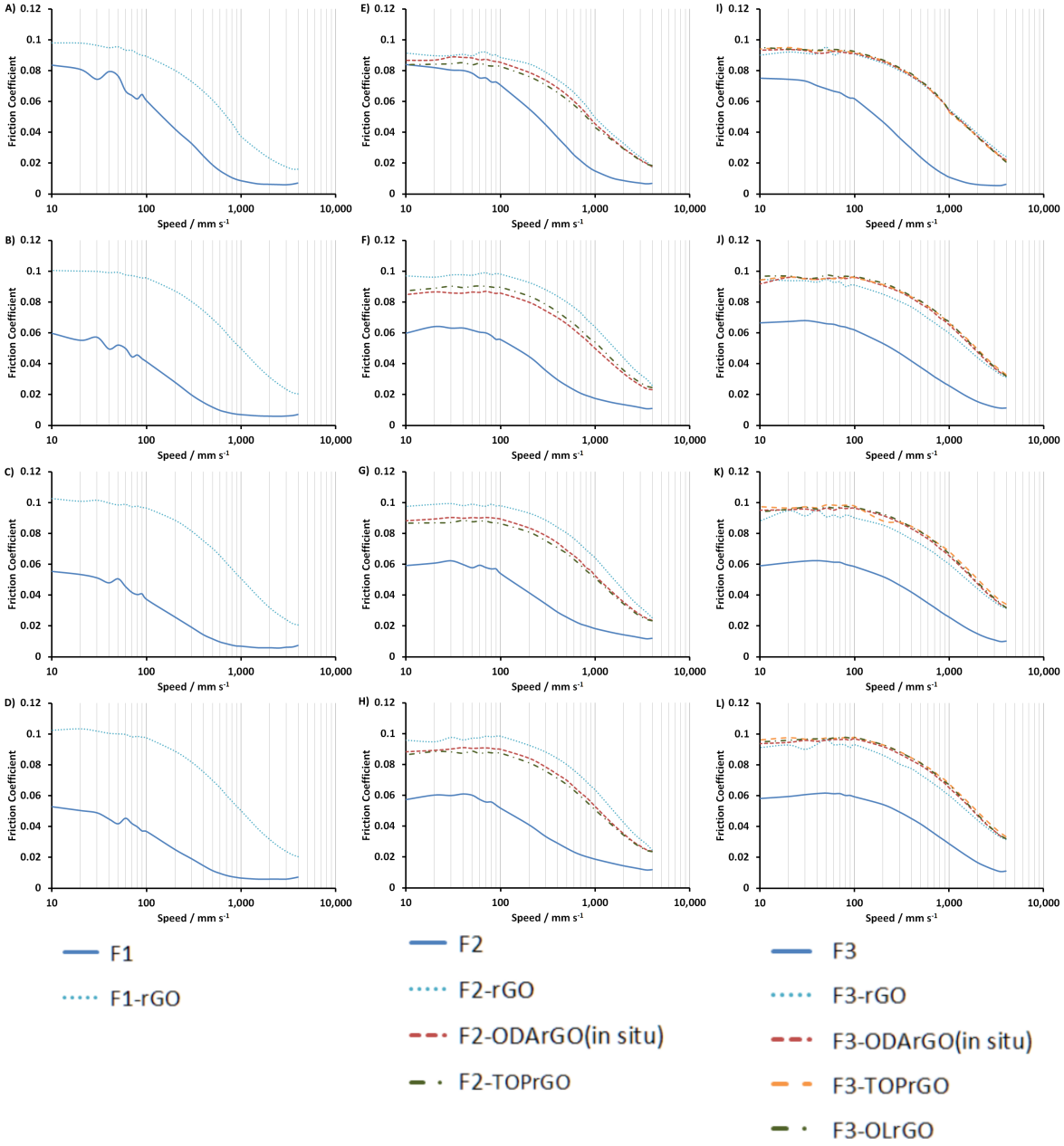

Figure 6.49: *The coefficient of friction of nanofluids containing rGO and f-rGOs utilising formulated oils as solvents along with the data for the pure formulated oils for A-D) F1, E-H) F2, and I-L) F3 under the hydrodynamic condition section of the testing regime after A,E,I) 0 minutes, B,F,J) 60 minutes, C,G,K) 120 minutes, and D,H,L) 180 minutes of testing in the boundary regime.*

Data from measurements taken under hydrodynamic conditions for dispersions of rGO and f-rGO in the formulated oils F1, F2, and F3 after 0 minutes, 60 minutes, 120 minutes and 180 minutes under the boundary testing regime are shown in figure 6.49. These data clearly demonstrate that the in all cases, the rise in coefficient of friction observed under boundary conditions is mirrored under hydrodynamic conditions, when the measurement speed is increased. This is the expected result based on the hypothesis, discussed above, that the process of sonication used to form the nanofluids is causing decomposition of the polymer-based viscosity modifiers in the formulated oils and affecting their viscosity as the behaviour of lubricants in the hydrodynamic regime is heavily influenced by the properties of the fluid component of the lubricant.

These large changes in both coefficient of friction and kinematic viscosity mean that the sonication of formulated oils, such as these, is not likely to be a successful method for the production of nanofluid based lubricants due to the risk of damage to other components within the lubricant such as viscosity modifiers. A more promising approach is to combine graphene based additives to the neat base oil and form the nanofluid before further additive packages are combined into the system as demonstrated in section 6.4.1.2.1.

6.5. Conclusion

The goal of the work presented in this chapter was to improve the tribological properties of lubricants for use in automotive applications. In order to achieve this, a range of nanofluids were produced using modified graphenes as additives, using modifiers to improve the concentration of graphenes achievable in each of the oils. This work fell into three sections: the modification of graphene to produce f-rGOs, the dispersion of these f-rGOs in commercial oils to produce nanofluids, and the tribological testing of the nanofluids produced to assess the impact of the f-rGOs on the performance of the oils as lubricants.

Functionalisation of graphene materials was performed through the covalent functional-

isation of rGO. Firstly ODA-rGO was produced using a well known literature method for other novel f-rGOs to be compared to. Following this, a novel method for the simultaneous functionalisation and reduction of GO was presented, which involved the heating of GO in the functionalising agent, in the absence of solvent. The process was shown, using techniques including TGA and XPS to simultaneously reduce the GO whilst also causing the functionalising agent to adhere to the graphene sheets. Using this method ODA-rGO, OL-rGO, TOP-rGO, and TOPO-rGO were produced and characterised.

The f-rGOs produced were then dispersed in a range of commercial oils provided by Shell Global Solutions using ultrasonication in order to form nanofluids. The concentration and stability of these nanofluids was assessed using UV-Vis spectroscopy. Changes in the dispersibility of the f-rGOs produced also act as an indication that functionalisation has been achieved successfully. It was shown that the concentrations achieved for each of the f-rGOs could be correlated to the polarity of the base oils with ODA-rGO and TOP-rGO dispersing best in more polar oils, while OL-rGO and TOPO-rGO were shown to disperse best in oils with the lowest polarity.

In order to assess the impact of these f-rGO additives, those combinations of oil and additive that gave the highest concentration, most stable nanofluids were produced on a larger scale in order to have their tribological properties assessed. The impact of the f-rGO additives on the kinematic viscosity, dynamic viscosity and the coefficient of friction of friction of the dispersions produced were analysed at Shell Global Solutions and, for nanofluids produced using base oils, there was little or no effect on viscosity as a result of the f-rGO additives. However, this was not the case for nanofluids using formulated oils as a solvent which exhibited significant changes in viscosity as a result of the addition of f-rGO. Further testing, through analysis of sonicated oils which did not contain f-rGO showed that this change in viscosity was due to the process of sonication used to disperse the f-rGOs and produce the nanofluids rather than the f-rGO itself. This behaviour was attributed to the degradation of the polymer viscosity modifiers present in the formulated oils as a result of ultrasonication. This hypothesis was not conclusively proven and so this topic is one that merits further

investigation.

Alongside the viscosity testing of the f-rGO nanofluids, their coefficients of friction were also tested in both the boundary and hydrodynamic friction regimes using a MTM. The results of these tests showed that the impact of the f-rGO additives depended on the exact combination of oil and additive used, with some combination causing an increase in the coefficient of friction while others caused a decrease. However, it seems that the change in coefficient of friction tends to be dependent on the oil chosen, rather than the chemistry of the f-rGO additive or its concentration.

As with their viscosity, nanofluids using formulated oils as solvents exhibited far greater changes in coefficient of friction than those using base oils, with a significant increase in coefficient of friction observed for all combinations. However, this increase is believed to be, once again, due to the breakdown of viscosity modifiers during sonication rather than as a result of the f-rGO additive.

As a result of this work, we can conclude that while graphene based additives can be successfully used to form stable nanofluids in commercial lubricants, the impact of these additives on the tribological properties of these lubricants is complex and cannot be easily predicted. Whilst some combinations of oil and additive acted to improve the performance of the lubricant, others acted to hinder it with little apparent pattern as to the outcome for a give nanofluid.

6.6. Further Work

Whilst a large number of combinations of base oils and additives were tested in the attempt find additives that could improve the tribological properties of lubricants, no correlation between the properties of the lubricants and the concentration of additives was ever observed. This may be in part due to the fact that each combination of lubricant and additive was only able to be tested at one concentration, its maximum concentration.

In order to establish the impact of concentration on the performance of graphene materials as lubricant additives it would be ideal to take some of the combinations of f-rGO and base oil that gave good improvements in coefficients of friction and recreate these dispersions at a range of concentrations before, once again, testing their tribological properties. Whilst it could be expected that dispersions with the highest concentrations of additive would give the greatest change in tribological properties, in practice it has been observed that this is not always the case with, in some examples, extremely low concentrations of additives having significant impact on tribological properties.

One of the factors that was not able to be determined within the timescale of this project was the degree of reduction achieved during the *in situ* reduction of FDGO to rGO performed in oils, as discussed in section 6.2.3.2. Determining this was challenging due to the difficulty of isolating the rGO from the oils after it had been formed *in situ* , leading to challenges in using the usual techniques for determining degree of reduction such as TGA, XPS, and UV-Vis. A proposed idea to overcome this would be to utilise the change in properties that occurs during reduction from insulating GO to conducting rGO.

It is likely that, in an electrically insulating base fluid, this change of conductivity of the additive could be detected through the use of impedance spectroscopy, which can monitor extremely small changes in the electrochemical properties of a material such as conductivity and resistivity. One caveat to this is that this change will only be detectable in insulating base oils and so it will still not be possible to detect these changes in conducting base fluids such as the PAG based OSP-18.

Given the conclusions drawn regarding the impact of sonication on the fully formulated oils (section 6.4.1.1 and section 6.4.1.2.3) and our hypothesis that the changes in tribological properties and viscosity observed are due to the degradation of the polymer viscosity modifiers present in the formulated oils a further avenue of study would be to study the viscosity modifiers in detail.

Due to the nature of commercial oils, which are produced by mixing pre-formulated

packages of additives with base oils to obtain a lubricant with the desired properties, the identity of many of the additives used is not disclosed. If the identity of the viscosity modifiers used in the formulated oils could be determined then sonication could be performed on these materials in isolation which could firstly confirm our hypothesis that sonication is causing degradation of these components. Following on from this, with careful analysis of any breakdown products formed, variation of the intensity and duration of the sonication could allow the breakup of these modifiers to be minimised whilst still allowing graphene based additives to be dispersed, providing a route to produce nanofluids by addition to a fully formulated oil. Alternatively it would be of interest to study the tribological properties of nanofluids, produced by mixing f-rGOs with base oils which had then been mixed with commercial additive packages to examine the impact of these additives on the a fully formulated oil without the impact of sonication on the viscosity modifier.

Finally, whilst thorough testing of the tribological properties of the nanofluids produced using graphene based additives was able to be performed, the impact of these additives on the thermal properties of the lubricants was not assessed during this project. Whilst not as significant to engine performance as tribological properties, the thermal properties of a lubricant are still important. For this reason, it would be interesting to determine if these additives have an effect on the thermal properties of lubricants; principally the thermal conductivity and specific heat capacity.

Measurement of thermal conductivity could be performed using the bespoke THW instrument that's development is described in section 4.2.1, while the measurement of specific heat capacity could be performed using DSC.

Chapter 7

Measurement of Thermal Properties of Liquids

One of the key properties of a lubricant in an internal combustion engine is its ability to transfer heat away from moving components and dissipate it into the cooling system. Failure to do this can lead to premature wear on moving parts, or even complete failure of the system due to excessive heat build up. Producing lubricants with enhanced thermal conductivity would allow the efficiency of these systems to be greatly improved as more power could be generated in a similar system without excess heat build up.

Another key component in internal combustion engines are coolants. These act to carry heat away from the lubricants, and other components, that are contained within the engine and carry it away through the cooling system to a radiator where it can be finally dissipated to the atmosphere. For similar reasons as with lubricants, improving the thermal conductivity of these lubricants will enhance the efficiency of engines. Improving the ability of these fluids to transfer thermal energy will allow the same amount of thermal energy to be carried away by a smaller volume of fluid, allowing the size of the cooling system, and thus overall weight of the engine to be decreased, improving the power to weight ratio of the unit.

As has been discussed in section 1.4.4 graphene's excellent thermal conductivity means that its inclusion in nanofluids, such as those produced in lubricants in chapter 6, or dispersions of graphene materials in coolants, is likely to have an positive impact on the thermal conductivity of these fluids.

In order to assess the thermal transport properties of fluids such as lubricants and coolants an important quality to test is their thermal conductivity, or the amount of thermal

energy that can be transferred through the fluid by conduction.

In order to test the impact that the presence of graphene additives in nanofluids would have on the thermal properties of dispersions two properties were tested: thermal conductivity and specific heat capacity. The methods used to measure these characteristics are described in chapter 4. Whilst specific heat capacity can be determined using DSC it was necessary to design and produce a bespoke instrument to measure the thermal conductivity of liquids. This process is detailed below.

7.1. Design and Manufacture of the THW Instrument

The method chosen to determine the thermal conductivity of the nanofluids produced was the THW method. An introduction to this means of measurement has been discussed in section 4.2.1.

7.1.1. Theoretical Model

The main difficulty with the THW method comes in modelling the behaviour of the wire enabling thermal conductivity to be determined from resistance. Early instruments tried to be fully rigorous in the models they produced which led to increasingly complex instruments and calculations attempting to account for the effects of convection, the ends of the wire, and the material surrounding the sample. However, Healy *et al.* showed that by careful instrument design these effects all become negligible and so the simplest model, ignoring these effects, can be used to process data from a well designed instrument.[426]

In this, simplest, case the wire is modelled as an infinite line heat source of constant heat flux per unit length, which loses heat radially, solely *via* conduction, into an infinite, incompressible medium of constant thermal diffusivity. In order to allow our instrument to

follow these assumptions it was designed to meet certain constraints, listed below:

- The diameter of the wire must be sufficiently narrow, relative to its length, that it can be assumed to be of infinite length - this allows the effects of the ends of the wire to be negated.
- The sample volume must be sufficiently large, relative to the volume of the wire, that it can be considered to be infinite - this allows the effects of the sample chamber itself to be negated.
- The measurement time must be short enough that the effects of convection are negligible on the hot wire.
- The wire must be composed of a material with an extremely linear temperature to resistance ratio.

Provided the above constraints are adhered to when designing the instrument then the behaviour of the wire can be described using equation 7.1: the Fourier equation for one dimensional transient heat in cylindrical coordinates.[426]

$$\frac{\partial T}{\partial t} = \frac{\kappa}{r}\frac{\partial}{\partial r}\left(r\frac{\partial T}{\partial r}\right) \tag{7.1}$$

In this equation T is the temperature at time t, r is the distance from the wire and κ is thermal diffusivity of the medium. As long as our instrument adheres to the assumptions described above, the solution to equation 7.1 is well known and can be found in the literature[427] to be:

$$T(t) - T_0 = \Delta T = \frac{q}{4\pi\lambda}\ln\left(\frac{4\kappa}{D^2 C}t\right) \tag{7.2}$$

In this case T_0 is a reference temperature, D is the diameter of the wire, q is the power applied to the wire during the measurement, and $\ln C = \gamma$ (γ being Euler's constant). Whilst

equation 7.2 enables us to calculate a link between thermal conductivity and temperature change in the wire, this is not what is measured by the THW instrument, which records the resistance in the wire. It is therefore necessary to make use of the well known link between temperature and the resistivity (ρ) of a material (equation 7.3).

$$\rho(T) = \rho_0 \left(1 + \alpha \left(T - T_0\right)\right) \tag{7.3}$$

T_0 is a reference temperature with ρ_o being the resistivity at that temperature and α is the thermal resistivity coefficient. Conversion of resistivity to resistance relies on the relation shown in equation 7.4.

$$R = \rho \frac{l}{A} \tag{7.4}$$

In this equation l is length and A is the cross sectional area of the material. Therefore, utilising equations 7.3 and 7.4 it is possible to possible to calculate the temperature of the wire from its resistance:

$$\begin{aligned} R &= \frac{\rho_0 l}{A} \left(1 + \alpha \left(T - T_0\right)\right) \\ T &= T_0 + \frac{RA}{\rho_0 l \alpha} - \frac{1}{\alpha} \end{aligned} \tag{7.5}$$

Converting a change in resistance (ΔR) to a change in temperature (ΔT) equation 7.5 becomes:

$$\Delta R = \frac{\rho_0 l \alpha}{A} \Delta T \tag{7.6}$$

Combining this link between the resistance of the wire and its temperature (equation 7.6)

with the solution to the Fourier equation (equation 7.2) gives us an equation that allows us to derive thermal conductivity by measuring the resistance of the hot wire:

$$\Delta R = \frac{\rho_0 l \alpha q}{A 4\pi\lambda} \ln\left(\frac{4\kappa}{D^2 C} t\right) \tag{7.7}$$

Equation 7.7 is the key equation in the calculation of thermal conductivity. The fact that ρ_0, l, α, q, A, κ, D, and C are all constants at any given temperature means a plot of ΔR against $\ln t$ will be a straight line which has a gradient defined by $\frac{\rho_0 l \alpha q}{A 4\pi\lambda}$ meaning the gradient of the graph is inversely proportional to thermal conductivity (λ).

In spite of all of the values mentioned above being constants at any given temperature, precise measurement of all of these would be a challenge and errors measuring them could impact on the accuracy of thermal conductivity calculations. Therefore, the most common approach is to calibrate instruments used to measure thermal conductivity using fluids with known conductivities close to those that are of interest. The calibration process will be outlined in detail in section 7.1.2.5.

7.1.2. Instrument Design

Whilst the process of measuring the thermal conductivity of fluids is well known, as discussed in section 4.2.1 there are still few examples of commercially available instruments that are able to measure thermal conductivity of liquids to the degree of precision required for the analysis of nanofluids.

It was therefore decided that, in order to measure thermal conductivity of the nanofluids produced, to produce our own THW instrument. From the range of devices described in the literature we aimed to pick and choose features that would make our device as accurate and as easy to build as possible. The instrument was required to be able to measure the thermal conductivity of fluids over a range of temperatures with good certainty and reproducibility. It was therefore decided that making use of computerised data acquisition was essential in

order to improve both usability and precision of the instrument.

The start point of the design was the ASTM standard test method for measurement of thermal conductivity of liquids, D2717-95(2009).[396] This document details a THW instrument, made up of a thin, Teflon coated, platinum wire encased inside a glass vessel. However, it was decided that the precise glass components of this design would be both too fragile, and challenging to produce to make it a practical approach. For this reason, rather than following the ASTM standard exactly, it was decided to derive our own design, based both on the standard document and the range of designs in the literature. The key details of this design follow below

7.1.2.1. Measurement Cell

Instead of the glass design, specified in the ASTM standard, it was decided that a more practical approach would be to construct the measurement cell out of metal both for ease of production and durability. The measurement cell of our instrument was produced from a cylindrical tube of machined aluminium with a flange at either ends. For ease of cleaning the bottom of the cell is sealed with a flat metal plate, bolted onto the flange which seals using a rubber O-ring Removing this plate allows easy access to the bottom of the cell for cleaning of the instrument. In keeping with this, it was decided that the rest of the instrument's outer shell should be constructed from machined aluminium in order to protect the electronic components. The dimensions of the measurement cell were chosen in order for it to have an internal volume that matches the volume that nanofluids are produced in. The volume of the measurement cell produced was 72 ml. However, as a result of displacement due to the hot wire and its support, the sample volume required to take a measurement was significantly lower than this, at 28 ml.

Photographs and schematics of the final instrument are shown in figure 7.1. Full technical drawings and dimensions for the instrument's casing can also be found in Appendix A.

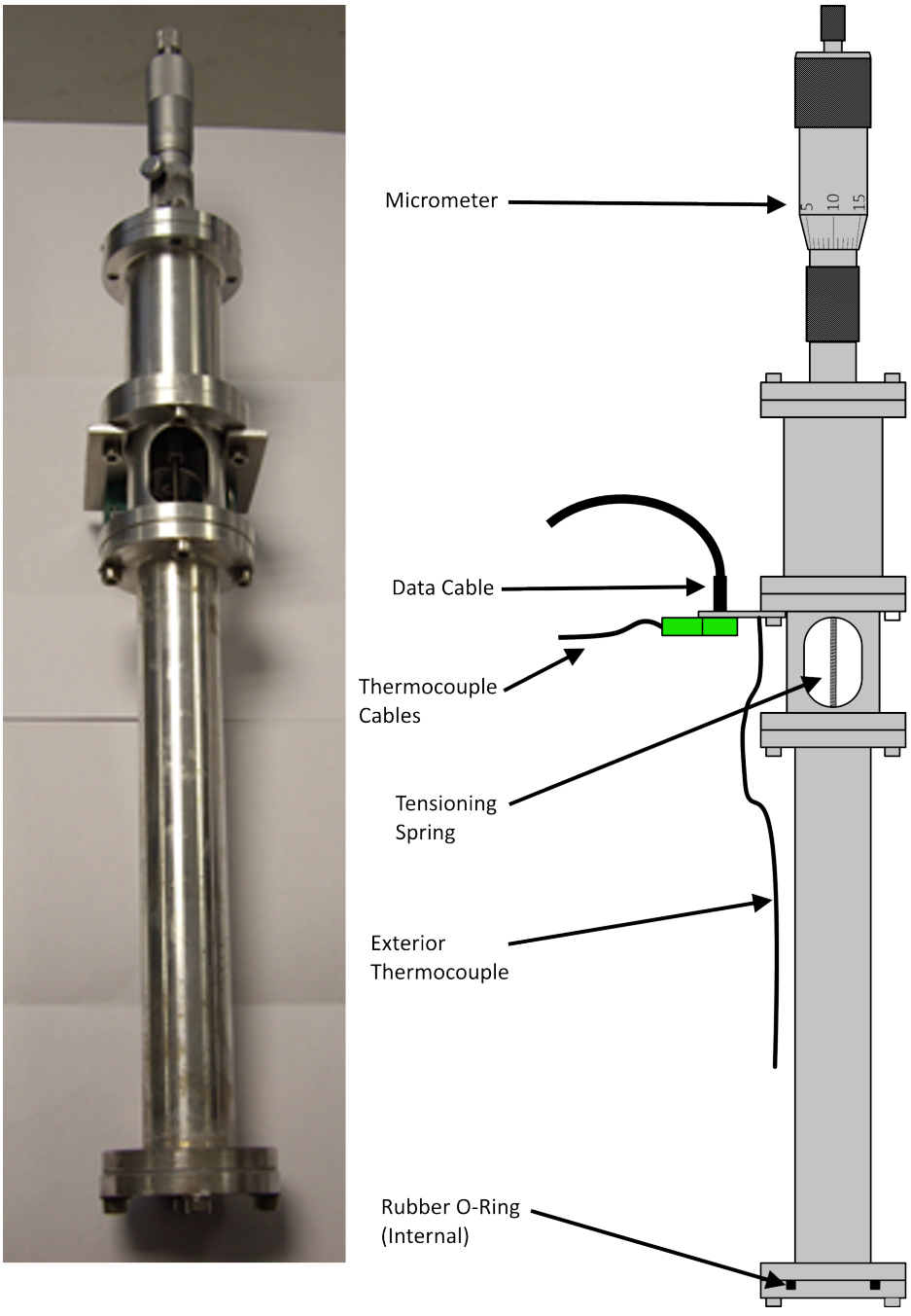

Figure 7.1: *(left) A photograph of the assembled THW instrument (right) A schematic of the instrument, showing: the micrometer for wire tension adjustment, the spring to maintain constant wire tension, the external thermocouple, and the outer casing of the instrument. The O-ring shown is sandwiched between the base plate and the cell body to create a watertight seal.*

7.1.2.2. Hot Wire

The hot wire is the key part of the THW instrument and its properties are vital to the success of the measurements. It is possible to make the hot wire out of a range of substances; however, those that perform best are materials with an extremely linear resistance to temperature relationship such as platinum or tantalum. In our case platinum was chosen due to the greater availability of fine diameter wire. The wire used has a diameter of 50 µm with a 9 µm Teflon coating. The insulating layer present on the platinum hot wire allows the thermal conductivity of electrically conducting liquids, such as water and water based coolants to be measured. This prevents current leakage into electrically conducting fluids, which can impact on the accuracy of results. The use of an insulated wire was originally proposed by Nagasaka and Nagashima who also proposed a series of mathematical corrections to the THW model in order to account for the presence of this insulating layer.[428] However, is has since been shown that these corrections are of negligible impact as long as the thickness of the insulating layer is less than the diameter of the wire.[429] In our instrument the hot wire is mounted in a rigid brass housing which has a half cylinder profile. This provides a strong base to mount the wire on and affords it some protection, whilst still leaving the wire accessible for cleaning. (figure 7.2)

An important design concern is that the hot wire must remain under tension in spite of any thermal expansion that occurs in the instrument. Several methods have been proposed to achieve this including: constructing the wire and support of the same material to make relative thermal expansion zero,[430] and utilising a fixed spring assembly to tension the hot wire.[431]

In order to isolate the hot wire from the effects of thermal expansion, both on the wire itself and the support it is mounted on, the top end of the hot wire in our instrument is attached to a small spring. The top of this spring is connected to a micrometer screw gauge which allows the tension on this spring, and thus on the wire itself, to be adjusted. The micrometer is used to set the tension on the spring such that the spring is sufficiently stretched

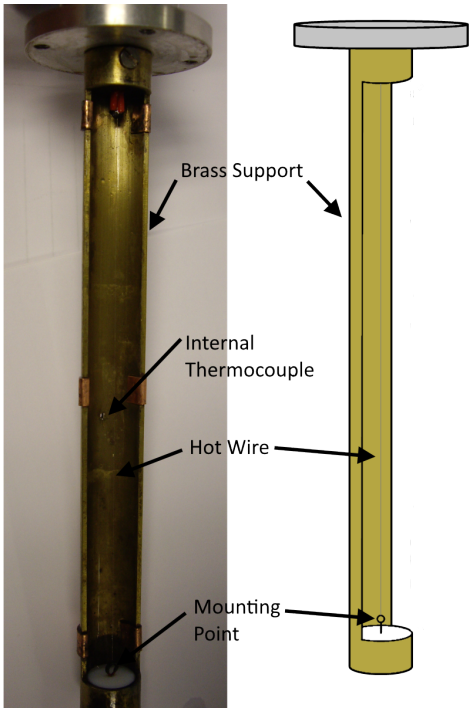

Figure 7.2: *(left) A photograph of the platinum hot wire mounted on its brass support (right) A schematic showing the mounting for the platinum wire, along with the position of the internal thermocouple.*

that if the wire were to expand, relative to its support, the spring would take up the slack and the wire would remain under tension: still acting as a linear heat source. However, it is also important that the tension on the spring not be too high, as this protects the wire from snapping if it were to contract relative to its support. The spring and micrometer assembly of the instrument are shown in figure 7.1.

7.1.2.3. Temperature Control

One of the key requirements for recording thermal conductivity data is the ability to take measurements over a range of well controlled temperatures. In order to achieve this certain elements were designed into the THW instrument. The instrument has been designed in such a way that the measurement cell can be immersed into a thermostatically controlled bath in order to set and maintain the measurement temperature. Temperature control was provided by a recirculating cooler which can pass thermally controlled fluid through the outside of a jacketed vessel; inside this vessel sits the measurement cell, surrounded by water to act as a thermal buffer (figure 7.3). In order to measure the temperature that readings

are taken at a pair of thermocouples are employed, one inside the measurement cell and the other outside, immersed in the bath surrounding the cell (figures 7.1 and 7.2). The choice to use a pair of thermocouples was made as it ensures that the temperature inside the bath is equilibrated with that inside the cell before measurements are taken, increasing the reliability of the instrument.

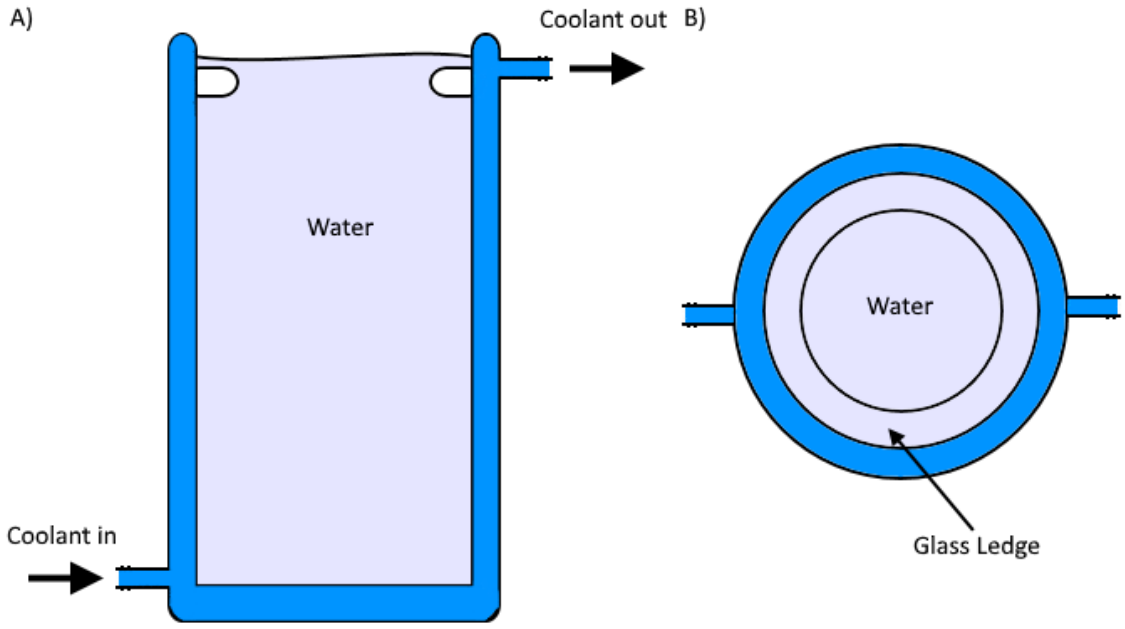

Figure 7.3: *A schematic showing the jacketed vessel used to control the temperature of the THW measurement cell in A) cross section, and B) plan view. The vessel is composed of hollow glass that is filled with coolant from a recirculating water bath. A glass lip surrounds the top of the vessel onto which the top flange of the measurement cell sits, suspending the cell within the vessel. The vessel is filled with water to act as a temperature buffer.*

7.1.2.4. Electronics

With the measurement cell design and construction complete, attention turned to the electronics required to record thermal conductivity measurements. As mentioned in section 7.1.1 the main goal of the instrument is to measure the resistance of the hot wire, which can then be converted to thermal conductivity. In order to achieve this the instrument makes use of a Wheatstone bridge circuit. This is a simple arrangement of four resistors which allows the resistance of an unknown component to be determined An example of a Wheatstone bridge circuit is shown in figure 7.4. If the resistances of R_1, R_2, and R_3 and

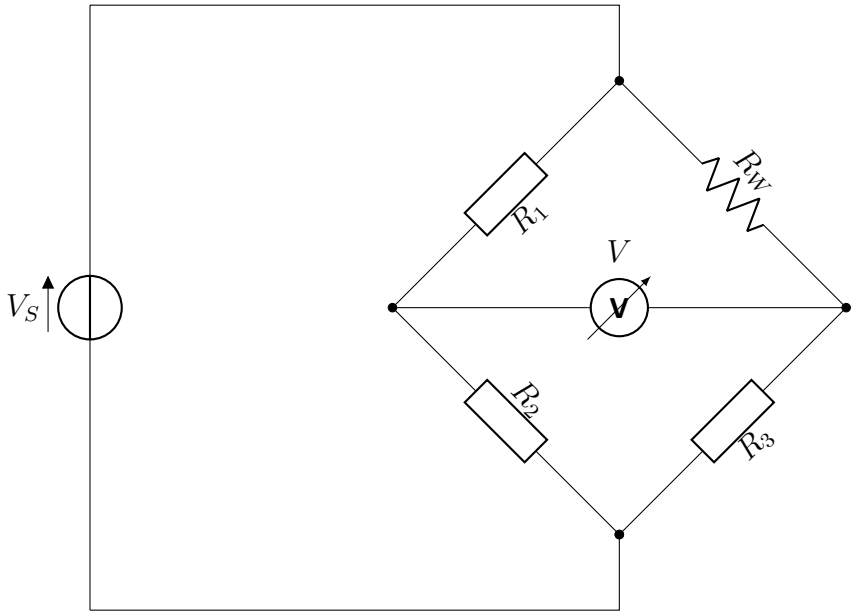

Figure 7.4: *A basic Wheatstone bridge circuit.*

V_S, the supply voltage, are all accurately known then it is possible to determine the resistance of the unknown component, R_W using equation 7.8 which is derived from Kirchhoff's laws.

$$V = \left(\frac{R_2}{R_1 + R_2} - \frac{R_3}{R_3 + R_W} \right) V_S \tag{7.8}$$

It is possible to simplify this situation further by replacing one of the resistors, R_2, with a variable resistor. This resistor can then be adjusted such that the voltage on the voltmeter, V, reads zero. In this configuration the Wheatstone bridge circuit is refereed to as being "in balance" and it is possible to simplify equation 7.8 to give the form shown in equation 7.9.

$$\begin{aligned} \frac{R_2}{R_1 + R_2} &= \frac{R_3}{R_3 + R_W} \\ R_W &= \frac{R_3 \left(R_1 + R_2 \right)}{R_2} - R_3 \end{aligned} \tag{7.9}$$

Instead of the usual practice of using a variable resistor to balance the Wheatstone bridge circuit our design, based on that of Bleazard and Teja, makes use of a switchable

decade array of resistors with very low temperature coefficients.[432,433] These resistors are arranged in such a way as to allow precise control of resistance over the range of 2000-3000 Ω at a resolution of 0.1 Ω. A circuit diagram for this setup is shown in figure 7.5. This has the advantage over a variable resistor of ensuring that the resistance of all components in the Wheatstone bridge is accurately known at any time, which is not possible with a variable resistor. This, in turn, significantly reduces the error in the thermal conductivity measurements made.

Whilst the above components are essential to making accurate thermal conductivity measurements certain other electronic circuitry is required simply to operate the instrument. The key parts are outlined below.

In order to balance the bridge before the start of the measurement it is necessary to apply a load across the Wheatstone bridge. However, if this were done using the full voltage load, V_S, it would cause the temperature of the wire and sample to rise, due to the current passing through the wire. Therefore the instrument is designed to be able to provide a reduced power supply for the purpose of balancing the bridge. This supply, of 0.1 V and the full supply of 10 V can be switched as required using a relay.

As the measurement taken by the instrument is one of resistance, it is important that the internal resistance of the apparatus does not change during the recording of data as this would cause drift in the results obtained. The main likely cause for this would be changes in the temperature of components due to the high current loads imposed. In order to prevent this, a "warm-up" step was introduced into the operating protocol. In order to allow the instrument to warm up without placing a current load onto the hot wire, changing the temperature of the sample, an extra resistor was added into the circuit with a similar resistance to that of the wire (8 Ω). This could be switched in to the circuit in place of the hot wire, though the use of relays, allowing the circuit to be loaded so it can reach thermal equilibrium. The component most susceptible to thermal variation is R_3 as, although it has a very low temperature coefficient, its current load is $\sim$0.55 A (meaning it dissipates around 3 W).

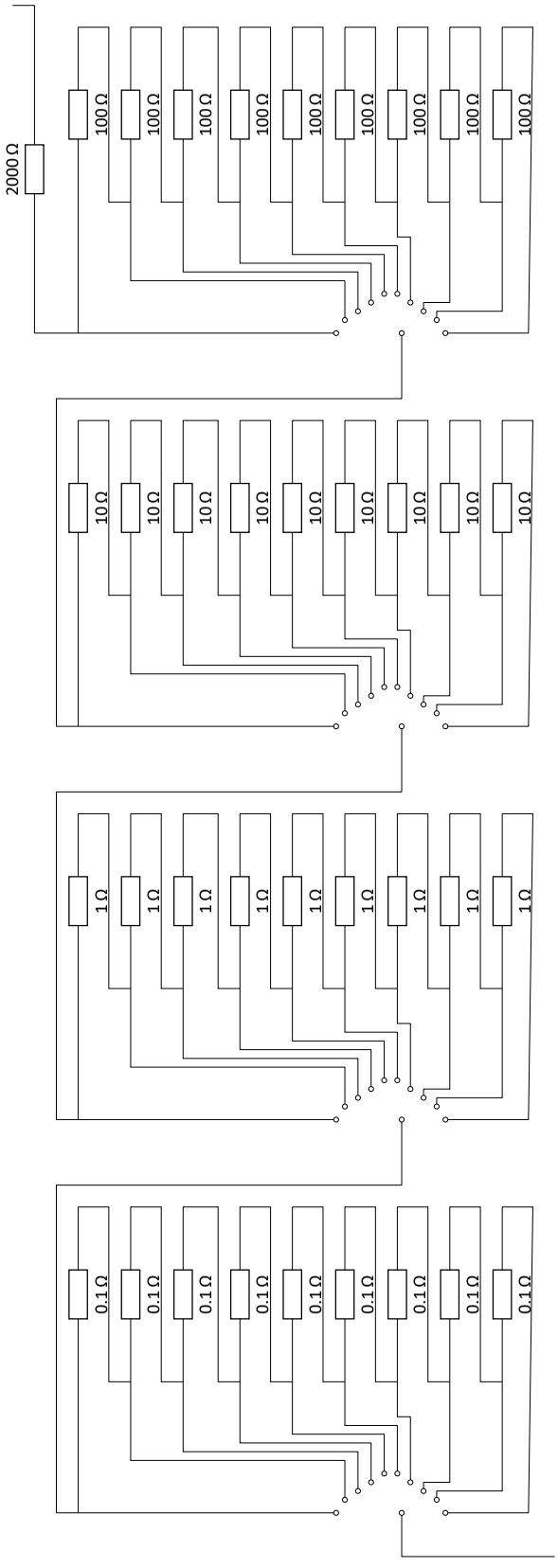

Figure 7.5: *The decade array of resistors used to replace the variable resistor in our hot wire apparatus.*

For this reason R_3 is mounted on a block of metal to act as a heat sink and help the resistor maintain a stable temperature while the instrument is in use.

7.1.2.5. Calibration

In order to obtain accurate measurements of thermal conductivity from the apparatus it is necessary to calibrate it using a fluid of a known thermal conductivity. If done properly, this will produce a calibration curve which allows the conversion of the data output by the instrument into thermal conductivity. This calibration will account for all other constants that affect the output of the instrument. As discussed in section 7.1.1 plotting $\ln t$ against ΔR will give a graph with a straight line with the equation:

$$\Delta R = \frac{\rho_0 l \alpha q}{A 4 \pi \lambda} \ln\left(\frac{4\kappa}{D^2 C} t\right) \tag{7.10}$$

which has a gradient of $\frac{\rho_0 l \alpha q}{A 4 \pi \lambda}$. The goal of calibration will be to determine a calibration constant, m, such that

$$\frac{d\Delta R}{d \ln t} = \frac{\rho_0 l \alpha q}{A 4 \pi \lambda} = \frac{m}{\lambda} \tag{7.11}$$

This allows simple conversion of gradient to thermal conductivity without it being required to measure the value of all the other constants included in the mathematical model.

Determination of m requires measurements to be taken for a fluid of known thermal conductivity over the operational temperature range of the instrument (5-65 °C). Ideally the fluid chosen should have as close a thermal conductivity to the fluids of interest as possible and for this reason it was decided that high purity water would be used as a calibrant. The thermal conductivity of water has been widely reported in the literature.[434]

The instrument was run using high purity water at intervals of 5 °C between 5 °C and 65 °C, repeating 20 times at each temperature. The data obtained was processed (as de-

scribed in section 7.1.3) in order to obtain a gradient for each measurement. These gradients were then plotted against the thermal conductivity of water to produce a calibration graph which can be used to calculate thermal conductivity for any fluid from the output of the instrument.

7.1.2.6. Computer Control and Data Acquisition

The measurements taken by the instrument were recorded using a National Instruments (NI) data acquisition (DAQ) card, which is also used to electronically control the instrument, giving an easily and precisely repeatable measurement protocol every time the instrument is used.

The DAQ card is configured to monitor inputs from the voltage across the Wheatstone bridge, the power supply voltage, and the thermocouples. However, in order to provide full computer control a series of outputs from the DAQ card were also configured to control the operation of the instrument. These consist of 1 analogue output channel of 0.1 V to be used as a supply voltage when balancing the bridge circuit as well as a series of digital outputs which are used to operate relays controlling switching the hot wire with the fixed resistor, activating the full voltage supply or the 0.1 V supply and switching the voltage supply on and off. Together, these outputs and inputs allow for automated running of the instrument with only minimal input from the user. In order to implement this automation it was decided to make use of the NI LabVIEW software package as this provides drivers for the NI DAQ card used and could be used to automate the operation of the instrument. A brief version of the procedure used to take thermal conductivity measurements is outlined below.

To take a measurement a sample is placed in the cell and this is them placed into the thermally controlled bath and allowed to equilibrate. Meanwhile the electronics are allowed to warm up by setting the full supply voltage, V_S, to 10 V and ensuring the hot wire is switched out of the circuit for the fixed resistor. In order to ensure all components reach thermal equilibrium the time of this warmup period can be adjusted within the LabVIEW program.

Through experimentation and monitoring for thermal drift in the voltage output of the instrument it was discovered that 90 minutes was a sufficient warmup time. As the fixed resistor, used in place of the hot wire, has a similar resistance to the wire it is possible to use this time to roughly balance the bridge and the bridge voltage is displayed by the front-end of the LabVIEW script to allow this.

In the meantime, the temperature of the thermostatic bath can be set and the sample's temperature can be allowed to equilibrate. This is achieved by monitoring both the internal and external thermocouples on the instrument, waiting for them to both show the same temperature. After the warmup and equilibration are complete, the electronics can then be set up to record a measurement. The LabVIEW script prompts the relays to switch the full voltage supply for the 0.1 V supply, and to switch the hot wire into the Wheatstone bridge in place of the fixed resistor. At this point the decade array of resistors should be adjusted to precisely balance the bridge and the value of R_2 recorded, allowing R_{W_0} to be calculated. As soon as the bridge is balanced measurements can then immediately begin. The LabVIEW script will prompt the full voltage supply to be restored and data acquisition can begin. The DAQ card is set to record the voltage across the Wheatstone bridge at a frequency of 1000 Hz over a period of 3 s. This time period is kept short as after this time the data no longer fits the models described in section 7.1.1 due to the effects of convection and so is no longer useful in determining thermal conductivity. At the end of the measurement the voltage load is removed from the wire and the system is allowed to relax for a few seconds. The script then repeats the measurement procedure as many times as requested and automatically saves the data as individual .txt files containing the time and voltages.

In order to increase the automation of the script it was modified in order to allow a delay to be introduced after a set of measurements had been taken. This allows the instrument to monitor the thermal conductivity of a system at a constant temperature, at set intervals over a long time period without input from the user, assuming the bridge balance remains constant which it has been observed to during testing. A copy of the LabVIEW script is included in Appendix B

7.1.3. Data Processing

As has been described above, the transient hot wire instrument we have designed allows us to measure ΔR over time as a current is passed through the wire. Making use of the models described in section 7.1.1 it is then possible to process this data to give the thermal conductivity of the fluid surrounding the wire using a plot of ΔR against $\ln(t)$. From this plot the gradient of the linear region can be used to determine the thermal conductivity.

In order to achieve repeatable and efficient data processing a Python script was created in order to both identify the linear region of the data from the hot wire instrument, and then plot a line of best fit over this data range to extract the gradient, which can then be converted to thermal conductivity. In order to achieve these goals a linear regression model was used to obtain the line of best fit for the data, due to the fact the ideal data from the models should be linear.

As mentioned above, for the calculation of thermal conductivity, a plot of ΔR against $\ln(t)$ is needed. However, the raw output from the instrument is not in this format and so some initial processing is necessary. The output file from the THW is made up of 2 data streams: time, and voltage. The conversion of t to $\ln(t)$ is trivial, although the first data point ($t = 0$) must be removed from the data before this operation as $\ln(0)$ is undefined. Conversion of V to ΔR is more involved and requires the use of the resistances within the Wheatstone bridge, discussed in section 7.1.2.4. The value for R_2 (the resistance of the variable resistance, figure 7.4) is recorded at the time the experiment was run and this value is imported into the Python script and, with the values of R_1 and R_3 (2000.0 Ω and 10.0 Ω respectively), is used to calculate the resistance of the hot wire at the start of the experiment (R_{W_0} *via* equation 7.12. The resistance of the hot wire at time t (R_{W_t}) can then be calculated (equation 7.13) using the voltage at time t (V_t) and the supply voltage, V_S (10.0 V). Taking the difference between R_{W_t} and R_{W_0} (equation 7.14) gives ΔR at any given time, t. ΔR can then be plotted against $\ln(t)$. An example of the data processed and plotted by the Python script is shown in figure 7.6.

$$R_{W_0} = \frac{R_3(R_1 + R_2)}{R_2} - R_3 \tag{7.12}$$

$$R_{W_t} = R_3 \left(\frac{V_S(R_1 + R_2)}{R_2 V_S - V_t(R_1 + R_2)} - 1 \right) \tag{7.13}$$

$$\Delta R = R_{W_t} - R_{W_0} = R_3 \left(\frac{V_S\,(R_1 + R_2)}{R_2 V_S - V_t\,(R_1 + R_2)} - \frac{R_1 + R_2}{R_2} \right) \tag{7.14}$$

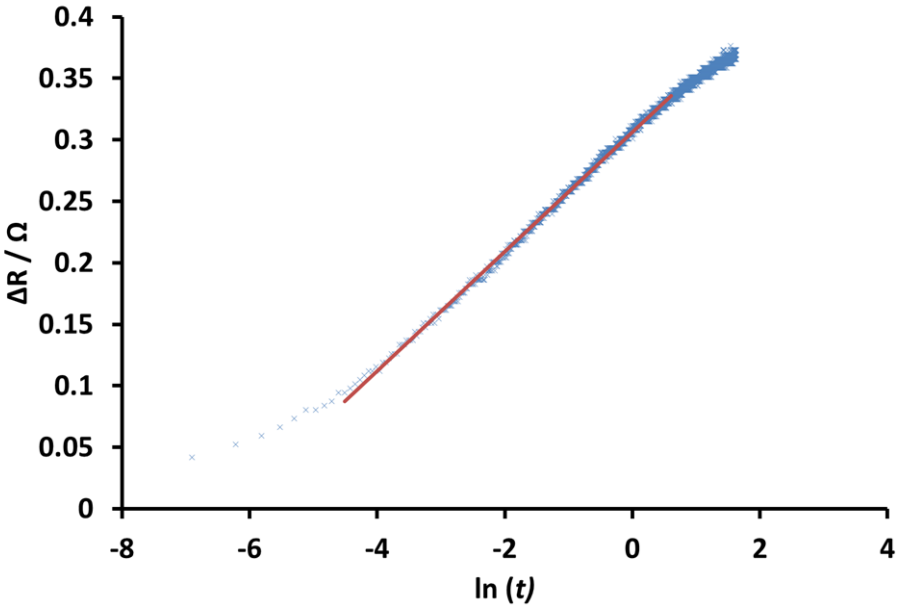

Figure 7.6: *An example of the plotted output of the THW data from the Python script used for data processing with the raw data shown as blue crosses, and the line of best fit determined by the program shown as a red line.*

Having plotted the data in the appropriate form, the main remaining challenge is the process of isolating the linear region of the data from the full data set. Due to experimental variability, and the frequency at which data is recorded, this linear region does not occur over the same values of $\ln(t)$ on each use of the instrument, particularly if the measurement temperature is changed. The approach taken to identify the region of interest in the data made use of the coefficient of determination (R^2) that can be extracted from any linear regression trend-line and gives information on how closely aligned the raw data is with that trend-line. This means, when plotting a linear trend line, that the value of R^2 will be at its

maximum when the data it is based on is also linear.

The Python script produced identified the linear region of the data by performing linear regression over data sets with every possible start and end point (above a minimum dataset length of 100 data points) and to select the data range with the highest value of R^2, which is the region that fits the linear regression most closely, and therefore that which is most linear in character. The linear regression model from this data range was then saved which gave the gradient of the linear portion of the graph. This gradient, as discussed in section 7.1.1, is inversely proportional to the thermal conductivity of the sample being measured. Once the unit has been calibrated, as described in section 7.1.2.5, it is then possible to convert this gradient into a thermal conductivity.

Whilst the above procedure was a great aid in removing the subjective element of data processing for the THW instrument, the large number of repeat readings taken (>20 at each temperature) meant that running the processing script on each of these data sets was a time consuming process. To aid this, the script was modified so that it could automatically detect the output files saved in a given directory, eliminate those that had been previously processed, and perform analysis on each remaining file in turn, automatically repeating this process for results taken at different temperatures or times, without the need for any user input. The results were saved as both a pictorial graph, in .png format (for quick visual confirmation that results are valid, an example of which is shown in figure 7.6), and as a .csv file containing all the numerical results generated for the files in that folder. This greatly improved the efficiency of processing data from the THW instrument. A full copy of the code used to process the data has been included in Appendix C.

7.2. Dispersion of GO in Coolant

In an attempt to test the impact of GO as an additive on the thermal properties of an applied thermal fluid dispersions of GO were produced in an automotive coolant provided

by Shell Global Solutions. This coolant is composed of approximately 97 % distilled water, combined with a commercial additive package containing corrosion inhibitors, heat transfer agents, and surface tension modifiers.

Due to the fact that the coolant is largely water based, potential graphene additives that will form stable dispersions will need to be hydrophilic, and therefore GO is an obvious choice. In order to test the ability of the coolant to disperse GO, as produced GO (synthesised using the Hummers method described in section 8.3.1) was dispersed in the commercial coolant by ultrasonication, as described in section 8.3.5, but at a concentration of approximately 5 mg ml^{-1}. Since as produced graphite oxide is synthesised as a slurry of graphite oxide in water the concentration of this slurry must be determined to allow dispersions of known concentrations to be produced. This was achieved *via* TGA. As produced graphite oxide was heated to 100 °C and held at this temperature until a constant mass was achieved. Mass loss at this temperature is likely to be due to the evaporation of solvent, and so the residual mass can be used to determine the concentration of graphite oxide in the slurry. For the graphite oxide used in this study, concentration was found to be 5.8 %.

It was observed that the dispersions produced were of an opaque brown colour due to the high concentration of GO suspended and that no GO was seen to settle out, indicating excellent stability of GO in the coolant.

As a result of the success of these trial dispersions it was decided to scale up the production of these nanofluids to produce a sufficient volume to use in a full scale engine test. This required 50 l of the GO-coolant dispersion to be produced. Doing this using the lab scale method of sonication used elsewhere in this work would be extremely impractical and time consuming as the effective sonication volume for the probe sonicator is limited to 50 ml. In order to practically achieve the production of nanofluids at the volumes required a different setup for sonication was devised which involved the use of a reservoir of coolant flowing, *via* a peristaltic pump, to a glass vessel surrounding the probe sonicator. Allowing the nanofluid to flow through the system ensures that a far greater volume of liquid can be sonicated. A

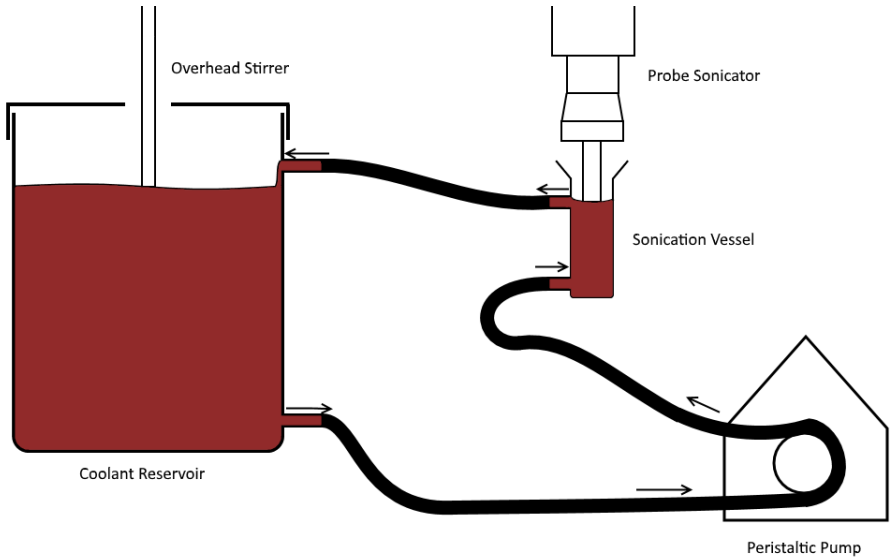

Figure 7.7: *A schematic of the flow sonication setup utilised for large volume production of nanofluids.*

schematic for this setup is shown in figure 7.7 and full details of the process used are presented in section 8.3.23.

Briefly, dispersions were produced by sonicating 3 l batches of coolant, mixed with 6 g of as produced graphite oxide for 2.5 h at 40 % sonication intensity. This aimed to produce a dispersion of GO with a concentration of 2 mg ml^{-1}. The peristaltic pump was set at a flow rate such that all of the coolant in the system would undergo sonication. This process was repeated to produce 51 l of dispersed GO in coolant.

The dispersion produced using this method was stable over a period of months, with no change in colour, turbidity or sedimented material at the bottom of the vessel. Due to the limitations of UV-Vis spectroscopy of GO (discussed in section 6.2.1) the concentration of the dispersion produced was determined gravimetrically. One factor that must be considered when doing this is that the additive package in the coolant will not evaporate and so its residual mass must be taken into account. 5 ml samples of pure coolant and GO-coolant nanofluids were heated under vacuum at 80 °C and were weighed at regular time intervals until the residual mass in the vials was constant. Subtracting the mean residual mass of the pure coolant from that of the GO-coolant dispersion, gave the residual mass of GO which could then be used to determine concentration. The results are presented in

table 7.1 and show that the GO-coolant dispersion had a final concentration of 0.5 mg ml^{-1}. Full details of this process are found in section 8.1.15. This was significantly lower than the theoretical maximum concentration for this dispersion of 2 mg ml^{-1}, however, the GO that was dispersed was stable over a long period of time and well dispersed.

Table 7.1: *Residual masses after heating under vacuum at 80 °C until constant mass was achieved for 5 ml vials of pure coolant and GO-coolant dispersions.*

Pure coolant residual / mg	43.8
GO-coolant residual mass / mg	68.8
GO residual mass / mg	25.0
GO Concentration / mg ml^{-1}	0.5

When testing the coolant in applications its pH is required to be in the range of 7-9 in order to avoid corrosion. This is unfortunate as GO is acidic an so was observed to cause a drop in pH of the coolant. To counteract this small quantities of 5 M NaOH were added to the coolant GO dispersion in order to raise the pH back to 8. The GO-coolant dispersion was shipped to Shell Global Solutions to allow its potential in a full scale system to be tested.

7.3. Thermal properties of Dispersions of GO

Given that the main application of coolants is to draw heat away from components it should be evident that the key properties of interest for GO-coolant nanofluids are their thermal properties. In order to investigate the effects of the addition of GO on the thermal properties of the GO-coolant dispersion the specific heat capacity and thermal conductivity of dispersions were studied using DSC and the THW methods as described in sections 4.2.1 and 4.2.2 respectively.

7.3.1. Specific Heat Capacity

The specific heat capacity of both the pure coolant and the GO-coolant dispersion were determined by DSC. The procedure used to obtain these data followed ASTM E1269-11 and is described in detail in section 8.1.12.[398] In brief, the liquid being tested is placed into hermet-

ically sealed DSC pans and its heat flux is measured over the temperature range of interest. The heat flux of an empty pan is then subtracted from this value to give the heat flux of the sample. This value is then used to calculate the specific heat capacity of the sample using a standard - in this case pure coolant measured by Shell Global Solutions.

When testing the specific heat capacity of liquids it is very important that the mass of the sample being tested does not change over the course of the measurement, as this will significantly affect the heat capacity calculated. As the coolant is majority water then evaporation will be an issue and could cause a change is mass. In order to mitigate this, 2 steps are taken. Firstly, hermetically sealed DSC pans should be used to prevent any solvent that does evaporate from escaping and causing a change in mass. Secondly, the temperature range of measurement should be carefully chosen to minimise evaporation, and the potential build up of high pressure in the pan due to the formation of gasses.

When studying the coolant, the ideal temperature range for measurement of specific heat capacity would match that of the engines it would be used in ($\sim$120 °C). However, as the main component of the coolant is water, this would cause significant evaporation (in engines this is avoided by pressurisation of the system). In spite of the pans being hermetically sealed, any significant pressure rises will result in the pans bursting. Therefore, when measuring specific heat capacity of the coolant, temperatures lower than the operating temperature must be used . For this reason specific heat capacity was measured over the range of 20-45 °C.

The specific heat capacities of pure coolant and the GO-coolant dispersion, are shown in figure 7.8. These data show that the addition of GO to the coolant causes an increase in the specific heat capacity of the coolant with over a 7 % rise in specific heat capacity observed at 45 °C. This is promising behaviour for the GO-coolant dispersion as higher heat capacities are favourable for coolants, since a smaller volume of coolant will be able to absorb the same amount of thermal energy. However, as a result of the limitations of this technique, discussed above, it is not possible to determine what the change in specific heat capacity

of the GO-coolant dispersion would be at the operating temperatures of the engine. The only way to determine the full impact of the GO on the coolant under operating conditions would be to perform a full scale engine test on the coolant.

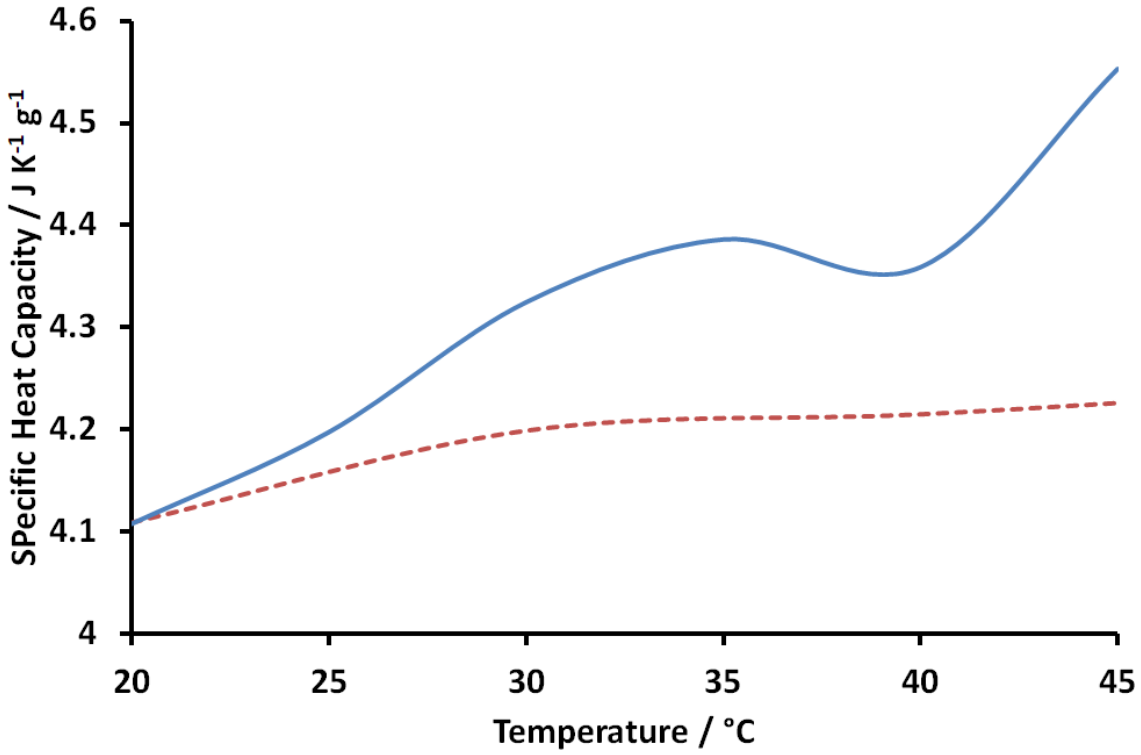

Figure 7.8: *The specific heat capacity of pure coolant (red dotted line) and a GO-coolant dispersion (solid blue line) as determined by DSC.*

7.3.2. Thermal Conductivity

In addition to testing the specific heat capacity of the coolant-GO dispersion, attempts were made to test its thermal conductivity using the instrument described in section 7.1. Initial tests were performed on the pure coolant, in order to measure its thermal conductivity.

Unfortunately, whenever measurements were taken with coolant in the measurement cell the platinum hot wire would break after approximately 50 measurements being taken. The reasons for this occurring are not entirely clear and this behaviour had not been observed when calibrating the instrument using high purity water. For this reason it is believed that one of the components of the additive package, used to create the coolant, is causing

degradation of the platinum wire, causing it to snap under the tension it is placed under by the instrument.

In spite of this, it was possible to collect some limited thermal conductivity data from the coolant and the GO-coolant dispersion. The procedure used to collect these data is described in section 8.1.13. Briefly, the thermostatic water bath was used to control the temperature of the measurement cell. Once the thermocouples inside and outside the cell were displaying the same temperature then the bridge was balanced and the instrument was used to measure the thermal conductivity of the sample. This was repeated 20 times at a given temperature before the thermostatic bath was used to increase the temperature of the system by 5 °C and the measurement repeated at the new temperature.

Ideally the range of temperatures over which the thermal conductivity is measured over should match up with the operating temperatures of the coolant in applications. However, as discussed previously the coolant is generally used in pressurised cooling systems at temperatures of 120 °C and due to the limitations of the thermostatic bath used it was not possible to exceed measurement temperatures of 80 °C. On top of this it appears that the degradation of the hot wire in the coolant is exacerbated at increased temperatures, meaning that no thermal conductivity values for the coolant were able to be obtained at temperatures above 45 °C.

The thermal conductivity of the pure coolant and the GO-coolant dispersion between 5-45 °C are shown in figure 7.9 and table 7.2. These data clearly show that the addition of GO to the coolant caused an increase in thermal conductivity of the coolant across all temperatures measured, with a percentage increase of 1.0-8.3 %.

As a result of the challenges of measuring the thermal conductivity of coolant and coolant dispersions with our instrument, further studies from this point were carried out on water, and dispersions of GO in water to determine the impact of GO on the thermal properties of water based fluids.

Table 7.2: *The thermal conductivity of the GO coolant dispersion produced compared with that of the pure coolant, alongside the percentage increase.*

Temperature / °C	Thermal Conductivity / W m^{-1} K^{-1}		Percentage Increase / %
	Pure Coolant	GO-Coolant Dispersion	
5	0.560 ± 0.002	0.577 ± 0.003	3.1
10	0.570 ± 0.001	0.580 ± 0.002	1.8
15	0.577 ± 0.002	0.589 ± 0.002	2.0
20	0.586 ± 0.002	0.593 ± 0.002	1.0
25	0.584 ± 0.002	0.611 ± 0.004	4.6
30	0.596 ± 0.003	0.646 ± 0.006	8.3
35	0.607 ± 0.002	0.643 ± 0.004	6.0
40	0.619 ± 0.003	0.633 ± 0.003	2.1
45	0.633 ± 0.003	0.640 ± 0.006	1.2

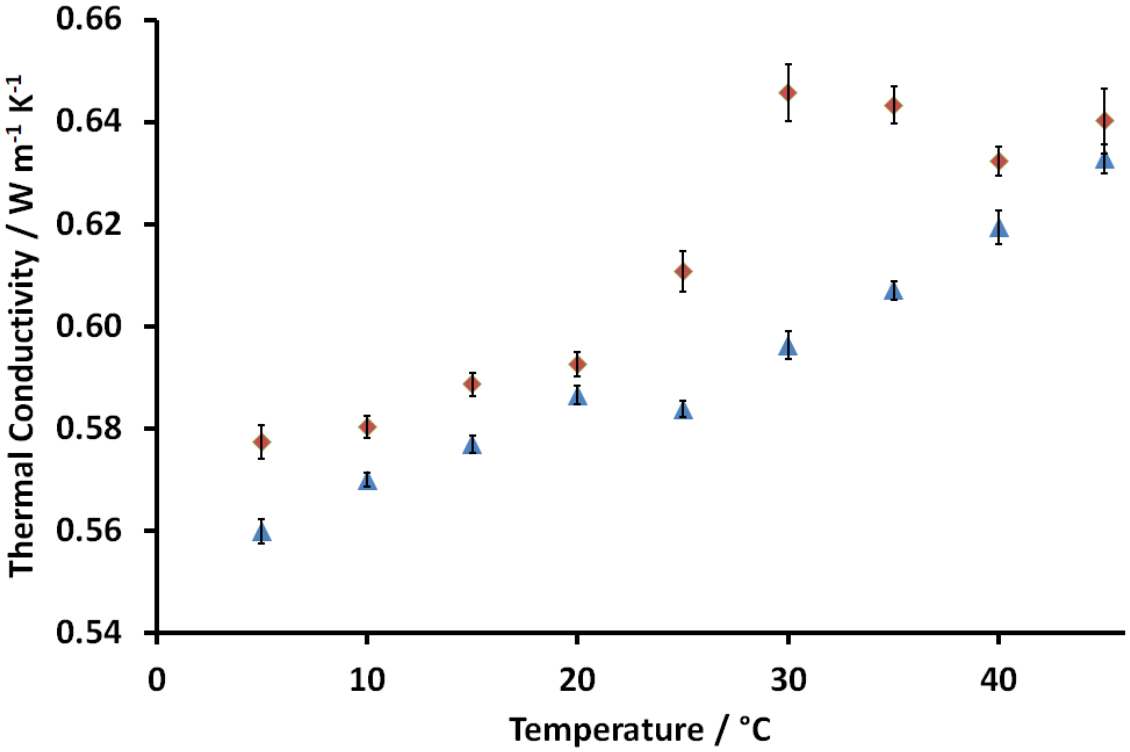

Figure 7.9: *The thermal conductivity of pure coolant (blue triangles) and the GO-coolant dispersion (red diamonds) over a range of temperatures.*

One concern that cannot be ignored when utilising GO as an additive in thermal fluids is the fact that GO undergoes reduction to rGO when held at an elevated temperature in solvents as discussed in section 1.6.1.3. As the operating temperature of the coolant is around 120 °C it is likely that under these conditions reduction would occur. If this were to occur then this could either have a positive or negative effect on the thermal conductivity of the dispersion as a result of the properties of the rGO formed.

rGO is well known to have a higher thermal conductivity than GO, as a result of its less defective structure and as a result of this it might be expected that the thermal conductivity of a dispersion of GO would increase as a result of the conversion of GO to rGO. However, it should not be ignored that this reduction also has a significant impact on the solution properties of the dispersed material. rGO is known to be significantly less dispersible in polar solvents than GO is and so it is likely that the thermal reduction of a high concentration dispersion of GO will lead to a significant decrease in the concentration of additive that can be maintained in solution which would have a negative impact on the thermal conductivity of the dispersion. Therefore, the overall impact on the thermal conductivity of the dispersion will depend on the balance of these two factors, which could lead to either a rise or a fall in thermal conductivity as a result of the reduction of GO.

In order to investigate the impact of heating, and the potential reduction of GO, on the thermal conductivity of dispersions, dispersions of GO in water were produced at 2.5 mg ml^{-1} and their thermal conductivities at a a range of temperatures, from 5-75 °C were measured. These data are presented in figure 7.10 and table 7.3.

These data clearly show that the presence of GO in the water dispersion has an effect on the thermal conductivity. At temperatures below 40 °C it is not possible to determine if the presence of GO has had an effect on the thermal conductivity of the dispersion due to the errors on the data recorded. However, above 40 °C it can be seen that a clear increase in thermal conductivity occurs as a result of the presence of GO. One observation that was made when recording these data is that the colour of the GO dispersion changed as a re-

Table 7.3: *The thermal conductivity of the GO-water dispersion produced compared with that of pure water, alongside the percentage increase.*

Temperature / °C	Thermal Conductivity / W m^{-1} K^{-1}		Percentage Increase / %
	Pure Water	GO-Water Dispersion	
5	0.568 ± 0.003	0.575 ± 0.012	1.4
10	0.578 ± 0.003	0.587 ± 0.012	1.6
15	0.588 ± 0.003	0.597 ± 0.012	1.5
20	0.598 ± 0.004	0.603 ± 0.012	0.9
25	0.606 ± 0.004	0.606 ± 0.014	-0.1
30	0.615 ± 0.004	0.631 ± 0.025	2.7
35	0.622 ± 0.004	0.630 ± 0.024	1.2
40	0.630 ± 0.004	0.645 ± 0.022	2.5
45	0.636 ± 0.004	0.652 ± 0.010	2.4
50	0.642 ± 0.004	0.665 ± 0.009	3.6
55	0.648 ± 0.004	0.674 ± 0.018	4.1
60	0.653 ± 0.004	0.676 ± 0.013	3.6
65	0.657 ± 0.004	0.682 ± 0.011	3.8
70	0.661 ± 0.004	0.691 ± 0.013	4.4
75	0.664 ± 0.004	0.699 ± 0.015	5.2

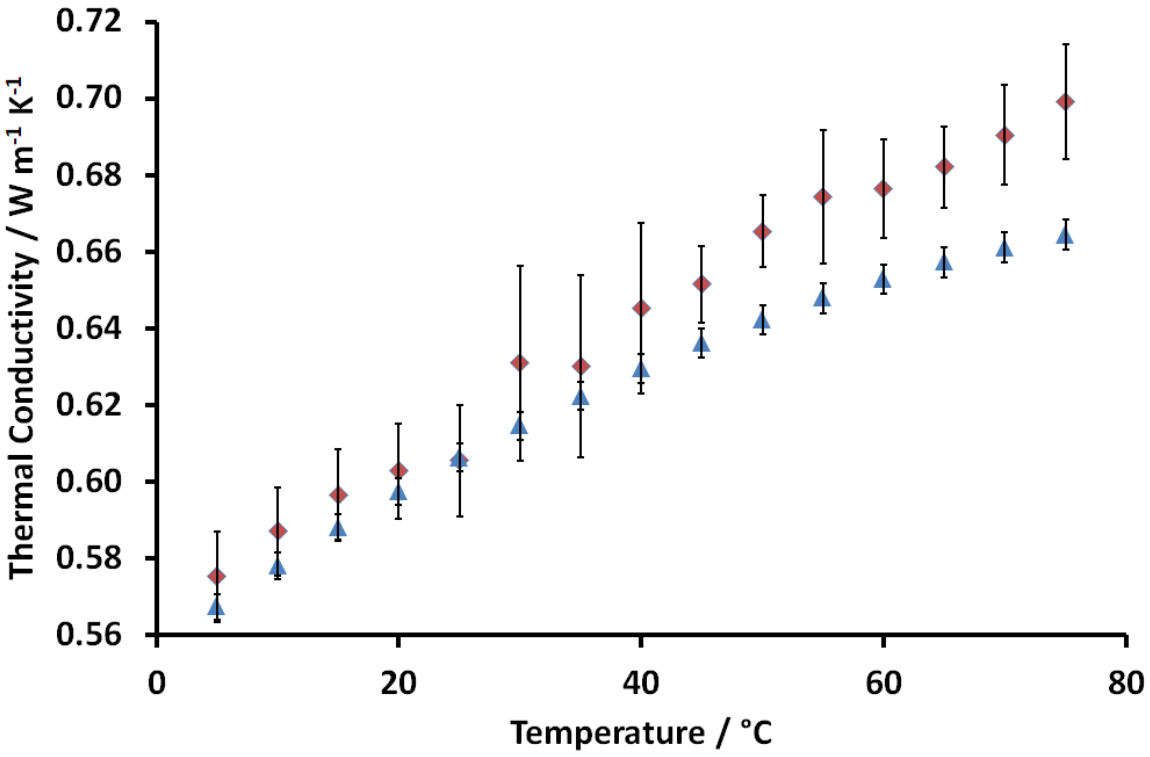

Figure 7.10: *The thermal conductivity of water (blue triangles) and the GO-water dispersion (red diamonds) over a range of temperatures.*

sult of being heated from brown to black which can be an indication of reduction. It was also observed that some particles of graphene material had dropped out of solution in the instrument.

In order to assess the degree of reduction that has occurred to the GO during the measurement of thermal conductivity the dispersion, after measurement, was analysed by UV-Vis spectroscopy. Using the position of the $\pi \rightarrow \pi^*$ plasmon peak the extent of reduction could be determined. Measurements were taken on the GO dispersion prior to testing of thermal conductivity, the solution after testing, and on a dispersion of the particulates that dropped out of solution during thermal conductivity testing. These data are shown in figure 7.11. The position of the $\pi \rightarrow \pi^*$ plasmon peak for each of these spectra is shown in table 7.4. These data clearly show no significant change in the either the position of the $\pi \rightarrow \pi^*$ plasmon peak, or the line shape in UV-Vis spectroscopy as a result of the measurement of thermal conductivity described above implying that no reduction of GO has occurred and so any changes in thermal conductivity reported are due to the quantity of GO in the dispersion and not its reduction to rGO.

Table 7.4: *The position of the $\pi \rightarrow \pi^*$ plasmon peak in the UV-Vis spectra of dispersions GO in water before and after measurement of thermal conductivity.*

	Position of $\pi \rightarrow \pi^*$ plasmon peak / nm
Before	230.5
Solution After	230.8
Particles After	230.2

From previous work on the reduction of GO by heating in solvents it is known that this reaction can take some time and the full reduction possible under these conditions may not have occurred during the measurements detailed above. For this reason, the program controlling the THW instrument was adapted to measure the thermal conductivity of the dispersion, held at a set temperature, at known time intervals. This measurement procedure is described in detail in section 8.1.13. Dispersions of GO were created by sonicating as produced graphite oxide in water and their thermal conductivities were tested at elevated temperatures over a period of 24 h to determine the effect of elevated temperature on the

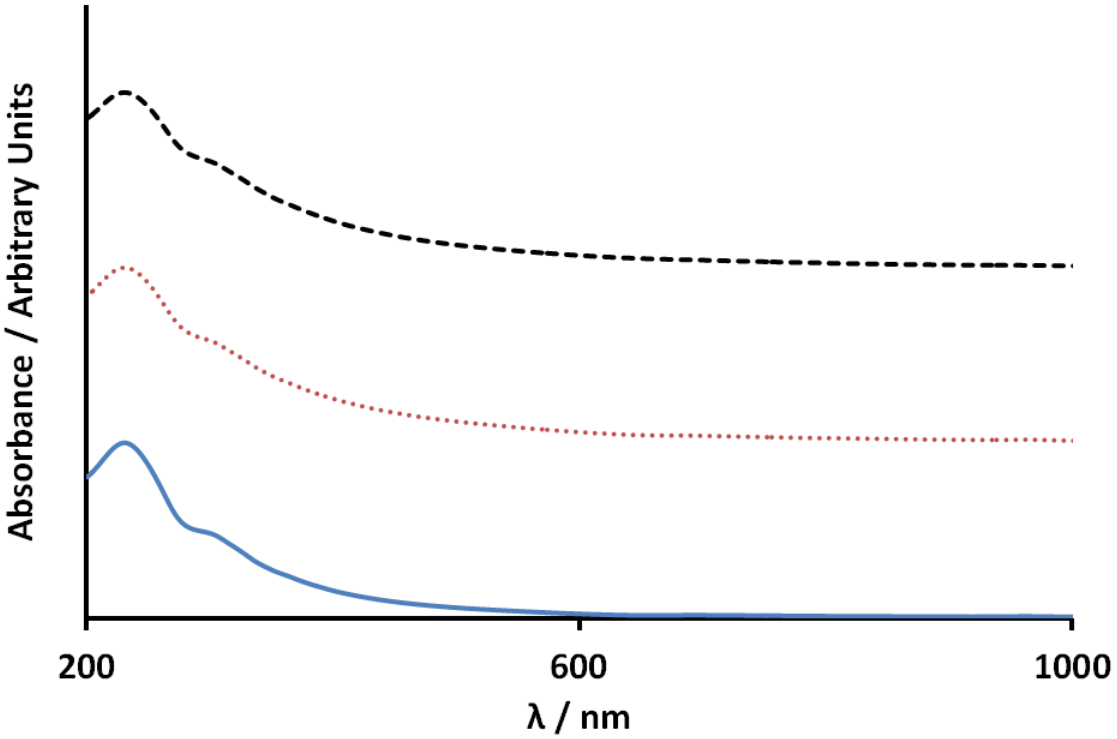

Figure 7.11: *UV-vis spectroscopy of the dispersion of GO prior to thermal conductivity testing (blue line), the solution after testing (red dotted line), and a dispersion of the particles that dropped out of solution during testing (black dashed line).*

thermal conductivity of the dispersion. The thermal conductivity of a 2.5 mg ml^{-1} dispersion of GO in water, held at 60 °C over a period of 24 h is shown in figure 7.12.

These data clearly show that, over the first few hours of the measurement, there is a decrease in the measured thermal conductivity of the GO dispersion before the thermal conductivity stabilises at 0.63$\pm$0.03 W m^{-1} K^{-1} after 5 h at 60 °C. From this behaviour it is evident that some change is occurring over the measurement period which is affecting the thermal conductivity of the dispersion.

In order to assess if any change was occurring in the degree of reduction of the GO in the dispersion during the thermal conductivity measurement the position of the $\pi \rightarrow \pi^*$ plasmon peak was analysed both before and after the thermal conductivity measurement and these data are shown in figure 7.13 and table 7.5. The fact that there is no significant change in peak position indicated that no significant reduction is occurring to the GO additive in the nanofluid as a result of heating to 60 °C for 24 h. Therefore the decrease in thermal conductivity over time is likely to be due to a decrease in the concentration of the

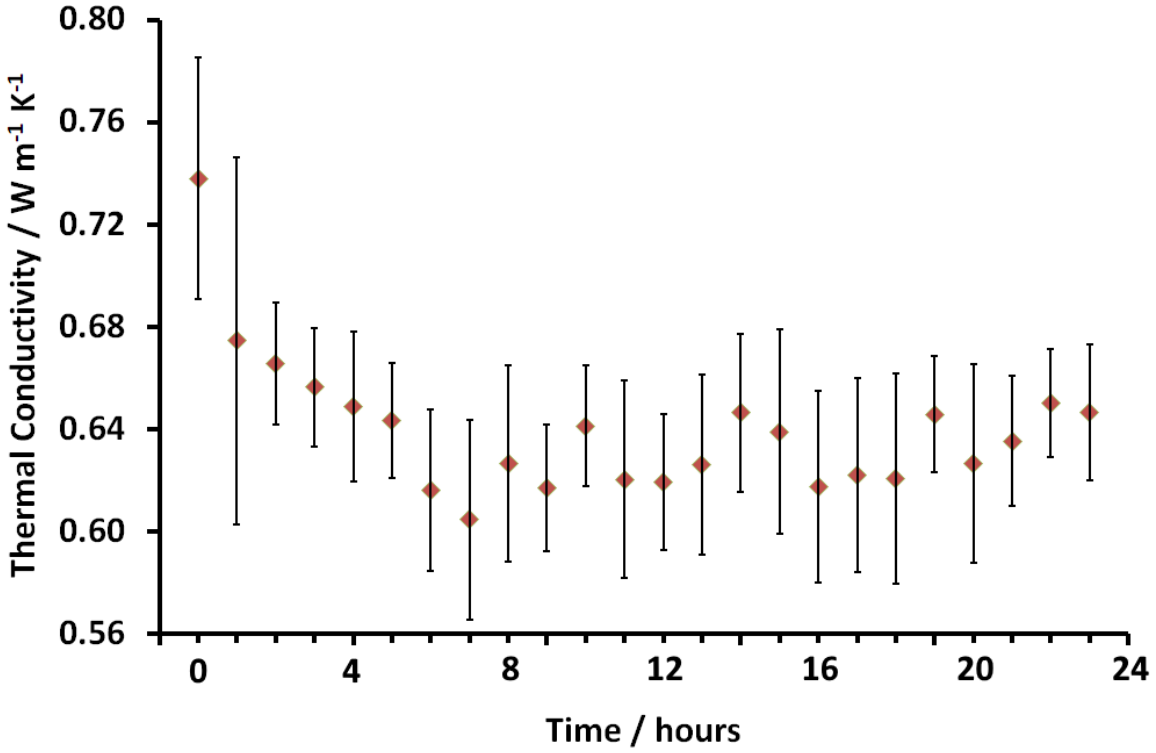

Figure 7.12: *The thermal conductivity of a dispersion of 2.5 mg ml^{-1} dispersion of GO over a period of 24 h whilst being held at 60 °C.*

GO modifier over time.

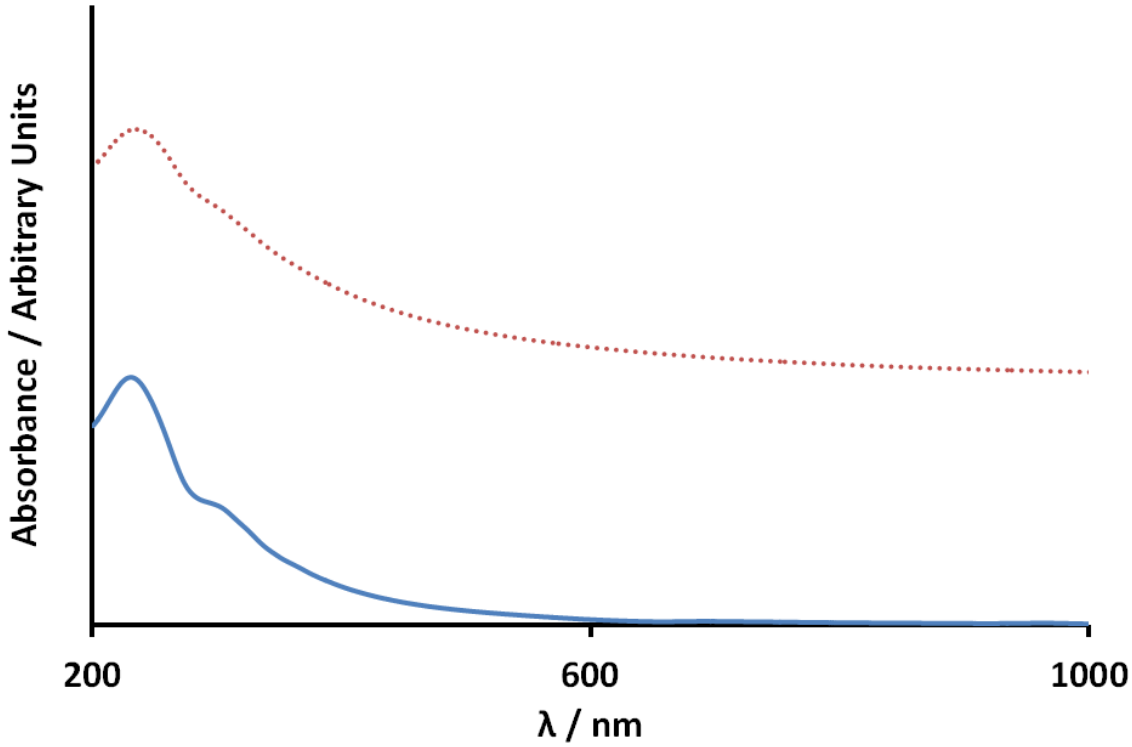

Figure 7.13: *UV-vis spectroscopy of the dispersion of GO prior to thermal conductivity testing (blue line), and the solution after testing (red dotted line).*

Table 7.5: *The position of the $\pi \rightarrow \pi^*$ plasmon peak in the UV-Vis spectra of dispersions GO in water before and after measurement of thermal conductivity for 24 h at 60 °C.*

	Position of $\pi \rightarrow \pi^*$ plasmon peak / nm
Before	230.5
After	233.5

Whilst the thermal conductivity of the GO dispersion begins significantly higher than that of pure water at 60 °C, by the end of the thermal conductivity measurement it has fallen significantly and is around the same as that of pure water. This could cause problems when utilising graphene dispersions in applications, as consistent thermal conductivity is an essential property.

One factor that must be considered is that the dispersions tested here are of GO in pure water and not in commercial coolant. This means that whilst results described here are likely to be similar in commercial coolant they may not be exactly the same. One factor that may have a significant impact is that the commercial coolant contains surfactants and dispersants, which could aid in maintaining the dispersion of GO and may reduce the fall in thermal conductivity observed for dispersions of GO in pure water. However, the problems discussed above that were encountered when testing thermal conductivity of coolant using our instrument prevented this from being tested.

7.4. Conclusion

Changes to both the thermal conductivity and specific heat capacity of thermal fluids have great potential to improve their performance in engines, by increasing both the amount of heat transferred and the rate at which it can be carried away. Improving both of these qualities will allow equivalent engine performance from power units with smaller coolant reservoirs and thus with lighter weights.

The methods used to test these properties have been discussed in section 4.2. In this chapter the development and testing of a THW instrument for the measurement of thermal conductivity of liquids. This THW instrument was then used to analyse the thermal conduc-

tivity of dispersions of graphene materials in both water and a commercially used coolant provided by Shell Global Solutions.

In order to further investigate the thermal properties of dispersions of GO in coolant, it was decided to test the performance of this dispersion in a power unit. This required a large volume of the coolant-GO dispersion to be produced. In order to achieve this a flow sonication setup was used in order to produce large volumes of graphene dispersions. Using gravimetric methods the concentration of this dispersion was determined to be 0.5 mg ml^{-1}. This dispersion was shipped to Shell Global Solutions for full scale engine testing.

In order to assess the impact of these graphene additives on the thermal properties of dispersions, nanofluids of GO were produced in both water and commercial coolant. The thermal conductivity and specific heat capacity of these dispersions were then measured. Using DSC it was shown that the addition of GO to the coolant caused a rise in the specific heat capacity across a range of temperatures. This means that a given volume of coolant has the potential to absorb more thermal energy than is possible for pure coolant, meaning the performance of the coolant is improved by the addition of GO.

The thermal conductivity of the dispersions produced was also assessed using the THW method and it was shown that in both coolant and pure water that the addition of GO additives caused an increase in thermal conductivity over the range of temperatures tested. One effect of testing thermal conductivity at elevated temperatures was that some changes in the dispersion were noted due to the heating of GO including a darkening in colour as well as some solid material dropping out of solution. These changes were investigated in more detail, with UV-Vis spectroscopy being used to show that no reduction had occurred to the GO during the thermal conductivity measurement. However, the thermal conductivity of a dispersion of GO held at 60 °C was shown to fall over time indicating that some change was occurring to the dispersion over time and this was attributed to a change in the concentration of the suspended GO. Therefore more work should be put into improving the stability of GO dispersions in order to maintain the improved thermal conductivity seen at the start

of the measurement.

These data show that dispersions of GO in coolants and other aqueous thermal fluids can be produced relatively easily and that these additives have a significant impact on the thermal properties of these dispersions, improving both the thermal conductivity and specific heat capacity. However, care must be taken with these dispersions when working at elevated temperatures to ensure that the reduction of GO to rGO does not destabilise the fluid under these conditions. This change from GO to rGO changes both the thermal and dispersions properties of the additive, and so further investigation of the impact of these changes will be needed.

7.5. Further Work

Given the improved thermal conductivity of dispersions of GO, in both water and the commercial coolant observed in the data above it is clear that graphene based nanofluids show great promise for increasing the thermal conductivity of thermal fluids. However, some challenges were discovered in this initial study which could be overcome, depending on the outcome of some of the work proposed in this section.

The first challenge encountered in this work was the incompatibility of the hot wire instrument designed with the commercial coolant used to disperse the graphene, hindering thermal conductivity measurements of coolant dispersions. If there was more time that could be dedicated to this matter it would be ideal to further investigate the reason that the coolant damages the hot wire. Whilst the easiest method to determine this would be to establish the contents of the additive package used to create the coolant, this information is extremely commercially sensitive and so unlikely to be obtained. An alternative method to allow testing the thermal conductivity of commercial coolant dispersions may be to change the materials used in the instrument, both to join the ends of the wire to the instrument, and to use a hot wire with a different insulating layer than Teflon or to replace the platinum

wire with a tantalum one. By making these changes, it would be hoped that dispersions using the commercial coolant would no longer cause the hot wire to become damaged and break during measurements, enabling more data on commercially relevant dispersions to be collected.

Whilst it has been shown that the addition of GO to both water and coolant is able to increase the thermal conductivity of dispersions over a range of temperatures, the impact of rGO on thermal conductivity was not investigated. Theoretically rGO should cause greater increases in thermal conductivity than GO due to its less defective electronic structure although forming dispersions of it in aqueous fluids such as water and coolant is more of a challenge. In order to produce high concentration dispersions of rGO, to give the greatest increases in thermal conductivity, it may be possible to employ some of the techniques for increasing the dispersibility of rGO described in chapters 5 and 6. Of particular interest is the potential to form rGO through *in situ* reduction of a GO dispersion, as described in section 6.2.3.2. This has the advantage that the conditions used to produce the rGO are the same as the operating conditions of the engines the coolants are used in. Therefore, if it is possible to produce dispersions of rGO that remain stable after synthesis these dispersions should also remain stable under the conditions they will be applied in.

Finally, these studies were all performed on dispersions at a single concentration of GO. Investigating the impact of changing the concentration of the graphene additive on the thermal properties of the dispersion would be of great interest as a balance must be struck between increasing the concentration of the additive and obtaining a stable dispersion when aiming to improve thermal properties. Another potential area of interest would be to investigate the effect of utilising graphite oxide as an additive, compared to GO at the same concentration.

Whilst the work in this chapter has focussed on the thermal properties of aqueous dispersions of graphene materials for use as coolants, it would also be informative to test the thermal properties of graphene nanofluids for use as lubricants, such as those produced in

chapter 6. Lubricants also play an essential role in the transfer of heat away from components in engines, which in turn is essential in reducing wear and so examining the impact of graphene additives on their thermal properties could be of interest in determining their potential in automotive applications.

CHAPTER 8

EXPERIMENTAL

8.1. Analytical Methodology

8.1.1. Solution State Nuclear Magnetic Resonance Spectroscopy

NMR spectroscopy in the solution state was performed on a Bruker Avance-400 NMR spectrometers. ^{1}H, ^{13}C, and ^{31}P spectra were recorded with chemical shifts reported in δ (ppm) relative to residual solvent protons (^{1}H), an external sample of tetramethylsilane (TMS) (^{13}C) or an external sample of 85 % H_3PO_4 (^{31}P).

8.1.2. Transmission Electron Microscopy

TEM was performed on a JEOL 2100 FEG TEM operated at 80 kV under high vacuum conditions. Samples were deposited on 300 mesh copper lacey carbon grids. Solid samples were first dispersed into volatile solvents (EtOH, MeOH or EtO_2) using mild bath sonication and then deposited onto grids by dropping from a pipette. Samples already in the form of dispersions or liquid were simply deposited from their liquid states onto grids using pipettes.

8.1.3. Raman Spectroscopy

Raman spectra were obtained using a Jobin Yvon LabRam Evolution HR spectrometer in a back scattered confocal configuration using a Nd:YAG laser (521 nm, 2.33 eV) equipped

with a CCD detector. All spectra were referenced to the A_{1_g} Raman active mode of silicon at 520 cm^{-1}. Samples were prepared by deposition from their liquid state, or by dispersion in EtOH, MeOH or EtO_2 by mild bath sonication followed by deposition onto glass microscope slides.

8.1.4. X-Ray Photoelectron Spectroscopy

8.1.4.1. Data Collection

XPS was performed at the NEXUS facility at Newcastle University on a Kratos AXIS Nova spectrometer using a monochromatic Al Kα source (1486.6 eV). Samples were drop cast onto small pieces of silicon (approximately 1 cm $\times$ 1 cm which had been cleaned with methanol) from a dispersion in either methanol or diethyl ether to from a continuous film of material across the surface of the silicon. The dispersions were produced by extremely brief bath sonication in order to disperse the material with minimal impact.

8.1.4.2. Fitting of Data

The XPS spectra recorded were analysed using the CASA XPS software package. Spectra were background corrected using a Tougaard background. The C=C peak was then fitted to these background corrected spectra using the line shape of the C1s peak of pure graphite (325 mesh) and the position of this peak corrected to 285 eV. Additional peaks were then fitted to the spectra based on the likely functionalities within the sample, constrained to peak positions reported in the literature $\pm$ 0.1 eV[270,386] using GL(30) line shapes with full width, half maximums constrained to 1.0-1.5.

8.1.5. Thermogravimetric Analysis

TGA was performed on a Perkin-Elmer Pyris 1 TGA under helium, nitrogen or air. Carbon samples (10-20 mg) were heated in a ceramic boat from 30-120 °C at 10 °C $minute^{-1}$, the

temperature was then held for 60 minutes at 120 °C. After this time the sample was heated to 900 °C at 10 °C minute^{-1}.

8.1.6. UV-Vis Spectroscopy

UV-Vis spectroscopy was performed on an Anglient Technologies Cary 5000 UV-Vis-NIR spectrometer. Spectroscopy was performed over a range of 175-1300 nm with samples run in quartz cuvettes with a path length of 1 cm.

8.1.7. ASAP Mass Spectrometry

ASAP-MS was performed on a on a Xevo QToF mass spectrometer fitted with an ASAP ion source (Waters Corp, Manchester, United Kingdom). Positive ions were recorded from 50-1000 Da.

8.1.8. High Performance Liquid Chromatography

HPLC was performed on a series 200 Perkin Elmer HPLC system using a methanol/water gradient on a 15 cm X-Bridge C18 column at a detector wavelength of 220 nm. Prior to HPLC samples were filtered over nylon membranes (Whatman, 0.45 µm pore size) to remove rGO that could clog the instrument.

In order to determine the concentration of NMP and DMF using HPLC calibration curves were produced by recording chromatograms for aqueous dispersions of NMP and DMF, under identical conditions, in the concentration range 0.05-0.5 vol. %. Plotting the peak intensity from the chromatogram against the concentration allowed a calibration graph to be produced for each fluid and linear regression was used to produce an equation to convert peak intensity to concentration.

8.1.9. Testing of Kinematic Viscosity

Testing of kinematic viscosity was performed at Shell Global Solutions in Hamburg, according to ASTM standards: D445-06, and D446-07.[400,401] Viscosity was determined using a Herzog HVM 472 viscometer. A known volume of the sample to be tested was passed through the instrument and the time taken for this to occur recorded and converted into viscosity. These measurements were repeated at 40 °C and 100 °C in order to obtain V_K 40 and V_K 100 respectively.

8.1.10. Testing of Dynamic Viscosity

The testing of Dynamic viscosity was performed at Shell Global Solutions in Hamburg using an USV produced by PCS instruments: model U115 LS-5477. Measurements were performed over the shear range of 1×10^6-1×10^7 s^{-1} at temperatures of 100 °C, 120 °C and 150 °C. The apparatus was flushed with neutral reference fluids between tests to ensure no traces of sample remain.

8.1.11. MTM Testing for Measurement of Coefficient of Friction

The testing of coefficients of friction of dispersions were performed at Shell Global Solutions testing facility in Hamburg. Measurements were performed using a PCS Instruments MTM: model MTM213 V2479. The MTM was set up using an AISI 52100, 3/4" steel ball and flat disc. 35 ml of oil was then added to the chamber and the instrument was heated to 120 °C. Once the temperature was stable measurement could then begin.

8.1.11.1. Hydrodynamic Step

In the test step for the hydrodynamic regime the ball was loaded against the disc with a force of 35 N, giving a contact pressure of $\sim$1 GPa. The ball and disc were then driven to rotate against one and other at a 50 % slide-roll ratio with a starting speed of 4 m s^{-1}. The speed was decreased in steps down to 5 mm s^{-1} over a period of 5 minutes. At each step a torque transducer was used to measure the friction between the ball and the disc.

8.1.11.2. Boundary Step

In the measurement step testing the boundary regime the load remained the same as in the hydrodynamic regime. The ball and disc were then rotated, with a 50 % slide-roll ratio at a constant speed of 50 mm s^{-1} and the friction was measured *via* the torque transducer every 60 s. The measurement was maintained for a period of 60 minutes.

8.1.11.3. Test Protocol

The full protocol for testing of the coefficient of friction of lubricants consisted of a combination of repeated hydrodynamic and boundary steps. After an initial hydrodynamic step the lubricant was tested under the boundary regime for 60 minutes to promote the formation of chemical films and run-in the surfaces. Following this, a second hydrodynamic step was performed, to examine the impact of changes to the surfaces due to film formation and running-in. The boundary and hydrodynamic steps were then repeated alternately until 180 minutes have elapsed after which the test finished with a final hydrodynamic step.

8.1.12. Determination of Specific Heat Capacity by Differential Scanning Calorimetry

DSC was performed on a Perkin Elmer DSC 8000. The procedure used to measure specific heat capacity was that detailed in ASTM E1269-11.[398] The instrument was first purged with

dry nitrogen. In order to prevent evaporation of volatile components high pressure stainless steel pans (volume 60 µL, part number 319-0218) with a viton O-ring seal were used. First, the heat capacity of a well known substance was measured as a standard. Two empty, clean pans and lids were weighed and heated from 20-50 °C at 20 °C minute^{-1} and the heat flow recorded. The instrument was then cooled and a sapphire disc (with a mass similar to the sample mass to be used) was placed into one of the pans and its mass recorded. The same heating profile as before was run and the heat flow recorded.

In order to record the specific heat capacity of a sample, the same procedure as described above was used, replacing the sapphire standard with the unknown sample. After heating the pan should be reweighed to ensure no mass loss has occurred. If >0.3 % of the starting mass has been lost then the measurement is not valid and should be repeated.

In order to determine the specific heat capacity, the difference in heat flow between the empty pan and the sample was measured at a given temperature. As the specific heat capacity of sapphire is well known, the measurements recorded for the sapphire disc were used to calculate a calibration factor for the instrument and pans, and this could be used to determine the specific heat capacity of the sample. Full details of this methodology can be found in ASTM E1269-11.[398]

8.1.13. Determination of Thermal Conductivity by the Transient Hot Wire Method

Measurement of thermal conductivity was performed on a bespoke THW instrument. The details of this instrument and the measurement procedure will be outlined below.

8.1.13.1. Instrument Design

The body of the THW instrument was produced from machined aluminium to match the technical drawings in Appendix A. At the top of the instrument, a micrometer screw gauge

attaches to the top end of a spring. The lower end of this spring is attached to a sliding piece of Delrin, allowing the spring to move freely.

The support for the hot wire was constructed from a brass tube with Delrin plugs in each end. The sliding Delrin piece moves through the top end plug and attaches to the top of the hot wire. The wire itself is a 50 µm platinum wire (99.99 % purity with a 9 µm Teflon coating (Goodfellow)). The base of the wire was attached to the lower Delrin plug.

Two K type thermocouples were included in the instrument, one inside the measurement cell and one outside. The signal from these are amplified before being read by the DAQ card. The final composition of instrument is shown in figures 7.1 and 7.2 and component diagrams are shown in Appendix A.

8.1.14. Electronics Design

Control of the instrument and data acquisition was performed using a NI USB-6008 DAQ card. The electronics for the hot wire were set up using a Wheatstone bridge configuration, with the hot wire as one of the resistors in the circuit. Instead of a variable resistor to balance the bridge, a decade array of resistors was used, allowing for resistance to be set in a range of 2000-3000 Ω with a resolution of 0.1 Ω. All resistors used had extremely low temperature coefficients in order to reduce error as a result of changes in temperature.

Several relays, controlled by the DAQ card allow the hot wire to be switched in and out of the circuit, replaced by a fixed resistor, the full voltage supply to be switched to a low voltage supply, and a third to remove the supply voltage from the circuit completely. The power supply for the circuit was able to provide a voltage of 1.25-10 V.

Full circuit diagrams for the instrument can be found in Appendix A and the procedure used to measure thermal conductivity is outlined below.

8.1.14.1. Thermal Control

Temperature control of the instrument was achieved using a Grant LTD6G recirculating cooler attached to the outer jacket of a jacketed glass vessel. The measurement cell of the instrument was placed into the interior of the vessel which was filled with water to help stabilise the temperature. The two thermocouples are then used to determine when thermal equilibrium throughout the instrument has been reached.

8.1.14.2. Varied Temperature Measurement

In order to measure the thermal conductivity of liquids across a range of temperatures the procedure outlined below was used. The supply voltage was set to 10 V, the hot wire switched out of the circuit, and the instrument was allowed to warm up and thermally equilibrate for 90 minutes.

After this time, the bath temperature was set to the lowest temperature of the range of interest and the sample was allowed to reach thermal equilibrium with the bath. The 10 V supply was then switched for the 0.1 V supply and the hot wire introduced to the circuit. This allows the Wheatstone bridge circuit to be balanced using the decade resistor array, which is achieved when the bridge output voltage is 0 V. Once this has been achieved then the full supply voltage can be returned, and the change in bridge voltage as the wire's temperature changes can be recorded over time. This measurement was repeated 20 times. After each measurement, the bath temperature was increased by 5 °C and allowed to equilibrate again. The measurement procedure was repeated for each temperature in the desired range to give a range of thermal conductivities at different temperatures.

The measurement procedure was controlled through the DAQ card using NI LabVIEW and a full copy of this program can be found in Appendix B.

8.1.14.3. Constant Temperature Measurement

In order to measure the thermal conductivity of liquids at a set temperature over a period of time the procedure outlined below was used. The supply voltage was set to 10 V, the hot wire switched out of the circuit, and the instrument was allowed to warm up and thermally equilibrate for 90 minutes.

After this time, the bath temperature was set to the desired measurement temperature and the sample was allowed to reach thermal equilibrium with the bath. The 10 V supply was then switched for the 0.1 V supply and the hot wire introduced to the circuit. This allows the Wheatstone bridge circuit to be balanced using the decade resistor array, which is achieved when the bridge output voltage is 0 V. Once this has been achieved then the full supply voltage can be returned, and the change in bridge voltage as the wire's temperature changes can be recorded over time. This measurement was repeated 20 times. This measurement procedure was then repeated every 60 minutes over a period of 24 h.

The measurement procedure was controlled through the DAQ card using NI LabVIEW and a full copy of this program can be found in Appendix B.

8.1.14.4. Data Processing

The data recorded by the LabVIEW script was processed using a Python script. This calculated thermal conductivity, from the instrument's output of voltage against time. The Wheatstone bridge was used to convert the bridge voltage into the resistance of the hot wire. A plot of the change in resistance against the natural log of the time will have a linear region, with a gradient inversely proportional to thermal conductivity.

In order to determine the position and gradient of this linear region, linear regression was used. Python was used to determine the R^2 coefficient of the lines of best fit over every possible range within the dataset. This is a measure of the goodness of fit, so the parameters of the line of best fit that give the highest R^2 value is taken to be the linear region, and this

region, taken with the calibration coefficient is used to calculate thermal conductivity from the resistance of the hot wire.

A copy of the Python script used to process the data can be found in Appendix C.

8.1.15. Gravimetric Measurement of the Concentration of GO-coolant dispersion

Measurement of the concentration of the GO-coolant dispersion, produced on a large scale as described in section 8.3.23, was performed gravimetrically . 5 ml of dispersion was placed into each of 5 28 ml vials and their masses recorded. These vials were placed into a vacuum oven (<10 mbar at 80 °C to evaporate the coolant, leaving the GO. The mass of these vials was recorded every 24 h until their masses were consistent for three consecutive measurements.

As the coolant contains a wide range of additives that are non-volatile, 5 vials containing 5 ml of pure coolant were also subjected to the same treatment and their masses recorded. The mean residual mass of the pure coolant was subtracted from the residual mass of GO-coolant dispersion. This gave the residual mass of GO, which was then used to calculate the concentration.

As a control, 5 empty 28 ml vials were also subjected to the same conditions and weighed every 24 h to prove that the mass of the vials does not change and contribute to the calculation of concentration under the conditions used.

8.2. Details of Laboratory Equipment Used

8.2.1. Ultrasonic Probe

Probe sonication was performed using a Cole Parmer ultrasonic processor (750 W) with a 1/2 ” probe.

8.2.2. Ultrasonic Bath

Bath sonication was performed in an in a Bandelin Sonorex Digitec DT 100 H ultrasonic bath (320 W, 35 kHz).

8.2.3. Centrifuge

Centrifugation was performed in an Eppendorf 5804 centrifuge using 40 ml centrifuge tubes with an Eppendorf high-speed fixed-angle rotor (F-34-6-38).

8.2.4. Vacuum Oven

Drying under vacuum was performed in a Binder VD series vacuum oven at a pressure of <10 mbar at the temperatures specified in the method.

8.2.5. Freeze Drying

Freeze drying was performed in a SP scientific BenchTop Pro freeze drier. Samples were frozen using liquid nitrogen and then the pressure reduced and held below the triple point of water to allow sublimation to occur.

8.3. Details of Experimental Methodology

8.3.1. Synthesis of Graphite Oxide

Graphite oxide was synthesised using the method originally proposed by Hummers and Offeman.[208] Quantities were scaled from the described method as required. Powdered graphite (10 g, 325 mesh) and sodium nitrate ($NaNO_3$, 5 g) were dispersed by stirring in concentrated sulphuric acid (H_2SO_4 230 ml, 1.83 S.G.) and cooled to 0 °C using a Grant LTD6G recirculating cooler. Potassium permanganate ($KMnO_4$, 30 g) was added carefully in small aliquots ensuring that the temperature of the reaction did not rise above 10 °C. Once addition was completed the temperature was raised to 35 °C for 30 minutes. 460 ml of high purity water was then added causing the reaction to heat to >90 °C. This elevated temperature was maintained for 15 minutes by external heating from the recirculating cooler. After allowing to cool to room temperature the reaction was poured into 1.4 l of high purity water and quenched by the addition of H_2O_2 ($\sim$10 ml, 30 %), causing a colour change from deep brown to a yellow/brown solution, until effervescence of gas ceased from the reaction. The graphite oxide produced was allowed to settle overnight. Once the supernatant became clear it was decanted and replaced by high purity water. This process was repeated until the graphite oxide begins to swell and absorb water, darkening in colour and no longer settling. Final washings were performed by centrifugation at 11 000 r.p.m. ($\sim$15 500 g) for 12 minutes, replacing the supernatant with high purity water after each washing until the supernatant remained at a neutral pH after centrifugation. The solid material was then isolated as a dark brown, gel-like substance containing approximately 95 % water by mass (from TGA).

8.3.2. Exfoliation of Graphite Oxide

Graphite oxide was converted to GO by ultrasonication. Samples were dispersed in high purity water at concentrations of 1-5 mg ml^{-1} and probe sonicated for 20 minutes (40 % amplitude, pulsed 5 s on, 5 s off, elapsed time 40 minutes) with a water/ice bath to control temperature. This produced a dispersion of GO.

8.3.3. Freeze Drying of Graphene Oxide

In order to remove residual water from GO freeze drying was used. A dispersion of GO was produced using the method described in section 8.3.2 and transferred into a round bottom flask. The contents of this flask was then shell frozen using liquid nitrogen, ensuring an even layer of material over the inside of the flask for optimum drying, before being attached to a freeze drier and dried for 72 hours to form a light brown, sponge like foam of FDGO.

8.3.4. Reduction of Graphene Oxide Using Hydrazine Monohydrate

Hydrazine reduction was performed using a procedure adapted from Park *et al.* [269] GO was dispersed in high purity water at approximately 5 mg ml^{-1} to which hydrazine monohydrate was added (1 µl per 3 mg of GO). This was then stirred and heated to 80 °C for 5 h during which time the dark brown colour of the GO dispersion is replaced by a black colour. As reduction occurs the decreased solubility of rGO means that it begins to precipitate out as a black powder or sponge. To isolate rGO the reaction is vacuum filtered over a polycarbonate membrane (Whatman Cyclopore, track etched, 0.2 µm pore size, 47 mm diameter) and then dried in a vacuum oven (60 °C, <10 mbar) for 24 h.

8.3.5. General Procedure for the Dispersion of Graphene Materials by Probe Sonication

Graphene materials were dispersed in fluids *via* probe sonication for 20 minutes (40 % amplitude, pulsed 5 s on, 5 s off, elapsed time 40 minutes) at a nominal concentration of 1 mg ml^{-1} (25 mg of graphene material in 25 ml of fluid) in 28 ml glass vials with a water/ice bath to control temperature.

8.3.6. In situ Reduction of GO in Oils

FDGO (25 mg) was added to oils (25 ml) in 28 ml vials at a concentration of 1 mg ml^{-1} and then dispersed by probe sonication for 20 minutes (40 % amplitude, pulsed 5 s on, 5 s off, elapsed time 40 minutes) while being cooled by a water/ice bath. The dispersions produced were then transferred to 50 ml round bottom flasks and heated to 120 °C for 24 h under reflux condensers with stirring. During this time the brown colour of GO gradually became black. After the reaction was complete the dispersions were allowed to cool and then transferred to 28 ml vials.

8.3.7. Functionalisation of GO with ODA

Functionalisation of GO with ODA was performed using a procedure reported by Jang *et al.* [380] GO dispersion containing 0.5 g of GO was diluted to 1 mg ml^{-1} in high purity water (total volume 500 ml). ODA (1.35 g) was dissolved in ethanol (100 ml) and gradually added to the GO dispersion. The reaction was then heated, with stirring to 60 °C for 16 h to form ODA-GO.

8.3.8. Chemical Reduction of ODA Functionalised GO Using Hydrazine

Reduction of ODA-GO was performed using a procedure adapted from Jang *et al.* [380] and Park *et al.* [269] Hydrazine monohydrate was added to the product of section 8.3.7 (167 µl, 1 µl per 3 mg of GO) and the reaction was heated to 80 °C for 2 h with stirring to form a black, insoluble powder, ODA-rGO. This was isolated *via* vacuum filtration over a nylon membrane (Millipore, 0.45 µm pore size, 47 mm diameter) followed by thorough washing with methanol and drying *in vacuo* (60 °C, <10 mbar) for 24 h.

8.3.9. Synthesis of rGO as a Control

As a control for the synthesis of ODA-rGO described in sections 8.3.7 and 8.3.8 a GO dispersion containing 0.5 g of GO was diluted to 1 mg ml^{-1}. 100 ml of ethanol was then added to the dispersion before it was heated to 60 °C for 16 h. Hydrazine monohydrate ((167 µl, 1 µl per 3 mg of GO) was then added and the reaction was heated to 60 °C with stirring for 2 h. The resulting rGO was isolated *via* vacuum filtration over a nylon membrane (Millipore, 0.45 µm pore size, 47 mm diameter) followed by thorough washing with methanol and drying *in vacuuo* (60 °C, <10 mbar) for 24 h.

8.3.10. One Step, Solvent Free, Functionalisation and Reduction of GO

In situ reduction and functionalisation of GO was achieved by mixing graphite oxide (0.5 g) with ODA (20 g). The mixture was heated to 60 °C and bath sonicated for 60 minutes to exfoliate graphite oxide to GO. The reaction was then placed into an oil bath and heated to 115 °C, without a condenser, to allow residual water from the GO to evaporate. Once the volume ceased to change then the temperature was raised to 180 °C for 18 h, causing

a colour change from brown to black as GO was converted to rGO. The reaction was then cooled to room temperature, allowing the ODA to solidify. The residual mixture of ODA and ODA-rGO was dissolved in toluene and washed by Soxhlet extraction with toluene for 72 h before being dried *in vacuo* (60 °C, <10 mbar) for 24 h leaving ODA-rGO.

This procedure was adapted with other high boiling reagents to functionalise graphene: OL to form OL-rGO, TOP to form TOP-rGO and TOPO to form TOPO-rGO.

8.3.11. Extraction and Preparation of Residual TOP and TOPO for ^{31}P NMR

In order to isolate the residual TOP and TOPO from the preparation of TOP-rGO and TOPO-rGO described above in section 8.3.10 the washing produced from the Soxhlet extraction were isolated and rotary evaporation was used to remove the toluene. This left a waxy white/yellow solid.

For analysis by NMR the solids described above were dissolved into d_8 toluene and pipetted into an NMR tube.

8.3.12. Heating of TOP and TOPO and preparation for NMR as a control

Control experiments to examine the effect of prolonged heating on TOP and TOPO were performed under conditions comparable to those described in section 8.3.10. 10 ml of TOP or 10 g of TOPO were placed into a 50 ml round bottomed flasks and heated, in an oil bath, to 180 °C, with stirring, for 24 h. After this time the reagents were allowed to cool.

In order to analyse the products of these reactions using NMR the products were dissolved into d_8 toluene and pipetted into NMR tubes for analysis.

8.3.13. Dispersion of Functionalised Reduced Graphene Oxides in Base Oils

To produce dispersions of f-rGOs in base oils 25 mg of the chosen f-rGO was added to 25 ml of the selected base oil in a 28 ml glass vial and probe sonicated for 20 minutes (40 % amplitude, pulsed 5 s on, 5 s off, elapsed time 40 minutes) with a water/ice bath to control temperature. This produced a dispersion of f-rGO with a maximum concentration of 1 mg ml^{-1}.

8.3.14. Sonication of Oils to Determine the Impact on Viscosity

Sonication of unmodified oils was performed by adding 25 ml of the selected oil to a 28 ml glass vial and probe sonicated for 20 minutes (40 % amplitude, pulsed 5 s on, 5 s off, elapsed time 40 minutes) with a water/ice bath to control temperature.

8.3.15. Production of NMP Predispersed rGO

To produce NMPrGO 25 mg of rGO was added to 25 ml of NMP in a 28 ml vial. This was then subjected to probe ultrasonication for 20 minutes (40 % amplitude, pulsed 5 s on, 5 s off, elapsed time 40 minutes) with a water/ice bath to control temperature. The produced dispersion was poured into MeCN (250 ml, HPLC grade) and then isolated using vacuum filtration over a nylon membrane (Millipore, 0.45 µm pore size, 47 mm diameter). The material isolated is NMPrGO.

8.3.16. Production of NMP Predispersed rGO without washing using MeCN

Unwashed NMPrGO was produced in the same way as described in section 8.3.15 except after sonication NMPrGO was isolated directly from NMP using vacuum filtration over a nylon membrane (Millipore, 0.45 µm pore size, 47 mm diameter).

8.3.17. Production of DMF Predispersed rGO

DMFrGO was prepared as described in section 8.3.15 except that DMF was used in place of NMP. The material isolated *via* filtration is DMFrGO.

8.3.18. Production of DMF Predispersed rGO without washing using MeCN

Unwashed DMFrGO was produced in the same way as described in section 8.3.17 except after sonication DMFrGO was isolated directly from DMF using vacuum filtration over a nylon membrane (Millipore, 0.45 µm pore size, 47 mm diameter).

8.3.19. Production of Dispersions of NMPrGO

Dispersions of NMPrGO in different solvents were prepared by the following procedure. NMPrGO (produced by the procedure described in section 8.3.15) was placed into a 28 ml vial and 25 ml of the desired solvent was then added. The mixture was then probe sonicated for 20 minutes (40 % amplitude, pulsed 5 s on, 5 s off, elapsed time 40 minutes) with a water/ice bath to control temperature. The dispersion produced was then centrifuged at 7500 r.p.m. ($\sim$7200 g) for 20 minutes to pull out any unstable particles leaving a stable dispersion of NMPrGO in the solvent used. The dispersions produced by this method have a

maximum concentration of 1 mg ml^{-1}.

8.3.20. Production of Dispersions of DMFrGO

Dispersions of DMFrGO in different solvents were prepared using the same procedure described in section 8.3.19 with DMFrGO (produced by the procedure described in section 8.3.17) in place of NMPrGO.

8.3.21. Sonication of NMP to Test for Fragmentation

25 ml of NMP was sonicated in a 28 ml vial using a probe sonicator for 20 minutes (40 % amplitude, pulsed 5 s on, 5 s off, elapsed time 40 minutes) with a water/ice bath to control temperature.

8.3.22. Production of Control Dispersions of rGO

8.3.22.1. Basic Dispersion of rGO in Water and Aqueous NMP and DMF

Dispersions of rGO for control experiments were produced by the following procedure. rGO (25 mg) added to a 28 ml vial with 25 ml of solvent and then probe sonicated for a period of 20 minutes (40 % amplitude, pulsed 5 s on, 5 s off, elapsed time 40 minutes). The resulting dispersion was centrifuged at 7500 r.p.m. ($\sim$7200 g) for 20 minutes in order to remove any unstable particles. Dispersions were also prepared in low concentrations of NMP and DMF (0.1-0.5 %) by the same method. The dispersions produced by this method have a maximum concentration of 1 mg ml^{-1}.

8.3.22.2. Predispersion of rGO Using Water as a Control

As a control, 25 mg of rGO was added to 25 ml of water in a 28 ml vial. This was then subjected to probe sonication for 20 minutes (40 % amplitude, pulsed 5 s on, 5 s off, elapsed time 40 minutes) with a water/ice bath to control temperature. The produced dispersion was poured into MeCN (250 ml, HPLC grade) and then isolated using vacuum filtration over a nylon membrane (Millipore, 0.45 µm pore size, 47 mm diameter). The material isolated was then placed into a 28 ml vial and 25 ml of water was then added. The mixture was probe sonicated for 20 minutes (40 % amplitude, pulsed 5 s on, 5 s off, elapsed time 40 minutes) with a water/ice bath to control temperature. The dispersion produced was then centrifuged at 7500 r.p.m. ($\sim$7200 g) for 20 minutes to pull out any unstable particles leaving a stable dispersion of rGO in water.

8.3.23. Dispersion of GO in Coolant

GO was dispersed in the coolant provided by Shell Global Solutions through ultrasonication. As produced graphite oxide was dispersed in coolant using the flow sonication apparatus described in section 7.2. The capacity of the reservoir was 3 l whilst the capacity of the sonication vessel was kept to 25 ml with the probe sonicator inserted into it to ensure sonication efficiency remained high.

Dispersion was performed by sonicating 3 l batches of coolant, mixed with 6 g of as produced graphite oxide (103 g of slurry) for 2.5 h at 40 % sonication intensity. The peristaltic pump was set at a flow rate such that all of the coolant in the system would undergo sonication twice. This process was repeated 17 times to produce 51 l of GO-coolant dispersion.

REFERENCES

[1] K. Lodders, in *Principles and Perspectives in Cosmochemistry: Lecture Notes of the Kodai School on 'Synthesis of Elements in Stars' held at Kodaikanal Observatory, India, April 29 - May 13, 2008*, ed. A. Goswami and E. B. Reddy, Springer, Berlin, Heidelberg, 2010, ch. Solar System Abundances of the Elements, pp. 379–417.

[2] H. W. Kroto, J. R. Heath, S. C. O'Brien, R. F. Curl and R. E. Smalley, *Nature*, 1985, **318**, 162–163.

[3] S. Iijima, *Nature*, 1991, **354**, 56–58.

[4] S. Iijima and T. Ichihashi, *Nature*, 1993, **363**, 603–605.

[5] M. M. J. Treacy, T. W. Ebbesen and J. M. Gibson, *Nature*, 1996, **381**, 678–680.

[6] M. F. Yu, O. Lourie, M. J. Dyer, K. Moloni, T. F. Kelly and R. S. Ruoff, *Science*, 2000, **287**, 637–640.

[7] S. Berber, Y.-K. Kwon and D. Tománek, *Phys. Rev. Lett.*, 2000, **84**, 4613–4616.

[8] J. Che, T. Çagin and W. A. Goddard III, *Nanotechnology*, 2000, **11**, 65–69.

[9] T. W. Odom, J. L. Huang, P. Kim and C. M. Lieber, *Nature*, 1997, **391**, 62–64.

[10] K. S. Novoselov, A. K. Geim, S. V. Morozov, D. Jiang, Y. Zhang, S. V. Dubonos, I. V. Grigorieva and A. A. Firsov, *Science*, 2004, **306**, 666–669.

[11] D. W. Johnson, B. P. Dobson and K. S. Coleman, *Curr. Opin. Colloid Interf. Sci.*, 2015, **20**, 367–382.

[12] P. R. Wallace, *Phys. Rev.*, 1947, **71**, 622–634.

[13] N. D. Mermin, *Phys. Rev.*, 1968, **176**, 250–254.

[14] J. C. Meyer, A. K. Geim, M. I. Katsnelson, K. S. Novoselov, T. J. Booth and S. Roth, *Nature*, 2007, **446**, 60–63.

[15] A. K. Geim and K. S. Novoselov, *Nat. Mater.*, 2007, **6**, 183–191.

[16] B. Partoens and F. M. Peeters, *Phys. Rev. B*, 2006, **74**, 075404.

[17] M. Dresselhaus and G. Dresselhaus, *Adv. Phys.*, 1981, **30**, 139–326.

[18] H. C. Schniepp, J. L. Li, M. J. McAllister, H. Sai, M. Herrera-Alonso, D. H. Adamson, R. K. Prud'homme, R. Car, D. A. Saville and I. A. Aksay, *J. Phys. Chem. B*, 2006, **110**, 8535–8539.

[19] W. Bao, L. Jing, J. Velasco Jr, Y. Lee, G. Lui, D. Tran, B. Standley, M. Aykol, S. B. Cronin, D. Smirnov, M. Koshino, E. McCann, M. Mockrath and C. N. Lau, *Nat. Phys*, 2011, **7**, 948–952.

[20] C. H. Lui, Z. Li, Z. Chen, P. V. Klimov, L. E. Brus and T. F. Heinz, *Nano Lett.*, 2011, **11**, 164–169.

[21] C. H. Lui, Z. Li, K. F. Mak, E. Cappelluti and T. F. Heinz, *Nat. Phys.*, 2011, **7**, 944–947.

[22] L. Zhang, Y. Zhang, J. Camacho, M. Khodas and I. Zaliznyak, *Nat. Phys*, 2011, **7**, 953–957.

[23] Z. Liu, K. Suenaga, P. J. F. Harris and S. Iijima, *Phys. Rev. Lett.*, 2009, **102**, 015501.

[24] J. Borysiuk, J. Sołtys and J. Piechota, *J. Appl. Phys.*, 2011, **109**, 093523.

[25] C. J. Tabert and E. J. Nicol, *Phys. Rev. B*, 2012, **86**, 075439.

[26] L. Malard, M. Pimenta, G. Dresselhaus and M. Dresselhaus, *Phys. Rep.*, 2009, **473**, 51–87.

[27] S. Shallcross, S. Sharma, E. Kandelaki and O. A. Pankratov, *Phys. Rev. B*, 2010, **81**, 165105.

[28] D. R. Lenski and M. S. Fuhrer, *J. Appl. Phys.*, 2011, **110**, 013720.

[29] A. Fasolino, J. H. Los and M. I. Katsnelson, *Nat. Mater.*, 2007, **6**, 858–861.

[30] E. Stolyarova, K. T. Rim, S. Ryu, J. Maultzsch, P. Kim, L. E. Brus, T. F. Heinz, M. S. Hybertsen and G. W. Flynn, *Proc. Natl. Acad. Sci. USA*, 2007, **104**, 9209–9212.

[31] A. Bianco, H. M. Cheng, T. Enoki, Y. Gogotsi, R. H. Hurt, N. Koratkar, T. Kyotani, M. Monthioux, C. R. Park, J. M. Tascon and J. Zhang, *Carbon*, 2013, **65**, 1–6.

[32] A. C. Ferrari, F. Bonaccorso, V. Fal'ko, K. S. Novoselov, S. Roche, P. Bøggild, S. Borini, F. H. L. Koppens, V. Palermo, N. Pugno, J. A. Garrido, R. Sordan, A. Bianco, L. Ballerini, M. Prato, E. Lidorikis, J. Kivioja, C. Marinelli, T. Ryhänen, A. Morpurgo, J. N. Coleman, V. Nicolosi, L. Colombo, A. Fert, M. Garcia-Hernandez, A. Bachtold, G. F. Schneider, F. Guinea, C. Dekker, M. Barbone, Z. Sun, C. Galiotis, A. N. Grigorenko, G. Konstantatos, A. Kis, M. Katsnelson, L. Vandersypen, A. Loiseau, V. Morandi, D. Neumaier, E. Treossi, V. Pellegrini, M. Polini, A. Tredicucci, G. M. Williams, B. Hee Hong, J. H. Ahn, J. Min Kim, H. Zirath, B. J. van Wees, H. van der Zant, L. Occhipinti, A. Di Matteo, I. A. Kinloch, T. Seyller, E. Quesnel, X. Feng, K. Teo, N. Rupesinghe, P. Hakonen, S. R. T. Neil, Q. Tannock, T. Lofwander and J. Kinaret, *Nanoscale*, 2015, **7**, 4598–4810.

[33] A. K. Geim, *Science*, 2009, **324**, 1530–1534.

[34] S. Chen, J. Zhu and X. Wang, *J. Phys. Chem. C*, 2010, **114**, 11829–11834.

[35] R. S. Edwards and K. S. Coleman, *Nanoscale*, 2013, **5**, 38–51.

[36] C. Lee, X. Wei, J. W. Kysar and J. Hone, *Science*, 2008, **321**, 385–388.

[37] G. Eda, G. Fanchini and M. Chhowalla, *Nature Nanotechnol.*, 2008, **3**, 270–274.

[38] K. S. Kim, Y. Zhao, H. Jang, S. Y. Lee, J. M. Kim, K. S. Kim, J. H. Anh, P. Kim, J. Y. Choi and B. H. Hong, *Nature*, 2009, **457**, 706–710.

[39] F. Withers, O. Del Pozo-Zamundio, A. Mishchenko, A. P. Rooney, A. Gholinia, K. Watanabe, T. Taniguchi, S. J. Haigh, A. K. Geim, A. I. Tartakovskii and K. S. Novoselov, *Nat. Mater.*, 2015, **14**, 301–306.

[40] K. I. Bolotin, K. J. Sikes, Z. Jiang, M. Klima, G. Fudenberg, J. Hone, P. Kim and H. L. Stormer, *Solid State Commun.*, 2008, **146**, 351–355.

[41] A. H. Castro Neto, F. Guinea, N. M. R. Peres, K. S. Novoselov and A. K. Geim, *Rev. Mod. Phys.*, 2009, **81**, 109–162.

[42] X. Du, I. Skachko, A. Barker and E. Y. Andrei, *Nat. Nanotechnol.*, 2008, **3**, 491–5.

[43] K. S. Novoselov, A. K. Geim, S. V. Morozov, D. Jiang, M. I. Katsnelson, I. V. Grigorieva, S. V. Dubonos and A. A. Firsov, *Nature*, 2005, **438**, 197–200.

[44] Y. Zhang, Y. W. Tan, H. L. Stormer and P. Kim, *Nature*, 2005, **438**, 201–204.

[45] K. S. Novoselov, Z. Jiang, Y. Zhang, S. V. Morozov, H. L. Stormer, U. Zeitler, J. C. Maan, G. S. Boebinger, P. Kim and A. K. Geim, *Science*, 2007, **315**, 1379–1379.

[46] A. A. Balandin, S. Ghosh, W. Bao, I. Calizo, D. Teweldebrhan, F. Miao and C. N. Lau, *Nano. Lett.*, 2008, **8**, 902–907.

[47] R. R. Nair, P. Blake, A. N. Grigorenko, K. S. Novoselov, T. J. Booth, T. Stauber, N. M. R. Peres and A. K. Geim, *Science*, 2008, **320**, 1308.

[48] J. S. Bunch, S. S. Verbridge, J. S. Alden, A. M. van der Zande, J. M. Parpia, H. G. Craighead and P. L. McEuen, *Nano Lett.*, 2008, **8**, 2458–62.

[49] R. Raccichini, A. Varzi, S. Passerini and B. Scrosati, *Nat. Mater.*, 2015, **14**, 271–279.

[50] P. Avouris and C. Dimitrakopoulos, *Mater. Today*, 2012, **15**, 86–97.

[51] R. Muñoz and C. Gómez-Aleixandre, *Chem. Vap. Deposition*, 2013, **19**, 297–322.

[52] W. W. Liu, S. P. Chai, A. R. Mohamed and U. Hashim, *J. Ind. Eng. Chem.*, 2014, **20**, 1171–1185.

[53] T. Dürkop, S. A. Getty, E. Cobas and M. S. Fuhrer, *Nano Lett.*, 2004, **4**, 35–39.

[54] C. Jacoboni, C. Canali, G. Ottaviani and A. A. Quaranta, *Solid-State Electron.*, 1977, **20**, 77–89.

[55] A. Sukhadolau, E. Ivakin, V. Ralchenko, A. Khomich, A. Vlasov and A. Popovich, *Diamond Relat. Mater.*, 2005, **14**, 589–593.

[56] M. Arenas, V. Acoff and R. Reddy, *SCi. Technol. Weld. Joi.*, 2004, **9**, 423–429.

[57] F. Bonaccorso, L. Colombo, G. Yu, M. Stoller, V. Tozzini, A. C. Ferrari, R. S. Ruoff and V. Pellegrini, *Science*, 2015, **347**, 1246501.

[58] Z. Chen, U. Gandhi, J. Lee and R. Wagoner, *J. Mater. Proc. Technol.*, 2016, **227**, 227–243.

[59] P. R. Somani, S. P. Somani and M. Umeno, *Chem. Phys. Lett.*, 2006, **430**, 56–59.

[60] M. José-Yacamán, M. Miki-Yoshida, L. Rendón and J. G. Santiesteban, *Appl. Phys. Lett.*, 1993, **62**, 657–659.

[61] W. Z. Li, S. S. Xie, L. X. Qian, B. H. Chang, B. S. Zou, W. Y. Zhou, R. A. Zhao and G. Wang, *Science*, 1996, **274**, 1701–1703.

[62] W. A. Yarbrough and R. Messier, *Science*, 1990, **247**, 688–696.

[63] A. Reina, X. Jia, J. Ho, D. Nezich, H. Son, V. Bulovic, M. S. Dresselhaus and J. Kong, *Nano Lett.*, 2009, **9**, 30–35.

[64] B. Wang, M. Huang, L. Tao, S. H. Lee, A. R. Jang, B. W. Li, H. S. Shin, D. Akinwande and R. S. Ruoff, *ACS Nano*, 2016, **10**, 1404–1410.

[65] A. Boscá, J. Pedrós, J. Martínez, T. Palacios and F. Calle, *Sci. Rep.*, 2016, **6**, 21676.

[66] Y. Zhang, L. Zhang and C. Zhou, *Acc. Chem. Res.*, 2013, **46**, 2329–2339.

[67] D. Badami, *Carbon*, 1965, **3**, 53–57.

[68] P. Sutter, *Nat. Mater.*, 2009, **8**, 171–172.

[69] C. Berger, Z. Song, T. Li, X. Li, A. Y. Ogbazghi, R. Feng, Z. Dai, A. N. Marchenkov, E. H. Conrad, P. N. First and W. A. de Heer, *J. Phys. Chem. B*, 2004, **108**, 19912–19916.

[70] W. Norimatsu and M. Kusunoki, *Phys. Chem. Chem. Phys.*, 2014, **16**, 3501–3511.

[71] L. Chen, Y. Hernandez, X. Feng and K. Müllen, *Angew. Chem. Int. Ed.*, 2012, **51**, 7640–7654.

[72] L. ”Zhi and K. Müllen, *J. Mater. Chem.*, 2008, **18**, 1472–1484.

[73] J. Wu, W. Pisula and K. Müllen, *Chem. Rev.*, 2007, **107**, 718–747.

[74] Y. Fogel, L. Zhi, A. Rouhanipour, D. Andrienko, H. J. Räder and K. Müllen, *Macromolecules*, 2009, **42**, 6878–6884.

[75] X. Yang, X. Dou, A. Rouhanipour, L. Zhi, H. J. Räder and K. Müllen, *J. Am. Chem. Soc.*, 2008, **130**, 4216–4217.

[76] X. Lu, M. Yu, H. Huang and R. S. Ruoff, *Nanotechnology*, 1999, **10**, 269–272.

[77] F. Bonaccorso, A. Lombardo, T. Hasan, Z. Sun, L. Colombo and A. C. Ferrari, *Mater. Today*, 2012, **15**, 564–589.

[78] O. Posudievsky, O. Khazieieva, V. Cherepanov, V. Koshechko and V. Pokhodenko, *J. Nanopart. Res.*, 2013, **15**, 2046.

[79] Y. Lv, L. Yu, C. Jiang, S. Chen and Z. Nie, *RSC Adv.*, 2014, **4**, 13350–13354.

[80] M. Yi and Z. Shen, *J. Mater. Chem. A*, 2015, **3**, 11700–11715.

[81] Y. Hernandez, V. Nicolosi, M. Lotya, F. M. Blighe, Z. Sun, S. De, I. T. McGovern, B. Holland, M. Byrne, Y. Gun'ko, J. J. Boland, P. Niraj, G. Duesberg, S. Krishnamurthy, R. Goodhue, J. Hutchinson, V. Scardaci, A. C. Ferrari and J. N. Coleman, *Nat. Nanotechnol.*, 2008, **3**, 563–568.

[82] M. Lotya, Y. Hernandez, P. J. King, R. J. Smith, V. Nicolosi, L. S. Karlsson, F. M. Blighe, S. De, Z. Wang, I. T. McGovern, G. S. Duesberg and J. N. Coleman, *J. Am. Chem. Soc.*, 2009, **131**, 3611–3620.

[83] M. Cai, D. Thorpe, D. H. Adamson and H. C. Schniepp, *J. Mater. Chem.*, 2012, **22**, 24992–25002.

[84] A. Ciesielski and P. Samori, *Chem. Soc. Rev.*, 2014, **43**, 381–398.

[85] J. N. Coleman, *Acc. Chem. Res.*, 2013, **46**, 14–22.

[86] Y. Hernandez, M. Lotya, D. Rickard, S. D. Bergin and J. N. Coleman, *Langmuir*, 2010, **26**, 3208–3213.

[87] A. A. Green and M. C. Hersam, *Nano Lett.*, 2009, **9**, 4031–4036.

[88] S. Vadukumpully, J. Paul and S. Valiyaveettil, *Carbon*, 2009, **47**, 3288 – 3294.

[89] J. Xu, D. K. Dang, V. T. Tran, X. Liu, J. S. Chung, S. H. Hur, W. M. Choi, E. J. Kim and P. A. Kohl, *J. Colloid Interf. Sci.e*, 2014, **418**, 37–42.

[90] K. R. Paton, E. Varrla, C. Backes, R. J. Smith, U. Khan, A. O'Neill, C. Boland, M. Lotya, O. M. Istrate, P. King, T. Higgins, S. Barwich, P. May, P. Puczkarski, I. Ahmed, M. Moebius, H. Pettersson, E. Long, J. ao Coelho, S. E. O'Brien, E. K. McGuire, B. M. Sanchez, G. S. Duesberg, N. McEvoy, T. J. Pennycook, C. Downing, A. Crossley, V. Nicolosi and J. N. Coleman, *Nat. Mater.*, 2014, **13**, 624–630.

[91] J. N. Coleman, *Adv. Funct. Mater.*, 2009, **19**, 3680–3695.

[92] T. Skaltsas, X. Ke, C. Bittencourt and N. Tagmatarchis, *J. Phys. Chem. C*, 2013, **117**, 23272–23278.

[93] G. Yoon, D. H. Seo, K. Ku, J. Kim, S. Jeon and K. Kang, *Chem. Mater.*, 2015, **27**, 2067–2073.

[94] C. Vallés, C. Drummond, H. Saadaoui, C. A. Furtado, M. He, O. Roubeau, L. Ortolani, M. Monthioux and A. Pénicaud, *J. Am. Chem. Soc.*, 2008, **130**, 15802–15804.

[95] L. M. Viculis, J. J. Mack, O. M. Mayer, H. T. Hahn and R. B. Kaner, *J. Mater. Chem.*, 2005, **15**, 974–978.

[96] T. Wei, Z. Fan, G. Luo, C. Zheng and D. Xie, *Carbon*, 2009, **47**, 337–339.

[97] D. D. L. Chung, *J. Mater. Sci.*, 1987, **22**, 4190–4198.

[98] X. Li, G. Zhang, X. Bai, X. Sun, X. Wang, E. Wang and H. Dai, *Nat. Nanotechnol.*, 2008, **3**, 538–542.

[99] W. Gu, W. Zhang, X. Li, H. Zhu, J. Wei, Z. Li, Q. Shu, C. Wang, K. Wang, W. Shen, F. Kang and D. Wu, *J. Mater. Chem.*, 2009, **19**, 3367–3369.

[100] S. Malik, A. Vijayaraghavan, R. Erni, K. Ariga, I. Khalakhan and J. P. Hill, *Nanoscale*, 2010, **2**, 2139–2143.

[101] S. Stankovich, D. A. Dikin, R. D. Piner, K. A. Kohlhaas, A. Kleinhammes, Y. Jia, Y. Wu, S. T. Nguyen and R. S. Ruoff, *Carbon*, 2007, **45**, 1558–1565.

[102] P. K. Ang, S. Wang, Q. Bao, J. T. L. Thong and K. P. Loh, *ACS Nano*, 2009, **3**, 3587–3594.

[103] B. C. Brodie, *Philos. Trans. R. Soc. London*, 1859, **149**, 249–259.

[104] D. V. Kosynkin, A. L. Higginbotham, A. Sinitskii, J. R. Lomeda, A. Dimiev, B. K. Price and J. M. Tour, *Nature*, 2009, **458**, 872–876.

[105] B. Xiao, X. Li, X. Li, B. Wang, C. Langford, R. Li and X. Sun, *J. Phys. Chem. C*, 2014, **118**, 881–890.

[106] L. Jiao, L. Zhang, X. Wang, G. Diankov and H. Dai, *Nature*, 2009, **458**, 877–880.

[107] L. Valentini, *Diamond Relat. Mater.*, 2011, **20**, 445–448.

[108] S. Mohammadi, Z. Kolahdouz, S. Darbari, S. Mohajerzadeh and N. Masoumi, *Carbon*, 2013, **52**, 451–463.

[109] P. Kumar, L. S. Panchakarla and C. N. R. Rao, *Nanoscale*, 2011, **3**, 2127–2129.

[110] L. Jiao, X. Wang, G. Diankov, H. Wang and H. Dai, *Nat. Nanotechnol.*, 2010, **5**, 321–325.

[111] C. Tiwary, B. Javvaji, C. Kumar, D. Mahapatra, S. Ozden, P. Ajayan and K. Chattopadhyay, *Carbon*, 2015, **89**, 217–224.

[112] T. Palacios, *Nature*, 2012, **483**, S40–S41.

[113] R. Balog, B. Jørgensen, L. Nilsson, M. Andersen, E. Rienks, M. Bianchi, M. Fanetti, E. Lægsgaard, A. Baraldi, S. Lizzit, Z. Sljivancanin, F. Besenbacher, B. Hammer, T. G. Pedersen, P. Hofmann and L. Hornekær, *Nat. Mater.*, 2010, **9**, 315–319.

[114] M. Y. Han, B. Özyilmaz, Y. Zhang and P. Kim, *Phys. Rev. Lett.*, 2007, **98**, 206805.

[115] X. Wang, Y. Ouyang, L. Jiao, H. Wang, L. Xie, J. Wu, J. Guo and H. Dai, *Nat. Nanotechnol.*, 2011, **6**, 563–567.

[116] D. Wei, Y. Liu, Y. Wang, H. Zhang, L. Huang and G. Yu, *Nano Lett.*, 2009, **9**, 1752–1758.

[117] Z. Jin, J. Yao, C. Kittrell and J. M. Tour, *ACS Nano*, 2011, **5**, 4112–4117.

[118] V. M. Pereira, A. H. Castro Neto and N. M. R. Peres, *Phys. Rev. B*, 2009, **80**, 045401.

[119] E. McCann and V. I. Fal'ko, *Phys. Rev. Lett.*, 2006, **96**, 086805.

[120] L. Zhang, J. Liang, Y. Huang, Y. Ma, Y. Wang and Y. Chen, *Carbon*, 2009, **47**, 3365–3368.

[121] F. Schwierz, *Nat. Nanotechnol.*, 2010, **5**, 487–496.

[122] M. C. Lemme, T. J. Echtermeyer, M. Baus and H. Kurz, *IEEE Electron Device Lett.*, 2007, **28**, 282–284.

[123] I. Meric, N. Baklitskaya, P. Kim and K. L. Shepard, IEEE International Electron Devices Meeting, 2008, pp. 1–4.

[124] X. Wan, G. Long, L. Huang and Y. Chen, *Adv. Mater.*, 2011, **23**, 5342–5358.

[125] J. Wu, H. A. Becerril, Z. Bao, Z. Liu, Y. Chen and P. Peumans, *Appl. Phys. Lett.*, 2008, **92**, 263302.

[126] Y. Xu, G. Long, L. Huang, Y. Huang, X. Wan, Y. Ma and Y. Chen, *Carbon*, 2010, **48**, 3308–3311.

[127] Z. Yin, S. Sun, T. Salim, S. Wu, X. Huang, Q. He, Y. M. Lam and H. Zhang, *ACS Nano*, 2010, **4**, 5263–5268.

[128] T. H. Han, Y. Lee, M. R. Choi, S. H. Woo, S. H. Bae, B. H. Hong, J. H. Ahn and T. W. Lee, *Nature Photon.*, 2012, **6**, 105–110.

[129] J. Wu, M. Agrawal, H. A. Becerril, Z. Bao, Z. Liu, Y. Chen and P. Peumans, *ACS Nano*, 2010, **4**, 43–48.

[130] Z. Liu, Q. Liu, Y. Huang, Y. Ma, S. Yin, X. Zhang, W. Sun and Y. Chen, *Adv. Mater.*, 2008, **20**, 3924–3930.

[131] S. S. Li, K. H. Tu, C.-C. Lin, C. W. Chen and M. Chhowalla, *ACS Nano*, 2010, **4**, 3169–3174.

[132] J. Lee, T. H. Han, M. H. Park, D. Y. Jung, J. Seo, H. K. Seo, H. Cho, E. Kim, J. Chung, S. Y. Choi, T. S. Kim, T. W. Lee and S. Yoo, *Nat. Commun*, 2016, **7**, 11791.

[133] F. Bonaccorso, Z. Sun, T. Hasan and A. C. Ferrari, *Nature Photon.*, 2010, **4**, 611–622.

[134] A. Burke, *J. Power Sources*, 2000, **91**, 37–50.

[135] M. Winter and R. J. Brodd, *Chem. Rev.*, 2004, **104**, 4245–4270.

[136] L. L. Zhang, R. Zhou and X. S. Zhao, *J. Mater. Chem.*, 2010, **20**, 5983–5992.

[137] J. Hassoun, F. Bonaccorso, M. Agostini, M. Angelucci, M. G. Betti, R. Cingolani, M. Gemmi, C. Mariani, S. Panero, V. Pellegrini and B. Scrosati, *Nano Lett.*, 2014, **14**, 4901–4906.

[138] G. Kucinskis, G. Bajars and J. Kleperis, *J. Power Sources*, 2013, **240**, 66–79.

[139] H. Wang, Y. Yang, Y. Liang, J. T. Robinson, Y. Li, A. Jackson, Y. Cui and H. Dai, *Nano Lett.*, 2011, **11**, 2644–2647.

[140] F. Wu, J. T. Lee, E. Zhao, B. Zhang and G. Yushin, *ACS Nano*, 2016, **10**, 1333–1340.

[141] L. Ji, M. Rao, H. Zheng, L. Zhang, Y. Li, W. Duan, J. Guo, E. J. Cairns and Y. Zhang, *J. Am. Chem. Soc.*, 2011, **133**, 18522–18525.

[142] J. Xiao, D. Mei, X. Li, W. Xu, D. Wang, G. L. Graff, W. D. Bennett, Z. Nie, L. V. Saraf, I. A. Aksay, J. Liu and J. G. Zhang, *Nano Lett.*, 2011, **11**, 5071–5078.

[143] Y. Li, J. Wang, X. Li, D. Geng, R. Li and X. Sun, *Chem. Commun.*, 2011, **47**, 9438–9440.

[144] E. Yoo and H. Zhou, *ACS Nano*, 2011, **5**, 3020–3026.

[145] W. Lv, Z. Li, Y. Deng, Q.-H. Yang and F. Kang, *Energy Storage Mater.*, 2016, **2**, 107–138.

[146] L. Qu, Y. Liu, J. B. Baek and L. Dai, *ACS Nano*, 2010, **4**, 1321–1326.

[147] R. Imran Jafri, N. Rajalakshmi and S. Ramaprabhu, *J. Mater. Chem.*, 2010, **20**, 7114–7117.

[148] E. Antolini, *Appl. Catal., B*, 2012, **123-124**, 52–68.

[149] J. L. Achtyl, R. R. Unocic, L. Xu, Y. Cai, M. Raju, W. Zhang, R. L. Sacci, I. V. Vlassiouk, P. F. Fulvio, P. Ganesh, D. J. Wesolowski, S. Dai, A. C. T. van Duin, M. Neurock and F. M. Geiger, *Nat. Commun.*, 2015, **6**, 6539.

[150] Y. Sun, Q. Wu and G. Shi, *Energy Environ. Sci.*, 2011, **4**, 1113–1132.

[151] J. Zhu, D. Yang, Z. Yin, Q. Yan and H. Zhang, *Small*, 2014, **10**, 3480–3498.

[152] S. Chatterjee, J. Wang, W. Kuo, N. Tai, C. Salzmann, W. Li, R. Hollertz, F. N□esch and B. Chu, *Chem. Phys. Lett*, 2012, **531**, 6–10.

[153] S. Stankovich, D. A. Dikin, G. H. B. Dommett, K. M. Kohlhaas, E. J. Zimney, E. A. Stach, R. D. Piner, S. T. Nguyen and R. S. Ruoff, *Nature*, 2006, **442**, 282–286.

[154] H. Kim and C. W. Macosko, *Polymer*, 2009, **50**, 3797–3809.

[155] H. J. Salavagione, G. Martínez and M. A. Gómez, *J. Mater. Chem.*, 2009, **19**, 5027–5032.

[156] H. Kim, Y. Miura and C. W. Macosko, *Chem. Mater.*, 2010, **22**, 3441–3450.

[157] G. Gonçalves, P. A. A. P. Marques, A. Barros-Timmons, I. Bdkin, M. K. Singh, N. Emami and J. Grácio, *J. Mater. Chem.*, 2010, **20**, 9927–9934.

[158] H. Kim, A. A. Abdala and C. W. Macosko, *Macromolecules*, 2010, **43**, 6515–6530.

[159] Y. Wang, Z. Shi and J. Yin, *Polymer*, 2011, **52**, 3661–3670.

[160] S. Villar-Rodil, J. I. Paredes, A. Martínez-Alonso and J. M. D. Tascón, *J. Mater. Chem.*, 2009, **19**, 3591–3593.

[161] T. Ramanathan, A. A. Abdala, S. Stankovich, D. A. Dikin, M. Herrera-Alonso, R. D. Piner, D. H. Adamson, H. C. Schniepp, X. Chen, R. S. Ruoff, S. T. Nguyen, I. A. Aksay, R. K. Prud'Homme and L. C. Brinson, *Nat. Nanotechnol.*, 2008, **3**, 327–331.

[162] X. Wang, Y. Hu, L. Song, H. Yang, W. Xing and H. Lu, *J. Mater. Chem.*, 2011, **21**, 4222–4227.

[163] K. H. Liao, S. Aoyama, A. A. Abdala and C. Macosko, *Macromolecules*, 2014, **47**, 8311–8319.

[164] S. Araby, I. Zaman, Q. Meng, N. Kawashima, A. Michelmore, H.-C. Kuan, P. Majewski, J. Ma and L. Zhang, *Nanotechnology*, 2013, **24**, 165601.

[165] K. Kalaitzidou, H. Fukushima and L. T. Drzal, *Compos. Sci. Technol.*, 2007, **67**, 2045–2051.

[166] B. Shen, W. Zhai, M. Tao, D. Lu and W. Zheng, *Compos. Sci. Technol.*, 2013, **86**, 109–116.

[167] T. Kuilla, S. Bhadra, D. Yao, N. H. Kim, S. Bose and J. H. Lee, *Prog. Polym. Sci.*, 2010, **35**, 1350–1375.

[168] J. R. Potts, D. R. Dreyer, C. W. Bielawski and R. S. Ruoff, *Polymer*, 2011, **52**, 5–25.

[169] J. Maxwell, *A Treatise on Electricity and Magnetism*, Clarendon Press, Oxford, 1873.

[170] Y. Wei, X. Huaqing and B. Dan, *Nanotechnology*, 2010, **21**, 055705.

[171] W. Yu, H. Xie and W. Chen, *J. Appl. Phys.*, 2010, **107**, 094317.

[172] N. K. Mahanta and A. R. Abramson, 13th IEEE Intersociety Conference on Thermal and Thermomechanical Phenomena in Electronic Systems (ITherm), 2012, pp. 1–6.

[173] H. Zhang, A. F. Fonseca and K. Cho, *J. Phys. Chem. C*, 2014, **118**, 1436–1442.

[174] T. T. Baby and S. Ramaprabhu, *J. Appl. Phys.*, 2010, **108**, 124308.

[175] T. Baby and S. Ramaprabhu, *Nanoscale Res. Lett.*, 2011, **6**, 289.

[176] W. Yu, H. Xie, X. Wang and X. Wang, *Phys. Lett. A*, 2011, **375**, 1323–1328.

[177] S. S. Jyothirmayee Aravind and S. Ramaprabhu, *J. Appl. Phys.*, 2011, **110**, 124326.

[178] H. Huang, J. Tu, L. Gan and C. Li, *Wear*, 2006, **261**, 140–144.

[179] J. Lin, L. Wang and G. Chen, *Tribol. Lett.*, 2011, **41**, 209–215.

[180] Z. Wei, Z. Ming, Z. Hongwei, T. Yu, W. Kunlin, W. Jinquan, J. Fei, L. Xiao, L. Zhen, Z. Peng and W. Dehai, *J. Phys. D Appl. Phys.*, 2011, **44**, 205303.

[181] S. Choudhary, H. P. Mungse and O. P. Khatri, *J. Mater. Chem.*, 2012, **22**, 21032–21039.

[182] V. Eswaraiah, V. Sankaranarayanan and S. Ramaprabhu, *ACS Appl. Mater. Interfaces*, 2011, **3**, 4221–4227.

[183] H. J. Song and N. Li, *Appl. Phys. A Mater. Sci. Process*, 2011, **105**, 827–832.

[184] I. Mahbubul, R. Saidur and M. Amalina, *Int. J. Heat Mass Transfer*, 2012, **55**, 874 – 885.

[185] Y. He, Y. Jin, H. Chen, Y. Ding, D. Cang and H. Lu, *Int. J. Heat Mass Transfer*, 2007, **50**, 2272–2281.

[186] C. Nguyen, F. Desgranges, N. Galanis, G. Roy, T. Mar□, S. Boucher and H. A. Mintsa, *Int. J. Therm. Sci.*, 2008, **47**, 103–111.

[187] W. Q. Lu and Q. M. Fan, *Eng. Anal. Boundary Elem.*, 2008, **32**, 282–289.

[188] R. Prasher, D. Song, J. Wang and P. Phelan, *Appl. Phys. Lett.*, 2006, **89**, 133108.

[189] K. Kalaitzidou, H. Fukushima and L. T. Drzal, *Carbon*, 2007, **45**, 1446–1452.

[190] H. M. Kim, J. K. Lee and H. S. Lee, *Thin Solid Films*, 2011, **519**, 7766–7771.

[191] Y. Cui, S. Kundalwal and S. Kumar, *Carbon*, 2016, **98**, 313–333.

[192] K. C. Kemp, H. Seema, M. Saleh, N. H. Le, K. Mahesh, V. Chandra and K. S. Kim, *Nanoscale*, 2013, **5**, 3149–3171.

[193] S. Wang, H. Sun, H. Ang and M. Tadé, *Chem. Eng. J.*, 2013, **226**, 336–347.

[194] L. Cao, Y. Liu, B. Zhang and L. Lu, *ACS Appl. Mater. Interf.*, 2010, **2**, 2339–2346.

[195] H. Xu, H. Dai and G. Chen, *Talanta*, 2010, **81**, 334–338.

[196] X. Kang, J. Wang, H. Wu, I. A. Aksay, J. Liu and Y. Lin, *Biosens. Bioelectron.*, 2009, **25**, 901–905.

[197] M. Du, T. Yang and K. Jiao, *J. Mater. Chem.*, 2010, **20**, 9253–9260.

[198] Y. Liu, X. Dong and P. Chen, *Chem. Soc. Rev.*, 2012, **41**, 2283–2307.

[199] S. Basu and P. Bhattacharyya, *Sens. Actuators, B*, 2012, **173**, 1–21.

[200] S. S. Varghese, S. Lonkar, K. Singh, S. Swaminathan and A. Abdala, *Sens. Actuators, B*, 2015, **218**, 160–183.

[201] J. Li, S. Guo, Y. Zhai and E. Wang, *Electrochem. Commun.*, 2009, **11**, 1085–1088.

[202] J. Li, S. Guo, Y. Zhai and E. Wang, *Anal. Chim. Acta*, 2009, **649**, 196–201.

[203] J. Gong, T. Zhou, D. Song and L. Zhang, *Sens. Actuators, B*, 2010, **150**, 491–497.

[204] C. X. Guo, Z. S. Lu, Y. Lei and C. M. Li, *Electroch. Commun.*, 2010, **12**, 1237–1240.

[205] H. Du, J. Ye, J. Zhang, X. Huang and C. Yu, *Electroanal.*, 2010, **22**, 2399–2406.

[206] X. Kang, J. Wang, H. Wu, J. Liu, I. A. Aksay and Y. Lin, *Talanta*, 2010, **81**, 754–759.

[207] J. Li, J. Chen, X.-L. Zhang, C.-H. Lu and H.-H. Yang, *Talanta*, 2010, **83**, 553–558.

[208] W. S. Hummers and R. E. Offeman, *J. Am. Chem. Soc.*, 1958, **80**, 1339.

[209] T. Szabó, O. Berkesi, P. Forgó, K. Josepovits, Y. Sanakis, D. Petridis and I. Dékány, *Chem. Mater.*, 2006, **18**, 2740–2749.

[210] U. Hofmann and R. Holst, *Ber. Dtsch. Chem. Ges. B*, 1939, **72**, 754–771.

[211] G. Ruess, *Monatsch. Chem.*, 1947, **76**, 381–417.

[212] A. Lerf, H. He, T. Riedl, M. Forster and J. Klinowski, *Solid State Ion.*, 1997, **101-103**, 857–862.

[213] H. He, T. Riedl, A. Lerf and J. Klinowski, *J. Phys. Chem.*, 1996, **100**, 19954–19958.

[214] A. Lerf, H. He, M. Forster and J. Klinowski, *J. Phys. Chem. B*, 1998, **102**, 4477–4482.

[215] D. R. Dreyer, S. Park, C. W. Bielawski and R. S. Ruoff, *Chem. Soc. Rev.*, 2010, **39**, 228–240.

[216] S. Mao, H. Pu and J. Chen, *RSC Adv.*, 2012, **2**, 2643–2662.

[217] J. P. Rourke, P. A. Pandey, J. J. Moore, M. Bates, I. A. Kinloch, R. J. Young and N. R. Wilson, *Angew. Chem. Int. Ed.*, 2011, **50**, 3173–3177.

[218] X. Fan, W. Peng, Y. Li, X. Li, S. Wang, G. Zhang and F. Zhang, *Adv. Mater.*, 2008, **20**, 4490–4493.

[219] C. Chen, W. Kong, H. M. Duan and J. Zhang, *Phys. Chem. Chem. Phys.*, 2014, **16**, 12858–12864.

[220] Z. Wu, C. U. P. Jr. and S. D. Gardner, *Carbon*, 1995, **33**, 597–605.

[221] R. Verdejo, S. Lamoriniere, B. Cottam, A. Bismarck and M. Shaffer, *Chem. Commun.*, 2007, 513–515.

[222] C. G. Salzmann, S. A. Llewellyn, G. Tobias, M. A. H. Ward, Y. Huh and M. L. H. Green, *Adv. Mater.*, 2007, **19**, 883–887.

[223] S. Fogden, R. Verdejo, B. Cottam and M. Shaffer, *Chem. Phys. Lett.*, 2008, **460**, 162–167.

[224] Z. Wang, M. D. Shirley, S. T. Meikle, R. L. Whitby and S. V. Mikhalovsky, *Carbon*, 2009, **47**, 73–79.

[225] H. R. Thomas, S. P. Day, W. E. Woodruff, C. Vallés, R. J. Young, I. A. Kinloch, G. W. Morley, J. V. Hanna, N. R. Wilson and J. P. Rourke, *Chem. Mater.*, 2013, **25**, 3580–3588.

[226] H. R. Thomas, C. Valles, R. J. Young, I. A. Kinloch, N. R. Wilson and J. P. Rourke, *J. Mater. Chem. C*, 2013, **1**, 338–342.

[227] D. Konios, M. M. Stylianakis, E. Stratakis and E. Kymakis, *J. Colloid Interf. Sci.*, 2014, **430**, 108–112.

[228] Y. Zhu, S. Murali, W. Cai, X. Li, J. W. Suk, J. R. Potts and R. S. Ruoff, *Adv. Mater.*, 2010, **22**, 3906–3924.

[229] L. Staudenmaier, *Ber. Dtsch. Chem. Ges.*, 1898, **31**, 1481–1487.

[230] N. I. Kovtyukhova, P. J. Ollivier, B. R. Martin, T. E. Mallouk, S. A. Chizhik, E. V. Buzaneva and A. D. Gorchinskiy, *Chem. Mater.*, 1999, **11**, 771–778.

[231] D. C. Marcano, D. V. Kosynkin, J. M. Berlin, A. Sinitskii, Z. Sun, A. Slesarev, L. B. Alemany, W. Lu and J. M. Tour, *ACS Nano*, 2010, **4**, 4806–4814.

[232] S. Lee, J. Oh, R. S. Ruoff and S. Park, *Carbon*, 2012, **50**, 1442–1444.

[233] G. Shao, Y. Lu, F. Wu, C. Yang, F. Zeng and Q. Wu, *J. Mater. Sci.*, 2012, **47**, 4400–4409.

[234] J. Chen, B. Yao, C. Li and G. Shi, *Carbon*, 2013, **64**, 225–229.

[235] M. J. McAllister, J. L. Li, D. H. Adamson, H. C. Schniepp, A. A. Abdala, J. Liu, M. H. Alonso, D. L. Milius, R. Car, R. K. Prud'homme and I. A. Aksay, *Chem. Mater.*, 2007, **19**, 4396–4404.

[236] A. Lerf, A. Buchsteiner, J. Pieper, S. Schöttl, I. Dekany, T. Szabo and H. P. Boehm, *J. Phys. Chem. Solids*, 2006, **67**, 1106–1110.

[237] B. Rezania, N. Severin, A. V. Talyzin and J. P. Rabe, *Nano Lett.*, 2014, **14**, 3993–3998.

[238] X. Zhou and Z. Liu, *Chem. Commun.*, 2010, **46**, 2611–2613.

[239] Q. Zheng, L. Shi, P. C. Ma, Q. Xue, J. Li, Z. Tang and J. Yang, *RSC Adv.*, 2013, **3**, 4680–4691.

[240] A. Dideykin, A. Aleksenskiy, D. Kirilenko, P. Brunkov, V. Goncharov, M. Baidakova, D. Sakseev and A. Ya.Vul', *Diamond Relat. Mater.*, 2011, **20**, 105–108.

[241] I. Ogino, Y. Yokoyama, S. Iwamura and S. R. Mukai, *Chem. Mater.*, 2014, **26**, 3334–3339.

[242] K. H. Liao, A. Mittal, S. Bose, C. Leighton, K. A. Mkhoyan and C. W. Macosko, *ACS Nano*, 2011, **5**, 1253–1258.

[243] C. Botas, A. M. Pérez-Mas, P. Álvarez, R. Santamaría, M. Granda, C. Blanco and R. Menéndez, *Carbon*, 2013, **63**, 576–578.

[244] J. I. Paredes, S. Villar-Rodil, A. Martínez-Alonso and J. M. D. Tascón, *Langmuir*, 2008, **24**, 10560–10564.

[245] M. M. Gudarzi, M. H. M. Moghadam and F. Sharif, *Carbon*, 2013, **64**, 403–415.

[246] S. Pei and H. M. Cheng, *Carbon*, 2012, **50**, 3210–3228.

[247] M. Agharkar, S. Kochrekar, S. Hidouri and M. A. Azeez, *Mater. Res. Bull.*, 2014, **59**, 323–328.

[248] N. A. Kotov, I. Dékány and J. H. Fendler, *Adv. Mater.*, 1996, **8**, 637–641.

[249] S. Stankovich, R. D. Piner, X. Chen, N. Wu, S. T. Nguyen and R. S. Ruoff, *J. Mater. Chem.*, 2006, **16**, 155–158.

[250] X. Gao, J. Jang and S. Nagase, *J. Phys. Chem. C*, 2010, **114**, 832–842.

[251] R. Wang, Y. Wang, C. Xu, J. Sun and L. Gao, *RSC Adv.*, 2013, **3**, 1194–1200.

[252] A. Furst, R. C. Berlo and S. Hooton, *Chem. Rev.*, 1965, **65**, 51–68.

[253] H. J. Shin, K. K. Kim, A. Benayad, S. M. Yoon, H. K. Park, I. S. Jung, M. H. Jin, H. K. Jeong, J. M. Kim, J. Y. Choi and Y. H. Lee, *Adv. Funct. Mater.*, 2009, **19**, 1987–1992.

[254] W. Gao, L. B. Alemany, L. Ci and P. M. Ajayan, *Nat. Chem.*, 2009, **1**, 403–408.

[255] J. Zhang, H. Yang, G. Shen, P. Cheng, J. Zhang and S. Guo, *Chem. Commun.*, 2010, **46**, 1112–1114.

[256] Y. Wang, Z. Shi and J. Yin, *ACS Appl. Mater. Interf.*, 2011, **3**, 1127–1133.

[257] O. Akhavan, M. Kalaee, Z. Alavi, S. Ghiasi and A. Esfandiar, *Carbon*, 2012, **50**, 3015–3025.

[258] M. F. Abdullah, R. Zakaria and S. H. S. Zein, *RSC Adv.*, 2014, **4**, 34510–34518.

[259] C. Zhu, S. Guo, Y. Fang and S. Dong, *ACS Nano*, 2010, **4**, 2429–2437.

[260] R. S. Edwards, *Ph.D. thesis*, Durham University, 2015.

[261] I. K. Moon, J. Lee, R. S. Ruoff and H. Lee, *Nat. Commun.*, 2010, **1**, 73.

[262] S. Pei, J. Zhao, J. Du, W. Ren and H. M. Cheng, *Carbon*, 2010, **48**, 4466–4474.

[263] G. Wang, J. Yang, J. Park, X. Gou, B. Wang, H. Liu and J. Yao, *J. Phys. Chem. C*, 2008, **112**, 8192–8195.

[264] X. Zhou, J. Zhang, H. Wu, H. Yang, J. Zhang and S. Guo, *J. Phys. Chem. C*, 2011, **115**, 11957–11961.

[265] S. Gilje, S. Han, M. Wang, K. L. Wang and R. B. Kaner, *Nano Lett.*, 2007, **7**, 3394–3398.

[266] C. Gómez-Navarro, R. T. Weitz, A. M. Bittner, M. Scolari, A. Mews, M. Burghard and K. Kern, *Nano Lett.*, 2007, **7**, 3499–3503.

[267] J. T. Robinson, M. Zalalutdinov, J. W. Baldwin, E. S. Snow, Z. Wei, P. Sheehan and B. H. Houston, *Nano Lett.*, 2008, **8**, 3441–3445.

[268] Y. Zhu, W. Cai, R. D. Piner, A. Velamakanni and R. S. Ruoff, *Appl. Phys. Lett.*, 2009, **95**, 103104.

[269] S. Park, J. An, J. R. Potts, A. Velamakanni, S. Murali and R. S. Ruoff, *Carbon*, 2011, **49**, 3019–3023.

[270] S. Park, J. An, I. Jung, R. D. Piner, S. J. An, X. Li, A. Velamakanni and R. S. Ruoff, *Nano Lett.*, 2009, **9**, 1593–1597.

[271] K. N. Kudin, B. Ozbas, H. C. Schniepp, R. K. Prud'homme, I. A. Aksay and R. Car, *Nano Lett.*, 2008, **8**, 36–41.

[272] X. Wang, L. Zhi and K. M□llen, *Nano Lett.*, 2008, **8**, 323–327.

[273] Z. S. Wu, W. Ren, L. Gao, J. Zhao, Z. Chen, B. Liu, D. Tang, B. Yu, C. Jiang and H. M. Cheng, *ACS Nano*, 2009, **3**, 411–417.

[274] H. A. Becerril, J. Mao, Z. Liu, R. M. Stoltenberg, Z. Bao and Y. Chen, *ACS Nano*, 2008, **2**, 463–470.

[275] Y. Qiu, F. Guo, R. Hurt and I. Külaots, *Carbon*, 2014, **72**, 215–223.

[276] Y. Zhou, Q. Bao, L. A. L. Tang, Y. Zhong and K. P. Loh, *Chem. Mater.*, 2009, **21**, 2950–2956.

[277] H. Wang, J. T. Robinson, X. Li and H. Dai, *J. Am. Chem. Soc*, 2009, **131**, 9910–9911.

[278] Y. Zhu, M. D. Stoller, W. Cai, A. Velamakanni, R. D. Piner, D. Chen and R. S. Ruoff, *ACS Nano*, 2010, **4**, 1227–1233.

[279] S. Dubin, S. Gilje, K. Wang, V. C. Tung, K. Cha, A. S. Hall, J. Farrar, R. Varshneya, Y. Yang and R. B. Kaner, *ACS Nano*, 2010, **4**, 3845–3852.

[280] V. H. Pham, T. V. Cuong, S. H. Hur, E. Oh, E. J. Kim, E. W. Shin and J. S. Chung, *J. Mater. Chem.*, 2011, **21**, 3371–3377.

[281] D. R. Dreyer, S. Murali, Y. Zhu, R. S. Ruoff and C. W. Bielawski, *J. Mater. Chem.*, 2011, **21**, 3443–3447.

[282] H. M. A. Hassan, V. Abdelsayed, A. E. R. S. Khder, K. M. AbouZeid, J. Terner, M. S. El-Shall, S. I. Al-Resayes and A. A. El-Azhary, *J. Mater. Chem.*, 2009, **19**, 3832–3837.

[283] Y. Zhu, S. Murali, M. D. Stoller, A. Velamakanni, R. D. Piner and R. S. Ruoff, *Carbon*, 2010, **48**, 2118–2122.

[284] L. J. Cote, R. Cruz-Silva and J. Huang, *J. Am. Chem. Soc.*, 2009, **131**, 11027–11032.

[285] V. Eswaraiah, S. S. Jyothirmayee Aravind and S. Ramaprabhu, *J. Mater. Chem.*, 2011, **21**, 6800–6803.

[286] H. Guo, M. Peng, Z. Zhu and L. Sun, *Nanoscale*, 2013, **5**, 9040–9048.

[287] M. F. El-Kady, V. Strong, S. Dubin and R. B. Kaner, *Science*, 2012, **335**, 1326–1330.

[288] V. Strong, S. Dubin, M. F. El-Kady, A. Lech, Y. Wang, B. H. Weiller and R. B. Kaner, *ACS Nano*, 2012, **6**, 1395–1403.

[289] Y. Z. Liu, C. M. Chen, Y. F. Li, X. M. Li, Q. Q. Kong and M. Z. Wang, *J. Mater. Chem. A*, 2014, **2**, 5730–5737.

[290] C. Coletti, C. Riedl, D. S. Lee, B. Krauss, L. Patthey, K. von Klitzing, J. H. Smet and U. Starke, *Phys. Rev. B*, 2010, **81**, 235401.

[291] T. S. Sreeprasad and V. Berry, *Small*, 2013, **9**, 341–350.

[292] V. Georgakilas, M. Otyepka, A. B. Bourlinos, V. Chandra, N. Kim, K. C. Kemp, P. Hobza, R. Zboril and K. S. Kim, *Chem. Rev.*, 2012, **112**, 6156–6214.

[293] T. Kuila, S. Bose, A. K. Mishra, P. Khanra, N. H. Kim and J. H. Lee, *Prog. Mater. Sci.*, 2012, **57**, 1061–1105.

[294] A. Criado, M. Melchionna, S. Marchesan and M. Prato, *Angew. Chem. Int. Ed.*, 2015, **54**, 10734–10750.

[295] V. Georgakilas, J. N. Tiwari, K. C. Kemp, J. A. Perman, A. B. Bourlinos, K. S. Kim and R. Zboril, *Chem. Rev.*, 2016, **116**, 5464–5519.

[296] M. Terrones, O. Mart?n, M. Gonz?lez, J. Pozuelo, B. Serrano, J. C. Cabanelas, S. M. Vega-D?az and J. Baselga, *Adv Mater.*, 2011, **23**, 5302–5310.

[297] V. Georgakilas, A. B. Bourlinos, R. Zboril, T. A. Steriotis, P. Dallas, A. K. Stubos and C. Trapalis, *Chem. Commun.*, 2010, **46**, 1766–1768.

[298] X. Zhang, L. Hou, A. Cnossen, A. C. Coleman, O. Ivashenko, P. Rudolf, B. J. van?Wees, W. R. Browne and B. L. Feringa, *Chem. Eur. J.*, 2011, **17**, 8957–8964.

[299] L. H. Liu, M. M. Lerner and M. Yan, *Nano Lett.*, 2010, **10**, 3754–3756.

[300] S. Vadukumpully, J. Gupta, Y. Zhang, G. Q. Xu and S. Valiyaveettil, *Nanoscale*, 2011, **3**, 303–308.

[301] T. A. Strom, E. P. Dillon, C. E. Hamilton and A. R. Barron, *Chem. Commun.*, 2010, **46**, 4097–4099.

[302] X. Zhong, J. Jin, S. Li, Z. Niu, W. Hu, R. Li and J. Ma, *Chem. Commun.*, 2010, **46**, 7340–7342.

[303] S. Niyogi, E. Bekyarova, M. E. Itkis, H. Zhang, K. Shepperd, J. Hicks, M. Sprinkle, C. Berger, C. N. Lau, W. A. deHeer, E. H. Conrad and R. C. Haddon, *Nano Lett.*, 2010, **10**, 4061–4066.

[304] A. Sinitskii, A. Dimiev, D. A. Corley, A. A. Fursina, D. V. Kosynkin and J. M. Tour, *ACS Nano*, 2010, **4**, 1949–1954.

[305] M. Fang, K. Wang, H. Lu, Y. Yang and S. Nutt, *J. Mater. Chem.*, 2009, **19**, 7098–7105.

[306] H. Liu, S. Ryu, Z. Chen, M. L. Steigerwald, C. Nuckolls and L. E. Brus, *J. Am. Chem. Soc.*, 2009, **131**, 17099–17101.

[307] Z. Liu, J. T. Robinson, X. Sun and H. Dai, *J. Am. Chem. Soc.*, 2008, **130**, 10876–10877.

[308] B. Chen, M. Liu, L. Zhang, J. Huang, J. Yao and Z. Zhang, *J. Mater. Chem.*, 2011, **21**, 7736–7741.

[309] S. Roy, N. Soin, R. Bajpai, D. S. Misra, J. A. McLaughlin and S. S. Roy, *J. Mater. Chem.*, 2011, **21**, 14725–14731.

[310] L. M. Veca, F. Lu, M. J. Meziani, L. Cao, P. Zhang, G. Qi, L. Qu, M. Shrestha and Y. P. Sun, *Chem. Commun.*, 2009, 2565–2567.

[311] M. Cano, U. Khan, T. Sainsbury, A. O?Neill, Z. Wang, I. T. McGovern, W. K. Maser, A. M. Benito and J. N. Coleman, *Carbon*, 2013, **52**, 363–371.

[312] Y. Xu, Z. Liu, X. Zhang, Y. Wang, J. Tian, Y. Huang, Y. Ma, X. Zhang and Y. Chen, *Adv. Mater.*, 2009, **21**, 1275–1279.

[313] X. Zhang, Y. Huang, Y. Wang, Y. Ma, Z. Liu and Y. Chen, *Carbon*, 2009, **47**, 334–337.

[314] T. A. Pham, B. C. Choi and Y. T. Jeong, *Nanotechnology*, 2010, **21**, 465603.

[315] C. Xu, X. Wang, J. Wang, H. Hu and L. Wan, *Chem. Phys. Lett.*, 2010, **498**, 162–167.

[316] N. Mohanty and V. Berry, *Nano Lett.*, 2008, **8**, 4469–4476.

[317] J. L. Yan, G. J. Chen, J. Cao, W. Yang, B. H. Xie and M. B. Yang, *New Carbon Mater.*, 2012, **27**, 370–376.

[318] H. R. Thomas, A. J. Marsden, M. Walker, N. R. Wilson and J. P. Rourke, *Angew. Chem. Int. Ed.*, 2014, **53**, 7613–7618.

[319] Y. Deng, Y. Li, J. Dai, M. Lang and X. Huang, *J. Polym. Sci. A Polym. Chem.*, 2011, **49**, 4747–4755.

[320] W. R. Collins, E. Schmois and T. M. Swager, *Chem. Commun.*, 2011, **47**, 8790–8792.

[321] D. Tasis, N. Tagmatarchis, A. Bianco and M. Prato, *Chem. Rev.*, 2006, **106**, 1105–1136.

[322] Y. L. Zhao and J. F. Stoddart, *Acc. Chem. Res.*, 2009, **42**, 1161–1171.

[323] J. Liu, L. Tao, W. Yang, D. Li, C. Boyer, R. Wuhrer, F. Braet and T. P. Davis, *Langmuir*, 2010, **26**, 10068–10075.

[324] D. W. Lee, T. Kim and M. Lee, *Chem. Commun.*, 2011, **47**, 8259–8261.

[325] D. Parviz, S. Das, H. S. T. Ahmed, F. Irin, S. Bhattacharia and M. J. Green, *ACS Nano*, 2012, **6**, 8857–8867.

[326] M. Zhang, B. Gao, Y. Li, X. Zhang and I. R. Hardin, *Chem. Eng. J.*, 2013, **229**, 399 – 403.

[327] S. Z. Zu, D. Zhou and B. H. Han, *J. Nanosci. Nanotechnol.*, 2013, **13**, 946–953.

[328] C. Lu, J. Li, X. L. Zhang, A. X. Zheng, H. H. Yang, X. Chen and G. N. Chen, *Anal. Chem.*, 2011, **83**, 7276–7282.

[329] D. Ihiawakrim, O. Ersen, F. Melin, P. Hellwig, I. Janowska, D. Begin, W. Baaziz, S. Begin-Colin, C. Pham-Huu and R. Baati, *Nanoscale*, 2013, **5**, 9073–9080.

[330] A. J. Patil, J. L. Vickery, T. B. Scott and S. Mann, *Adv. Mater.*, 2009, **21**, 3159–3164.

[331] H. Bai, Y. Xu, L. Zhao, C. Li and G. Shi, *Chem. Commun.*, 2009, 1667–1669.

[332] K. Jo, T. Lee, H. J. Choi, J. H. Park, D. J. Lee, D. W. Lee and B.-S. Kim, *Langmuir*, 2011, **27**, 2014–2018.

[333] D. A. Dougherty, *Science*, 1996, **271**, 163–168.

[334] S. Y. Jeong, S. H. Kim, J. T. Han, H. J. Jeong, S. Y. Jeong and G. W. Lee, *Adv. Funct. Mater.*, 2012, **22**, 3307–3314.

[335] H. Gao, S. Zhang, F. Lu, H. Jia and L. Zheng, *Colloid Polym. Sci.*, 2012, **290**, 1785–1791.

[336] Y. K. Yang, C. E. He, R. G. Peng, A. Baji, X. S. Du, Y. L. Huang, X. L. Xie and Y. W. Mai, *J. Mater. Chem.*, 2012, **22**, 5666–5675.

[337] A. G. Hsieh, C. Punckt, S. Korkut and I. A. Aksay, *J. Phys. Chem. B*, 2013, **117**, 7950–7958.

[338] A. G. Hsieh, S. Korkut, C. Punckt and I. A. Aksay, *Langmuir*, 2013, **29**, 14831–14838.

[339] M. Fernández-Merino, J. Paredes, S. Villar-Rodil, L. Guardia, P. Solís-Fernández, D. Salinas-Torres, D. Cazorla-Amorós, E. Morallón, A. Martínez-Alonso and J. Tascón, *Carbon*, 2012, **50**, 3184–3194.

[340] S. Yoon and I. In, *J. Mater. Sci.*, 2011, **46**, 1316–1321.

[341] H. Wang, B. Xia, Y. Yan, N. Li, J.-Y. Wang and X. Wang, *J. Phys. Chem. B*, 2013, **117**, 5606–5613.

[342] E. Ou, Y. Xie, C. Peng, Y. Song, H. Peng, Y. Xiong and W. Xu, *RSC Adv.*, 2013, **3**, 9490–9499.

[343] M. Ayán-Varela, J. Paredes, S. Villar-Rodil, R. Rozada, A. Martínez-Alonso and J. Tascón, *Carbon*, 2014, **75**, 390–400.

[344] Y. Arao and M. Kubouchi, *Carbon*, 2015, **95**, 802–808.

[345] C. J. Shih, S. Lin, M. S. Strano and D. Blankschtein, *J. Am. Chem. Soc.*, 2010, **132**, 14638–14648.

[346] E. Y. Choi, W. S. Choi, Y. B. Lee and Y. Y. Noh, *Nanotechnology*, 2011, **22**, 365601.

[347] C. Hansen, *Hansen Solubility Parameters: A User's Handbook*, Taylor & Francis, Boca Raton, 2nd edn., 2007.

[348] H. C. Yau, M. K. Bayazit, J. H. G. Steinke and M. S. P. Shaffer, *Chem. Commun.*, 2015, **51**, 16621–16624.

[349] J. C. Meyer, F. Eder, S. Kurasch, V. Skakalova, J. Kotakoski, H. J. Park, S. Roth, A. Chuvilin, S. Eyhusen, G. Benner, A. V. Krasheninnikov and U. Kaiser, *Phys. Rev. Lett.*, 2012, **108**, 196102.

[350] S. Rubino, S. Akhtar and K. Leifer, *Microsc. Microanal.*, 2016, **22**, 250–256.

[351] S. Horiuchi, T. Gotou, M. Fujiwara, R. Sotoaka, M. Hirata, K. Kimoto, T. Asaka, T. Yokosawa, Y. Matsui, K. Watanabe and M. Sekita, *Jpn. J. Appl. Phys.*, 2003, **42**, L1073.

[352] J. Meyer, A. Geim, M. Katsnelson, K. Novoselov, D. Obergfell, S. Roth, C. Girit and A. Zettl, *Solid State Commun.*, 2007, **143**, 101 – 109.

[353] J. Plitzko and J. Mayer, *Ultramicroscopy*, 1999, **78**, 207 – 219.

[354] S. Silva and V. Stolojan, *Thin Solid Films*, 2005, **488**, 283 – 290.

[355] M. H. Gass, U. Bangert, A. L. Bleloch, P. Wang, R. R. Nair and A. K. Geim, *Nat. Nanotechnol.*, 2008, **3**, 676 – 681.

[356] M. K. Tynan, D. W. Johnson, B. P. Dobson and K. S. Coleman, *Nanoscale*, 2016, **8**, 13303–13310.

[357] C. J. Shearer, A. D. Slattery, A. J. Stapleton, J. G. Shapter and C. T. Gibson, *Nanotechnology*, 2016, **27**, 125704.

[358] D. Li, M. Müller, R. Kaner and G. Wallace, *Nat. Nanotechnol.*, 2008, **3**, 101–105.

[359] D. Chen, L. Li and L. Guo, *Nanotechnology*, 2011, **22**, 325601.

[360] D. Luo, G. Zhang, J. Liu and X. Sun, *J. Phys. Chem. C*, 2011, **115**, 11327–11335.

[361] S. Gurunathan, J. W. Han, V. Eppakayala and J. H. Kim, *Int. J. Nanomedicine*, 2013, **8**, 1015–1027.

[362] M. Lotya, P. J. King, U. Khan, S. De and J. N. Coleman, *ACS Nano*, 2010, **4**, 3155–3162.

[363] U. Khan, H. Porwal, A. O'Neill, K. Nawaz, P. May and J. N. Coleman, *Langmuir*, 2011, **27**, 9077–9082.

[364] U. Khan, A. O'Neill, M. Lotya, S. De and J. N. Coleman, *Small*, 2010, **6**, 864–871.

[365] R. Su, S. F. Lin, D. Q. Chen and G. H. Chen, *J. Phys. Chem. C*, 2014, **118**, 12520–12525.

[366] F. Tuinstra and J. L. Koenig, *J. Chem. Phys*, 1970, **53**, 1126–1130.

[367] A. C. Ferrari and J. Robertson, *Phys. Rev. B*, 2001, **64**, 075414.

[368] A. C. Ferrari and J. Robertson, *Phys. Rev. B*, 2000, **61**, 14095–14107.

[369] A. C. Ferrari and D. M. Basko, *Nat. Nanotechnol.*, 2013, **8**, 235–246.

[370] A. C. Ferrari, J. C. Meyer, V. Scardaci, C. Casiraghi, M. Lazzeri, F. Mauri, S. Piscanec, D. Jiang, K. S. Novoselov, S. Roth and A. K. Geim, *Phys. Rev. Lett.*, 2006, **97**, 187401.

[371] A. C. Ferrari, *Solid State Commun.*, 2007, **143**, 47–57.

[372] A. Jorio, E. H. M. Ferreira, M. V. O. Moutinho, F. Stavale, C. A. Achete and R. B. Capaz, *Phys. Status Solidi B*, 2010, **247**, 2980–2982.

[373] A. Kaniyoor and S. Ramaprabhu, *AIP Adv.*, 2012, **2**, 032183.

[374] H. Y. Nan, Z. H. Ni, J. Wang, Z. Zafar, Z. X. Shi and Y. Y. Wang, *J. Raman Spectrosc.*, 2013, **44**, 1018–1021.

[375] D. Bom, R. Andrews, D. Jacques, J. Anthony, B. Chen, M. S. Meier and J. P. Selegue, *Nano Lett.*, 2002, **2**, 615–619.

[376] J. D. Saxby, S. P. Chatfield, A. J. Palmisano, A. M. Vassallo, M. A. Wilson and L. S. K. Pang, *J. Phys. Chem.*, 1992, **96**, 17–18.

[377] L. S. K. Pang, J. D. Saxby and S. P. Chatfield, *J. Phys. Chem.*, 1993, **97**, 6941–6942.

[378] A. M. Rodríguez and P. V. Jiménez, *Thermochim. Acta*, 1984, **87**, 113–122.

[379] H. K. Jeong, M. H. Jin, K. P. So, S. C. Lim and Y. H. Lee, *J. Phys. D: Appl. Phys.*, 2009, **42**, 065418.

[380] J. Jang, V. H. Pham, S. H. Hur and J. S. Chung, *J. Colloid Interf. Sci.*, 2014, **424**, 62–66.

[381] W. L. Bragg, *Nature*, 1912, **90**, 410.

[382] W. H. Bragg and W. L. Bragg, *Proc. R. Soc. Lond. A*, 1913, **88**, 428–438.

[383] L. Stobinski, B. Lesiak, A. Malolepszy, M. Mazurkiewicz, B. Mierzwa, J. Zemek, P. Jiricek and I. Bieloshapka, *J. Electron Spectrosc. Relat. Phenom.*, 2014, **195**, 145–154.

[384] A. Buchsteiner, A. Lerf and J. Pieper, *J. Phys. Chem. B*, 2006, **110**, 22328–22338.

[385] J. Ding, W. Yan, W. Xie, S. Sun, J. Bao and C. Gao, *Nanoscale*, 2014, **6**, 2299–2306.

[386] S. Stankovich, R. D. Piner, X. Chen, N. Wu, S. T. Nguyen and R. S. Ruoff, *J. Mater. Chem.*, 2006, **16**, 155–158.

[387] R. Rozada, J. I. Paredes, S. Villar-Rodil, A. Martínez-Alonso and J. M. D. Tascón, *Nano Res.*, 2013, **6**, 216–233.

[388] G. Sobon, J. Sotor, J. Jagiello, R. Kozinski, M. Zdrojek, M. Holdynski, P. Paletko, J. Boguslawski, L. Lipinska and K. M. Abramski, *Opt. Express*, 2012, **20**, 19463–19473.

[389] F. Sette, G. K. Wertheim, Y. Ma, G. Meigs, S. Modesti and C. T. Chen, *Phys. Rev. B*, 1990, **41**, 9766–9770.

[390] D. Nuvoli, L. Valentini, V. Alzari, S. Scognamillo, S. B. Bon, M. Piccinini, J. Illescas and A. Mariani, *J. Mater. Chem.*, 2011, **21**, 3428–3431.

[391] ISO, *Guidelines for the characterization of dispersion stability*, International Organization for Standardization ISO TR 13097:2013, 2013.

[392] L. Schramm, *Emulsions, Foams, and Suspensions: Fundamentals and Applications*, Wiley, Weinheim, 2005.

[393] T. L. Doane, C.-H. Chuang, R. J. Hill and C. Burda, *Acc. Chem. Res.*, 2012, **45**, 317–326.

[394] M. J. Assael, K. D. Antoniadis and W. A. Wakeham, *Int. J. Thermophys.*, 2010, **31**, 1051–1072.

[395] J. W. Haarman, *Physica*, 1971, **52**, 605–619.

[396] ASTM, *Standard Test Method for Thermal Conductivity of Liquids*, ASTM International ASTM D2717-95(2009), 2009.

[397] *Decagon Devices*, `https://www.decagon.com/en/thermal/instruments/kd2-pro/`, Accessed: 05-04-2017.

[398] ASTM, *Standard Test Method for Determining Specific Heat Capacity by Differential Scanning Calorimetry*, ASTM International ASTM E1269-11, 2011.

[399] ASTM, *Standard Test Method for Thermal Diffusivity by the Flash Method*, ASTM International ASTM E1461-13, 2013.

[400] ASTM, *Standard Test Method for Kinematic Viscosity of Transparent and Opaque Liquids (and Calculation of Dynamic Viscosity)*, ASTM International ASTM D445-06, 2006.

[401] ASTM, *Standard Specifications and Operating Instructions for Glass Capillary Kinematic Viscometers*, ASTM International ASTM D446-07, 2007.

[402] *PCS Instruments*, http://www.pcs-instruments.com/product/mtm-mini-traction-machine/, Accessed: 05-12-2016.

[403] G. Minatchy, P. Thomas, P. Bilas, N. Nomede-Martyr and L. Romana, *Tribol. Lett.*, 2014, **56**, 443–456.

[404] Y. Rai, A. Neville and A. Morina, *Lubr. Sci.*, 2016, **28**, 449–471.

[405] B. M. Ginzburg, M. V. Baidakova, O. F. Kireenko, D. G. Tochil'nikov and A. A. Shepelevskii, *Tech. Phys.*, 2000, **45**, 1595–1603.

[406] E. Carson, *Ph.D. thesis*, University of Kansas, 1914.

[407] K. P. Lee, N. C. Chromey, R. Culik, J. R. Barnes and P. W. Schneider, *Toxicol. Sci.*, 1987, **9**, 222.

[408] K. Sitarek and J. Stetkiewicz, *Int. J. Occup. Med. Environ. Health*, 2008, **21**, 73–80.

[409] G. L. Kennedy, *Crit. Rev. Toxicol.*, 2012, **42**, 793–826.

[410] S. Eigler, C. Dotzer and A. Hirsch, *Carbon*, 2012, **50**, 3666–3673.

[411] C. N. McEwen, R. G. McKay and B. S. Larsen, *Anal. Chem.*, 2005, **77**, 7826–7831.

[412] R. W. Taft and M. J. Kamlet, *J. Am. Chem. Soc.*, 1976, **98**, 2886–2894.

[413] M. J. Kamlet and R. W. Taft, *J. Am. Chem. Soc.*, 1976, **98**, 377–383.

[414] M. J. Kamlet, J. L. M. Abboud and R. W. Taft, in *Progress in Physical Organic Chemistry*, John Wiley & Sons, Inc., New York, 1981, vol. 13, pp. 485–630.

[415] A. de Juan, G. Fonrodona and E. Casassas, *TrAC, Trends Anal. Chem.*, 1997, **16**, 52–62.

[416] G. Wang, B. Wang, J. Park, J. Yang, X. Shen and J. Yao, *Carbon*, 2009, **47**, 68–72.

[417] T. M. McCoy, M. J. Pottage and R. F. Tabor, *J. Phys. Chem., C*, 2014, **118**, 4529–4535.

[418] C. Xu, X. Shi, A. Ji, L. Shi, C. Zhou and Y. Cui, *PLoS One*, 2015, **10**, 1–15.

[419] R. S. Ningthoujam, A. Gautam and N. Padma, *Phys. Chem. Chem. Phys.*, 2017, **19**, 2294–2303.

[420] M. Green, *J. Mater. Chem.*, 2010, **20**, 5797–5809.

[421] J. Liu, H. Jeong, J. Liu, K. Lee, J.-Y. Park, Y. Ahn and S. Lee, *Carbon*, 2010, **48**, 2282–2289.

[422] H. Liu, J. S. Owen and A. P. Alivisatos, *J. Am. Chem. Soc.*, 2007, **129**, 305–312.

[423] F. Wang, R. Tang and W. E. Buhro, *Nano Lett.*, 2008, **8**, 3521–3524.

[424] G. J. Price and P. F. Smith, *Polym. Int.*, 1991, **24**, 159–164.

[425] E. V. Chubarova, E. Y. Melenevskaya and V. V. Shamanin, *J. Macromol. Sci. B*, 2013, **52**, 873–896.

[426] J. J. Healy, J. J. de Groot and J. Kestin, *Physica C*, 1976, **82**, 392–408.

[427] H. M. Roder, *J. Res. Nat. Bur. Stand.*, 1981, **86**, 457–493.

[428] Y. Nagasaka and A. Nagashima, *J. Phys. E: Sci. Instrum.*, 1981, **14**, 1435–1440.

[429] W. Yu and S. U. Choi, *Rev. Sci. Instrum.*, 2006, **77**, 076102.

[430] M. Assael, C. F. Chen, I. Metaxa and W. Wakeham, *Int. J. Thermophys.*, 2004, **25**, 971–985.

[431] M. Kostic and K. Simham, Proceedings of the 6th WSEAS International Conference on Heat and Mass Transfer, 2009, pp. 71–78.

[432] J. G. Bleazard and A. S. Teja, *J. Chem. Eng. Data*, 1995, **40**, 732–737.

[433] R. Perkins, H. Roder and C. Nieto de Castro, *J. Res. Natl. Inst. Stand. Technol.*, 1991, **96**, 247–269.

[434] M. L. V. Ramires, C. A. Nieto de Castro, Y. Nagasaka, A. Nagashima, M. J. Assael and W. A. Wakeham, *J. Phys. Chem. Ref. Data*, 1995, **24**, 1377–1381.

Appendix A

Technical Drawings for the THW Instrument

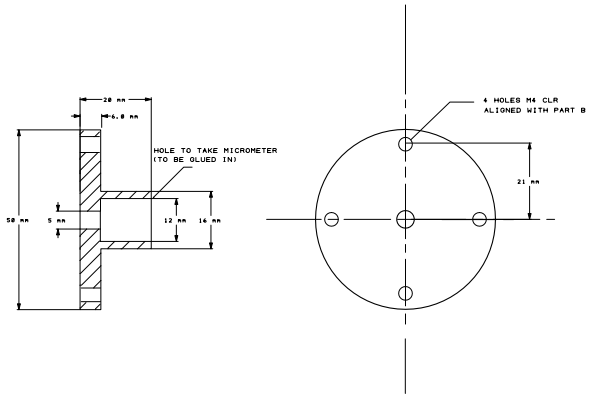

PART A MICROMETER MOUNT
(ALUMINIUM)

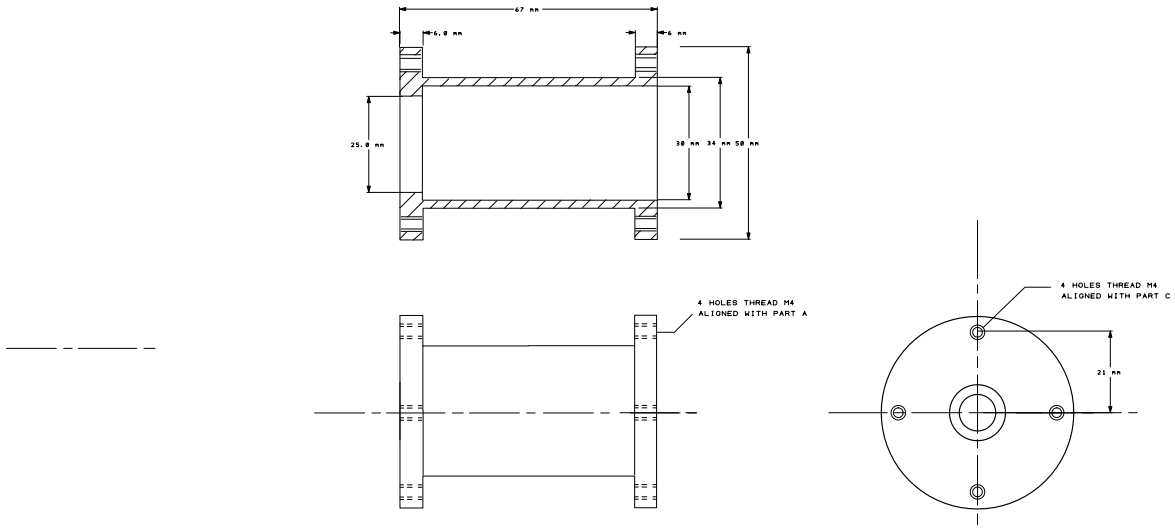

PART B COMPRESSION SPRING HOUSING
(ALUMINIUM)

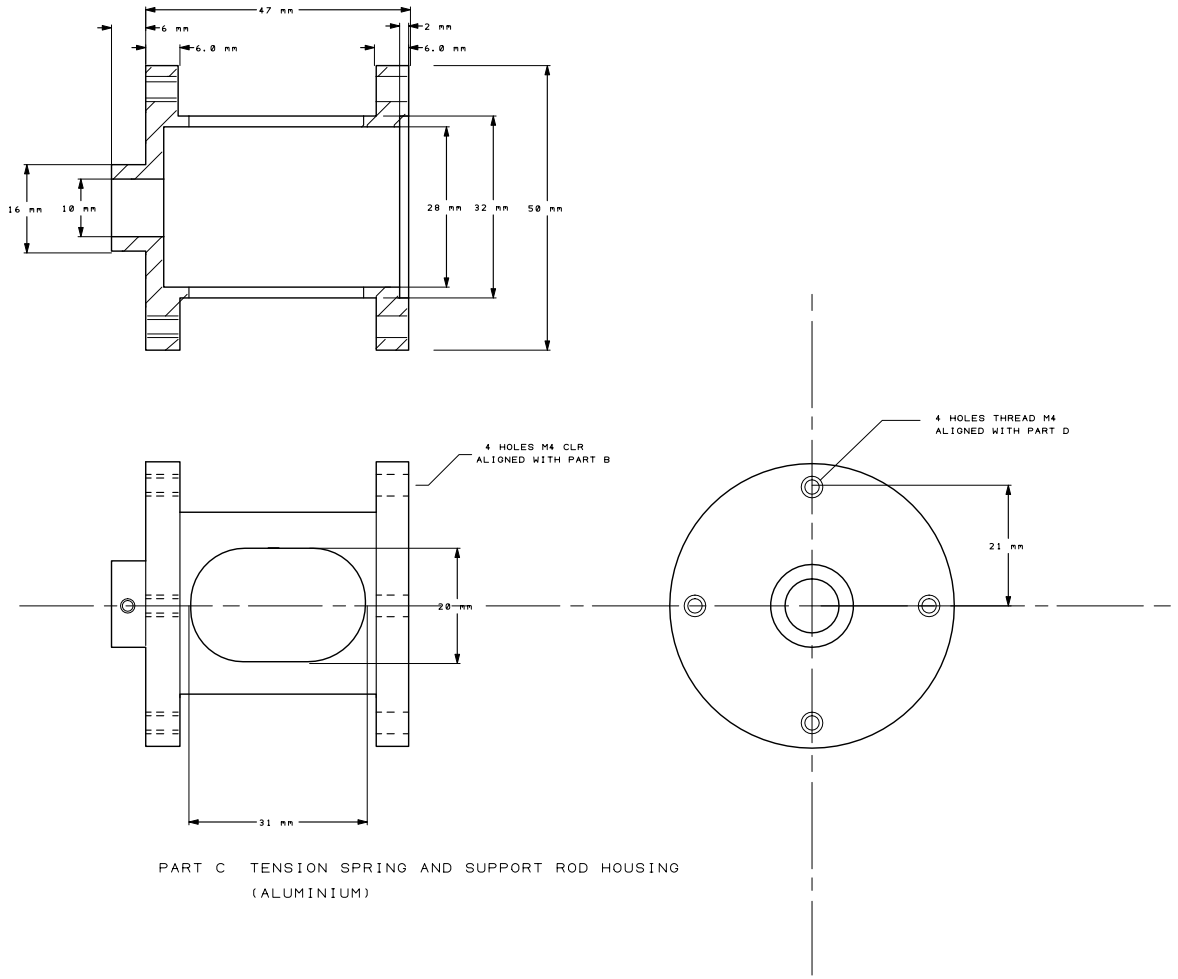

PART C TENSION SPRING AND SUPPORT ROD HOUSING
(ALUMINIUM)

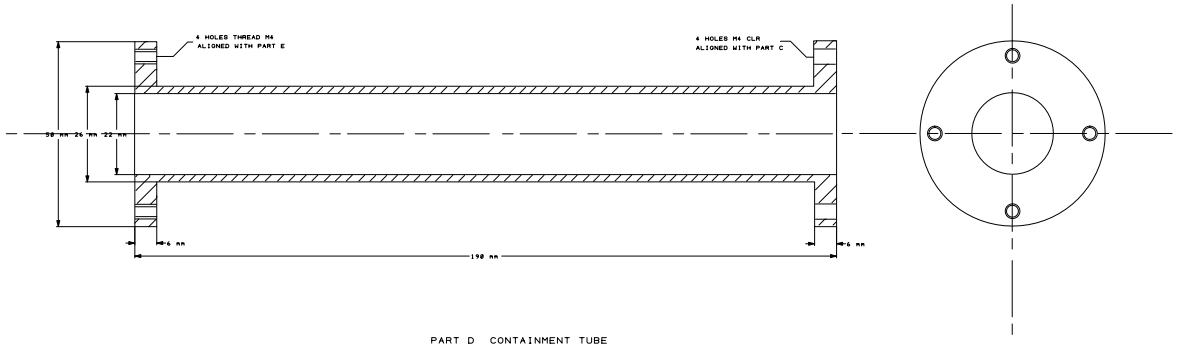

PART D CONTAINMENT TUBE
(ALUMINIUM)

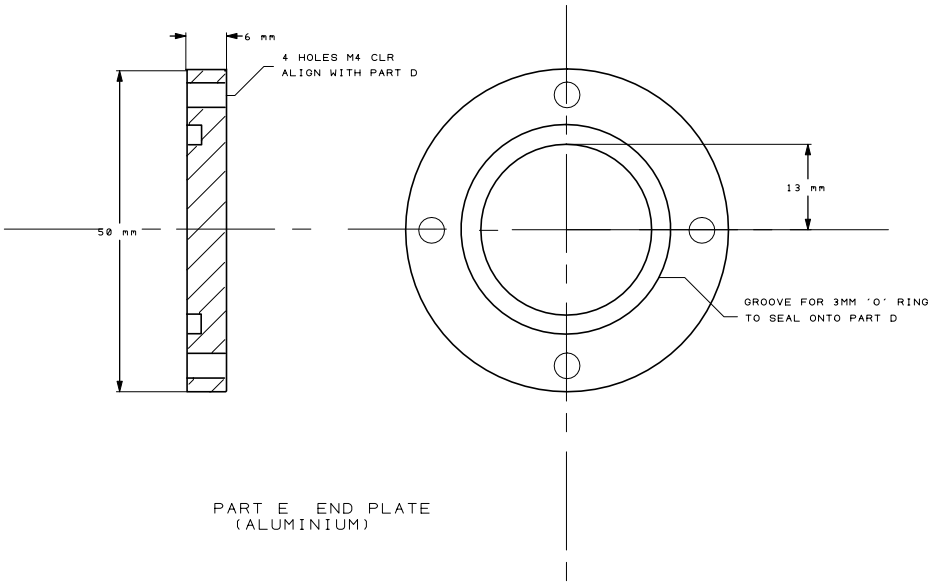

PART E END PLATE
(ALUMINIUM)

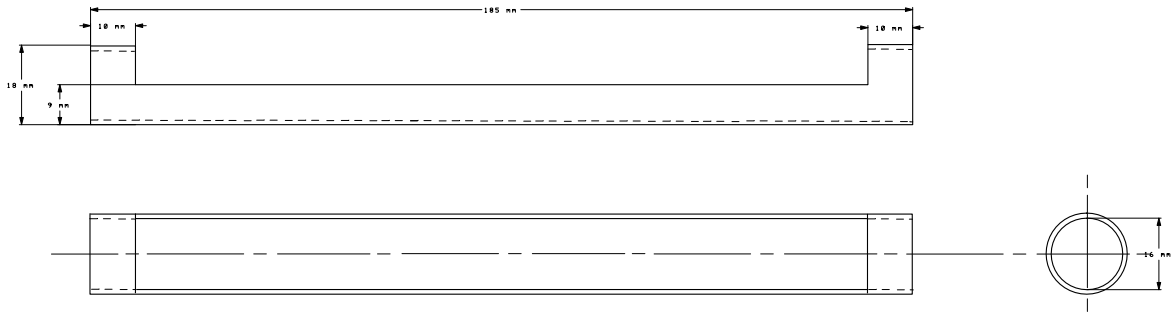

PART F WIRE SUPPORT
BRASS - FORMED FROM 0.75" OD 0.065" WALL THICKNESS TUBE

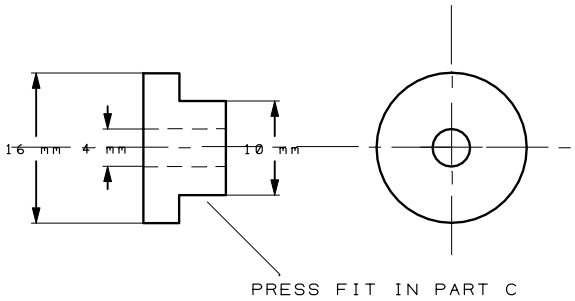

PART G SLIDING ROD GUIDE
(DELRIN OR SIMILAR)

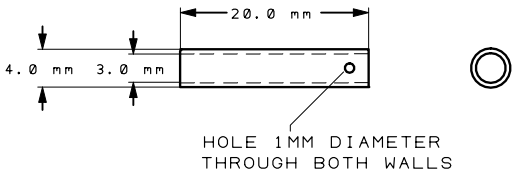

PART H SLIDING ROD
(BRASS)
SLIDING FIT IN PART G

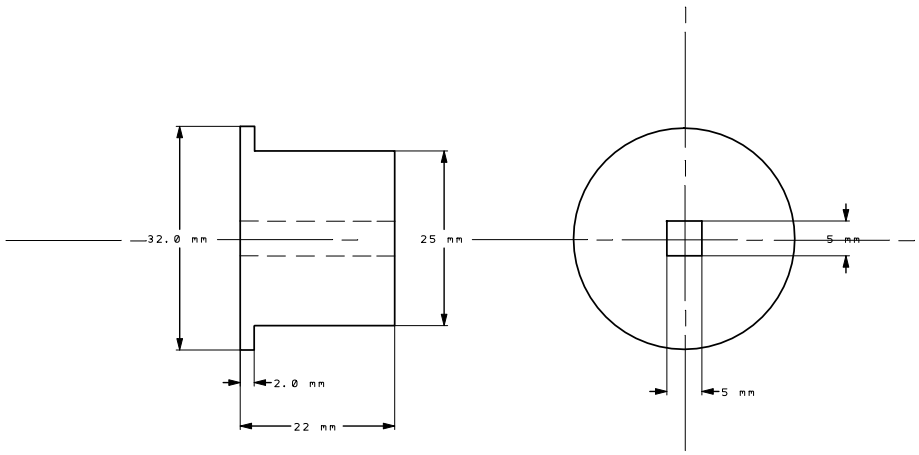

PART J SPRING ROD GUIDE
(DELRIN OR SIMILAR)

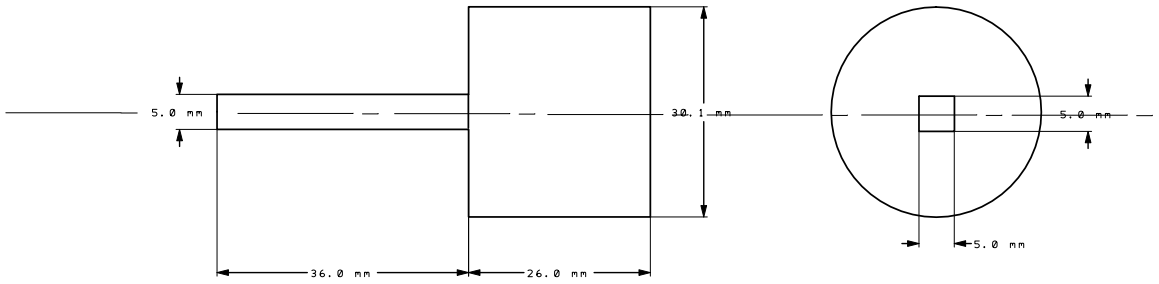

PART K SPRING ROD
(ALUMINIUM)
SQUARE SECTION SLIDING FIT IN PART J

Electronic Drawings for the THW Instrument

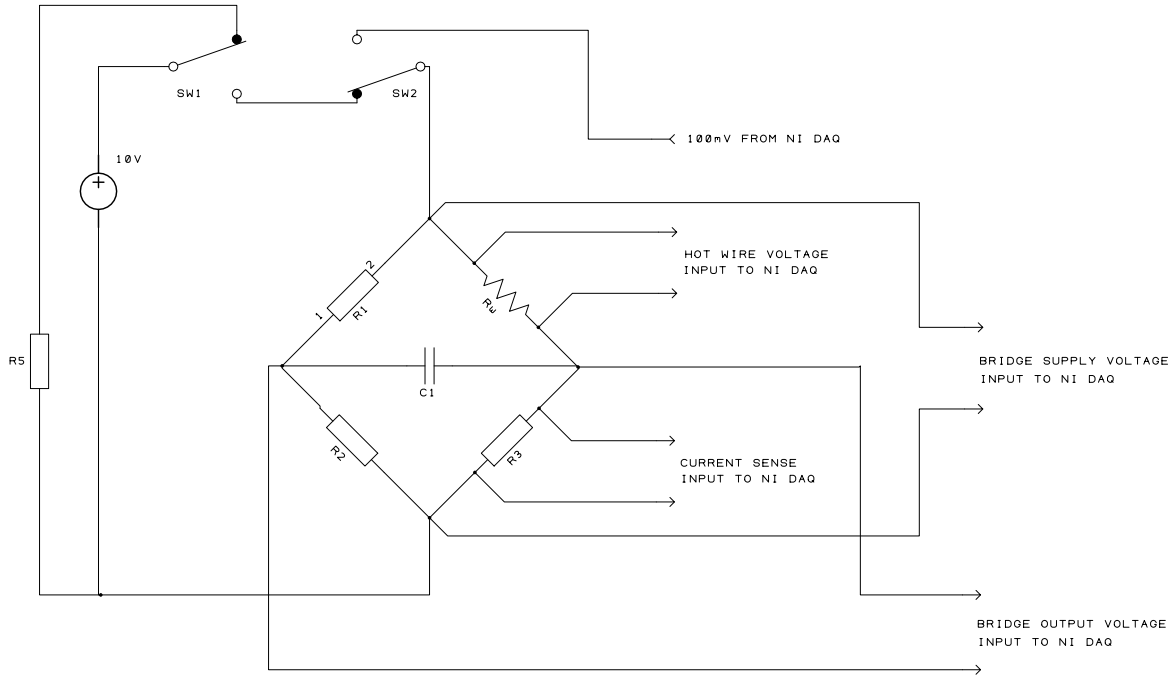

THE ANALOGUE INPUTS TO THE NI DAQ MUST BE SET AS DIFFERENTIAL INPUTS AND NOT SINGLE ENDED GROUND REFERENCED EXCEPT FOR BRIDGE SUPPLY VOLTAGE WHICH IS GROUND REFERENCED.

SW1 AND SW2 (RL1 AND RL2 ON POWER SUPPLY BOARD) ARE CONTROLLED BY DIGITAL OUTPUTS FROM THE NI DAQ.

NOT SHOWN IS AN ADDITIONAL SWITCH (RL3 ON POWER SUPPLY CIRCUIT) WHICH CONNECTS A FIXED RESISTOR (R3 AND R4 ON POWER SUPPLY BOARD)IN PLACE OF THE HOT WIRE FOR INITIAL BRIDGE STABILISATION.

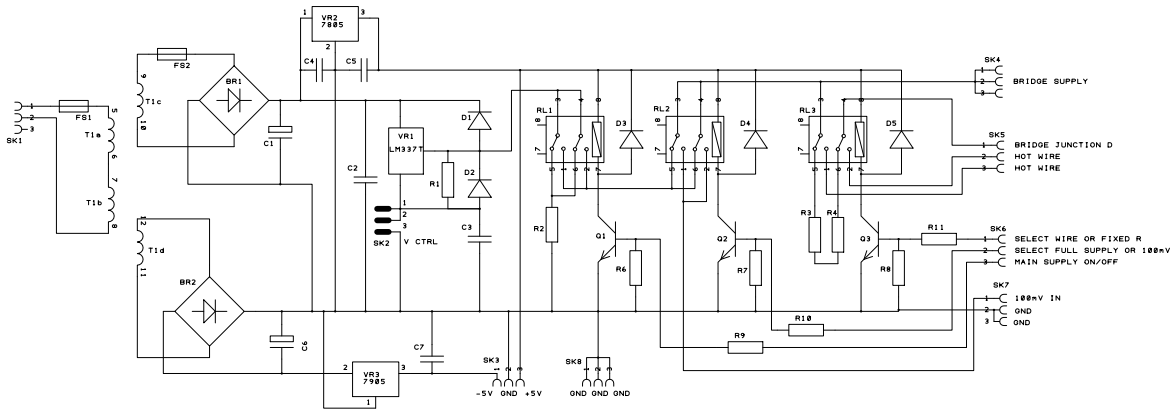

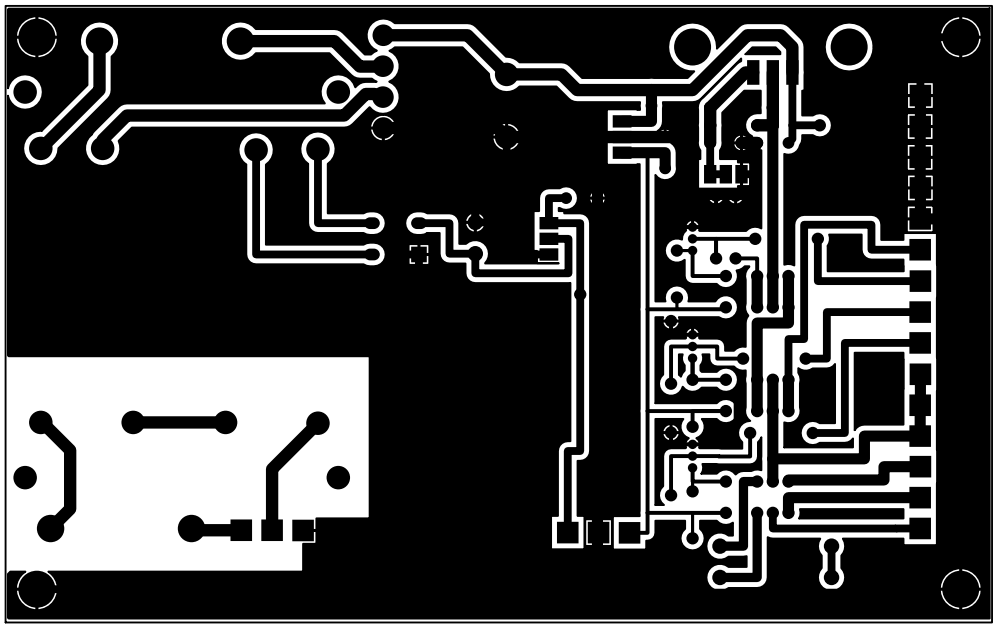

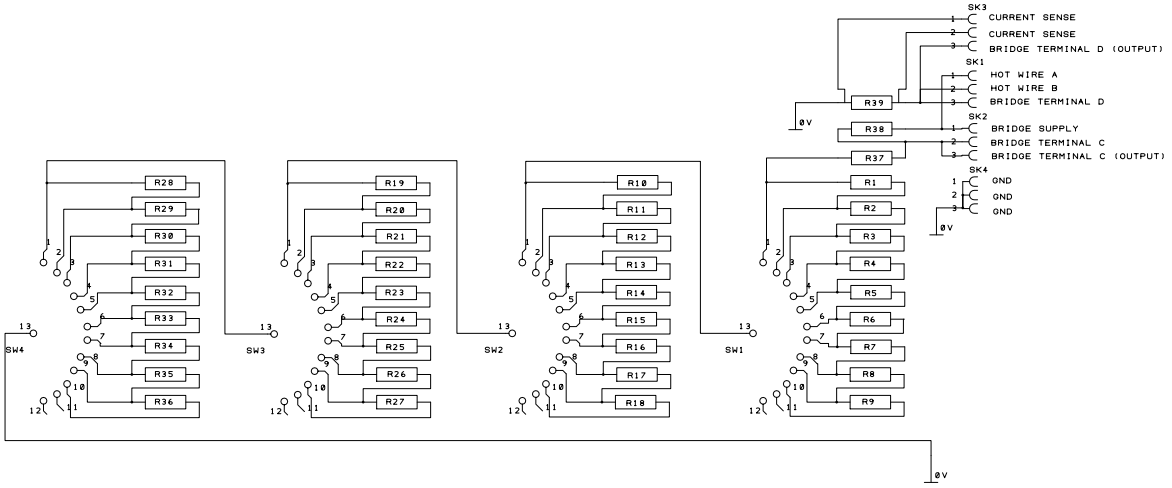

SW4 RANGE 0.1 TO 0.9R
R28 TO R36 0.1R

SW3 RANGE 1R TO 9R
R19 TO R27 1R

SW2 RANGE 10R TO 90R
R10 TO R18 10R

SW1 RANGE 100R TO 900R
R1 TO R9 100R

R37 = 2000R AND TOGETHER WITH THE SWITCHED RESISTORS ARE REPRESENTED BY R2 IN THE BRIDGE CIRCUIT.
R2 IS THEREFORE ADJUSTABLE BETWEEN 2000R AND 3000R IN 0.1R INCREMENTS.

R38 = 2000R AND IS REPRESENTED BY R1 IN THE BRIDGE CIRCUIT.

R39 = 10.000R AND IS REPRESENTED BY R3 IN THE BRIDGE CIRCUIT.

IF THE HOT WIRE RESISTANCE IS NOMINALLY 8R THEN THE BRIDGE WILL BE BALANCED WHEN R2 = 2500R

R39 IS ALSO USED AS A CURRENT SENSE ELEMENT. THE VOLTAGE MEASURED ACROSS R39 IS EQUIVALENT TO THE CURRENT THROUGH THE HOT WIRE MULTIPLIED BY TEN.

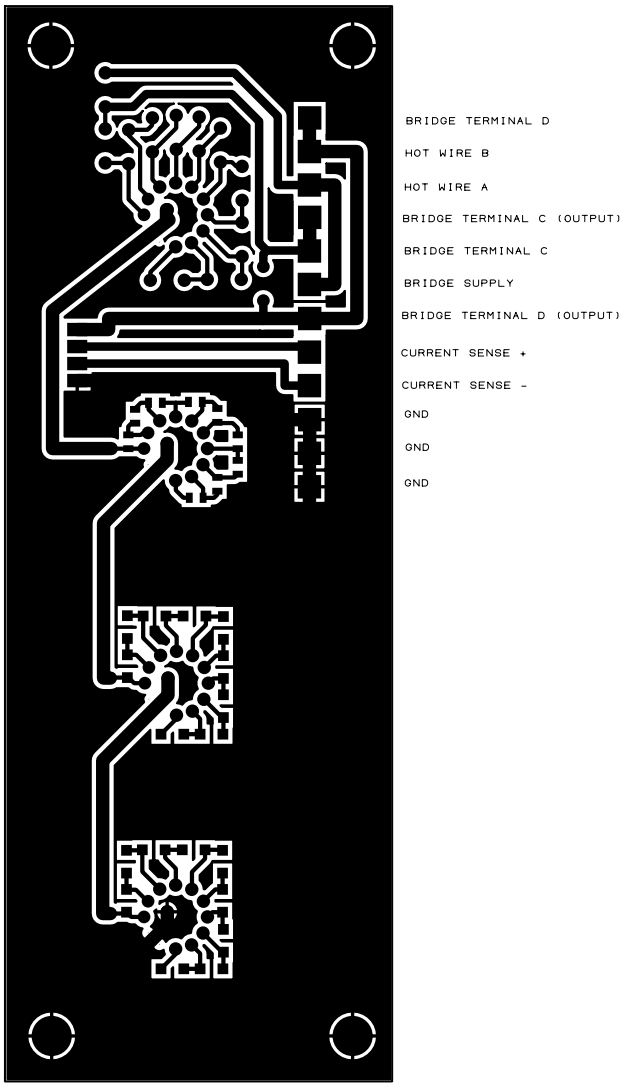
BRIDGE TERMINAL D
HOT WIRE B
HOT WIRE A
BRIDGE TERMINAL C (OUTPUT)
BRIDGE TERMINAL C
BRIDGE SUPPLY
BRIDGE TERMINAL D (OUTPUT)
CURRENT SENSE +
CURRENT SENSE -
GND
GND
GND

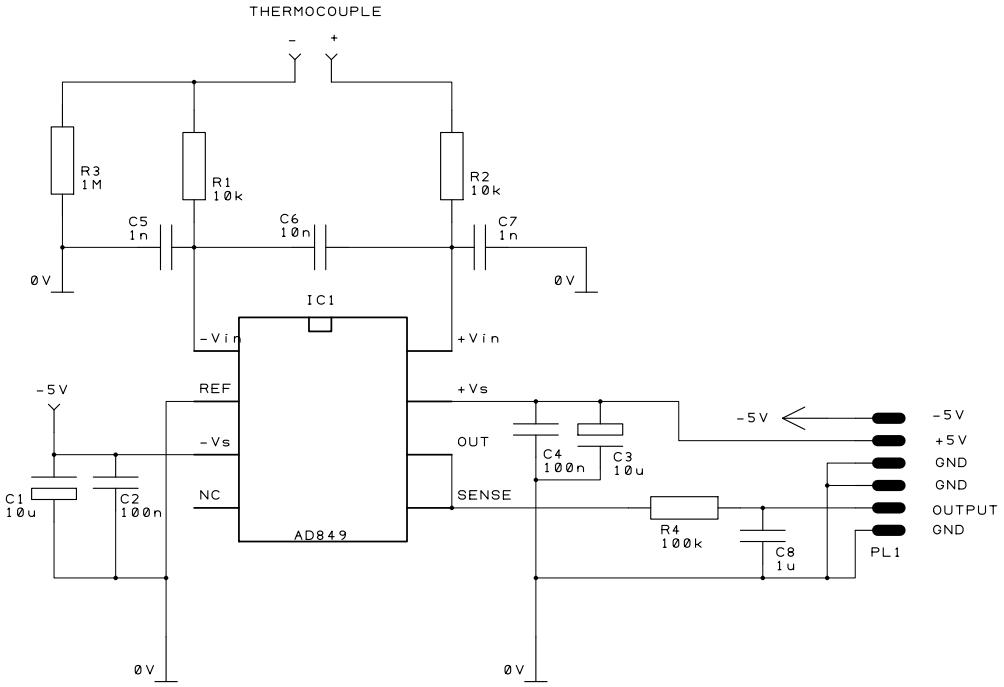

AD849 THERMOCOUPLE AMPLIFIER

OUTPUT 5mV/C

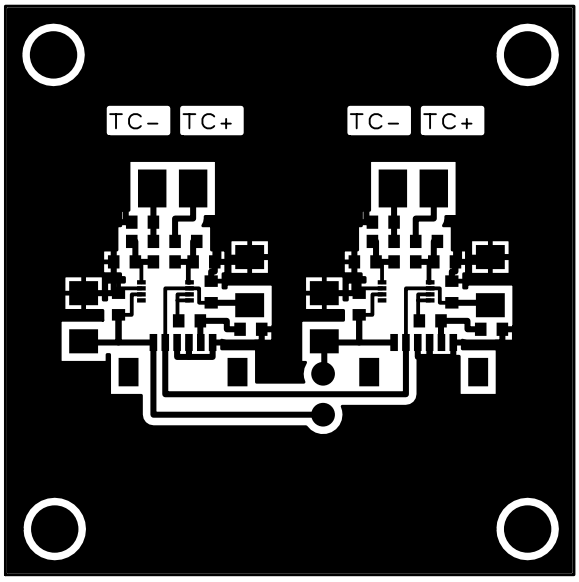

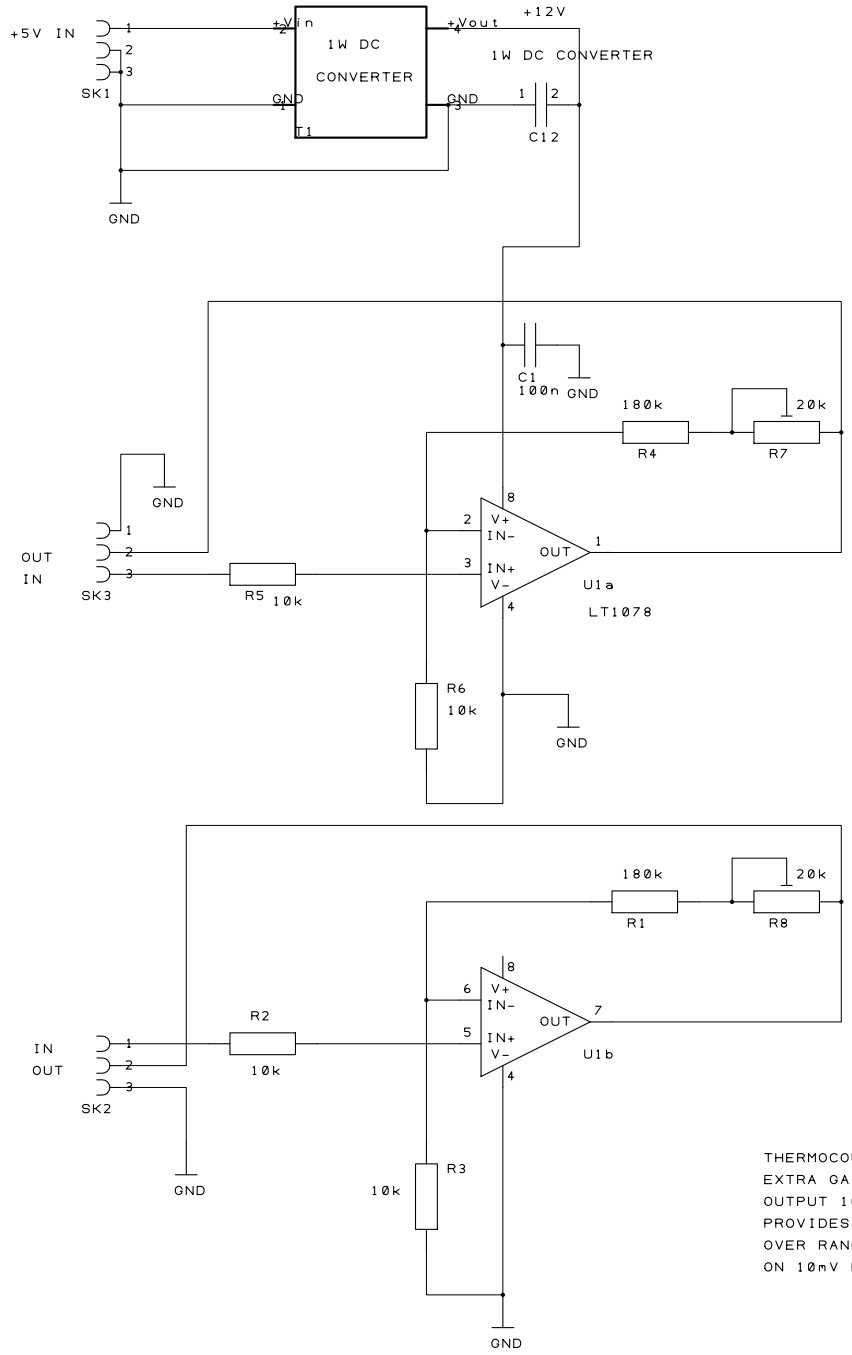

THERMOCOUPLE AMPLIFIER
EXTRA GAIN STAGE
OUTPUT 100mV/DEGREE C
PROVIDES FOR 0.1 DEGREE C RESOLUTION
OVER RANGE 0 TO 100 DEGREES C
ON 10mV RESOLUTION DAQ ANALOGUE INPUT

Appendix B

LabVIEW Script for Operation of the THW Instrument

LabVIEW Script for Variable Temperature and Calibration

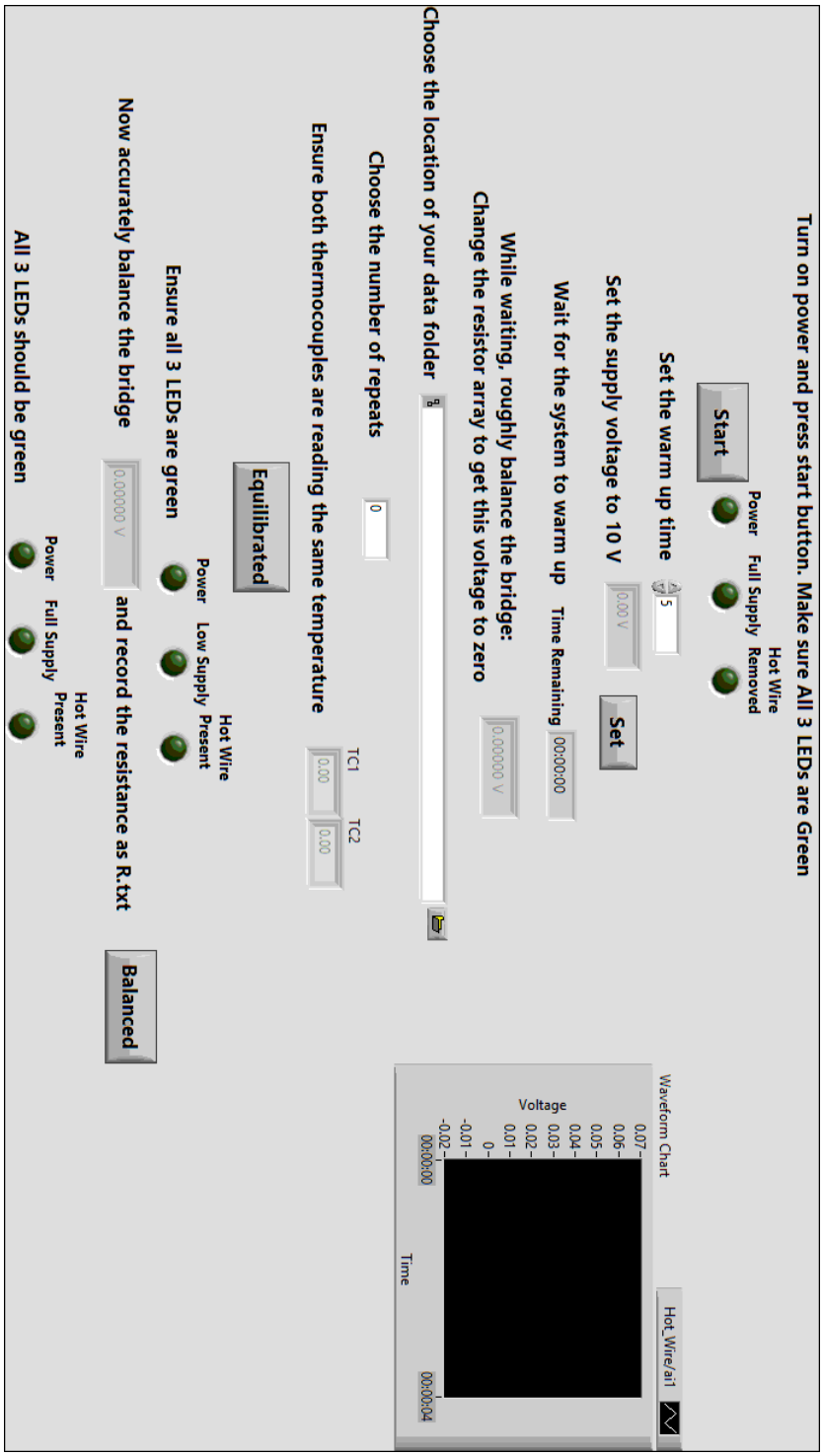

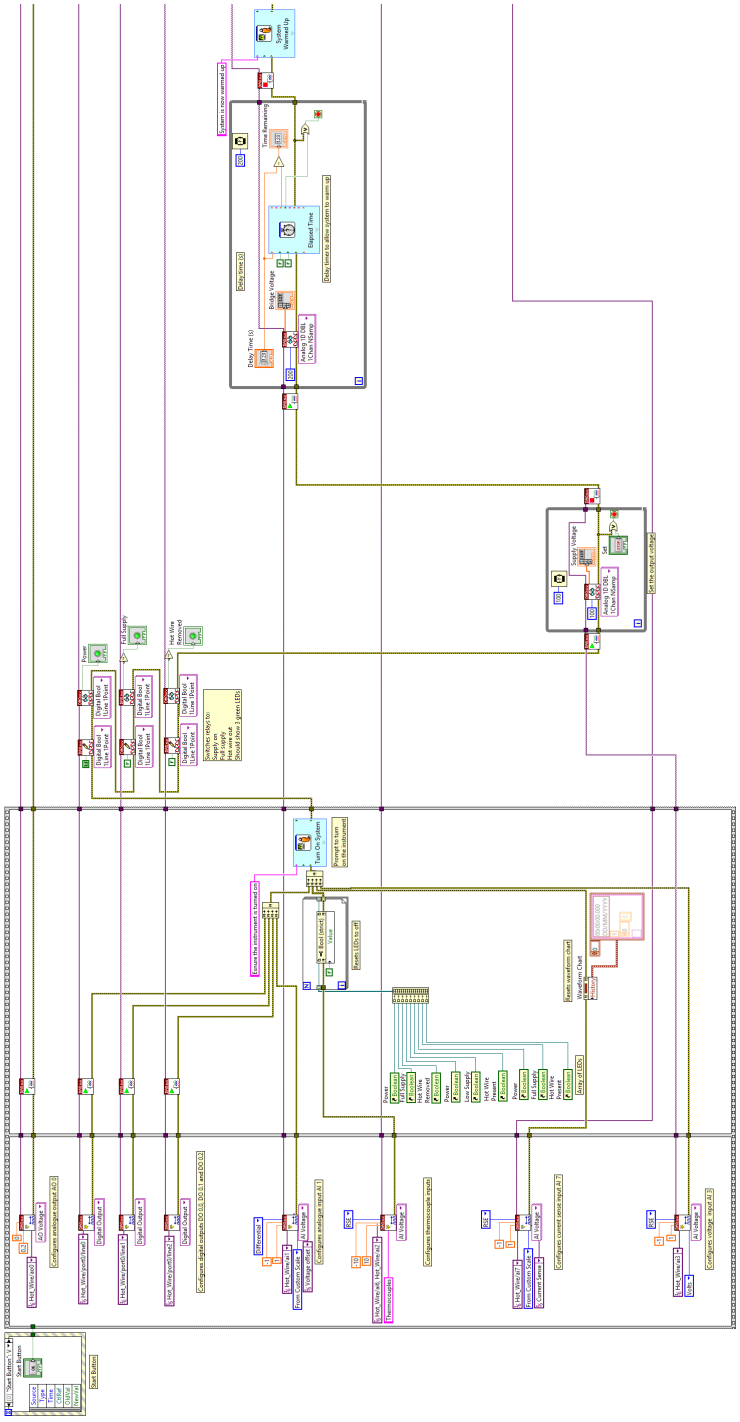

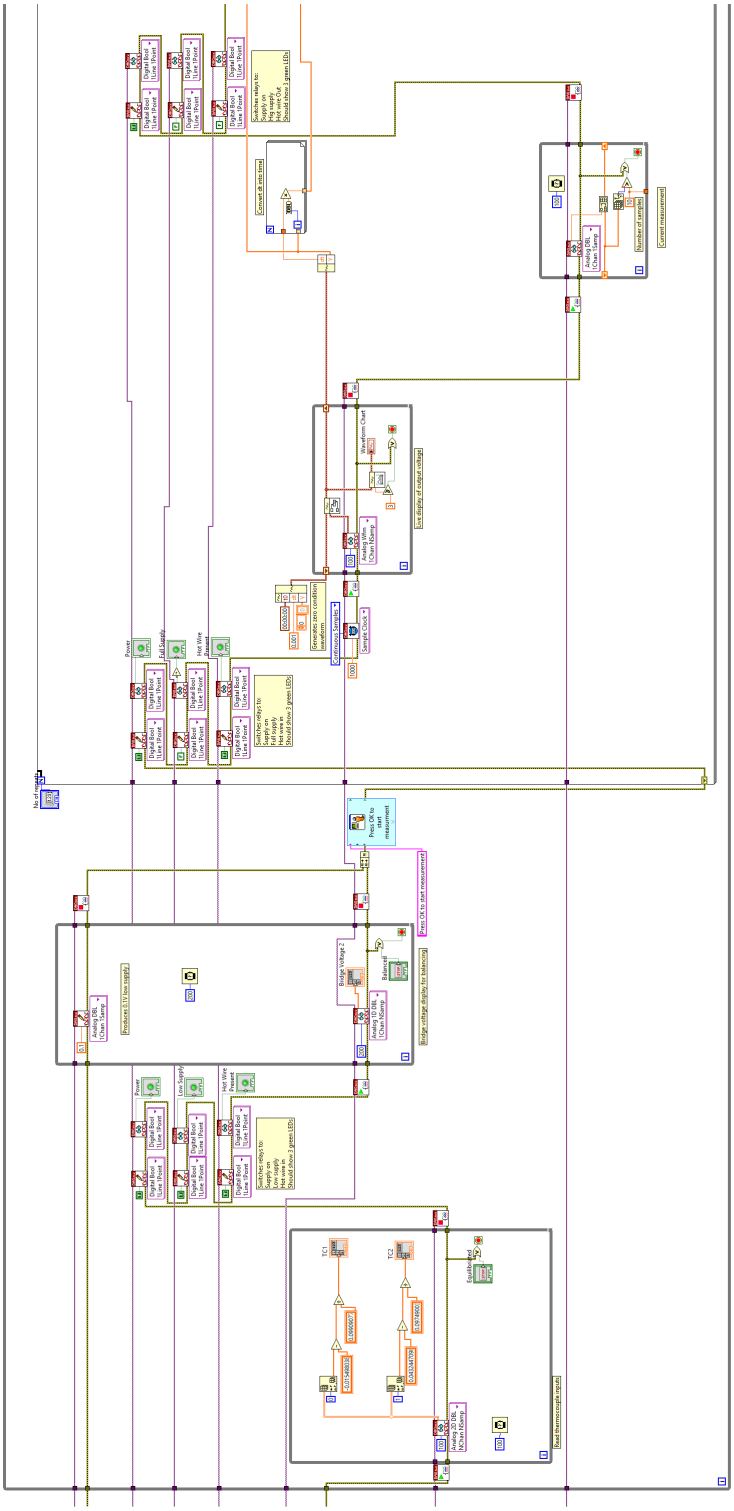

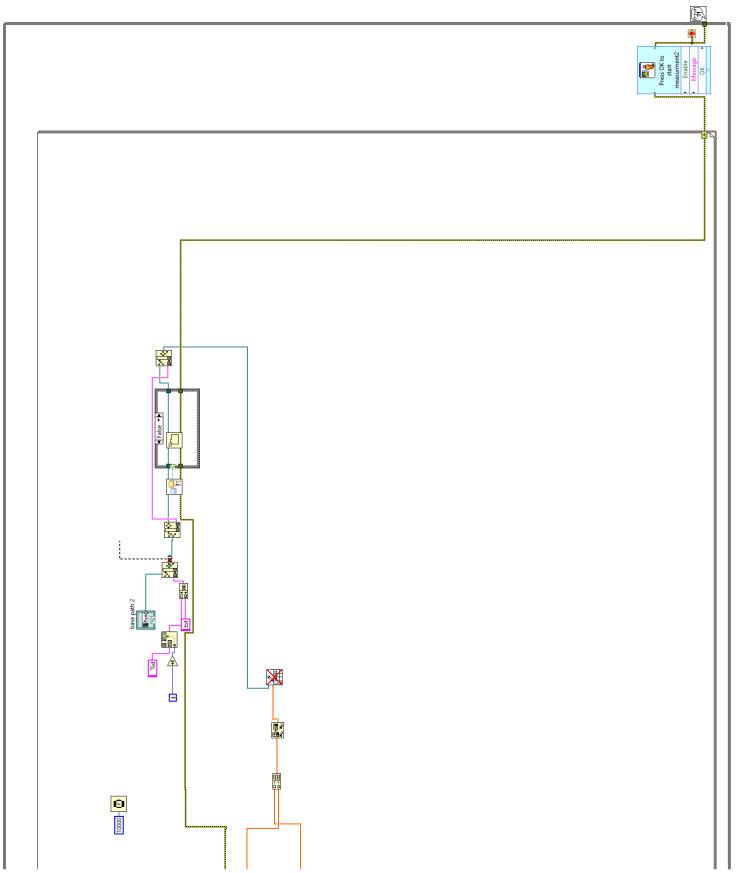

LabVIEW Script for Constant Temperature

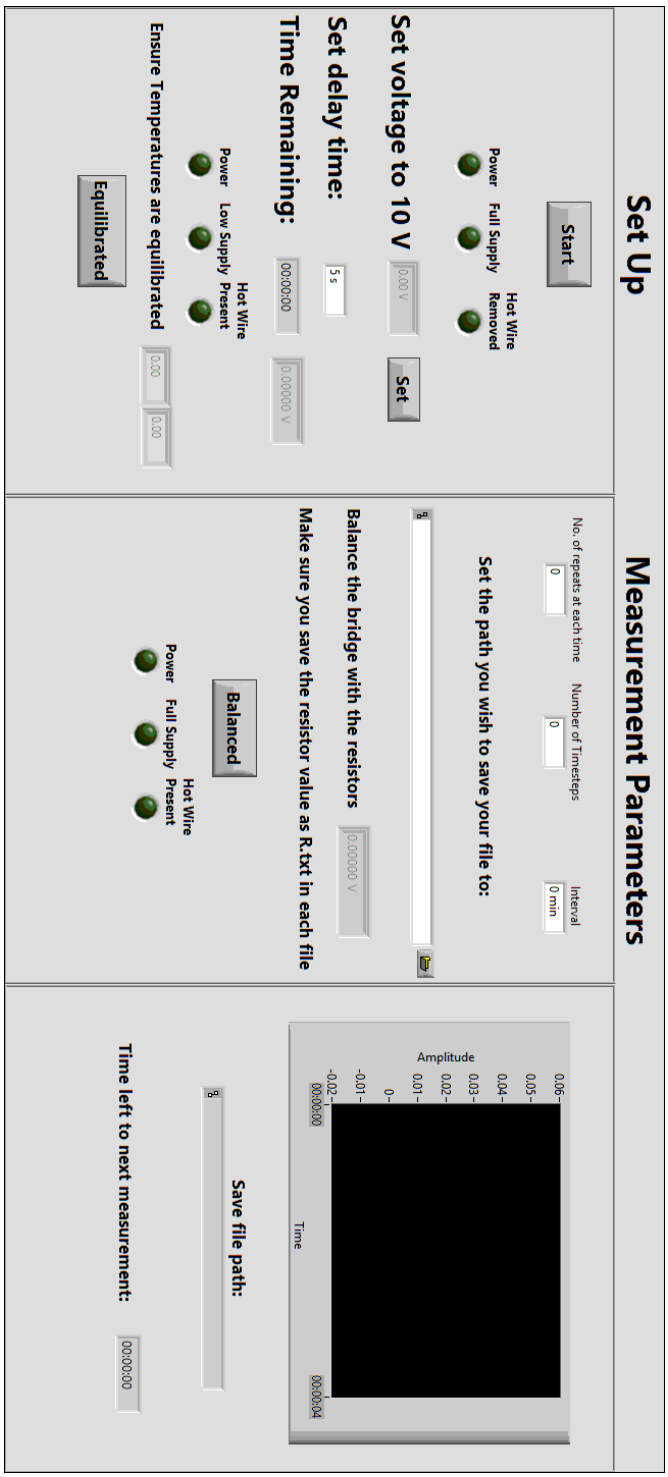

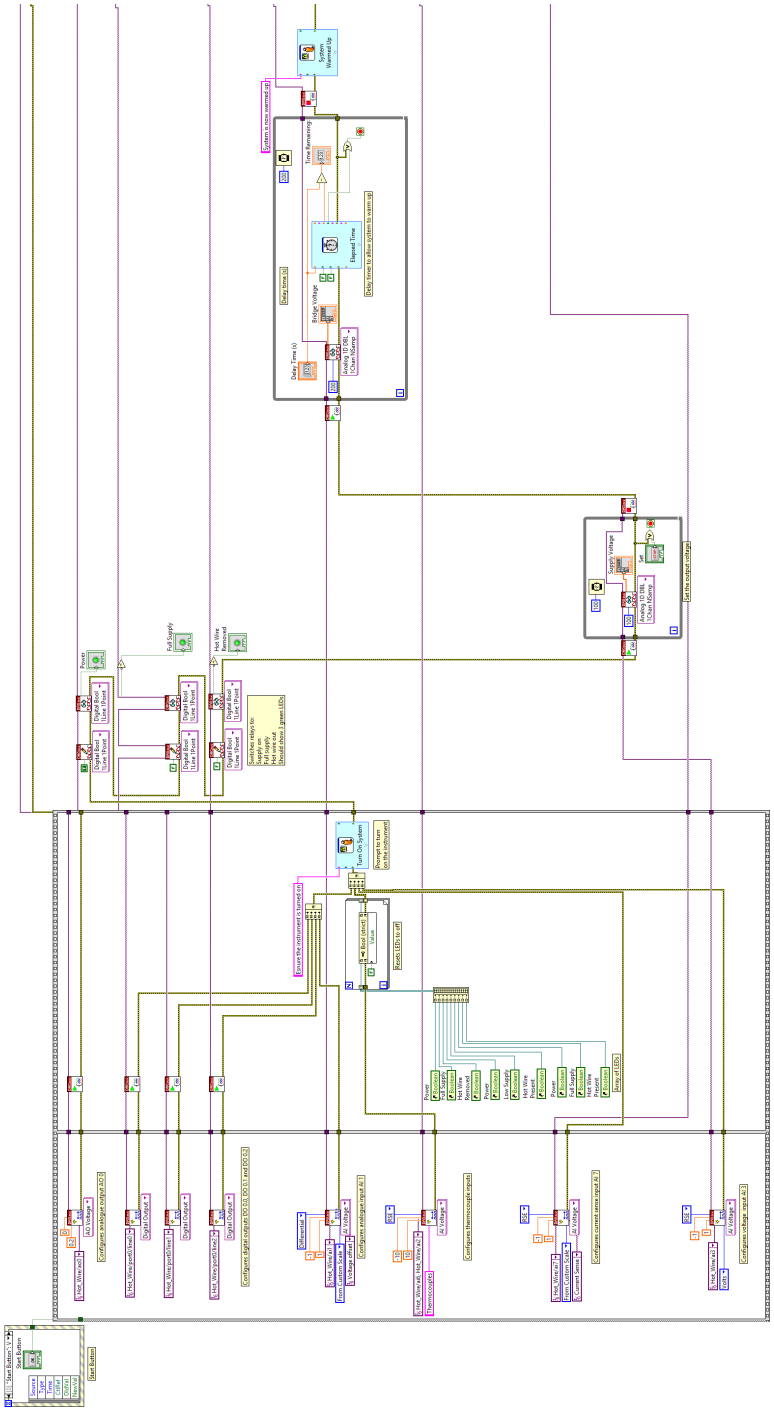

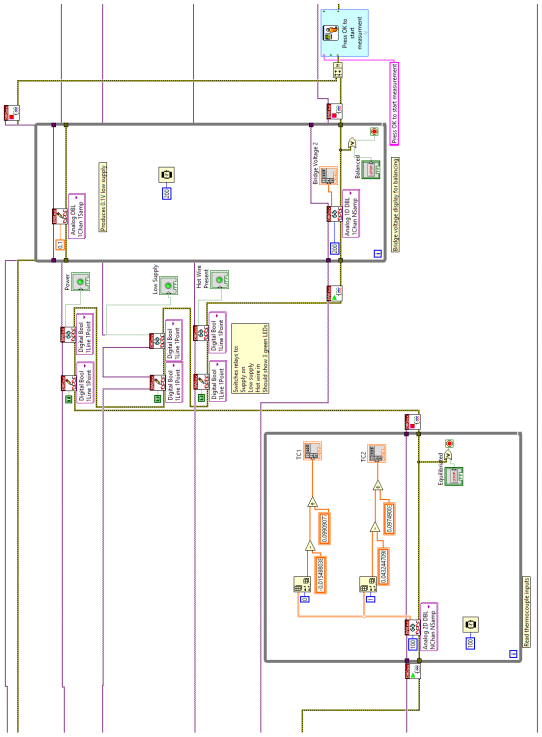

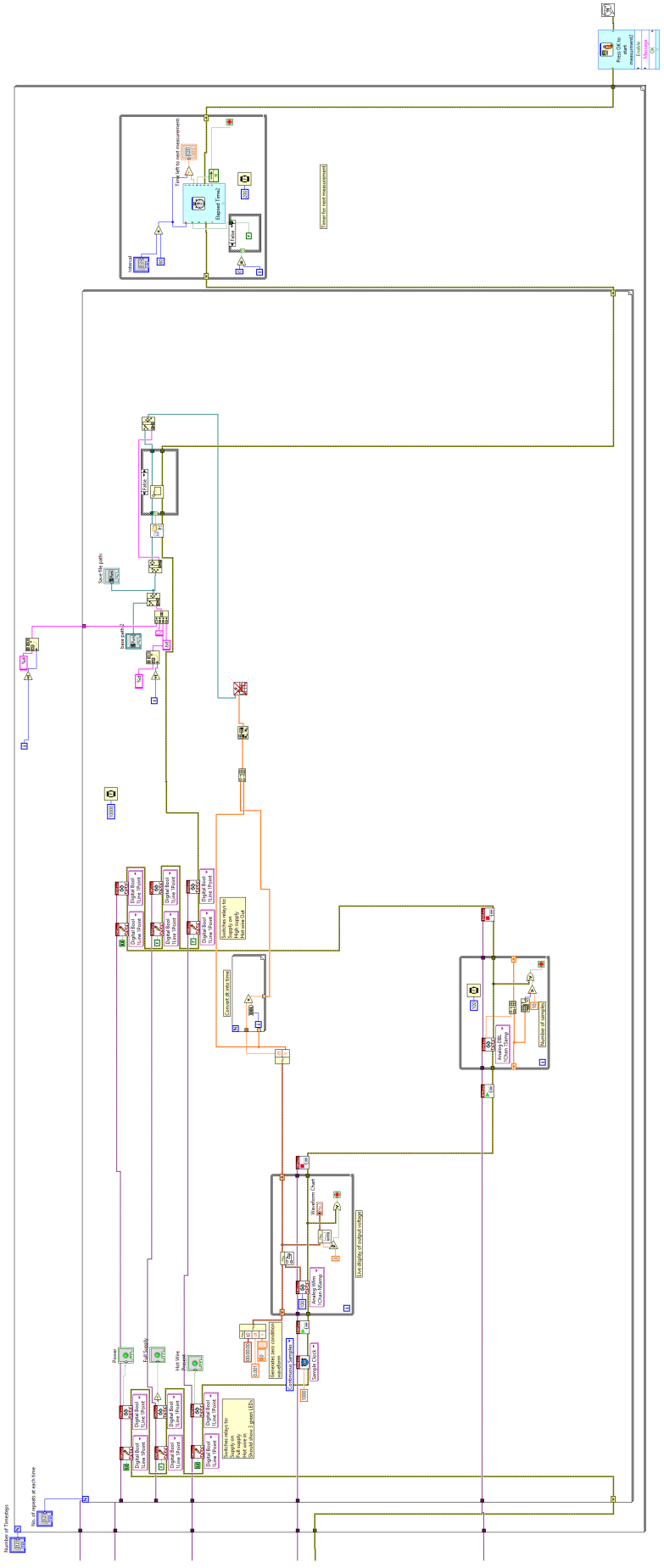

Appendix C

Python Code for Processing Hot Wire Data

```
# -*- coding: utf-8 -*-
import os
import numpy as np
import matplotlib.pyplot as plt
from scipy import stats
import csv
from datetime import datetime

def getFolderList(direc):
    Folder = []
    folderList = os.listdir(direc)
    for folderName in folderList:
        if not (folderName[-3:] == '.py'
        or folderName[-4:] == '.pyc'
        or folderName[-4:] == '.csv'
        or folderName[-4:] == '.pdf'
        or folderName[-4:] == '.txt'): # exclude unwanted files
            Folder.append(str(folderName))
    return Folder

if __name__ == '__main__':

    folder_list = getFolderList('./')

minfitlen = 100# minimum number of fit points
interval = 2# step interval

print folder_list

for folder in (folder_list):

    def getFileList(direc):
        dataFiles = []
        fileList = os.listdir(folder)
        for fileName in fileList:
            if (fileName[-4:] == '.txt'): # imports all .txt files
                if not (fileName[0] == 'R'): # except those starting with
    ↪ R
                    dataFiles.append(str(fileName))
        return dataFiles

    def getProcessedList(direc):
        Processed = []
        processedList = os.listdir(folder)
        for PFN in processedList:
```

```
45              if (PFN[-4:] == '.png'): # imports all .png files
46                  Processed.append(str(PFN))
47          return Processed
48
49      print 'Starting'+folder
50      file_list = getFileList('./')
51      processed_list = getProcessedList('./')
52
53      stripped_list = []
54      for done in processed_list:
55          stripped = done.strip( '.png' )
56          stripped_list.append(str(stripped))
57
58      processed_txt = [x + '.txt' for x in stripped_list]
59
60      new_files = list(set(file_list)-set(processed_txt))
61      print 'Unprocessed files are:'
62      print new_files
63
64      gradients = []
65      intercepts = []
66      equations = []
67      rsq_maxs = []
68      errors = []
69      best_starts = []
70      best_ends = []
71      lenfile_list = len(new_files)
72      time = []
73      lntime = np.log(time)
74      rlntime = np.reshape(lntime, len(lntime))
75      tlntime = np.transpose(rlntime)
76
77      final_list = [folder +'/'+ x for x in new_files]
78
79      for files in (final_list):
80          print'Starting' + files
81          rawdata=np.genfromtxt(files) # gets raw data
82
83          data=np.delete(rawdata,0,0) # removes t=0 data point
84
85          (time, voltage) = np.hsplit(data,2) # splits data into time and
    ↪ voltage arrays
86
87          lntime = np.log(time) # takes the log of the time array
88          R_file = folder + '/R.txt'
89          R_2=np.genfromtxt(R_file) # gets the value of R_2
```

```
90
91          R_1 = 2000.0 # fixed resistor values in ohms
92          R_3 = 10.0
93
94          R_w0 = ((R_3*(R_1+R_2))/R_2-R_3) # calculation of R_w at balance
95
96          V_s = 10.0 # supply voltage
97
98          R_w = R_3 *(((V_s*(R_1 + R_2))/((R_2 * V_s)-(voltage*(R_1 + R_2))
    ↪ ))-1) # calculation of R_w from voltage
99
100         delta_R = R_w - R_w0 # calculate delta_R
101
102         rdelta_R = np.reshape(delta_R, len(delta_R))# reshape arrays to
    ↪ be 1D
103         rlntime = np.reshape(lntime, len(lntime))# reshape arrays to be 1
    ↪ D
104
105         tdelta_R = np.transpose(rdelta_R)# transpose arrays
106         tlntime = np.transpose(rlntime)# transpose arrays
107
108         lfl=int(lenfile_list)
109         num=int(1+(final_list.index(files)))
110
111         rsq = 0
112         rsq_max = 0
113         start = 0
114         end = 0
115
116         for start in range(0,len(tlntime)-minfitlen,interval):
117             for end in range(start+minfitlen, len(tlntime),interval):
118
119                 slope, intercept, r_value, p_value, std_err = stats.
    ↪ linregress(tlntime[start:end],tdelta_R[start:end])
120
121                 rsq = 0
122                 rsq += r_value**2
123
124                 if rsq > rsq_max:
125                     best_start = start
126                     best_end = end
127                     rsq_max = rsq
128                     best_error = std_err
129                     best_grad = slope
130                     best_intercept = intercept
131                     equation = 'y=' + str(slope) + 'x+' + str(intercept)
```

```
132
133         gradients.append((best_grad))
134         intercepts.append((best_intercept))
135         equations.append((equation))
136         rsq_maxs.append((rsq_max))
137         errors.append((best_error))
138         best_starts.append((best_start))
139         best_ends.append((best_end))
140
141         fit = tlntime[best_start:best_end]*best_grad+best_intercept
142         reducedtlntime = tlntime[best_start:best_end]
143
144         print files
145         print "R squared"
146         print rsq_max
147         print "Gradient:"
148         print best_grad
149         print "Intercept"
150         print best_intercept
151
152         print 'Line of best fit'
153         print equation
154
155         print "From:"
156         print best_start
157         print tlntime[best_start]
158         print "to:"
159         print best_end
160         print tlntime[best_end]
161
162         plt.figure(1)
163         plt.plot(tlntime, tdelta_R, "x")
164         plt.plot(reducedtlntime, fit, "-r")
165         plt.savefig(files[:-4]+'.png')
166         plt.clf()
167
168     else:
169         print 'no files found'
170
171     best_start_times = tlntime[best_starts]
172     best_end_times = tlntime[best_ends]
173     best_start_times=best_start_times.tolist()
174     best_end_times=best_end_times.tolist()
175
176     filelabel=['File Name']
177     file_list=filelabel+new_files
```

```
    gradlabel=['Gradient']
    gradients=gradlabel+gradients
    interceptlabel = ['Intercept']
    intercepts = interceptlabel+intercepts
    equationlabel = ['Equation']
    equations = equationlabel+equations
    rsq_maxlabel=['R Squared']
    rsq_maxs=rsq_maxlabel+rsq_maxs
    errorslabel=['Error']
    errors=errorslabel+errors
    beststartlabel=['Start Point']
    best_starts=beststartlabel+best_starts
    starttimelabel=['Start Time']
    best_start_times=starttimelabel+best_start_times
    bestendlabel=['End Point']
    best_ends=bestendlabel+best_ends
    endtimelabel=['End Time']
    best_end_times=endtimelabel+best_end_times

    filename = datetime.now().strftime("%Y%m%d-%H%M%S")
    Results_file = folder + '/' + filename + ' Results.csv'
    csvHandle = open(Results_file, 'wb')
    writer = csv.writer(csvHandle)
    writer.writerow(file_list)
    writer.writerow(gradients)
    writer.writerow(equations)
    writer.writerow(intercepts)
    writer.writerow(rsq_maxs)
    writer.writerow(errors)
    writer.writerow(best_starts)
    writer.writerow(best_start_times)
    writer.writerow(best_ends)
    writer.writerow(best_end_times)
    csvHandle.close()
    print 'printing' + filename

    print 'Finished'+folder
print "done"
```

Appendix D

Characterisation of GO & rGO

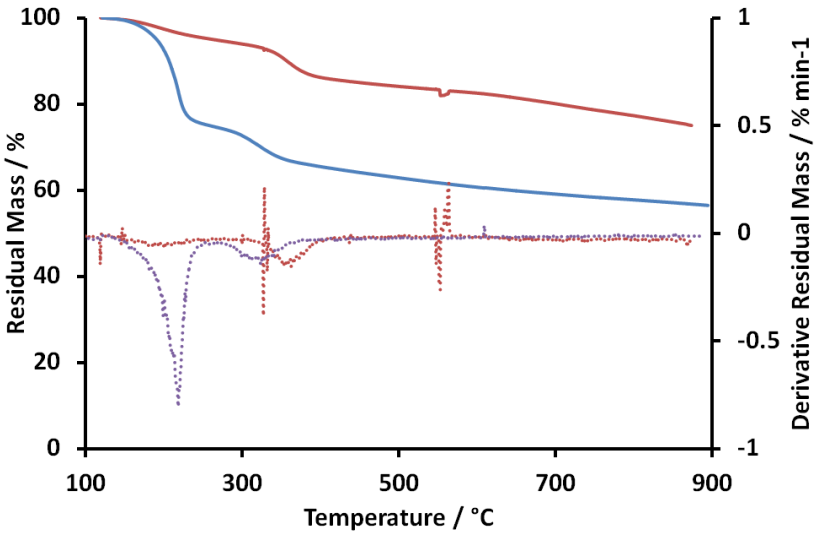

TGA in nitrogen of GO (blue) and hydrazine rGO (red) along with the dreivatives of these plots (dotted lines).

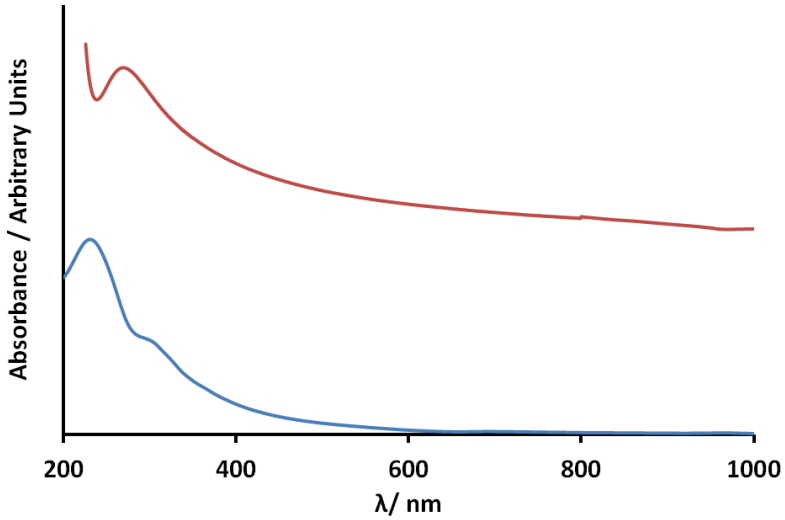

UV-Vis spectra of GO (blue) and rGO (red) in water, showing the position of the $\pi \rightarrow \pi^*$ plasmon peak.

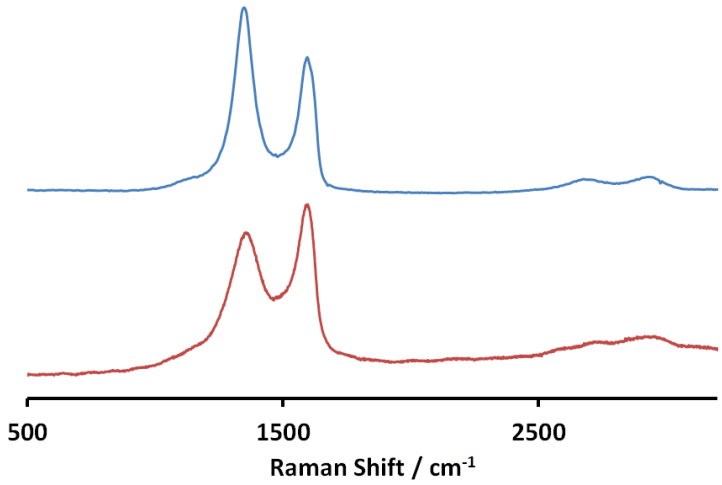

Raman spectra of GO (blue) and rGO (red)

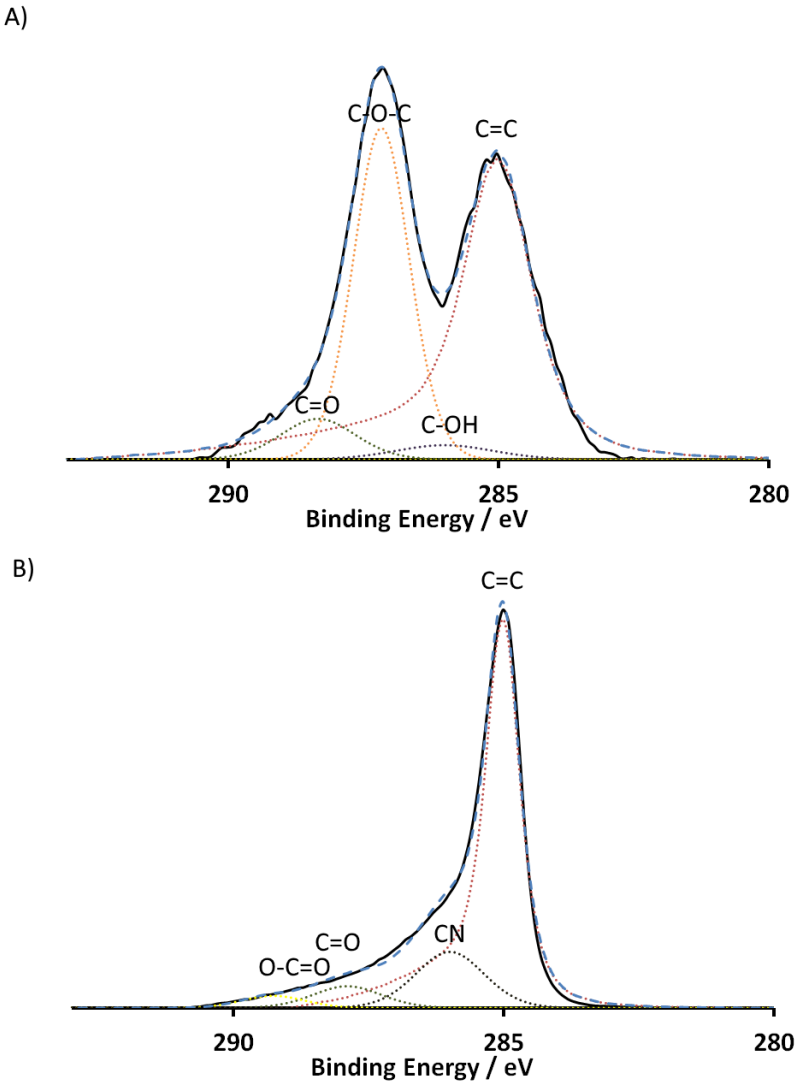

XPS of the C1s peak for A) GO and B) rGO showing the C1s spectrum (black line), the fit envelope (blue dashed line) and the fitted peaks (dotted lines).

ASAP-MS of 0.1 % 0.3 % NMP

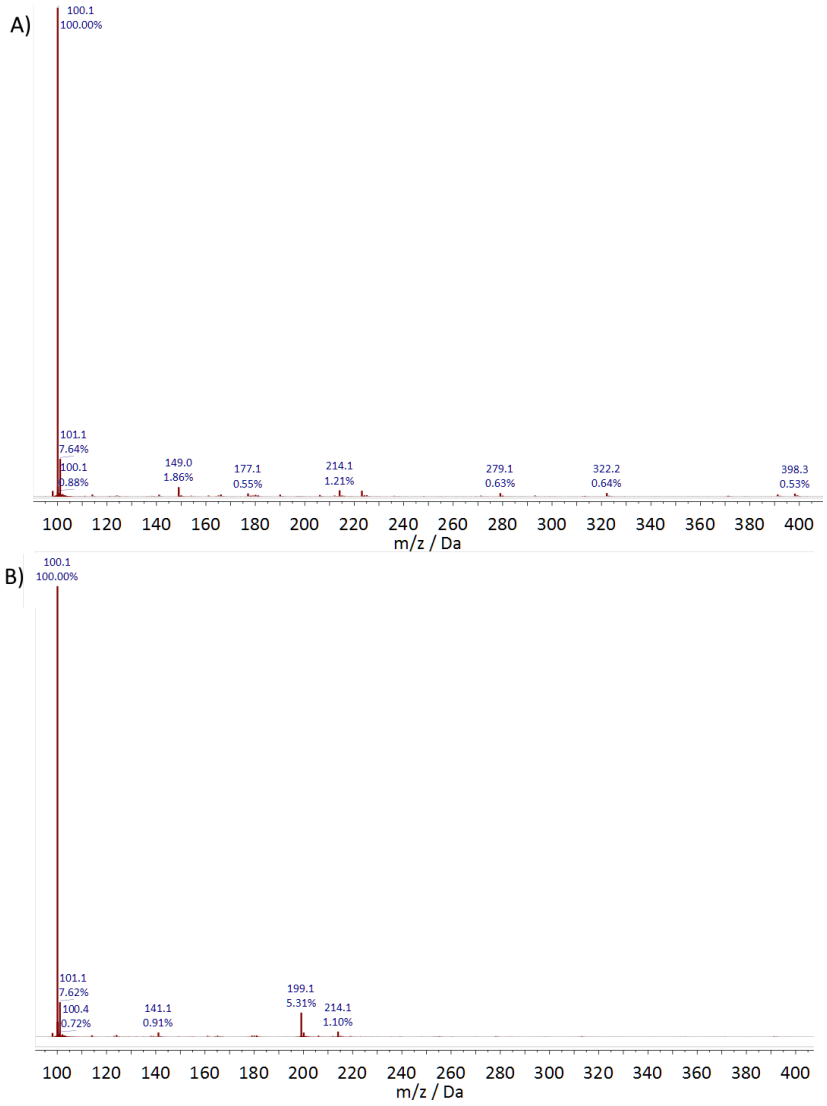

ASAP mass spectra of aqueous NMP at A) 0.1 vol. %, and B) 0.3 vol. %.

HPLC Calibration Curves

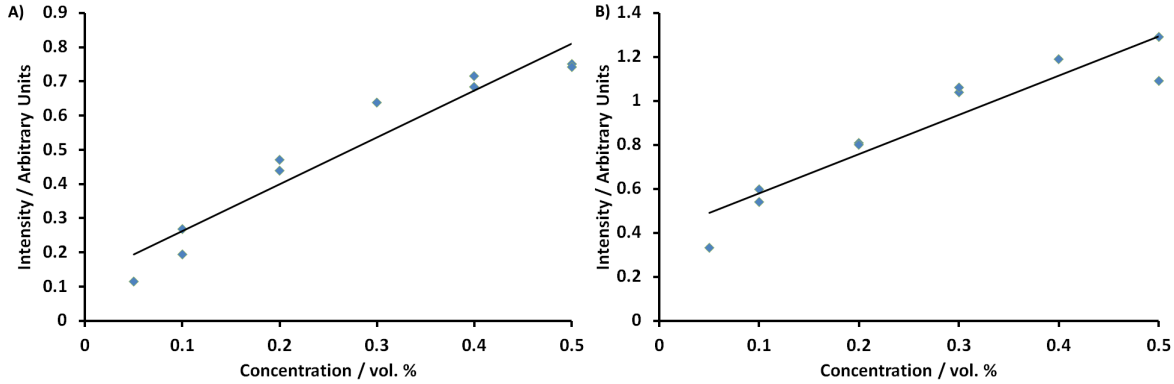

Calibration curves to allow the concentration of aqueous solutions of NMP and DMF to be determined using HPLC. A) NMP, with the equation of the trend line being $y = 1.37 \times 10^6 x + 1.25 \times 10^5$*, and B) DMF, with the equation of the trend line being* $y = 1.79 \times 10^6 x + 4.02 \times 10^5$.

UV-Vis of Control Aqueous Dispersions of rGO

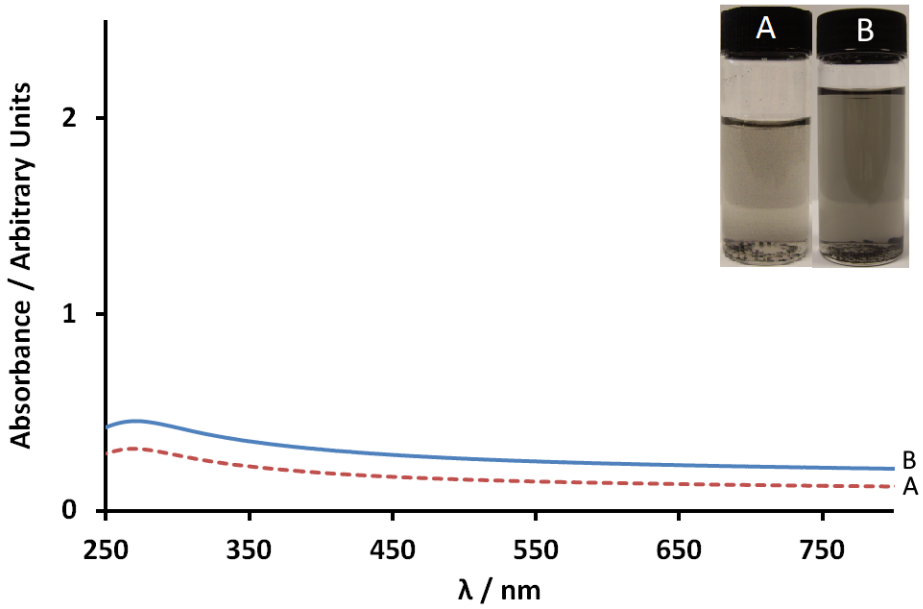

UV-Vis spectra and photographs (inset) of dispersions of A) rGO in water and B) rGO that has been dispersed in water, filtered, washed with MeCN and redispersed in water by sonication

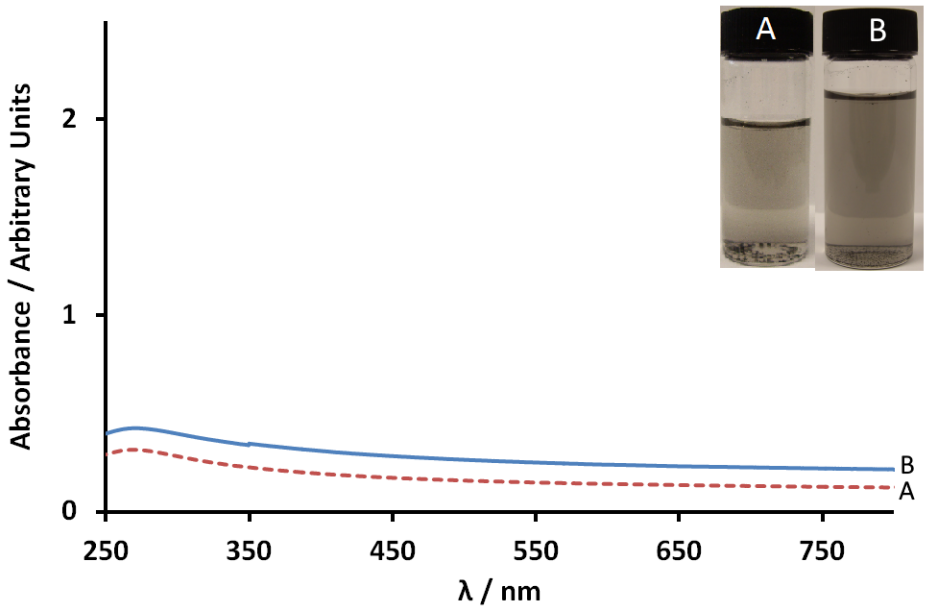

UV-Vis spectra and photographs (inset) of dispersions of rGO in water produced using A) 20 minutes of sonication and B) 40 minutes of sonication

Characterisation of DMFrGO

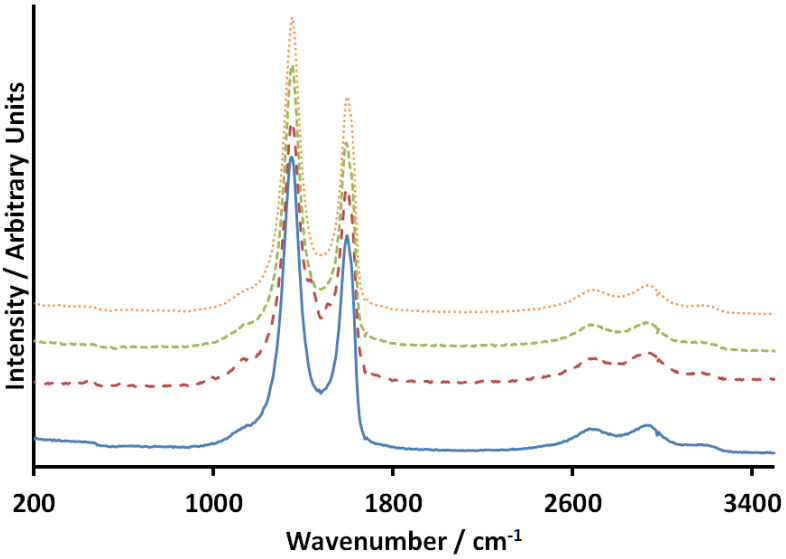

Raman spectra of rGO (blue line), rGO that has been dispersed in water (red dashed line), NMPrGO (green dashed line), and DMFrGO (orange dotted line) (intensities normalised to the height of the G band and offset by 0.2 for clarity).

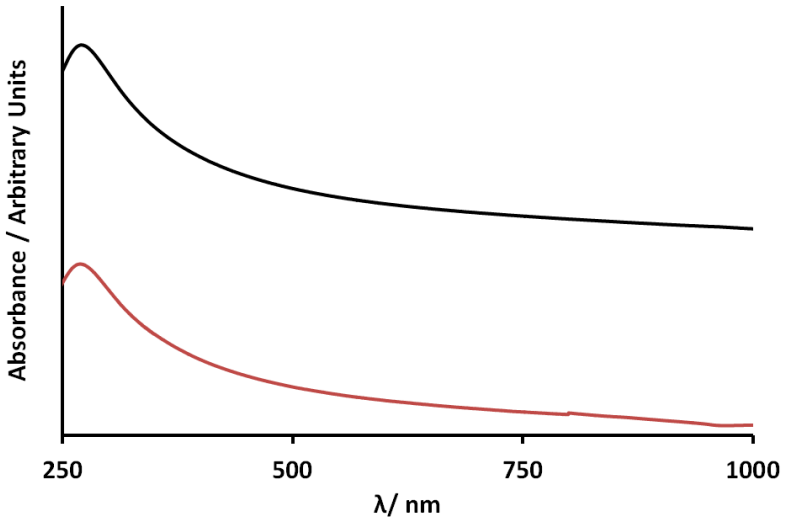

UV-Vis spectra of rGO (red) and DMFrGO (black) dispersed in water showing the position of the $\pi \rightarrow \pi^*$ *plasmon peak.*

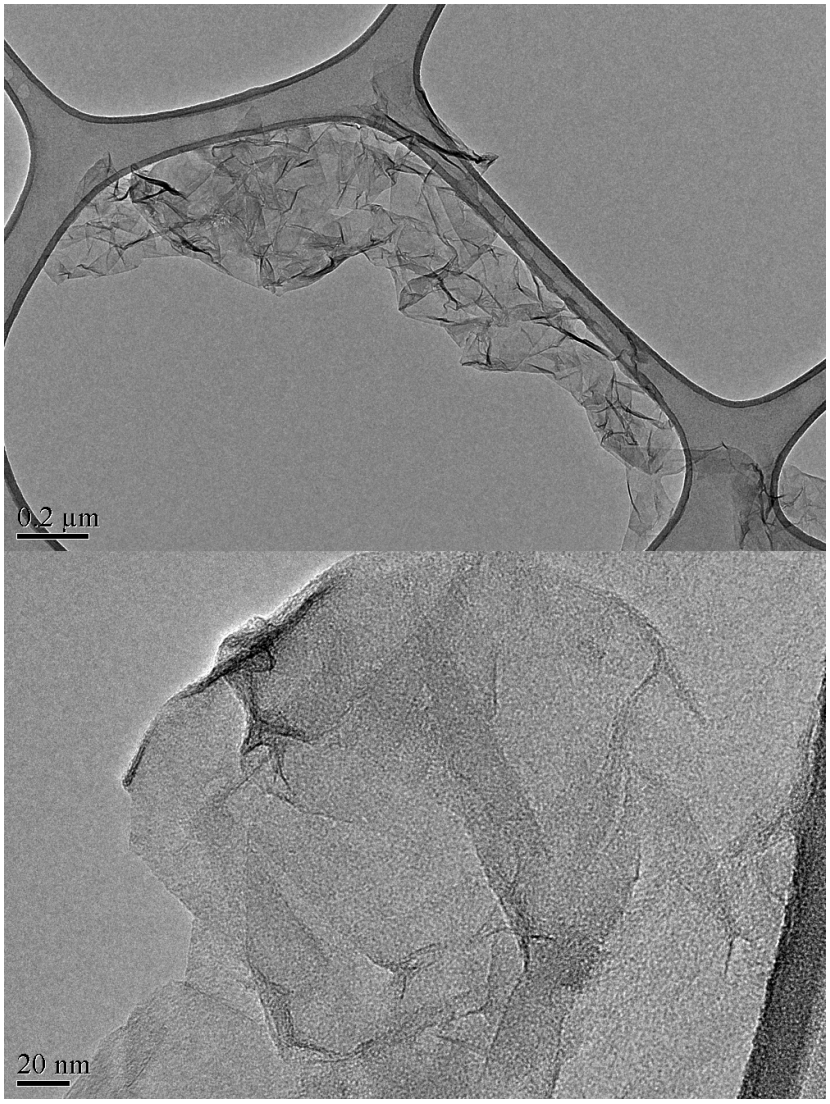

TEM of DMFrGO isolated from water, showing the sheets to have similar dimensions and folding to rGO.

Solution State NMR of NMP Before and After Sonication

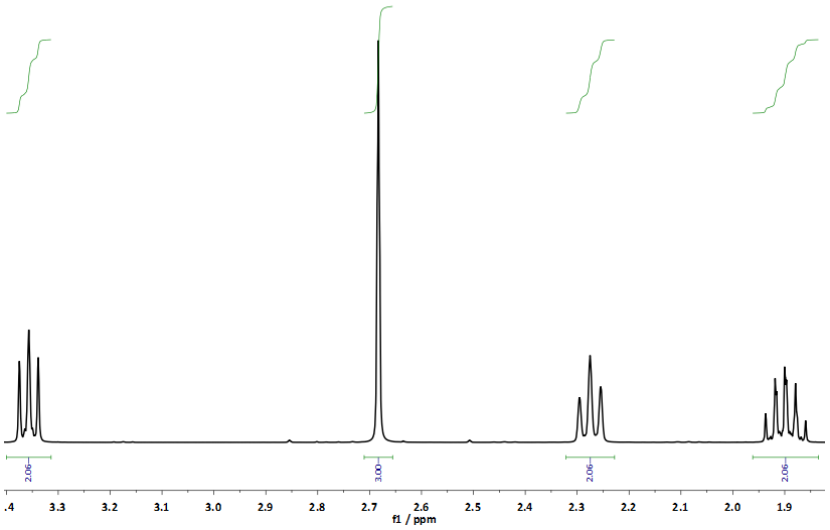

^{1}H Solution state NMR in D_2O of untreated NMP.

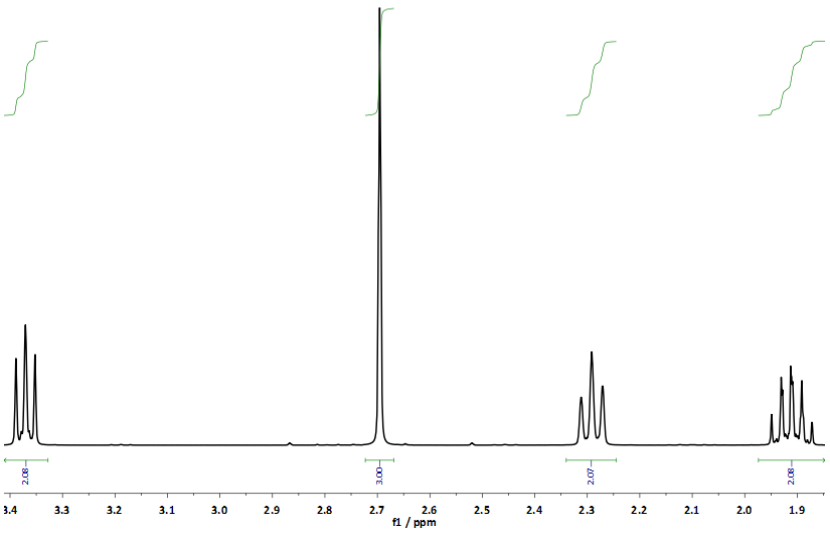

^{1}H Solution state NMR in D_2O of NMP sonicated using the procedure described in section 8.3.21.

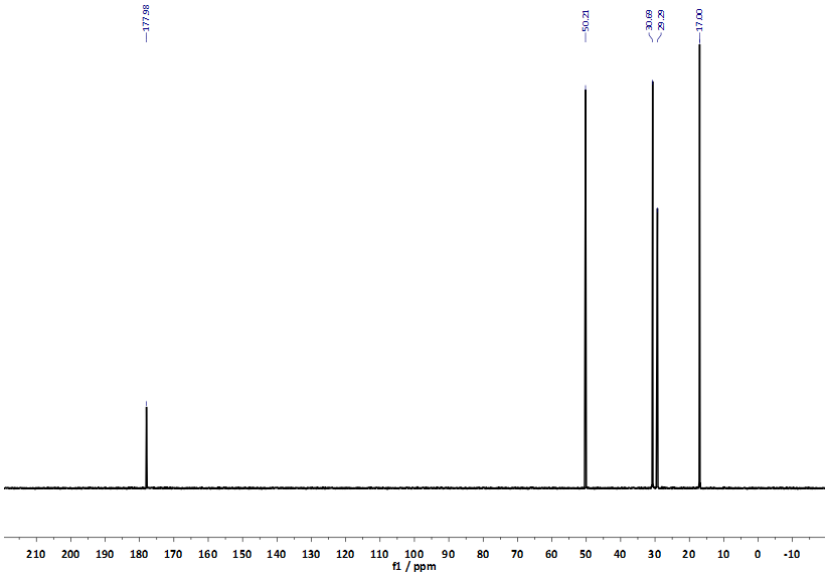

^{13}C Solution state NMR in D_2O of untreated NMP.

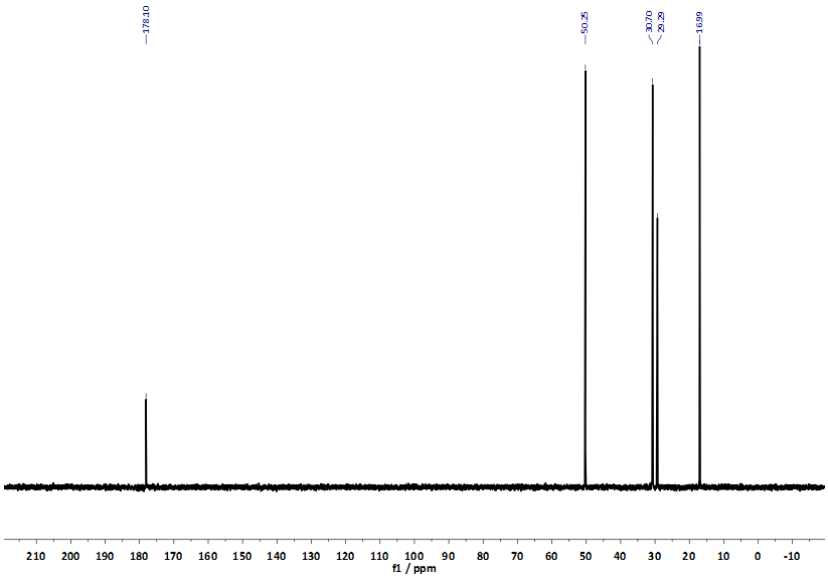

^{13}C Solution state NMR in D_2O of NMP sonicated using the procedure described in section 8.3.21.

XPS of functionalised rGOs

Survey Scans

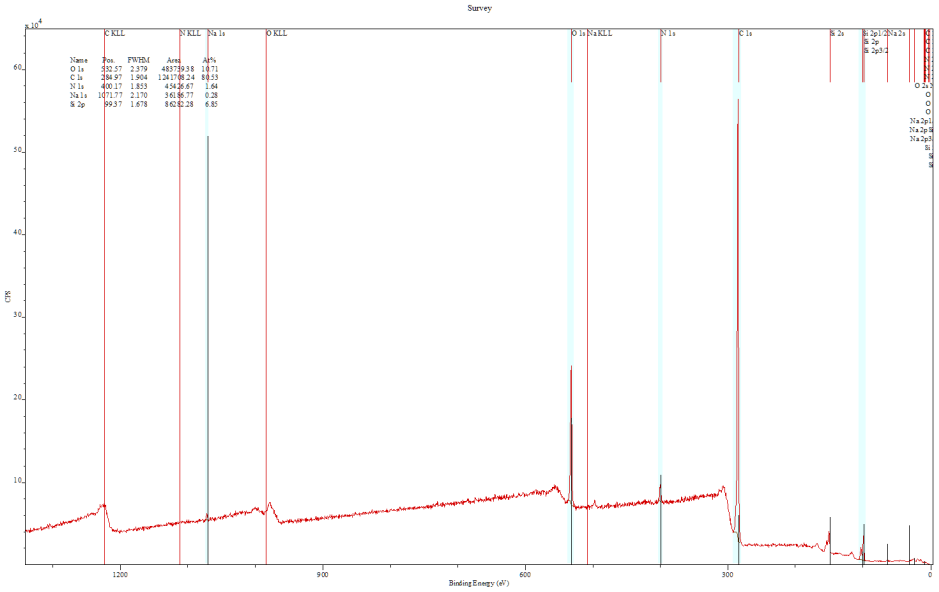

Survey scan of ODArGO produced by the method of Jang et al..[380] Overlay shows the relative abundance of each element, however some oxygen content will arise due to the oxide layer on the silicon substate used to deposit the samples wich is also the reason for the detection of silicon. Sodium is most likely to be present as a result of contamination

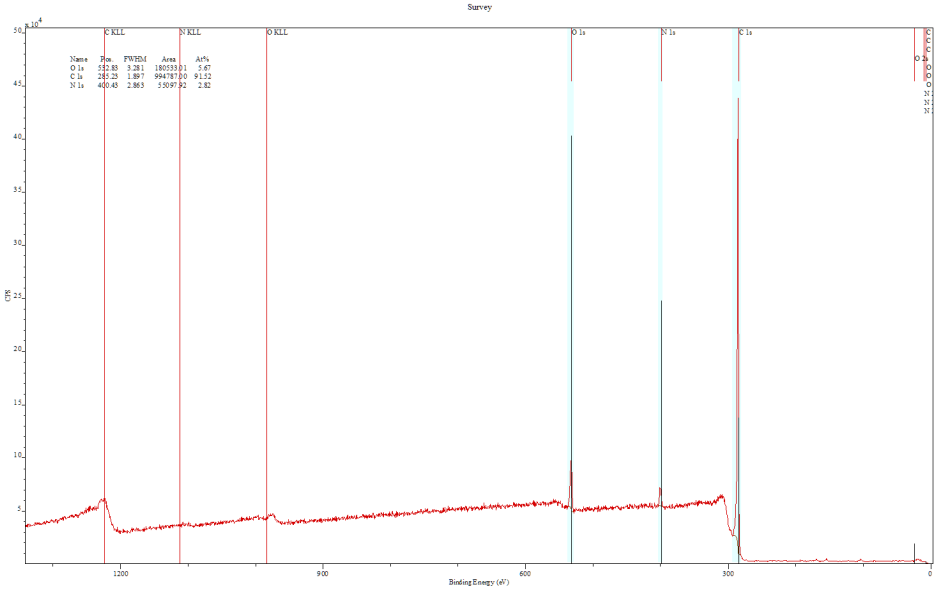

Survey scan of ODArGO produced in situ reduction and functionalisation. Overlay shows the relative abundance of each element, however some oxygen content may arise due to the oxide layer on the silicon substate used to deposit the samples.

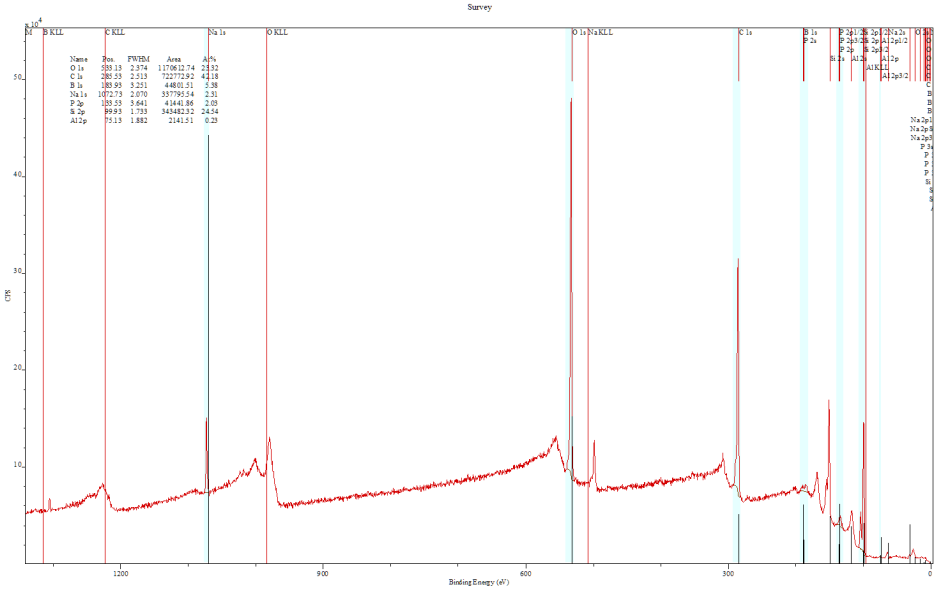

Survey scan of TOPrGO produced in situ reduction and functionalisation. Overlay shows the relative abundance of each element, however some oxygen content will arise due to the oxide layer on the silicon substate used to deposit the samples wich is also the reason for the detection of silicon. Aluminium and boron are detected as a result of sampe processing. Sodium is most likely to be present as a result of contamination.

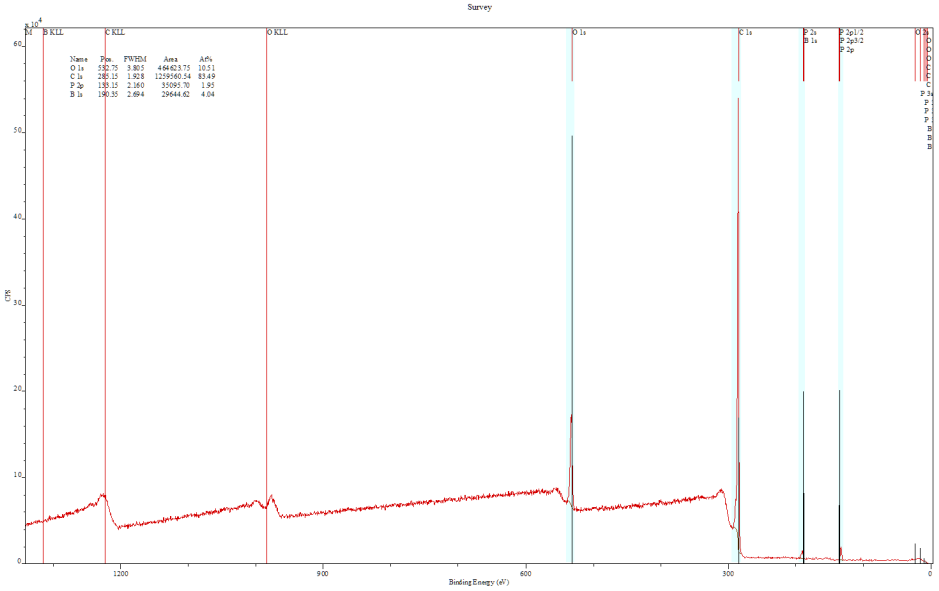

Survey scan of TOPOrGO produced in situ reduction and functionalisation. Overlay shows the relative abundance of each element, however some oxygen content will arise due to the oxide layer on the silicon substate used to deposit the samples. Boron is detected as a result of sampe processing.

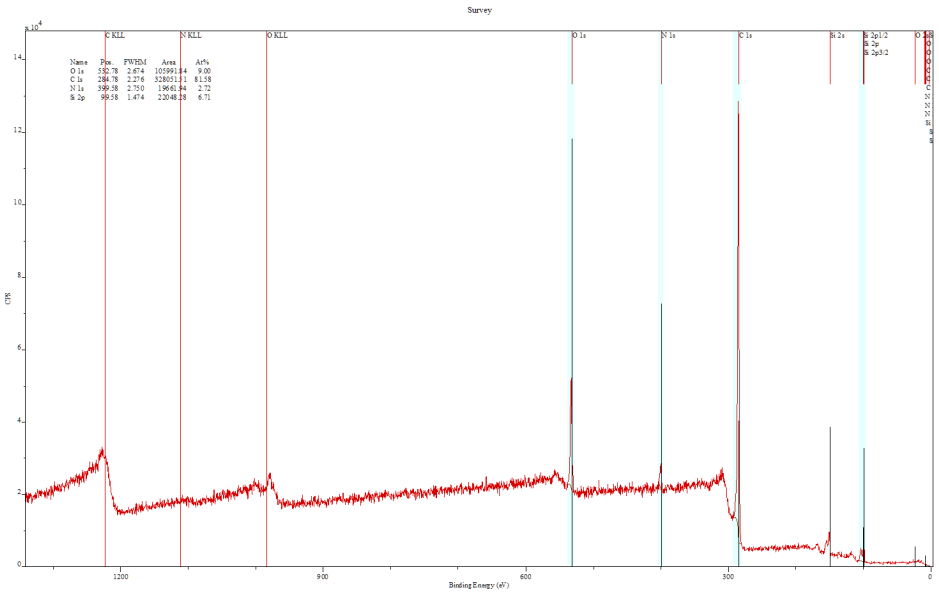

Survey scan of OLrGO produced in situ reduction and functionalisation. Overlay shows the relative abundance of each element, however some oxygen content will arise due to the oxide layer on the silicon substate used to deposit the samples wich is also the reason for the detection of silicon.

N1s Peak

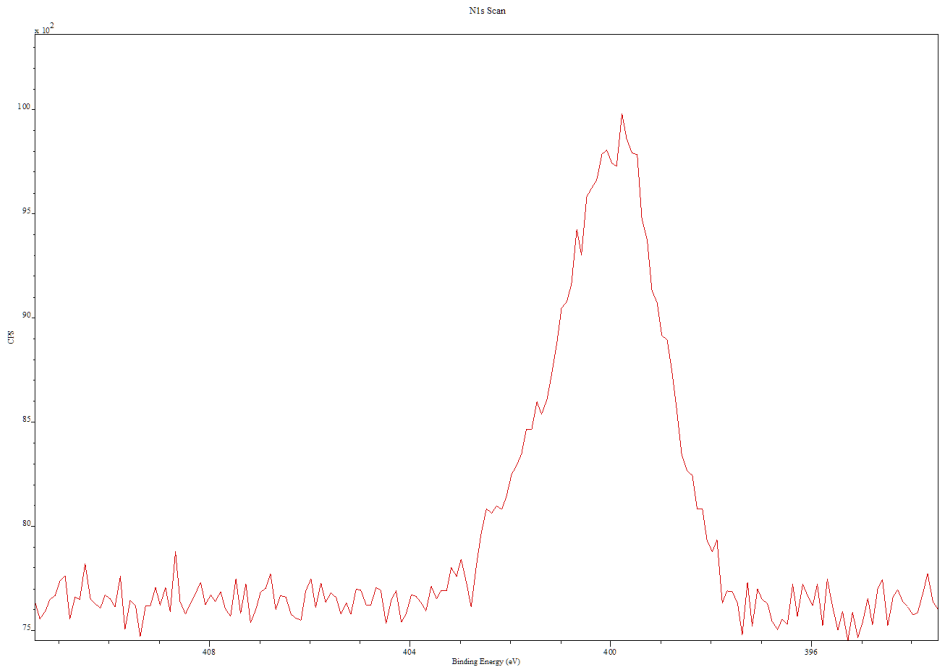

The N1s XPS peak of ODArGO produced by the method of Jang et al..[380]

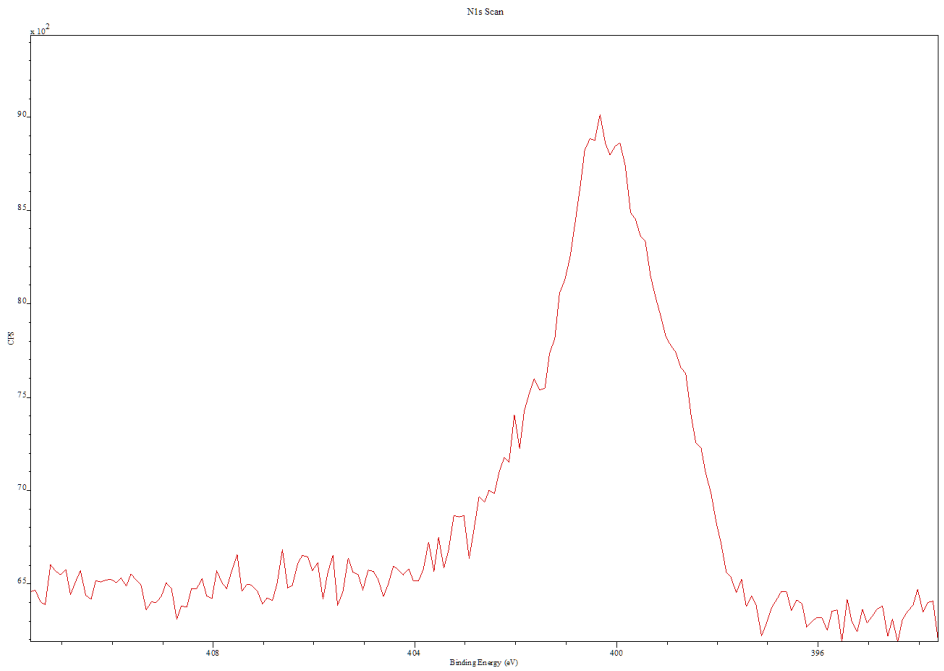

The N1s XPS peak of ODArGO produced via in situ reduction and functionalisation.

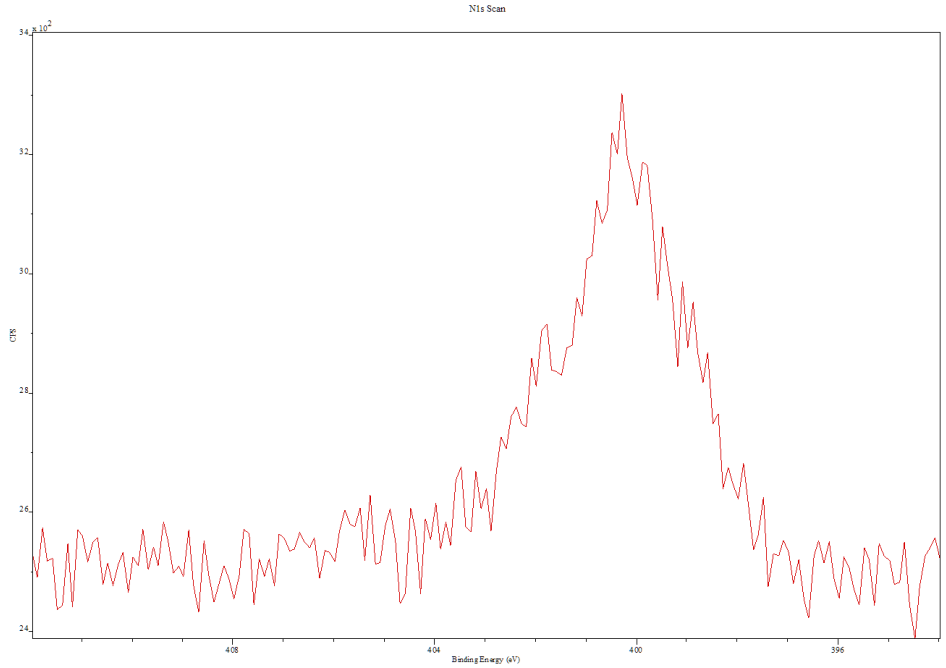

The N1s XPS peak of OLrGO produced via in situ reduction and functionalisation.

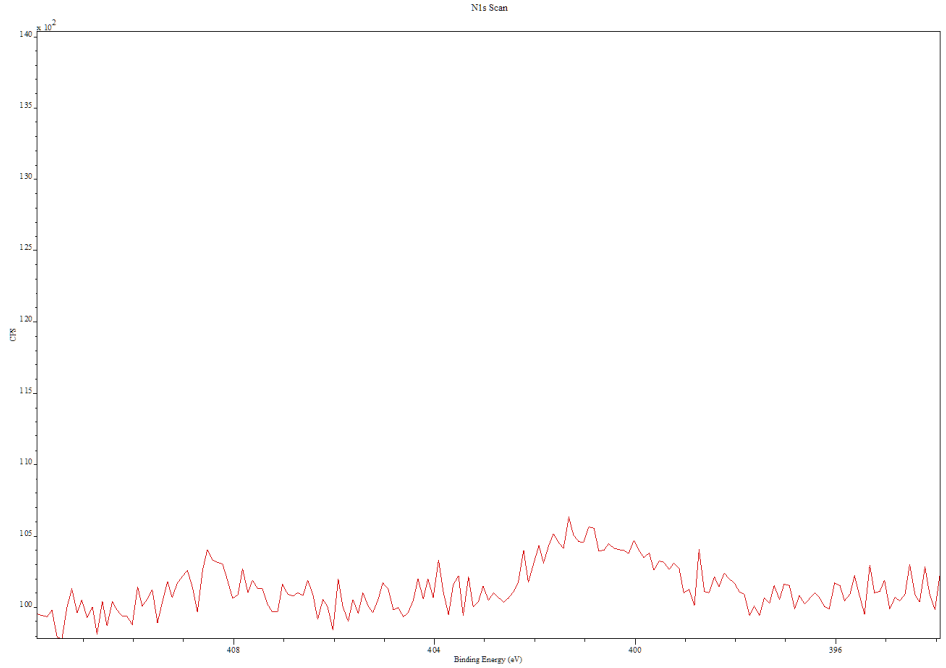

The N1s XPS peak of TOPrGO produced via in situ reduction and functionalisation.

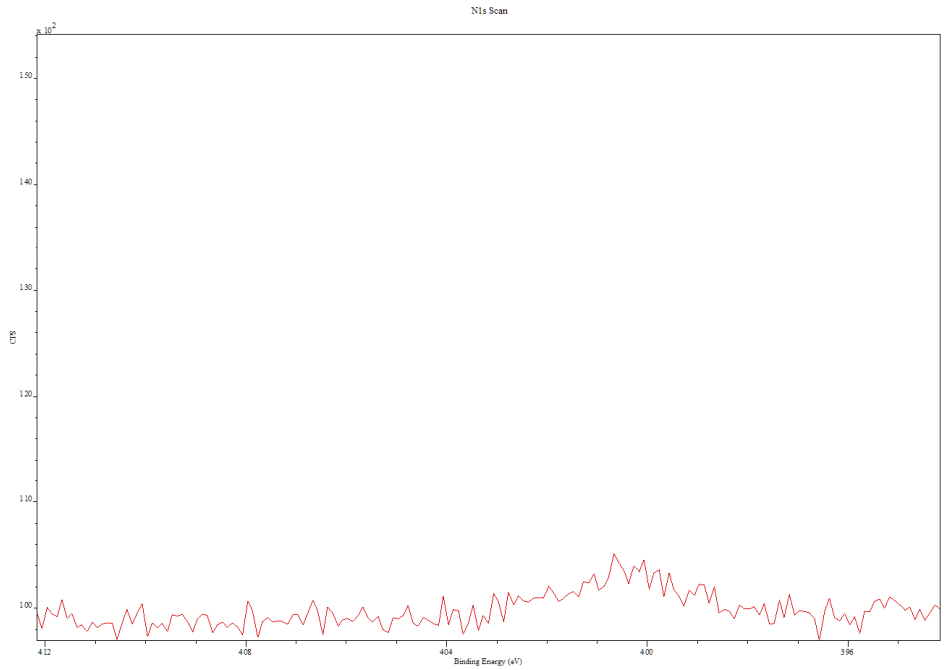

The N1s XPS peak of TOPOrGO produced via in situ reduction and functionalisation.

P2p Peak

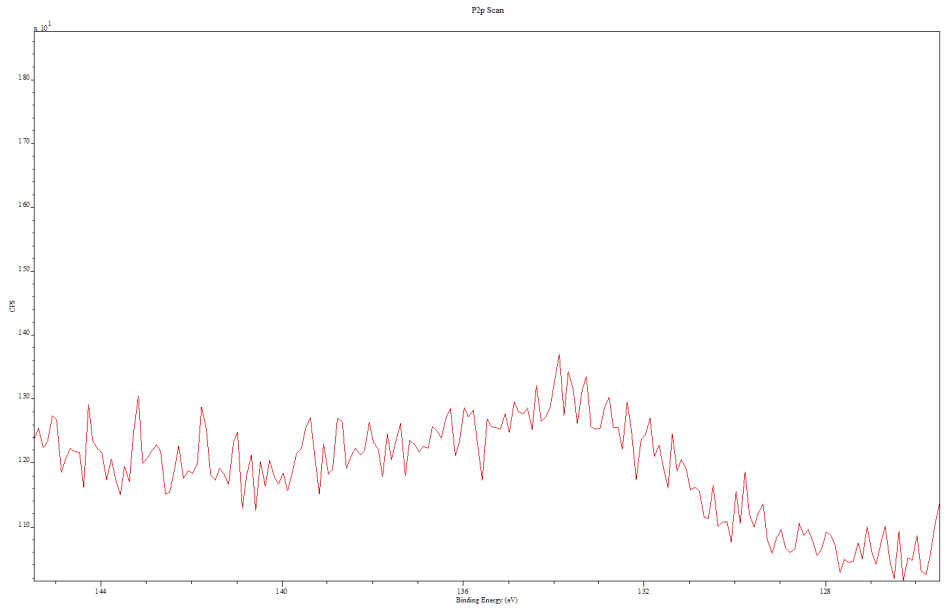

The P2p XPS peak of ODArGO produced by the method of Jang et al..[380]

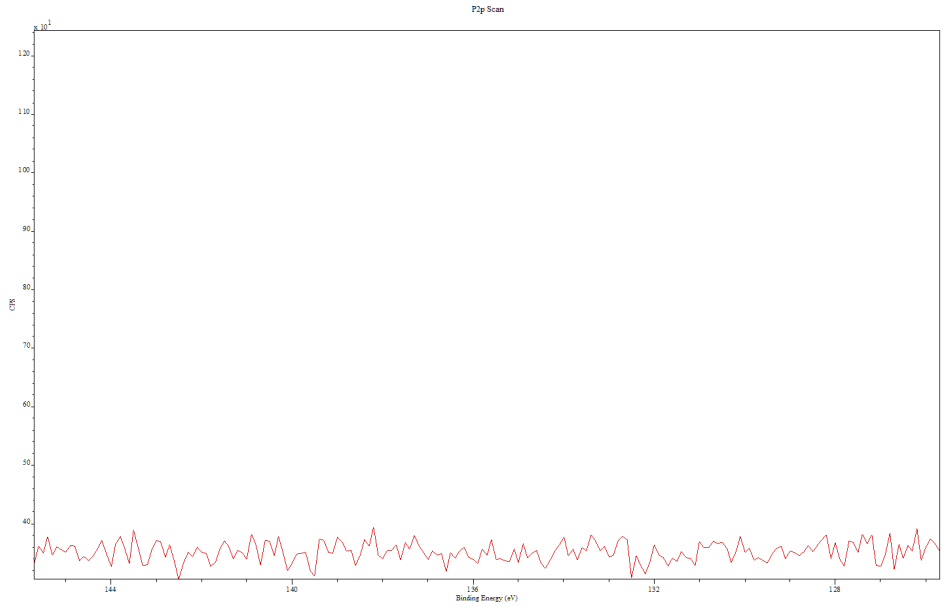

The P2p XPS peak of ODArGO produced via in situ reduction and functionalisation.

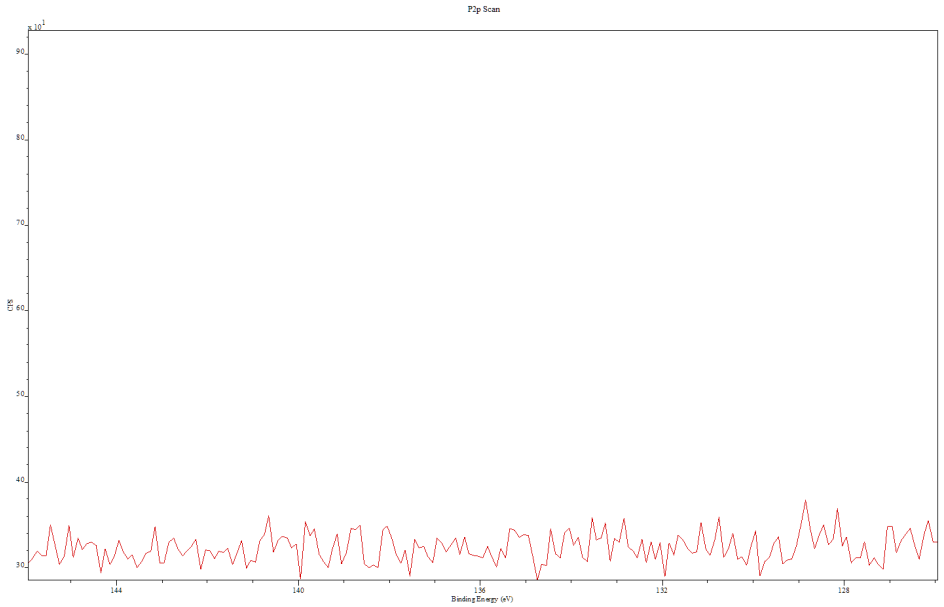

The P2p XPS peak of OLrGO produced via in situ reduction and functionalisation.

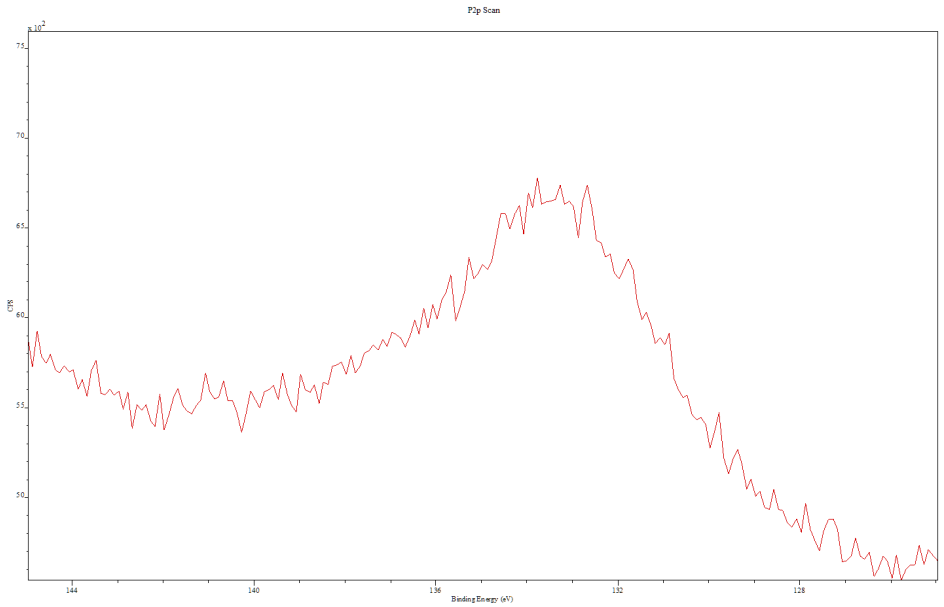

The P2p XPS peak of TOPrGO produced via in situ reduction and functionalisation.

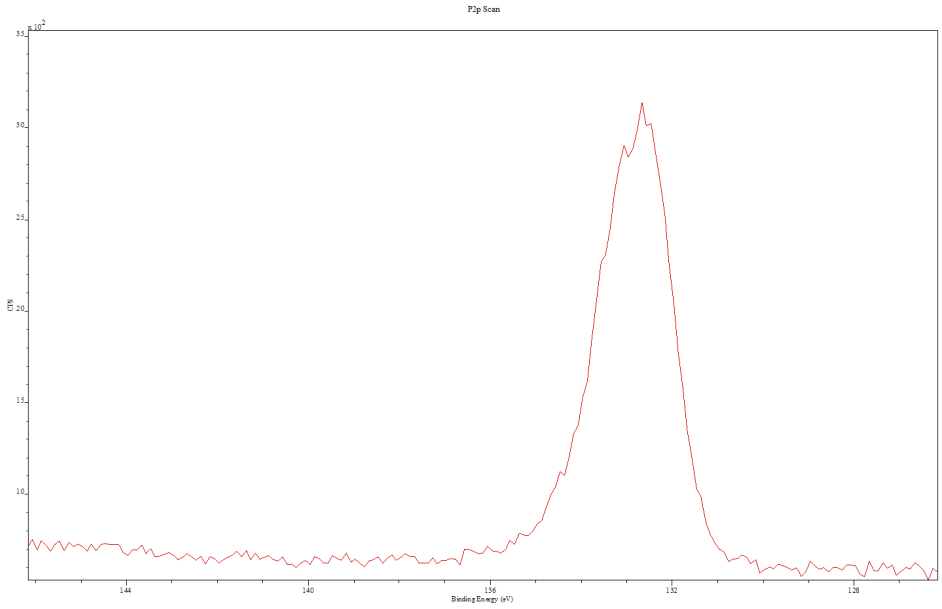

The P2p XPS peak of TOPOrGO produced via in situ reduction and functionalisation.

Solution State NMR Analysis of TOPrGO and TOPOrGO

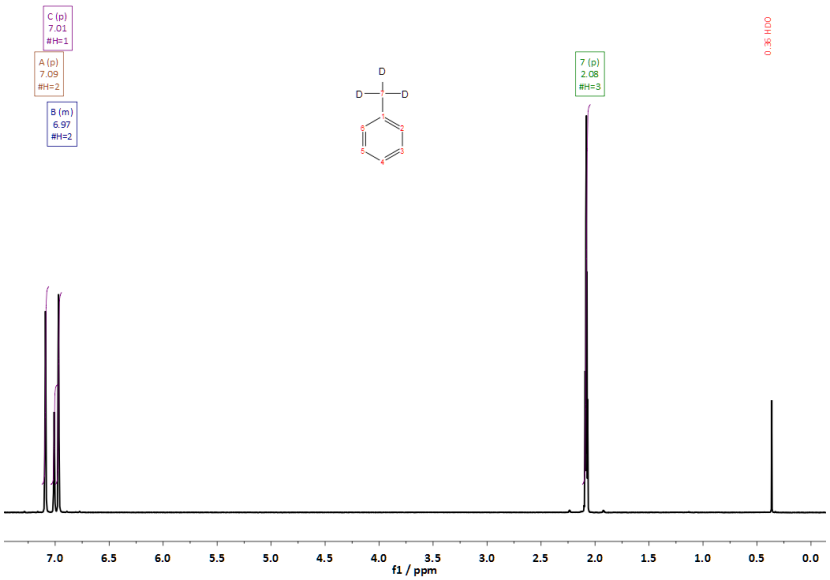

Solution state ^{1}H NMR of the pure d_8 toluene used as a solvent for solution state NMR.

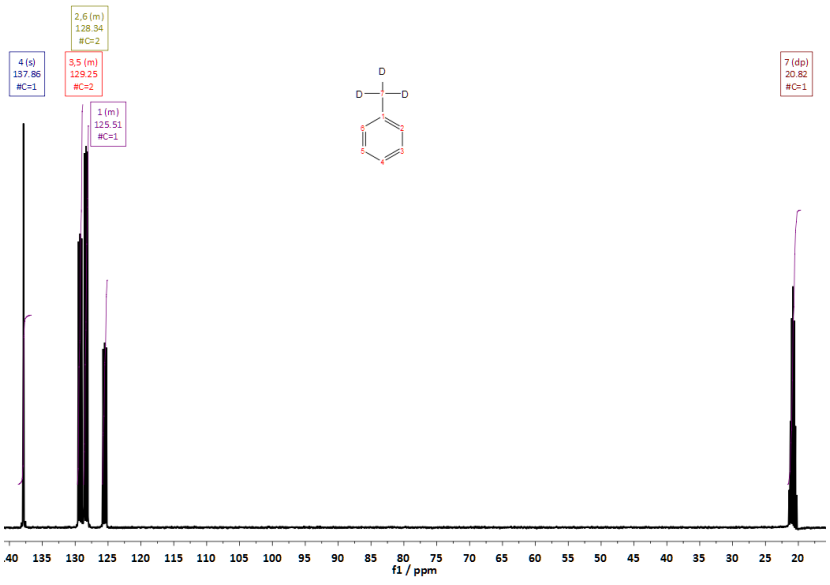

Solution state ^{13}C NMR of the pure d_8 toluene used as a solvent for solution state NMR.

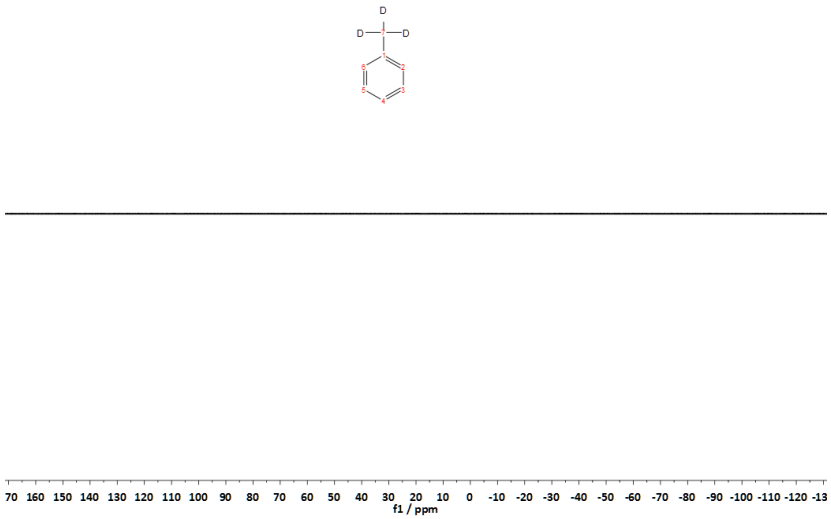

Solution state ^{31}P NMR of the pure d_8 toluene used as a solvent for solution state NMR.

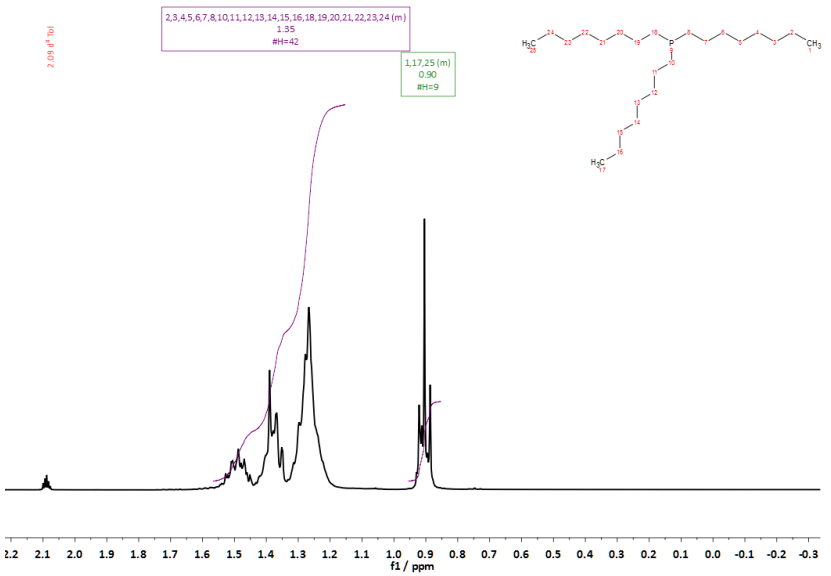

Solution state ^{1}H NMR of TOP as received from Sigma Aldrich.

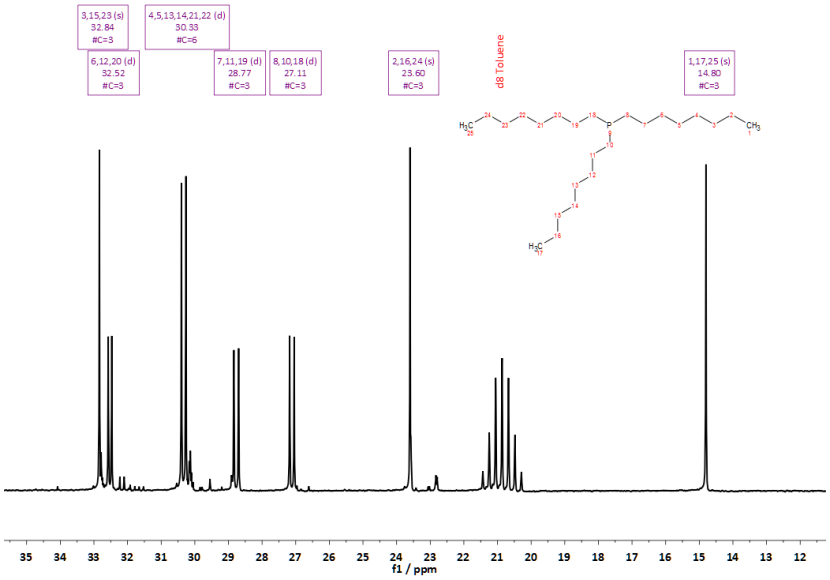

Solution state ^{13}C NMR of TOP as received from Sigma Aldrich.

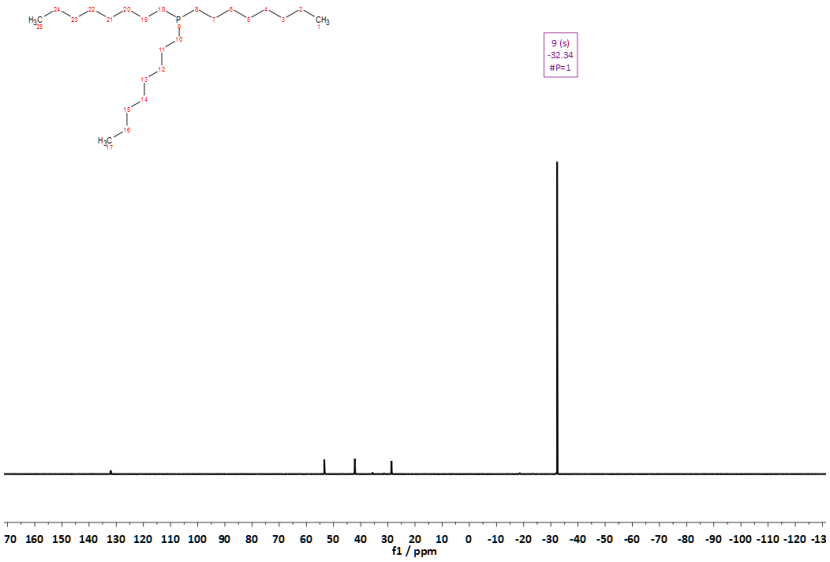

Solution state ^{31}P NMR of TOP as received from Sigma Aldrich.

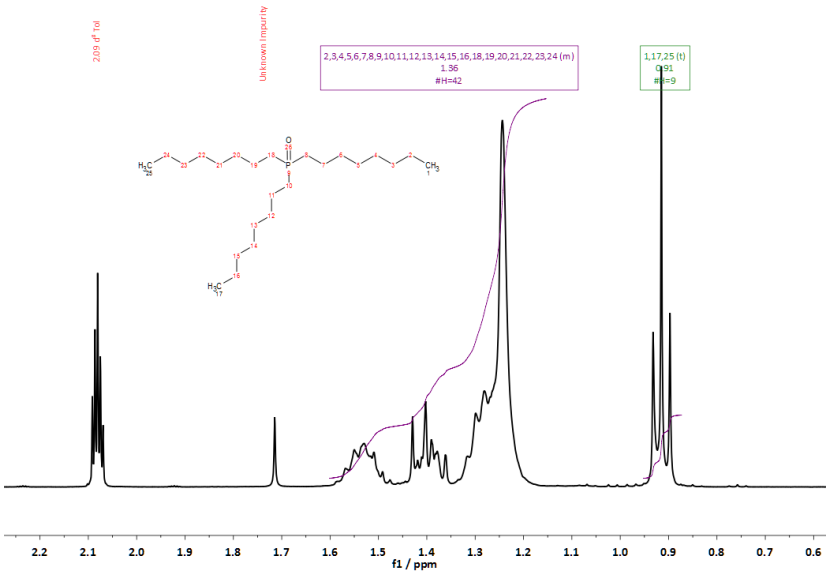

Solution state ^{1}H NMR of TOPO as received from Sigma Aldrich.

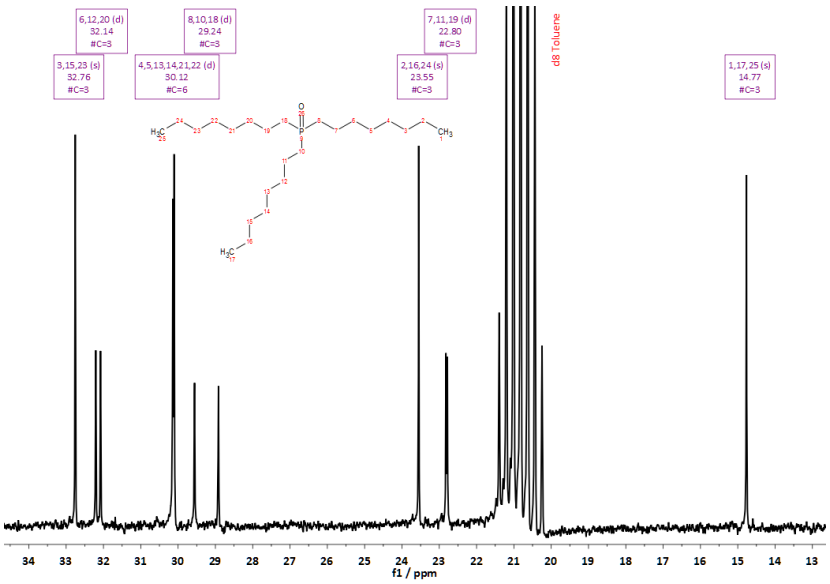

Solution state ^{13}C NMR of TOPO as received from Sigma Aldrich.

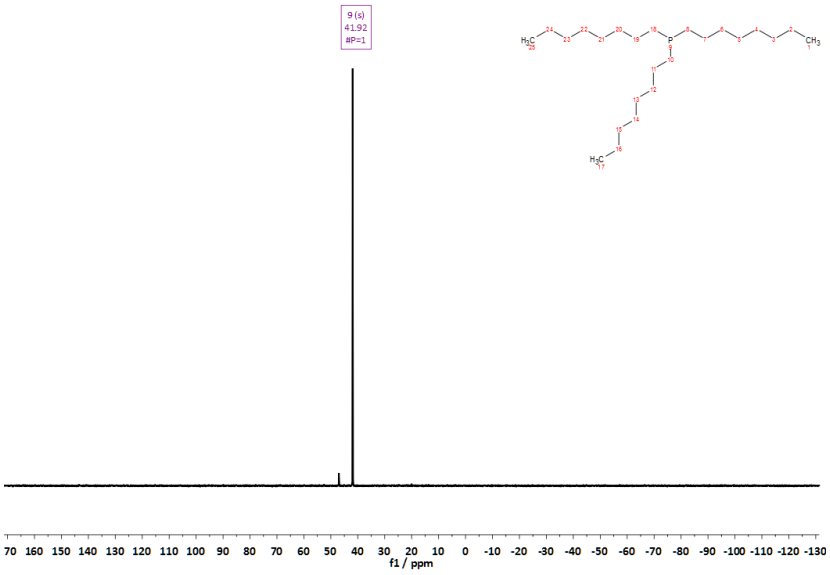

Solution state ^{31}P NMR of TOPO as received from Sigma Aldrich.

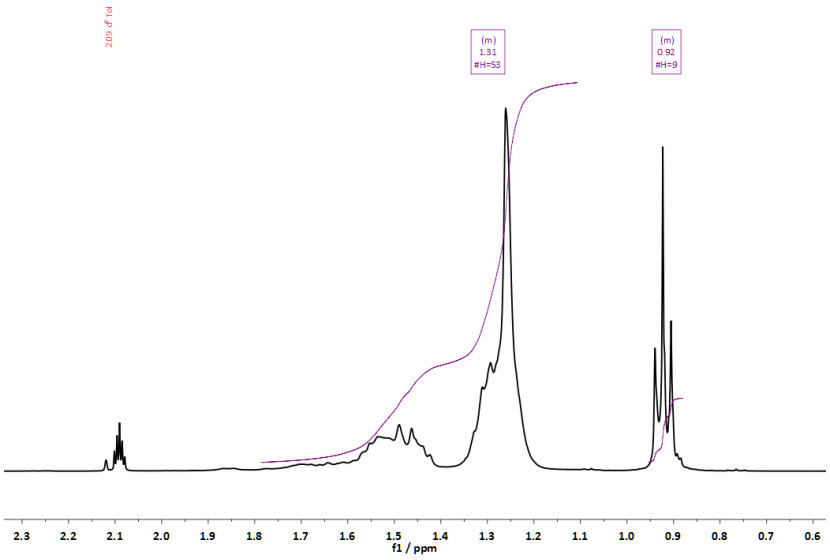

Solution state ^{1}H NMR of the by-products of the reaction to synthesise TOPrGO.

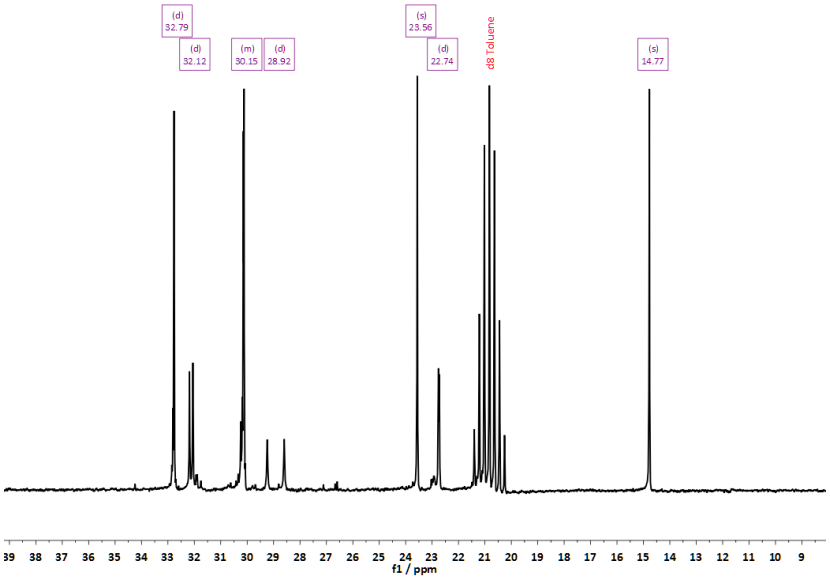

Solution state ^{13}C NMR of the by-products of the reaction to synthesise TOPrGO.

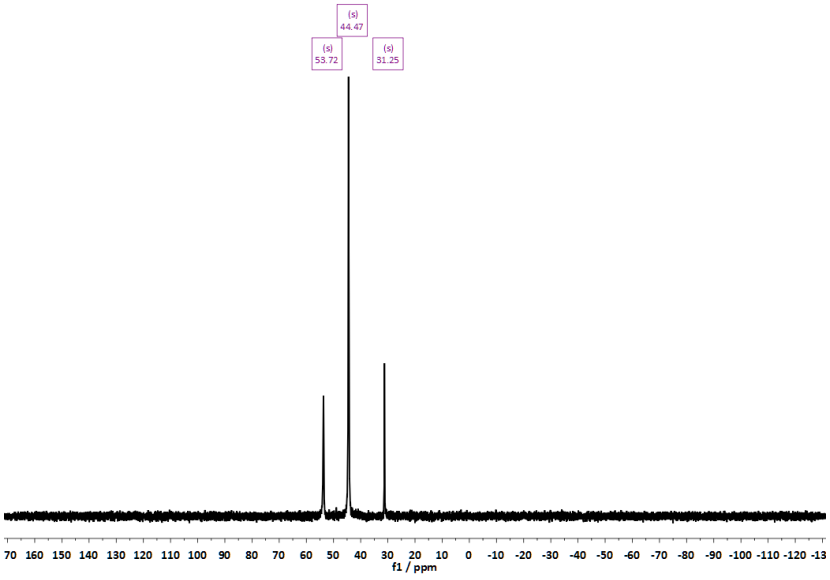

Solution state ^{31}P NMR of the by-products of the reaction to synthesise TOPrGO.

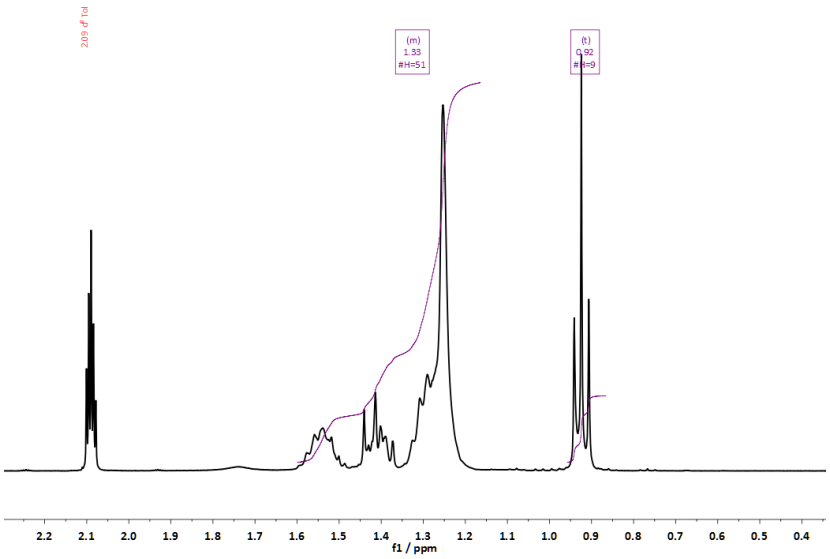

Solution state ^{1}H NMR of the by-products of the reaction to synthesise TOPOrGO.

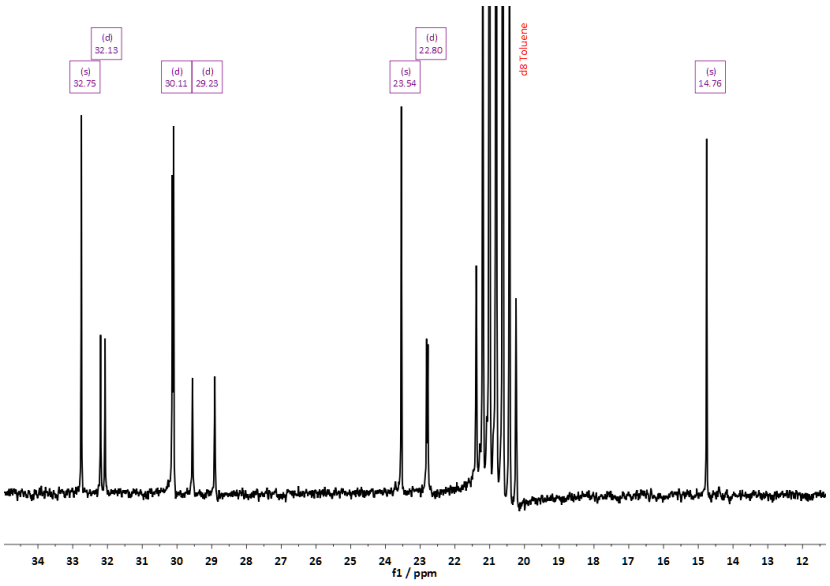

Solution state ^{13}C NMR of the by-products of the reaction to synthesise TOPOrGO.

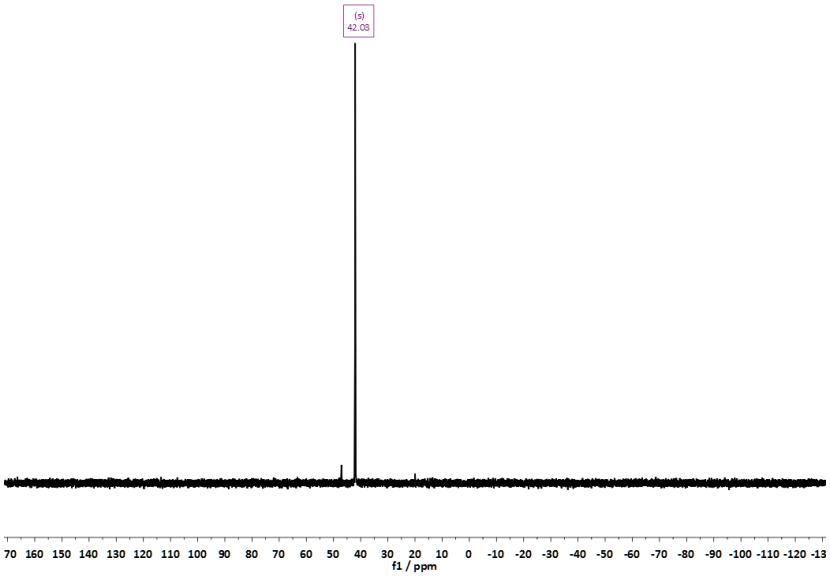

Solution state ^{31}P NMR of the by-products of the reaction to synthesise TOPOrGO.

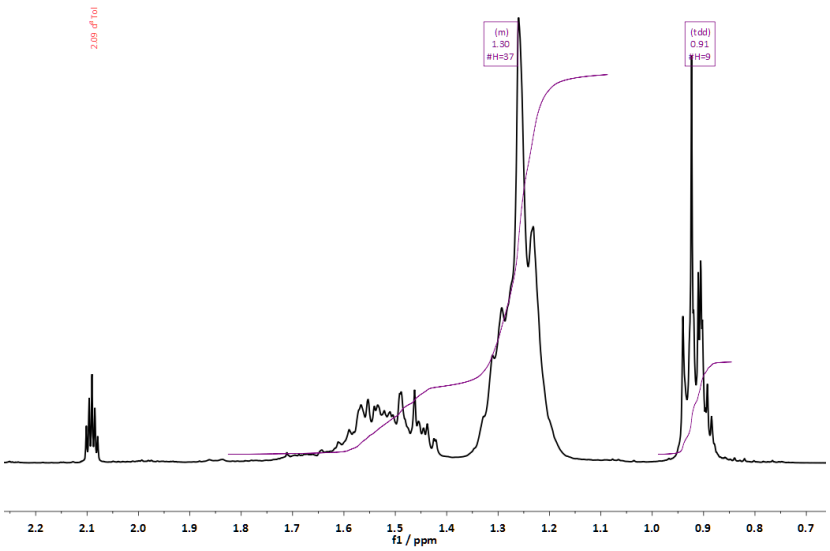

Solution state ^{1}H NMR of the product of the control reaction involving the heating of TOP.

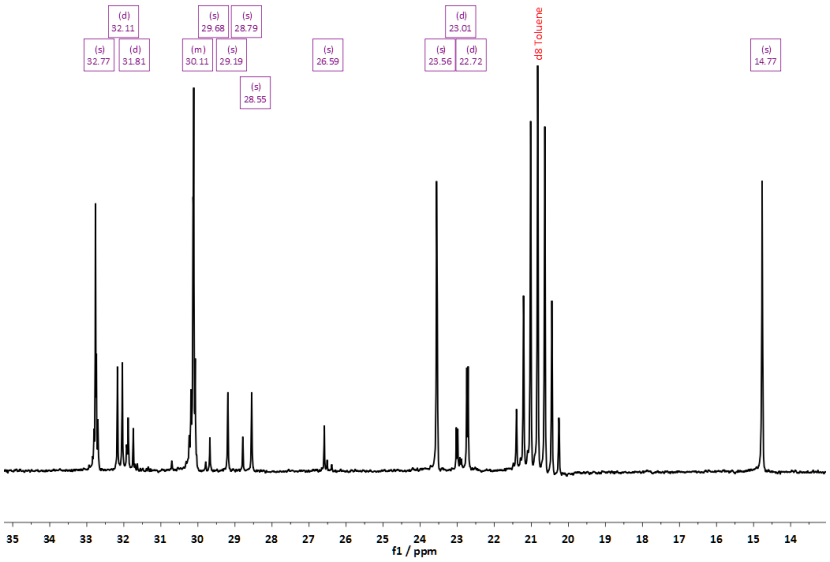

Solution state ^{13}C NMR of the product of the control reaction involving the heating of TOP.

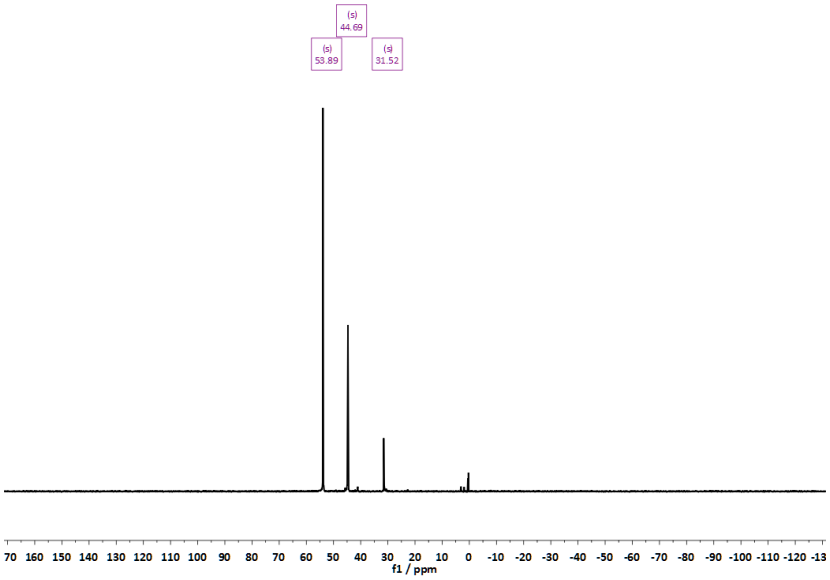

Solution state ^{31}P NMR of the product of the control reaction involving the heating of TOP.

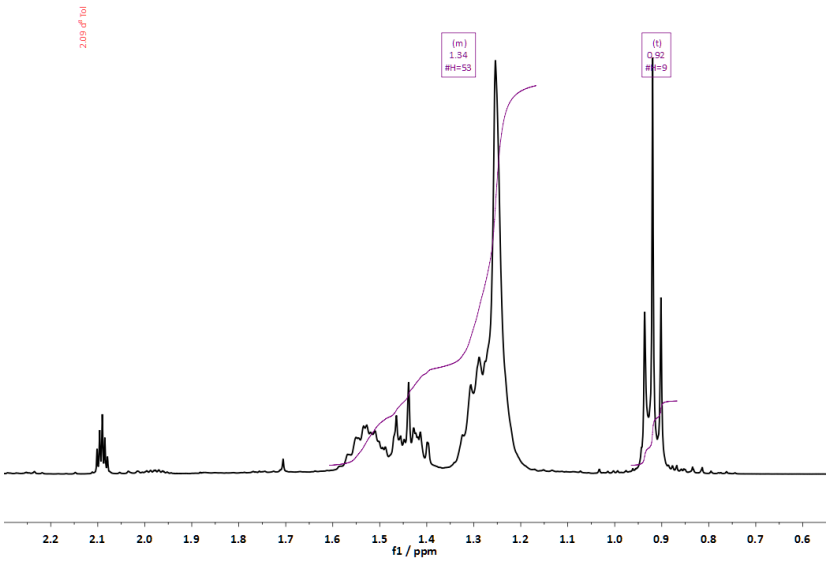

Solution state ^{1}H NMR of the product of the control reaction involving the heating of TOPO.

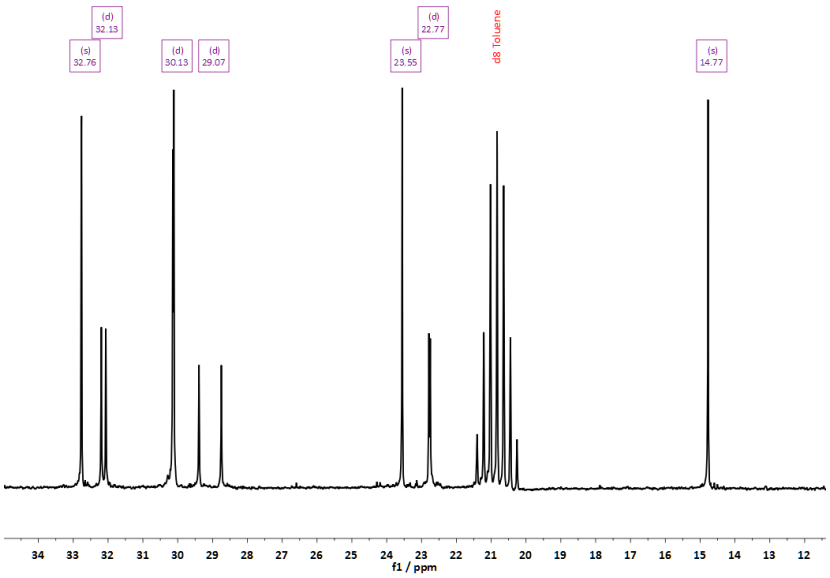

Solution state ^{13}C NMR of the product of the control reaction involving the heating of TOPO.

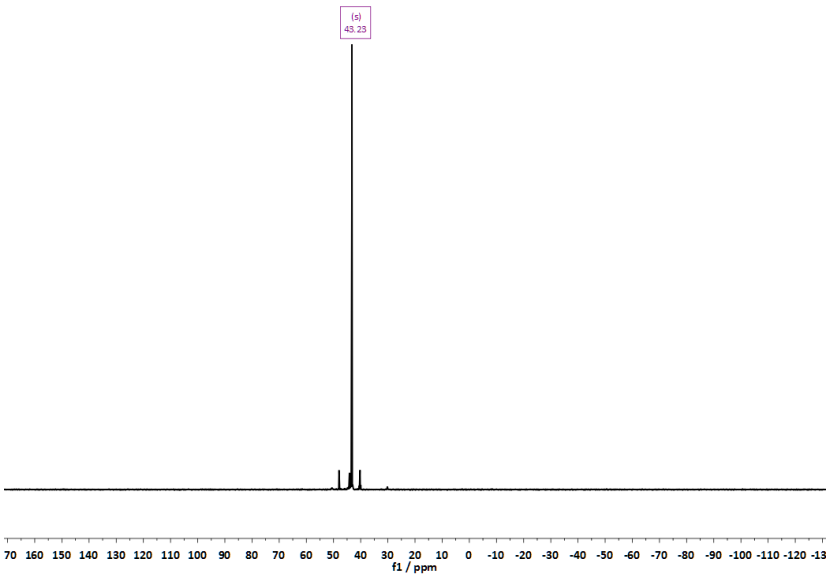

Solution state ^{31}P NMR of the product of the control reaction involving the heating of TOPO.